Nanoparticle Focussing Using Aerodynamic Lenses and a Divergent Nozzle

by

Hasan Jumaah Mrayeh

A thesis
presented to the University of Waterloo
in fulfillment of the
thesis requirement for the degree of
Doctor of Philosophy
in
Mechanical and Mechatronics Engineering

Waterloo, Ontario, Canada, 2021

Examining Committee Membership

The following served on the Examining Committee for this thesis. The decision of the Examining Committee is by majority vote.

External Examiner:	Chao Zhang Professor, Department of Mechanical & Materials Engineering University of Western
Supervisor(s):	Fue-Sang Lien Professor, Department of Mechanical & Mechatronics Engineering University of Waterloo
Internal Member:	Ehsan Toyserkani Professor, Department of Mechanical & Mechatronics Engineering University of Waterloo
Internal Member:	Carolyn Ren Professor, Department of Mechanical & Mechatronics Engineering University of Waterloo
Internal-External Member:	Omar Ramahi Professor, Department of Electrical & Computer Engineering University of Waterloo

Author's Declaration

I hereby declare that I am the sole author of this thesis. This is a true copy of the thesis, including any required final revisions, as accepted by my examiners.

I understand that my thesis may be made electronically available to the public.

Abstract

Since the COVID-19 pandemic has been a global crisis that has posed enormous and diverse challenges to humanity, it has revealed the urgent need for further study into a variety of properties of viruses, including virus particle size. The virus particle size ranges from 0.1 μm to 0.3 μm. As a result, based on the size of the COVID-19 virus particle, this thesis addresses the challenges encountered in focussing sub-300 nm nanoparticles using an aerodynamic lens and introduces a procedure for developing aerodynamic lens systems that can be used for measuring nanoparticle size. Perhaps this research will serve as a starting point for finding a solution or assist in the discovery of a cure for the global epidemic. The research undertaken for this thesis has also demonstrated how ANSYS Fluent (2021R1) software can be used for simulating a computational fluid dynamic (CFD) for an effective lens and nozzle configuration.

Employing ANSYS Fluent enabled the creation of a computational technique for developing and evaluating an aerodynamic lens and a divergent nozzle for focussing a flow that transmits particles as small as 300 nm through a sharp-edged plate orifice. A two-dimensional CFD for gas-solid flow based on the Lagrangian model for measuring the size of nanoparticles is presented. This study also introduces an advanced aerodynamic lens configuration with two sharp orifices rather than a conventional flat orifice. Because of their low inertia and high diffusivity, the focussing performance of conventional aerodynamic lenses degrades dramatically as particle diameters drop below 300 nm. For this work, theoretical and computational analyses for concentrating nanoparticles smaller than 300 nm were conducted. Fluent software, which automates lens configuration, was utilized for simulating the gas flow field and assessing the possibility of focussing sub-300 nm nanoparticles. The initial step was to devise a method for optimizing the lens dimensions and operating conditions involved in nanoparticle focussing. It was discovered that lighter carrier gases aid in the focussing of smaller nanoparticles and that multiple lenses performing at suboptimal Stokes numbers can focus a diverse range of nanoparticle sizes.

Additional developments included expressions for the operating pressure and lens measurements that decrease particle diffusion while maintaining subsonic flow. A new technique was also introduced in this study: the utilization of a novel model of pipe containing inside grooves that incorporate the size of the diameter and thickness of the lenses used in focussing the nanoparticles. The benefit of these grooves is that they enable the position of the lenses inside the pipe to be changed in case the lens needs to be moved to the left or right, if other lenses need to be added, or if only one lens is used for the same pipe employed in the experiment. As well, a computational simulation methodology was established for analyzing the performance of aerodynamic lens systems. Particle trajectory CFD was ap-

plied as a means of enhancing the lens and nozzle configuration. A technique for measuring the diameter of the nanoparticle (sub-300 nm) passing through an aerodynamic lens and divergent nozzle was also devised: nanoparticles are injected into the inlet and then passed through the aerodynamic lenses, and the nozzle throws them at 1 atm pressure.

A further outcome of this research was the development of a computational methodology for determining the exact focus characteristics of aerodynamic lens systems based on the use of the Lagrangian method for tracing particle trajectories. This work also entailed a comprehensive summary of the advancements and challenges associated with measuring the minimum nanoparticle size in an aerodynamic lens from the simulation perspective compared to the available experimental, computational, and numerical perspectives. The initial assumption was that the flow was continuous and subsonic, and the investigation determined the smallest particle size that can be accurately focussed on an axis with two lenses when consideration of diffusion is neglected. A systematic procedure was then described for facilitating the determination of the smallest particles that can be focussed. The final conclusion of this study is that the use of the Lagrangian method and improved aerodynamic lens design for the focussing of sub-300 nm spherical particles using a carrier gas (air) as the primary phase and carbon particles as the secondary phase is effective.

The simulation conducted revealed that lens performance is similar to that predicted by the design guidelines, indicating that the aerodynamic lens and divergent nozzle can focus particles as small as 300 nm. A nanoparticle lens system was computationally and theoretically designed, developed, and evaluated. Focussing was observed for particles ranging in size from 3 nm to 300 nm. The simulation results were compared with those of further detailed trajectory simulations based on CFD calculations published by Middha and Wexler and by Wang et al.. The model results were validated computationally based on a comparison of the simulation output with the available experimental data from the work of Tan et al. in order to verify the validity and efficiency of using the aerodynamic lens for measuring the size of sub-300 nm nanoparticles.

Acknowledgements

I want to express my sincerest gratitude to my advisor, Professor Fue-Sang Lien, for his guidance, encouragement, and support throughout my graduate studies. His insight, knowledge, and experience have been invaluable for this research. His personal integrity and devotion to science have been an enormously positive influence on me. It has been a privilege for me to learn both science and windsurfing from him during the years I have known him.

I truly appreciate all of my colleagues' help, valuable discussions, and friendship. I would like to thank Jason Benninger (Thermo-Fluids Lab Technician), Ben Tan, Wala Bkari, Professor Cecile Devaud, Jian Zou, Professor Jawad Muraih, Mr. Spencer Small (Engineering Counsellor), and Paul Boctor. I am very grateful to the members of the Examining Committee who kindly agreed to review this thesis: Professor Chao Zhang, Professor Omar Ramahi, Professor Ehsan Toyserkani, and Professor Carolyn Ren. I want to express my sincere appreciation to my lovely country (IRAQ), the Iraqi Ministry of Higher Education and Scientific Research, the Iraqi Cultural Attachés in Washington and Ottawa, the University of Al-Muthanna, and the University of Waterloo for their financial support. In addition, many thanks to Canada, the Canadian people, and the Canadian government; you have my love and respect.

Last but not least, I would like to thank my wife, Akbal Mrayeh, and children (Ali Ridha, Fatima, Zahraa, Mohammad, and Lujain) for their love, understanding, support, and sacrifice throughout the years of my graduate studies. I am also indebted to my parents and other members of my family for their ongoing support during my school years. This thesis research was supported financially by the Ministry of Higher Education and Scientific Research of the Republic of Iraq and by Al-Muthanna University in Iraq. The computational and experimental studies for this work were carried out with the use of resources provided by the University of Waterloo.

Dedication

(To my dear parents and siblings, my beloved my wife and my children)

Table of Contents

List of Figures

List of Tables

Chapter 1

Introduction

Focussing based on aerodynamics is a principle broadly utilized for generating nanoparticles in the form of narrow beams using what is termed an aerodynamic lens, an approach that has been developed by a number of investigators [87, 88]. During the last decade, aerodynamic lens systems have revolutionized the mechanical and chemical processing of aerosol particles through the use of mass spectrometers [27]. Based on the focussing of nanoparticles taken from the air, a typical aerodynamic lens application is used for providing input to an aerosol mass spectrometer [34, 62, 78, 125, 124, 132, 134, 143, 56, 151], for nanostructured material synthesis [157, 166, 110, 47, 22], and for microscale device fabrication [113, 31, 43, 29]. Since particle beams were first invented by Murphy and Sears [103], the technology of concentrating beams of nanoparticles in a wider size range using an aerodynamic lens has been found valuable in several applications, including micropatterning and material synthesis [126, 143], inlets in biomaterial structures [56], smooth metal thin films[151], and nanoparticle mass spectrometers [41, 124].

A variety of advanced studies have reported lens systems designed to work under conditions significantly different from those employed by many of the original researchers [87, 88]. Liu et al. [87, 88] have demonstrated

that aerodynamic focussing has a variety of applications, including enhancing transport efficiency, improving measurement resolution, and the precise depositing of micropatterns on a substrate. Numerous researchers have also developed high-pressure aerodynamic lens systems (2,500 Pa to 20,000 Pa) for nanoparticle measurement studies [124, 126, 125]. While numerous numerical, theoretical, and experimental investigations of aerodynamic lens systems have been conducted by a number of researchers, and their simulations have been repeated by multiple additional investigators using a compressible flow model [162, 163, 87, 88], detailed computational and experimental studies are still needed in order to describe the performance of an aerodynamic lens system.

Previously, typical aerodynamic lens designs have been commonly used for focussing large particles, but focussing small nanoparticles presents a significant challenge (a nanoparticle is a small particle that ranges between 1 nm and 100 nm in size). Because of their low levels of inertia, small nanoparticles follow the gas streamlines, and only a small fraction of them can be focussed. Nanoparticle defocussing is caused by their high degree of diffusivity, which causes beam widening and particle loss. The key aspect of this study is the modification of the aerodynamic lens system fabricated by Middha and Wexler (2003) [97] and by Wang et al. (2005) [152] and compared with the experimental data from the work of Tan et al. (2015), (2007) [141, 138], combined with the use of ANSYS Fluent software (2021R1) for evaluating the focussing system of an aerodynamic lens. Because of the wide applications for aerodynamic lenses, this thesis illustrates the development of aerodynamic lenses-nozzles through the use of computational fluid dynamics (CFD) software ANSYS Fluent for simulating a gas flow field and evaluating the possibility of focussing sub-300 nm nanoparticles in order to provide a reliable and quick lens evaluation and a useful design.

The first step is to define the computational relations applied for designing aerodynamic lens-nozzle dimensions. A typical aerodynamic lens

nozzle gradually focuses spherical particles ranging from 3 nm - 300 nm. As well, most of the lens systems currently utilized are the same design as the system described by a number of previous investigators [87, 88]. The validation of the lens design is next reported based on a comparison of the predictions with some of the detailed computational and empirical studies described in the literature. The results of these comprehensive calculations have been established and are included in the design orifice specified in this thesis. In contrast, an aerodynamic lens system consisting of two orifices inside a cylindrical pipe has been designed, which permits the simultaneous focus of a variety of nanoparticle sizes [152].

Since the mechanisms involved in particle size measurement using aerodynamic lenses as orifices have been extensively studied in order to characterize nanoparticle focussing, a goal of this research was to determine whether a size measurement technique for nano-sized particles can be established using a series of commercially available aerodynamic lenses.

1.1 Research Problem and Contributions

1.1.1 Problem Statement

The concept of using an aerodynamic lens for nanoparticle detection has received significant attention and extensive investigation from a number of research groups over the past two decades, due mainly to the several advantages aerodynamic lens techniques can offer, such as low cost and ease of fabrication [125, 124]. Because these techniques are based on the inertial and diffusional properties of the particles [134, 143], they also provide greater sensitivity and the ability to detect small particles.

The problem is that using fewer than two lenses for detecting small nanoparticles (ranging in size from 1 nm to 100 nm) and focussing them in

order to measure their sizes is difficult. A challenge therefore arises when the measurement of nanoparticle sizes with the use of one or two lenses is attempted. However, the research presented in this thesis has addressed this challenge through the development of an enhanced aerodynamic lens design that represents an improvement over one consisting of a conventional flat orifice. ANSYS Fluent was used for simulating a CFD that would produce an efficient lens and nozzle design. This thesis presents a two-dimensional CFD for a gas-solid flow based on the use of the Lagrangian model for measuring nanoparticle size. This model is a pipe containing inside grooves that match the diameter and thickness of the lenses used for focussing the nanoparticles. The benefit of these grooves is that they enable the position of the lenses inside the pipe to be changed in case the lens needs to be moved to the left or right, if other lenses need to be added, or if only one lens needs to be used for the same pipe employed in the experiment. This design also permits lenses to be used in the inlet and outlet. Depending on the length of the pipe and the number of grooves inside it, it can therefore be used as either a long or a short pipe.

Benefits for future research include the ability to use one or two lenses to detect and focus small nanoparticles in order to measure their sizes. This advantage is important because of its possible role in addressing the concerns that have been raised about the potentially harmful effects of nanoparticles on the environment and human health. Nanoparticles can have adverse health consequences because of their effect as particles or as carriers of toxic elements. Nanoparticle exposure could lead to numerous harmful health conditions, such as aortic and other heart diseases, stroke, chronic bronchitis, respiratory tract infections, and asthma.

1.1.2 Research Objectives

This research was targeted at an examination of aerodynamic lenses for nanoparticle focussing and their simulation. To this end, the primary objectives of this work included the following:

1. **Develop** a model of an axisymmetric orifice as a useful tool for efficiently focussing nanoparticles with a size smaller than 300 nm.
2. **Design** a nozzle that can provide stability to the fluid inside the pipe so that the fluid velocity is close to the sonic speed and the nanoparticles can be detected after they pass through the lenses in order to focus the particles.
3. **Design** grooves within the pipe to hold the orifices and the installed inlet and outlet lenses.
4. **Acquire** a basic understanding of the factors that affect the fluid (air) containing the nanoparticles (carbon), whose diameters range from 3 nm - 300 nm and which pass through two lenses and one divergent nozzle.
5. **Propose** a method for measuring the size of nanoparticles in the air using an orifice that focusses on small nanoparticles.
6. **Measure** nanoparticle sizes and characteristics.
7. **Validate** the aerodynamic lens design through the computational method and compare it with other available experimental data.

The goal of the research presented in this doctoral dissertation thesis was to implement a method for modelling an aerodynamic lens by passing nanoparticles across the orifices. Different techniques available for modelling and designing an aerodynamic lens were examined, and the most promising

approach was used as a basis for implementation. The aim was to produce a technique that would meet the following requirements:

1. It would work as a model within existing CFD solvers.
2. For the purposes of this research, it would enable the modelling of an aerodynamic lens based on the use of two orifices and one divergent nozzle.
3. It would be effective with a multiphase model through the application of the Lagrangian method.

The new approach was implemented using a method chosen to work with a commercial CFD solver: ANSYS Fluent. The method presented in this thesis is limited to two-dimensional modelling. The simulation results were compared with the findings from other simulations (with the findings from the work of Middha and Wexler [97] and Wang et al. [151]), including the experimental data from the work of Tan et al. [141, 138].

1.1.3 Novelty of the Work Presented Here

The work presented in this thesis was targeted at filling gaps in both the understanding of flows through aerodynamic lenses and the ability to provide a computationally efficient and accurate model that can be used for measuring the size and axial velocity of nanoparticles. The result was an extension of the predictive abilities of ANSYS Fluent modelling to provide enhanced capabilities beyond what was previously achievable, on a scale massive enough to enable the creation of an aerodynamic lens system with sufficient resolution to be employed for design optimization.

The novelty of the results presented here is apparent in two distinct areas, which are briefly introduced and identified below. With respect to

the first benefit, the study of aerodynamic lens geometry has not yet been thoroughly researched, either computationally or experimentally. A better understanding of the impact of these geometries can now be applied for designing and developing a new generation of efficient aerodynamic lens system enhancements. The second area is related to the current lack of a complete modelling methodology capable of reducing the number of aerodynamic lenses required for focussing small nanoparticles under variable flow conditions and at the same time immediately incorporating detailed results into an aerodynamic lens system. The use of ANSYS Fluent for simulating the model means that the development and introduction of this model provides a new analysis tool that expands the ability of predictive performance modelling. The new tool requires no a priori manufacturing and testing data, thus shortening the development cycle and significantly reducing prototyping costs by avoiding the costly manufacture of fabrication tooling.

The enhanced understanding of aerodynamic lens characteristics acquired through the completion of the work described here offers new insights into lens development within these geometries, the experimental validation of computationally observed phenomena, and a method for incorporating these data into a more complete aerodynamic lens system upon completion of the current work. This study was conducted not only to fulfil the requirements necessary for designing and developing aerodynamic lens systems but also to demonstrate the ability of ANSYS CFD codes with respect to the accurate and consistent prediction of aerodynamic lens performance for a wide range of particle-focussed aerodynamic lens systems that make use of a variety of technologies for detecting and measuring particle size.

1.1.4 Research Approach

Although a variety of studies have been related to the focussing of nanoparticles with an aerodynamic lens, researchers remain uncertain about the effect of orifice size on the focussing of nanoparticles, a deficit that manifests as an obstacle to the capture of small nanoparticles by a conventional aerodynamic lens. Identification of nanoparticle properties (physical and chemical properties as well as their unique size, shape, and structure) will help provide an understanding of the approach involving the focussing of nanoparticles with an aerodynamic lens, leading to the design of a lens that can avoid shock formation in an orifice, an effect that degrades the focussing performance of that orifice. Assumptions that underlie such an approach to nanoparticle focussing with an aerodynamic lens include consideration of neutral particles and the absence of shock formation in the orifice. For the development of an aerodynamic lens model, which was the goal of this research, these assumptions required either verification or disproving. The aerodynamic lens model under study in this research was modified to take into account consideration of these parameters, including avoidance of shock formation.

An additional factor is that previous studies of nanoparticle focussing with an aerodynamic lens model also failed to include consideration of the effects of particle parameters such as shape, charge state, material, aggregation, and gas characteristics such as temperature, density, velocity, and pressure. The reality is that these features affect the diameter and simulation data, thus making their consideration essential for the development of an application appropriate for all scenarios.

1.2 Dissertation Outline

The first element in this research was the design of a systematic technique for improving lens specifications and operating conditions in order to address the issues related to the low levels of inertia and high degree of diffusivity associated with nanoparticles so that an aerodynamic lens-nozzle system for focussing nanoparticles could be built. An aerodynamic lens system was then devised for focussing particles smaller than 300 nm. Extensive computational simulations and experimental evaluation (using available experimental data [141, 138]) were applied for investigating the performance of the aerodynamic lens-nozzle system. The final step was to parameterize the modelling process and introduce it into the aerodynamic lens-nozzle design tool so that the convenience and performance of the lens design could be tested and the effects of the tests and computational simulations be established. Figure 1.1 depicts the overall structure of this thesis.

The thesis is divided into nine chapters. Chapter 1 introduces and outlines the research problem and explains the motivation, problem statement, research objectives, novelty of the work, and research approach. These considerations served as the foundation for the thorough literature review presented in Chapter 2, which also includes background information about the sources and properties of nanoparticles and aerodynamic lenses. Historical and current applications of the design and numerical simulation of aerodynamic lens systems are also presented. Chapter 3 discusses several aspects of the general theoretical background underlying multiphase flow simulation and describes two numerical methods for detecting solid particles: Eulerian and Lagrangian. The theory that articulates nanoparticle motion in aerodynamic lenses and a divergent nozzle is presented in Chapter 4. As a preliminary to an explanation of the measurement of the flowrate and pressure decrease across orifices, a theory of the fluid flow through aerodynamic lenses and then through a divergent nozzle is first detailed. With

respect to focussing nanoparticles, a systematic procedure for optimizing operating conditions and lens measurements is then defined.

CFD simulations are set out in Chapter 5, which also covers the modelling and effects of laminar flow; the general principles of multiphase flow simulation using the Lagrangian method; and techniques related to a theoretical method, computational research, and data analysis. The computational simulation technique used for accurately characterizing the focussing performance of aerodynamic lens-nozzle systems is described in detail in this chapter. The flow field is obtained by solving Navier-Stokes equations, and the particle trajectories are determined by solving Lagrangian equations. As a result, the Lagrangian method was chosen for the simulation since it is only utilised on rare occasions when the purpose is to predict particle trajectories. Based on the procedure itemized in Chapter 4, this simulation method was then used for evaluating the performance of an aerodynamic lens system designed to focus sub-300 nm nanoparticles. The effects of the carrier gas, particle density, and lens design on focussing efficiency were investigated. The design of grooves within the pipe to hold the orifices, and the installed inlet and outlet lenses is explained in Chapter 6. This method parameterizes the knowledge about aerodynamic lenses that has been gained from the simulations and experiments, thus allowing the quick and convenient design of lens systems.

The experimental setup used for studying nanoparticle focussing is described in Chapter 7, which also explains the experimental validation of the model through a comparison of the simulation results with the experimental data in order to verify the validity and efficiency of the aerodynamic lens used for measuring the size of sub-300 nm nanoparticles. The research presented in this thesis is summarized in Chapter 8, which also lists recommendations for future research. It should be noted that Chapters 3 to 7 of this thesis contain material that has previously been published or submitted for publication in peer-reviewed journals. With some editing modifications,

all of these Chapters have been treated as standalone papers. References for the original papers are provided under List of Publications at the end of Chapter 8 (Chapter 9). The final elements of the thesis are the references and appendices (Appendix A and Appendix B).

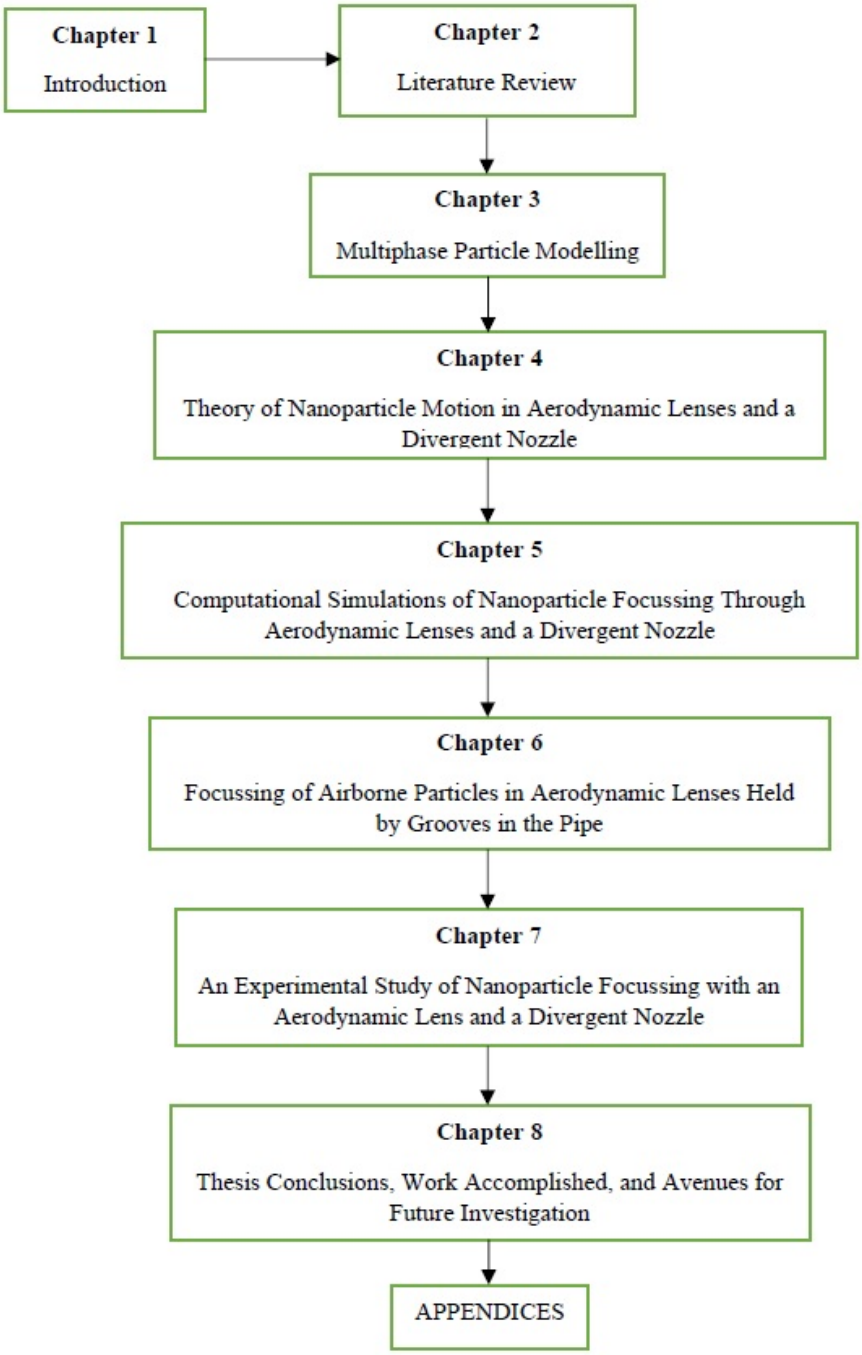

Figure 1.1: Overall structure of this thesis

Chapter 2

Literature Review

2.1 Introduction

ANSYS Fluent software (2021R1) is a useful computational simulation tool for studying the interactions of aerodynamic lenses with nanoparticles, thus providing opportunities for improving design concepts related to the detection and measurement of particle size. Advancements in aerodynamic lens design have enhanced the effectiveness of computational tools with respect to evaluating new nanoparticle detection or measurement concepts. In this regard, this chapter begins with an explanation of the sources and properties of nanoparticles and ends with a summary of the problem definition. An introduction to the basic concepts related to these areas is also included, along with outlines of prior related studies.

2.1.1 Nanoparticle Sources

Air pollution can include an excess of chemicals, complex mixtures of gases, liquids, particulate matter, or biological materials in harmful amounts. Other substances that are considered major air pollutants are (SO_2), (O_3), (CO), (NOx), and (VOCs). However, the most common type of air pollutants are

nanoparticles, a term that refers to a complex mixture of small airborne particles generated from a variety of sources [45], such as transportation, industry, urban activities, agricultural burning, dust particulates, volcanic emissions, combustion, cooking, heating, polymers [101], cleaning, laser printers [149], photocopiers, agriculture [17], welding, sea spray [17], and land use. Advances in nanotechnology [95] have led to the generation of other examples of nanoparticle sources: drug delivery [61], injections, inhalable medicines, and tracers.

Since the end of 2019, the COVID-19 epidemic has been a worldwide crisis, posing enormous and diverse challenges to humanity. The epidemic has negatively impacted on public health systems and harmed socio-economic development globally. Henry [53] demonstrated the sources of atmospheric particles and their effects on public health. The COVID-19 pandemic is a harsh reminder that viral dynamics are frequently a narrative of numbers, whether in a single human host or a wave of infection across continents [71]. Furthermore, the COVID-19 pandemic has exposed the urgent need for more studies into a variety of characteristics of viruses, including virus particle size. COVID-19 viruses, which are carried by air, are a significant family of human and veterinary pathogens that may cause enteric and respiratory illnesses. Respiratory failure, gastroenteritis, nephritis, hepatitis, encephalitis, and progressive demyelinating illness are all symptoms of COVID-19 virus infection [105].

The most attractive characteristic of nanoparticles is their small size, which also determines their behaviour [54]. However, their small size also makes for extensive interaction with biological systems [72, 109, 119, 72, 38]. Concerns have been raised regarding the possible adverse impact of nanoparticles on the environment and human health due to the effects of the particles themselves or to their role as carriers of toxic elements [149, 38, 108, 144]. While large nanoparticles are less toxic than small ones because of their larger size and smaller total collective surface area [107, 109, 119],

structured nanoparticles that are smaller than cells can penetrate those cells, and since nanoparticles are not separated from the upper respiratory tract, they are inhaled into deeper areas of the body [18, 94, 107, 145]. Some researchers have shown that the airborne COVID-19 virus exhibited a bimodal distribution in Fangcang Medical Staff Area, with "sub-micron aerosols" (0.25 μm - 0.5 μm aerodynamic diameter) likely from protective apparels and "super-micron aerosols" (>2.5 μm aerodynamic diameter) [90]. Because of what the world is currently suffering from the COVID-19 pandemic, so that, since 2021, variants of the virus have emerged or become dominant in many countries, with the Delta, Alpha and Beta variants being the most virulent. As of 5 September 2021, more than 220 million cases and 4.56 million deaths have been confirmed, making it one of the deadliest pandemics in history (*www.cbc.ca*). Virus particle size ranged from 0.1 μm to 0.3 μm. Images of COVID-19 particles taken with a cryo-EM revealed enveloped and spherical shapes, as shown in Figure 2.1:

As a result, based on the size of the COVID-19 virus particle, this research will investigate particle sizes ranging from 1 nm to 300 nm. Perhaps this research will serve as a starting point for finding a solution or assist in the discovery of a cure for the global epidemic.

The consequences of all of these factors are that nanoparticle exposure can result in numerous adverse health effects, such as aortic heart disease and other heart disorders, stroke, chronic bronchitis, respiratory infections, and asthma [84, 96, 45]. Nanoparticles that have been charged have a five to six times higher accumulation in the lungs and cause more negative health effects [100]. The hope is that minimizing nanoparticle exposure in enclosed buildings (houses, offices, or nanotechnology labs) and personal exposure at an occupational level might provide adequate protection against nanoparticle exposure [45]. As a result, nanoparticles have very high solid deposits (more than 90 %) in the alveoli, for example, and are also distributed through blood flow [18, 94, 107, 145].

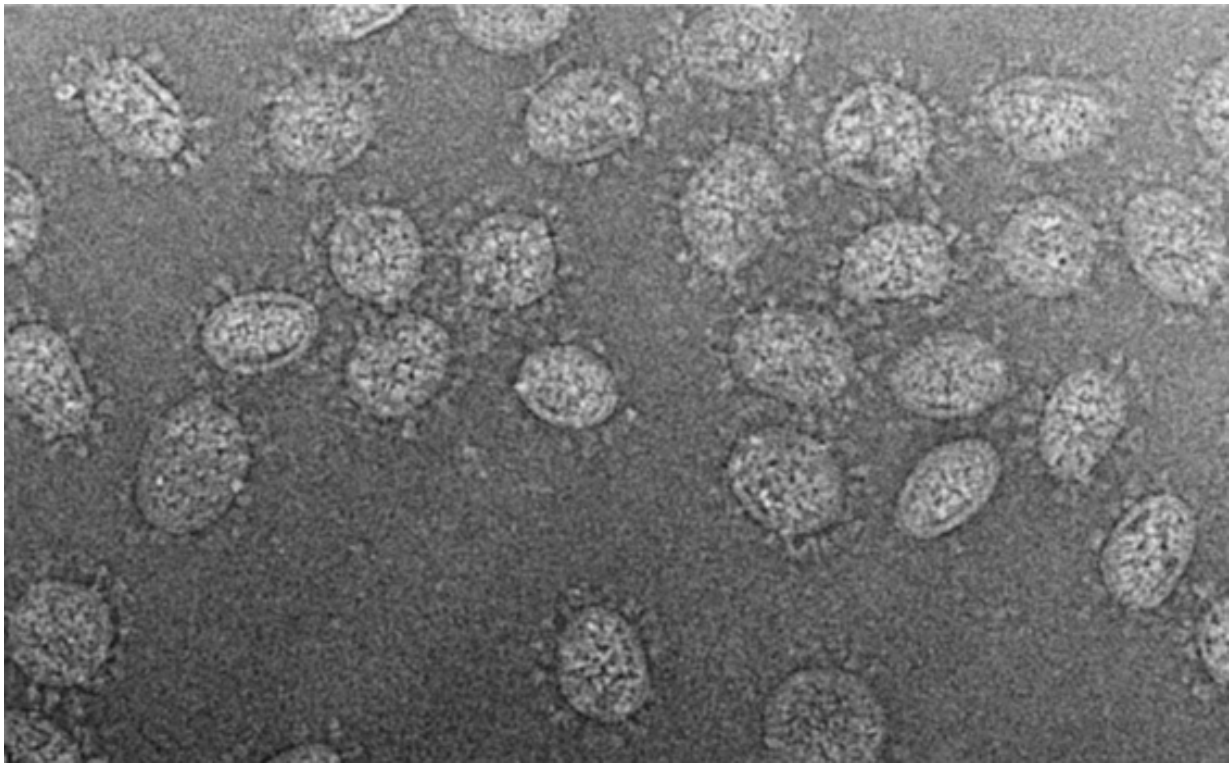

Figure 2.1: Cryo-EM of corona viruses in vitreous ice [105]

Nanoparticles have also become relevant in technological innovations that rely on their small size. Almost all online particle sizing and chemical analysis methods make use of particle beams. Ever since they were first produced by Murphy and Sears [103], particle beams have been used in a variety of particle research fields. A number of researchers have employed particle beams for aerosol particle analysis. In their work, Hall and Beeman [49] used particle beams to study secondary electron emission from polystyrene latex sphere beams. Allen and Gould [7] used particle beams for the spectrometric analysis of individual aerosol particles, and Seapan et al. applied them as a means of measuring the fundamental properties of aerosol particles. Sinha and Friedlander [130] employed particle beams to measure the mass distribution of chemical species in a polydisperse aerosol. Dhaneke

and Flachsbart [24] developed techniques for producing specific beams for measurement purposes: aerosol beam focussing (ABF) and aerosol beam spectrometry (ABS). These techniques can be used for determining the distribution and chemical composition of various sizes of aerosol particle intervals. In their work, Estes et al. [39] explored the characteristics of a capillary-generated particle beam.

In these methods, the particle beam is generated by expanding a gas-particle suspension through a single orifice or through multiple orifices. Israel and Friedlander applied this type of method to produce a particle beam with particle sizes ranging from 126 nm to 365 nm [58]. Liu et al. employed both theoretical and experimental techniques to study particle beams generated by an aerodynamic lens-nozzle expansion [87, 88]. The calculations of these researchers provided valuable knowledge about the variables that influence both beam performance and particle terminal velocity (number of lenses, lens-nozzle geometry). However, the work of Liu et al. was limited to particles near the axis and to small particles (dp $<$ 250 nm) [87, 88]. In their calculations, the flow fields in the aerodynamic lenses were assumed to be incompressible or isentropic, while the supersonic free-jet expansion through the nozzle was calculated using a quasi-one-dimensional approximation and an analytical expression like the one used in the method developed by Dahneke and Cheng [25, 20]. Liu et al. centralized particles to an area close to the axis by causing the gas-particle suspension to pass through a series of orifices (referred to as an aerodynamic lens system) before expanding the gas into a vacuum through a final nozzle [87, 88].

Particle beams with lower divergence angles are extremely useful in a wide range of applications. Particle beams with controllable measurements and divergences are used in almost all online particle sizing and chemical analysis techniques. The particle beam is produced in these techniques by expanding a gas-particle suspension via single or multiple orifice systems. With respect to the maximum beam divergence appropriate for existing

particle measurement devices, single nozzle systems are inadequate. Typically, particle size is determined by calculating particle time-of-flight over a given distance using light scattering. This calculation is used to compute the particle terminal velocity, which is then applied in order to determine the dimensions of the particle. Tafreshi et al. [135] designed a new aerodynamic nozzle configuration for producing low-divergence cluster beams. To achieve their aerodynamic focussing effects, they fixed a simple aerodynamic lens in the pipe, and studied the resulting collimation and cluster mass selections.

An aerodynamic lens system has been shown to perform the same function as a sheath flow without slowing the particle-sampling process or complicating gas handling. Interest in aerodynamic lenses has grown in recent years because collimated particle beams have made it possible to measure the size and composition of particle samples online [64]. Mallina et al. discovered that only particles within a narrow size range (referred to as the maximum collimation diameter) are effectively collimated, and even such maximally collimated particles have a divergence angle in the order of 0.008 rad [93]. These measurements are critical for identifying the source of atmospheric particles as well as their impact on human health [53].

2.1.2 Nanoparticle Focussing

A specific research objective was to create an aerodynamic lens system (ALS) designed for focussing a nanoparticle size to the smallest possible diameter while keeping the computational and experimental setup straightforward and easily adaptable to different samples. Designing lenses with these capabilities ensures that a greater number of particles can pass through them, resulting in more particles that can be focussed as they cross through the lenses. Roth et al. [120] created a three-lens system for focussing 500 nm particles in this way, as illustrated in Figure 2.2 [120].

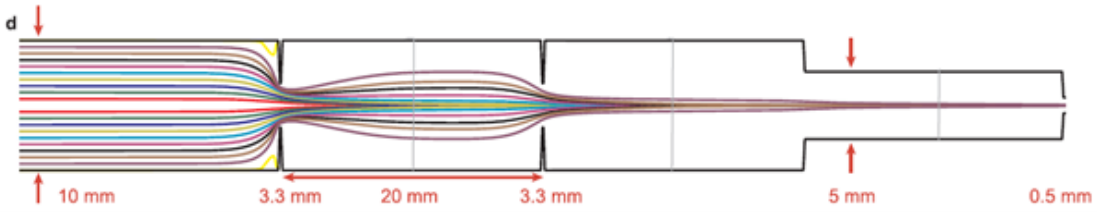

Figure 2.2: Three-lens-system for focussing 500 nm particles [120]

Mallina et al. [93] demonstrated that the narrow-beam diameter produced by a nozzle is normally limited to a very small range of particle diameters. Zhang et al. [162] developed a five-lens system with a nozzle inlet for focussing 500 nm particles and showed that the measured trajectories of 500 nm particles like the ones depicted in Figure 2.3 provide a fundamental explanation of the factors that control the formation of a beam containing particles with diameters ranging from 5 nm to 10,000 nm [162].

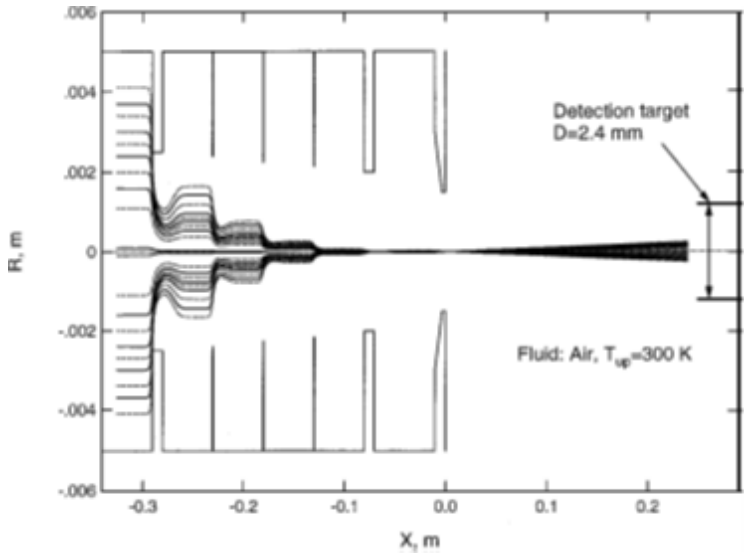

Figure 2.3: Schematic of an aerodynamic lens system and nozzle inlet showing the calculated trajectories of 500 nm particles [162]

Liu et al. [87, 88] conducted the first detailed computational and ex-

perimental analyses of aerodynamic lenses. They demonstrated that highly collimated particle beams could be generated without the use of sheath air. When particles within a critical size range (the minimum particle size) pass through a contraction, they drift toward the axis and can be collimated to form a focussed beam through the connections of a series of aerodynamic lenses. Liu et al. [87] used the incompressible and compressible axisymmetric Navier-Stokes equations as well as a one-dimensional experimental correlation for flows downstream from the nozzle in order to determine the flow field in the lens and the attached nozzle.

However, the aim of the work presented here was to design an aerodynamic lens model. For this study, nanoparticles were produced through the sonic expansion of airborne particles to a vacuum by means of two lenses and a single divergent nozzle. It has been shown that beam divergence can be greatly decreased if, prior to the sonic expansion to vacuum, the airborne particles are moved through an aerodynamic lens system consisting of two lenses and a single divergent nozzle. For this reason, a numerical investigation was directed at examining nanoparticle motion in expansions of an airborne particle suspension using lenses and a divergent nozzle. This study also involved an exploration of particle motion through two lenses and sonic expansion to vacuum through a divergent nozzle. This designed aerodynamic lens-nozzle inlet system is detailed in Figure 2.4.

Since aerodynamic lenses and an isolated divergent nozzle are the fundamental components of any aerodynamic lens-nozzle inlet system, a basic understanding of these components is needed for designing an inlet system with the desired sampling rate, collimation, and transmission properties. When a gas is subsonically contracted and expanded into an orifice, the belief is the corresponding nanoparticles will follow the fluid streamlines if the nanoparticles have less inertia than the gas. Real nanoparticles, on the other hand, may be displaced against the axis of symmetry or may affect the front surface of the lens. The first of these consequences causes

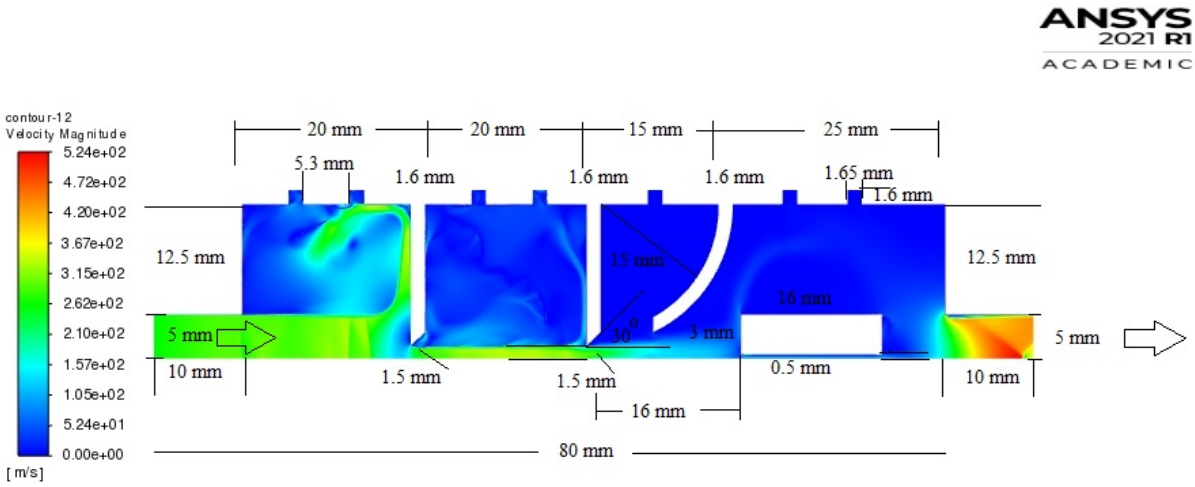

Figure 2.4: Details of the optimized aerodynamic lens-nozzle inlet system used in this study

nanoparticle collimation near the axis, while the second leads to the loss of nanoparticles. Maximal nanoparticle displacement occurs at the Stokes number of the particle, St, and major impact loss starts at $St \geq 1$.

Other essential parameters are the dimensionless geometry of the lens and the Reynolds number of the flow. It has been discovered that when a gas containing suspended particles is supersonically expanded to the vacuum via a nozzle at the operating pressure of the lens, the divergence of a nanoparticle beam is a function of the Reynolds number, the nozzle geometry, and the Stokes number of the particle. More precisely, additional findings have revealed that a stepped nozzle helps minimize beam divergence in general and that nanoparticle velocity scales with the speed of sound [162]. For these reasons, this research entailed the development of a model of the axisymmetric orifices as a useful tool that can efficiently focus nanoparticles with a size smaller than 300 nm. This objective was achieved through the construction of a focussing and measurement system

consisting of two aerodynamic lenses and a divergent nozzle, and through the acquisition of a basic understanding of the factors affecting the fluid (air) containing nanoparticles (carbon) with diameters ranging from 3 nm to 300 nm. The process was enhanced by the inclusion of fabricated grooves inside the top and bottom of the pipe, thus shortening the development cycle and significantly reducing prototyping costs by avoiding the costly manufacture of fabrication tooling. An additional feature of this research is two-dimensional computational fluid dynamics (CFD) for a gas-solid flow based on the Lagrangian model for measuring the size of nanoparticles.

2.2 Principles of Particle Dispersion

Particle dispersion can be divided into three distinct processes: mixing, spreading, and bulk transport. The method of generating a homogeneous mixture, usually of two or more particle streams, is known as mixing. Spreading occurs as particles move through unoccupied regions where particle focussing then decreases as a result of the spreading. The final process is bulk particle transport from one field to another. Although any of these modes of dispersion can happen independently, in the case of particle-laden jets, all three take place at the same time [10]. When the Lagrangian method is used for measuring particle dispersion, several different forces must be determined concurrently in order to produce the resulting trajectory vector for a given time step. Moreover, these forces are classified as the most important forces acting on a particle. While these forces can have a substantial cumulative effect on particle trajectory, the extent to which each force influences particle motion is dependent on a variety of factors, including the size and density of a specific particle.

2.2.1 Drag Forces

One of the most critical forces acting in multiphase flows is the drag force. The standard method for calculating drag force is as follows:

$$\overrightarrow{F}_{drag} = C_D \frac{\pi}{8} \rho_c d_p^2 \overrightarrow{U}^2 \tag{2.1}$$

Where C_D represents the drag coefficient, ρ_c the continuous phase density, d_p the particle diameter, and $\overrightarrow{U}$ the particle velocity. The value of the drag coefficient, C_D, varies depending on the particle and flow properties, remaining roughly constant at $C_D = 0.44$ for large particles (Rep > 1000) since the effects of the inertia of the particle are dominant in this range. This region is commonly referred to as the Newtonian region. At the other end of the spectrum, for very small particles (Rep < 1), the presumption is that the effects of the inertia of the particle are negligible compared to the magnitude of the viscous forces. In this case, the drag coefficient is written as in Equation 2.2:

$$C_D = \frac{24}{Re_p} \tag{2.2}$$

For particles where ($1 <$ Rep < 1000), experimentation has revealed that the drag coefficient can be calculated according to Equation 2.3 [54]:

$$C_D = \frac{24}{Re_p} \left(1 + 0.15 Re_p^{0.687}\right) \tag{2.3}$$

2.2.2 Particle Trajectory Equation

The Lagrangian method was used to obtain particle trajectories. To consider Brownian diffusion in Lagrangian studies, the random Brownian force,

as well as the friction, must be included in Newton's equations of motion. The Langevin equation is the fundamental equation, and it incorporates both frictional and random forces [73]. Where Brownian motion is the random motion of a small particle immersed in a fluid. When the effects of Brownian force and drag force must be taken into account, Lagrangian particle tracking is employed for tracking the particles. The following is the Langevin equation that governs particle motion [152]:

$$m_p \frac{\overrightarrow{dU}_p}{dt} = \overrightarrow{F}_{drag} + \overrightarrow{F}_{Br} \tag{2.4}$$

$$\frac{dx_p}{dt} = \overrightarrow{U}_p \tag{2.5}$$

Where $\overrightarrow{U}_p$ is the particle velocity, t is time, $\overrightarrow{F}_{drag}$ and $\overrightarrow{F}_{Br}$ are the drag and Brownian forces per unit mass, respectively, and x is the particle position. In this investigation, the gas flow was laminar, and the particles were considered to be spherical. As a result, turbulence dispersion and lift force were not taken into account. It is important to note that while ignoring lift force is appropriate for spherical particles, it might result in substantial errors for nonspherical particles [87, 88]. The terms in Equation 2.4 that specify the particle drag force and Brownian force for micron particles ($> 1\mu m$) are defined in equations (2.1, 2.2, and 2.3). The terms in Equation 2.4 that designate the particle drag force for submicron particles ($< 1\mu m$) are defined as follows:

$$\overrightarrow{F}_{drag} = \frac{3\pi\mu d_p(\overrightarrow{U}_f - \overrightarrow{U}_p)}{m_p C_c} \tag{2.6}$$

Where μ is the dynamic viscosity of the carrier gas, d_p identifies the particle diameter, $\overrightarrow{U}_f$ is flow velocity, and $\overrightarrow{U}_p$ is particle velocity, m_p is

particle mass, and C_c is the Cunningham slip correction factor as shown in equation (2.7).

$$C_c = 1 + \frac{2\lambda}{d_p}(1.257 + 0.4e^{-\frac{1.1d_p}{2\lambda}}) \tag{2.7}$$

In Equations 2.6 and 2.7, λ denotes the mean free path, and ρ_p denotes particle density. Mean free path λ is described by the following expression:

$$\lambda = \frac{\mu}{P\sqrt{\frac{2M}{\pi RT}}} \tag{2.8}$$

Where P is the pressure before the focussing orifice, M is the molecular weight of the gas, R is the universal gas constant (8.314J/K.mol), and T is the temperature. The fluctuation-dissipation theorem [73] describes the characteristics of the Brownian force per unit mass, as illustrated in the equations below:

$$\overrightarrow{F}_{Br}(t) = 0 \tag{2.9}$$

$$\overrightarrow{F}_{Br}(t).\overrightarrow{F}_{Br}(t^{'}) = \frac{2KTf\delta(t^{'} - t)}{m_p^2} \tag{2.10}$$

Where k represents the Boltzmann constant, T represents the local temperature, f represents the friction coefficient. $\delta(t^{'} - t)$ is the Dirac-delta function, where $t^{'}$ and t are times. Traditionally, there is no correlation between effects in any distinct time intervals $t^{'}$ and t, according to the Dirac-delta function in time. The fluctuating force has a Gaussian distribution [46], which is defined by these moments, according to the remaining mathematical specification of this dynamical model. As a result, the white

noise's delta function must be replaced by a numerical representation of $1/\Delta t$.

$$\delta(t^{'}-t) = \{ \begin{matrix} \frac{1}{\Delta t}, \text{when } t^{'} \text{ and } t \text{ in the time step } \Delta t \\ 0, \text{On the contrary} \end{matrix} \} \tag{2.11}$$

Thus, at each time step, the Brownian force per unit mass in direction i may be expressed as:

$$\overrightarrow{F}_{Br} = G_i \sqrt{\frac{\pi S_0}{\Delta t}} \tag{2.12}$$

Where G_i denotes independent Gaussian random numbers with zero mean and unit variance, and:

$$S_0 = \frac{216 v k T}{\pi^2 \rho d_p^5 (\frac{\rho_p}{\rho})^2 C_c} \tag{2.13}$$

The kinematic viscosity is v, the gas density is ρ, and the particle mass density is ρ_p. Therefore, to determine the drag force and Brownian force on particles, we utilized user-defined functions (see Appendix A).

2.3 Particle Characteristics and Flow Interactions

2.3.1 Stokes Number

With respect to particle dispersion, several different characteristics are factors in the determination of the particle geometry and the particle's relationship to the flow. One of the most widely used particle characteristics is the Stokes number, St, which quantifies the ratio of the aerodynamic response time of a particle (also known as the relaxation time) [59] to the

timescale of the flow of a structure. The size range of the particles that are being focussed on is established by the Stokes number of the particle, St, which is basically the ratio of the inertial forces of the particle to the drag force, [97]. Equation 2.14 provides a means of calculating the Stokes number of a system:

$$St = \frac{\rho_p d_p^2 U}{18\mu\delta} \tag{2.14}$$

Where δ is the typical length of the structure of interest. In the case of free jet structures, this value can vary depending on position, but it is commonly used as an initial approximation of the nozzle diameter [35]. The Stokes number can be used to classify various particle behaviours within flows. Particle flows with a Stokes number less than one, for example, tend to serve as flow tracers because the particle reaction time is sufficiently low to allow the particles to change direction rapidly within the flow structure. In cases in which the Stokes number is close to one, the particles behave similarly and also exhibit some lag relative to the flow streamlines [51, 15]. Where the Stokes number is greater than one, the aerodynamic response time is reasonably long, so that the particle is not greatly influenced by fluctuations in the flow field and tends to take a more rectilinear path. Smaller particles (those with a Stokes number less than one) tend to follow the streamlines to avoid crossing the centreline, while larger particles (those with a Stokes number greater than one) are less disturbed by the flow and therefore cross the centreline [97]. Particles with intermediate levels of inertia are thus separated from the streamlines and focussed on the axis so that particles with specific Stokes numbers congregate at the axis.

2.3.2 Particle Tracking in an Injection System

To provide a better understanding of the effect of an injection system on particle distribution for the particle sizes and densities detailed below, a

particle injection system was developed based on a Lagrangian tracking scheme for discrete phase modelling (DPM) on the surface, as shown in Figure 2.5 [161].

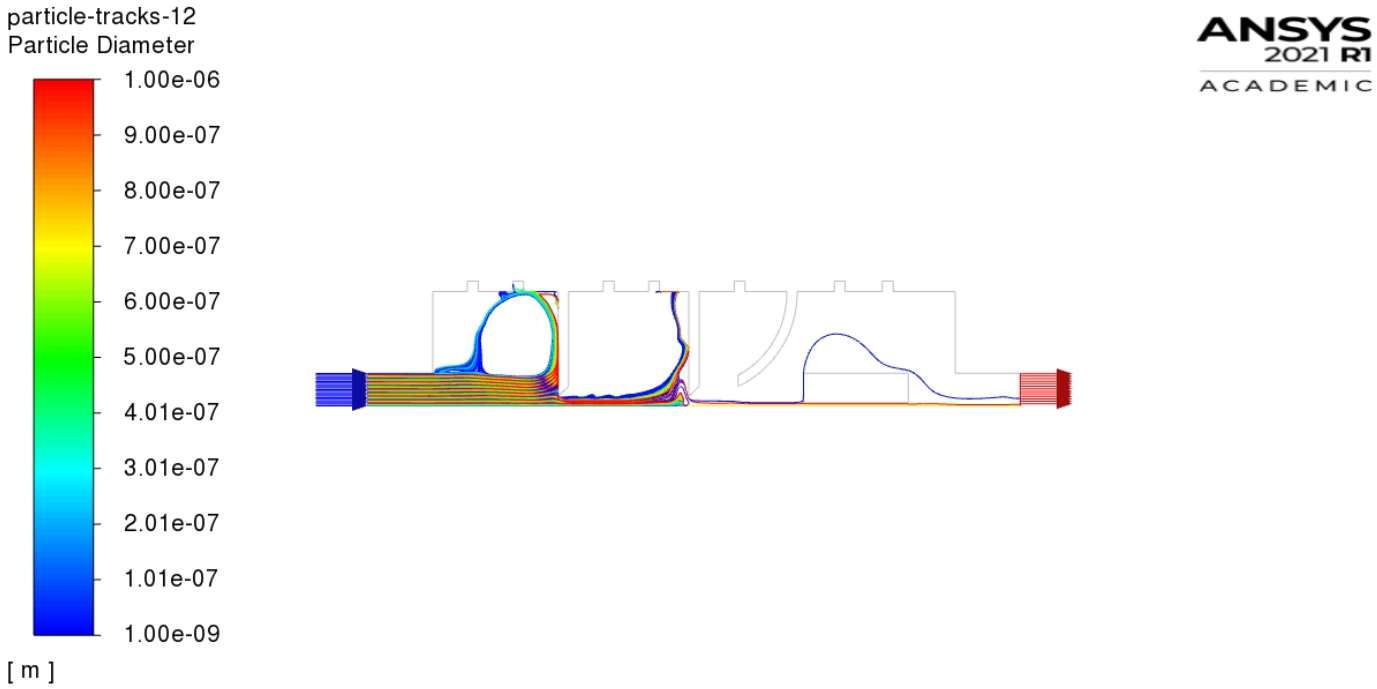

Figure 2.5: Use of a Lagrangian tracking scheme for discrete phase modelling (DPM) at the pipe inlet

To ascertain any polydisperse characterization, the injections were modelled after computational measurements of the diameters of a variety of particles in order to determine both the variance (if any) from the manufacturer's prescribed diameters as well as the standard deviation of the particle diameters. The Newtonian assumption of C_D=0.44 was used to solve the equations for the smallest particles. The Reynolds number of the particles was determined to be less than 1000, suggesting a laminar flow. In both of these cases, the Reynolds number of the particle is significantly greater than one, putting it squarely outside the Stokes region. Particles are injected using the surface injection type from the inlet to produce the

most accurate solution. However, the number of particles is limited by the number of meshed cells at the inlet. The particle tracking scheme utilized within the injection system thus allowed the use of the previously mentioned two-way step coupling. A further factor was that employing a Lagrangian tracking scheme required a large number of runs (because with the Lagrangian method, individual particles are traced over time, revealing a particle trajectory). The interaction of the particle with the walls of the injection system was regulated with the use of the "reflect" boundary condition on all exterior faces of the mesh except those indicated in Figure 2.5. As a result, any interaction of the particle with the walls will alter its trajectory according to the coefficient of restitution.

2.4 Knowledge Gaps and Research Needed

While particle focussing is an important process in nanoparticle research, commercially available devices are still lacking. Those on the market are expensive, and their performance under varied operating conditions is not well characterized. The progress of nanoparticle studies can be improved through greater availability of particle sources, which would allow researchers to evaluate the effects of a wider range of nanoparticles for an application of interest. CFD modelling would be beneficial with respect to providing an enhanced understanding of effective particle focussing. Although there have been numerous advances in nanoparticle focussing, prior to the research conducted for this thesis, there was still a need to consider the effect of focussing nanoparticles with an aerodynamic lens. While aerodynamic lens systems have been the subject of numerous research projects, these theoretical and experimental studies have been based on underlying assumptions that must be included in any discussion of the impact of nanoparticles on a lens. The following questions and considerations guided the direction of the research presented in this thesis:

1. **C**an all the assumptions used in previous aerodynamic lens models be validated? (Chapter 5).

2. **D**oes an aerodynamic lens system exist? (Chapter 2).

3. **I**f it does, what is the critical diameter of the nanoparticles below which an aerodynamic lens could focus them? (Chapter 2).

4. **D**o small nanoparticles behave as gas molecules or as nanoparticles? (Chapter 2).

5. **W**hy cannot nanoparticles smaller than 3 nm be measured by simulation software? (Chapter 5).

6. **H**ow can the efficiency of a lens be increased for small nanoparticles? (Chapter 5).

7. **H**ow can a systematic understanding of factors that affect the nanoparticles focussed with an aerodynamic lens be acquired so that it becomes clear how they interact with one another? (Chapter 4.

8. **D**esigning aerodynamic lenses has been shown to be achievable since multiple researchers have reported the experimental and simulated design of these lenses, but their methods have varied substantially. Considering the numerous parameters that have an impact on an aerodynamic lens for use in particle focussing, how can an understanding of nanoparticle focussing with an aerodynamic lens be expanded? (Chapters 6 and 7).

9. **E**ven with the extensive research related to aerodynamic lenses, the effects of all possible parameters are not yet fully understood. Carbon has been the focus of the most recent study and exhibits properties with promising potential for use in this field, which should be explored. (Chapter 5).

10. **W**hile the ability of an aerodynamic lens to focus nanoparticles was believed to be excellent, until now it had not yet been tested, either under laboratory or practical conditions. The scope of the work presented here included the addition of information to the knowledge base related to aerodynamic lens design and the impact of critical parameters as well as an investigation of the ability of an aerodynamic lens to focus nanoparticles. (Chapter 5).

11. **W**ith respect to the Lagrangian model using ANSYS Fluent, the question was whether an Eulerian simulation could be performed using a multiphase model. (Chapter 3).

12. **I**f not, how could a Lagrangian model be utilized, given the individual particle tracks? How important are the tracks with respect to the simulation? How do particles affect flow? (Chapter 3).

2.5 Summary

The literature review presented in this chapter has revealed a critical need for the ability to measure nanoparticles that are focussed with an aerodynamic lens by eliminating the effect of the orifice on the nanoparticles. A more appropriate approach is needed to the acquisition of an understanding of the aerodynamic lens approach, a goal that motivated the research presented in this thesis. This investigation was centred on a computational approach to the development of a new aerodynamic lens system, and this research has contributed to the body of knowledge by demonstrating the potential impact of nanoparticles on the orifice. This impact has been practically demonstrated through direct experiments, as described in subsequent chapters. The main innovations and contributions of the research can be summarized as follows:

1. A sharp-edged plate orifice has been designed.
2. A divergent nozzle has been designed.
3. A pipe containing inside grooves that match the diameter and thickness of the lenses has been designed.
4. The understanding of aerodynamic lens systems has been advanced.
5. The effects of particle properties, particle focussing, and nanoparticle measurement in relation to aerodynamic lenses have been investigated and quantified.
6. A correlated aerodynamic lens model for experimental and simulation use has been proposed.

As well, because the computational investigation of the effect of particle size on an aerodynamic lens system is inherently interdisciplinary, this aspect of the research required the tackling of a series of challenges. The resulting enhanced understanding of aerodynamic lens systems represents a fundamental contribution to the development and application of particle focussing and particle size measurement.

Chapter 3

Multiphase Particle Modelling

3.1 Introduction

This chapter presents general theoretical background related to multiphase flow simulation. While both multiphase and gas-solid flows are generic terms, with an overall similar generic setup [133], individual models and computational techniques can vary significantly from case to case. With respect to the simulation of a gas-solid flow, two basic methods are applied in order to simulate the formation of solid particles: the Eulerian method and the Lagrangian method, as shown in Figure 3.1.

Both methods are often applied for computational and numerical simulations of multiphase flows [133]. A fundamental assumption underlying this approach is that the dispersed phase occupies a small volume fraction, implying that the dispersed phase elements are not too close to one another and can therefore be viewed as isolated [75, 23, 4]. As a result, the interaction between the multiphase flow and the influence of the second phase would be significant enough to warrant consideration [4].

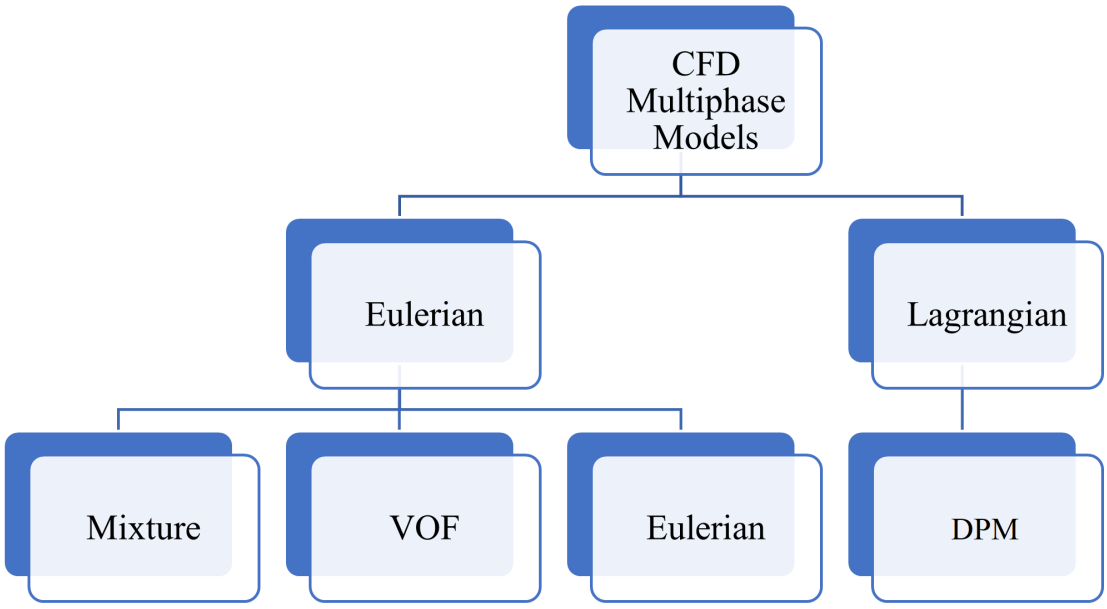

Figure 3.1: Multiphase modelling approaches in ANSYS Fluent

3.2 Lagrangian Particle-Tracking Theory

This section explains the mechanism of Lagrangian particle tracking and the application of this theory. First, Lagrangian particle tracks are compared with streamlines, the results of which have been incorporated into the CFD code and post-processor features of this study. This comparison clarifies the discrepancies between these two elements and highlights how the algorithm is implemented using the CFD codes. Fluid flows often carry solids with them, meaning that the majority of fluid flows subjected to CFD analysis are multiphase fluids, such as air as a gas, with carbon as a solid. Simple examples include combustion exhaust from vehicles and power stations, in which small particles of soot and other solids are often transported with the gases. In such cases, when small solid particles are transported along with the fluid, in simple terms, the transport of just a single particle in a

fluid flow can be examined. This approach must be extended to include instances when a variety of different particles are found in the fluid flow. This further explanation begins with a discussion of the concept of streamlines, as illustrated in Figure 3.2.

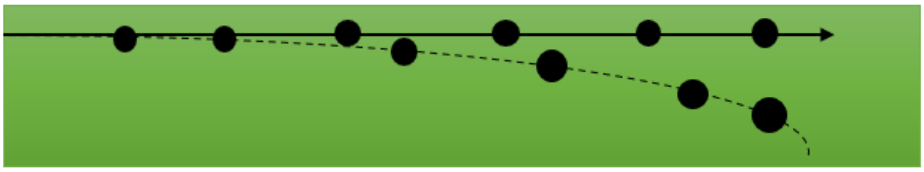

Figure 3.2: Transport of small solid particles along with the fluid, described based on the transport of only a single particle in the fluid flow

If nanoparticles of varied sizes are injected into the fluid flow, it will be found that they tend to follow the streamlines of the flow. In Figure 3.2 the streamline is just a straight flow or a plain channel flow, and the black dots represent solids. If the particles are very light, it is expected that they will be transported along the pipe in the straight solid line indicated from left to right, thus following the streamlines. However, if some of those particles are substantially heavier or quite a bit bigger, rather than being transported in a straight line along the pipe, these heavier particles fall toward the bottom of the pipe, as represented by the downward dotted-line curved trajectory in Figure 3.2. In this case, if streamlines are relied on for working out the path of the solids in the pipe flow, the conclusion would be incorrect, and a different approach that takes particle mass into account is needed.

In addition to the particles moving down toward the bottom of the pipe, they are also expected to move more slowly than the fluid, as depicted in Figure 3.3.

The conclusion is, therefore, that streamlines are ineffective for tracking the trajectories of heavy or large particles and a different technique must be employed: Lagrangian particle tracking, which is illustrated in Figure

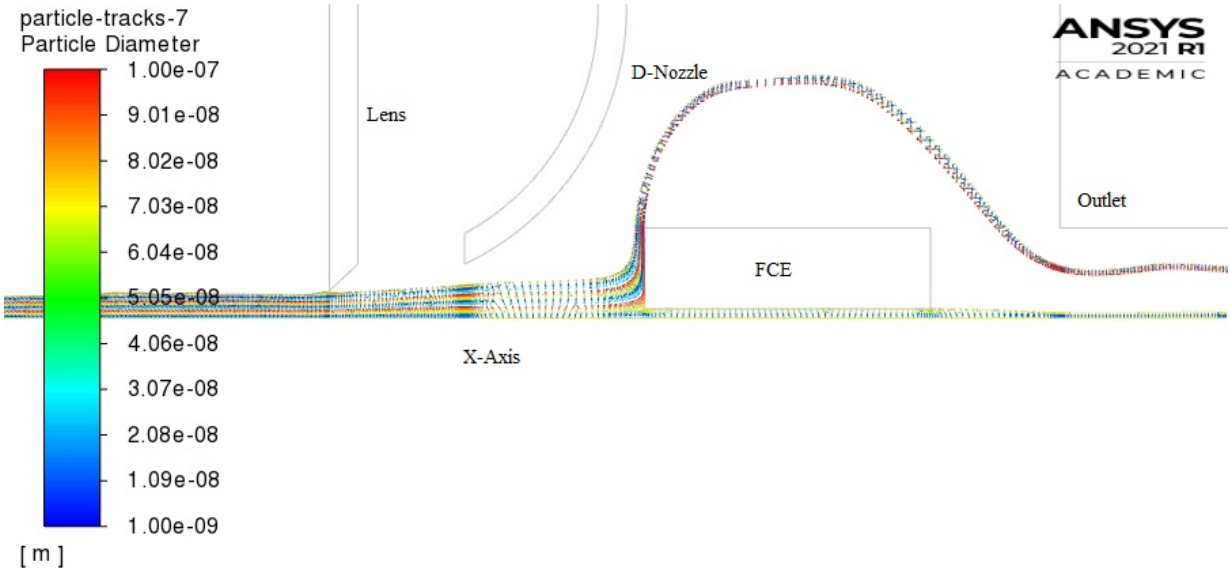

Figure 3.3: Particles moving toward the bottom of the pipe and expected to move more slowly than the fluid

3.4, can be used to provide a more accurate computation of particle motion [133].

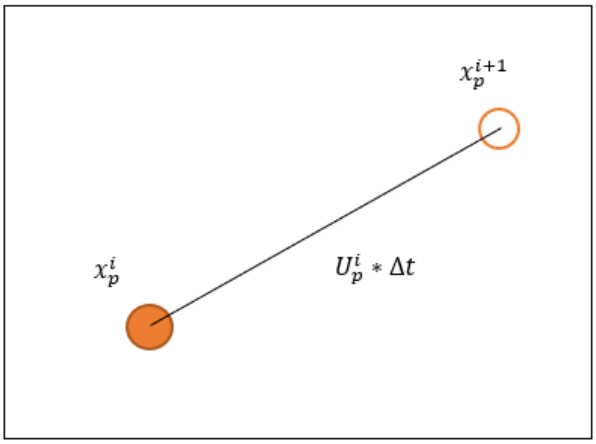

Figure 3.4: Lagrangian particle track, which yields a more accurate computation of particle motion

To demonstrate the superiority of Lagrangian particle tracking first requires a detailed explanation of the mathematics that form the basis of the streamline technique. With streamlines, it is important to solve the following differential equation [148]:

$$\frac{dx_p}{dt} = \overrightarrow{U}_p \tag{3.1}$$

Where dx_p/dt is the rate of change in the particle position over time, $\overrightarrow{U}_p$ is the velocity of the particle, and dx_p denotes the particle position. This step is critical because a moving fluid and moving particles do not necessarily exhibit the same velocity. In streamlines, if there is a particle with no mass or very little mass, it moves with the fluid flow, in which case, the particle velocity $\overrightarrow{U}_p$ equals the local fluid velocity $\overrightarrow{U}$:

$$\overrightarrow{U}_p = \overrightarrow{U} \tag{3.2}$$

Equation 3.1 can therefore be solved because the fluid velocity is known from the solution for the CFD equations. An explicit time-stepping approach can then be used for solving Equation 3.2 for the streamlines [148], as indicated in equation 3.3:

$$\frac{dx_p}{dt} = \overrightarrow{U}_p \;\rightarrow\; \frac{\overrightarrow{x}_p^{\,i+1} - \overrightarrow{x}_p^{\,i}}{\Delta t} = \overrightarrow{U}_p^{\,i} \tag{3.3}$$

where $\overrightarrow{x}_p^{\,i}$ is the current particle position, as shown in Figure 3.5, which can then be used for establishing the next particle position $\overrightarrow{x}_p^{\,i+1}$.

This step can be achieved if Equation 3.3 is rearranged to give Equation 3.4:

$$\overrightarrow{x}_p^{\,i+1} = \overrightarrow{x}_p^{\,i} + \overrightarrow{U}_p^{\,i}\Delta t \tag{3.4}$$

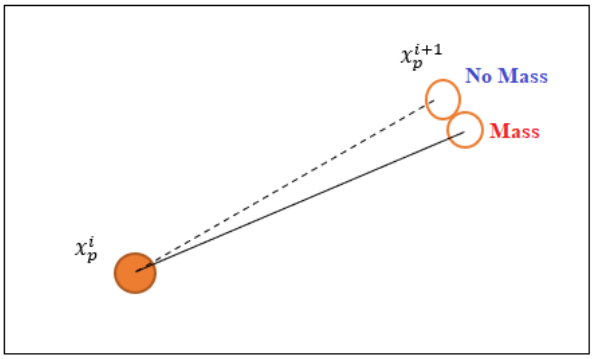

Figure 3.5: Current particle position indicated by $\overrightarrow{x_p}^i$

where $\overrightarrow{x}_p^{i+1}$ specifies the next particle position, $\overrightarrow{x}_p^i$ indicates the current particle position, $\overrightarrow{U}_p^i$ denotes the contribution of the particle velocity, and Δt represents the time step. Figure 3.5 is a visual representation of this step. The particle must move from one location in the CFD mesh to another point in the CFD mesh. Because a streamline approach is used in this instance, the velocity of the particle is equal to that of the local fluid. The CFD mesh can be considered along with the solution and the local velocity interpolated at that point because the local fluid velocity is equal to the local particle velocity. Repeated applications of Equation 3.4 can then be applied to work out each subsequent position of the particle until a complete trajectory of a single particle is established through the flow field of the fluid. The key is to use the local fluid velocity at each position of the particle in order to determine the trajectory of the particle at that point as well as where its next position will be, which is how streamlines can be employed to establish the path of a nanoparticle or a particle with no mass. Although, as depicted in Figure 3.6, a particle that has mass is the more common occurrence in such flows, the same method can be used for updating the position of such a particle when the value of $\overrightarrow{x}_p^{i+1}$ is known:

$$\overrightarrow{x}_p^{i+1} = \overrightarrow{x}_p^{i} + \overrightarrow{U}_p^{i} * \Delta t \qquad \overrightarrow{U}_p \neq \overrightarrow{U} \tag{3.5}$$

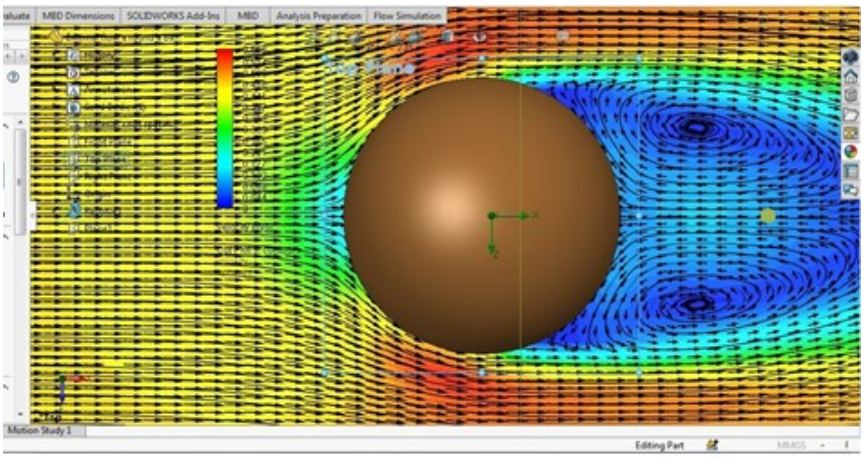

Figure 3.6: More commonly found particle with mass

The difference in this case is that the velocity of the particle is not equal to that of the local fluid, a discrepancy that can be attributed to the drag on the particle and its weight, factors that would be expected to alter its trajectory slightly in a downward direction, with very different results than would be obtained with the streamline technique. In this case, because the velocity of the particle differs from that of the local fluid in the mesh, it must be calculated based on the balance of forces acting on that particle.

3.2.1 Force Balance

The force balance and how it can be derived for a single particle are explained in this subsection. The starting point is Newton's second law, governing the forces acting on a solid particle:

$$\overrightarrow{F} = m_p \overrightarrow{a} \qquad \overrightarrow{F} = m_p \frac{\overrightarrow{dU}_p}{dt} \tag{3.6}$$

Where m_p is the mass of the particle, a is the rate of change of the velocity of the particle over time. Equation 3.7 then describes the forces acting on the particle.Several different contributions are present:

$$m_p \frac{\overrightarrow{dU}_p}{dt} = \overrightarrow{F}_{drag} + \overrightarrow{F}_{Buoyancy} + \overrightarrow{F}_{Others} \tag{3.7}$$

For the purposes of this method, and depending on the type of flow field in evidence, there may be additional forces acting on the particle. Since this discussion serves as an introduction, the drag force is examined since this is the main force acting on a particle and often has the greatest magnitude. Figure 3.7 provides a visual example of the force balance acting on a particle.

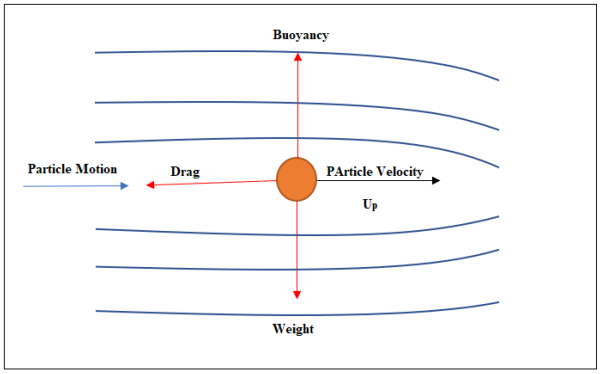

Figure 3.7: Composition of the force balance for a solid particle moving from left to right in a fluid

For determining the composition of the force balance for a particle, such as the visual example of a spherical particle moving from left to right in a fluid shown in Figure 3.7, noting both the forces and the direction of their action on the particle are very important. Drag is applied from right to left, the weight of the particle is acting downward, and the buoyancy is acting upward. These observations are quite straightforward for a particle moving horizontally in a fluid.

However, if the particles are moving at an angle in the flow field, when the force balance is redrawn, it can be seen that the weight of the particle still acts vertically downward, or more correctly, in the direction of gravity, and the buoyancy force still acts vertically upward in the opposite direction. In contrast, the direction of the drag force changes because it always acts in a direction opposite to that of the particle's motion, i.e., its velocity. When the force balance is established for this case, these factors, as illustrated in Figure 3.8, must be taken into consideration.

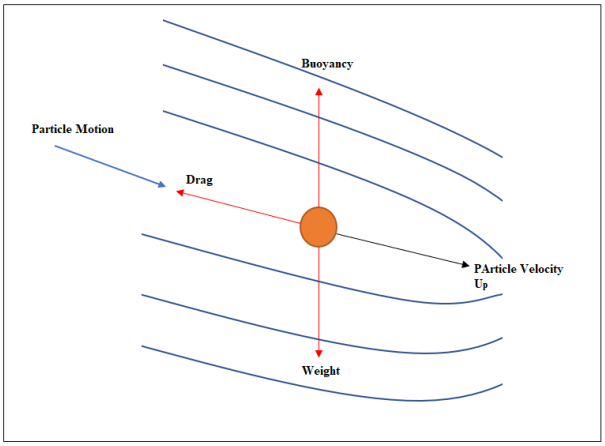

Figure 3.8: Particles moving at an angle in the flow field

In the next situation, rather than moving through a fluid, the spherical particle instead moves within a fluid that is also moving. There is no change in the direction of the weight or the buoyancy force. The difference now is that, because the fluid and the particle are both in motion, the drag force is acting in the direction of $\overrightarrow{U}_p - \overrightarrow{U}$, which must be taken into account when that force is computed. Figure 3.9 illustrates this case.

The buoyancy and weight acting on the particle are the simplest forces to establish since it is a given that the weight of the particle always acts in the direction of $\overrightarrow{g}$, the gravitational acceleration vector. Using this vector rather than a coordinate direction such as x, y, or z is important since, in a

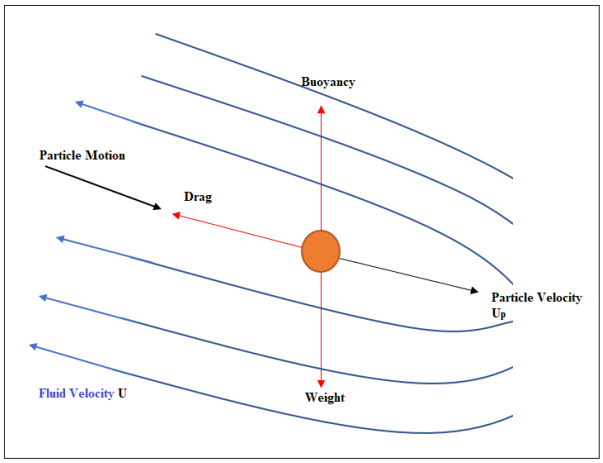

Figure 3.9: Case in which the fluid and the particle are both moving, thus affecting the calculation of the drag force

CFD simulation, the user's choice of vertically upward direction is unknown ahead of time. The weight of the particle can thus be given by:

$$\overrightarrow{F}_{Weight} = \rho_p \overrightarrow{g} V_p \tag{3.8}$$

Where ρ_p is the density of the particle, $\overrightarrow{g}$ is the gravitational acceleration, and V_p is the volume of the particle. The gravitational force experienced by the nanoparticles is obtained from the upcoming expressions, which are presented in Equation 3.9:

$$\overrightarrow{F}_{Gravitational} = \frac{\pi d_p^3 \rho_p}{6} \overrightarrow{g} \tag{3.9}$$

If the buoyancy force is the weight of the fluid displaced by the particle, the buoyancy force can be calculated as (Equation 3.10):

$$\overrightarrow{F}_{Buoyancy} = \rho_f \overrightarrow{g} V_p \tag{3.10}$$

For Lagrangian particle tracks, the weight and the buoyancy forces can be combined into a single vector acting on the particle, resulting in Equation 3.11:

$$\overrightarrow{F}_{Vertical} = (\rho_p - \rho_f)\overrightarrow{g}V_p \tag{3.11}$$

The interesting feature of this force is that it is dependent on the density of the particle relative to the fluid, which determines whether the particle will move upward or downward. If the particle is denser than the background fluid, it would be expected to sink:

$$(\rho_p - \rho_f) > 0$$

However, if the particle is lighter than the background fluid, i.e., with less density, it will move up in the flow field:

$$(\rho_p - \rho_f) < 0$$

This formulation of buoyancy in the weight factor allows for the ability of the particle to move in that direction regardless of its density.

3.2.2 Drag Force

Drag force is more complicated to compute; it would be expected to take the general form [16] expressed in Equation 3.12:

$$\overrightarrow{F}_{drag} = \frac{1}{2}\rho_f C_D \left|\overrightarrow{U} - \overrightarrow{U}_p\right| (\overrightarrow{U} - \overrightarrow{U}_p)A_p \tag{3.12}$$

Where A_p is the projected area in the direction of the flow. The specific form of the drag force that is used for Lagrangian particle tracks is the general one from Equation 3.12. However, it should be noted that, rather

than U^2, the way in which velocity has been expressed requires that the drag forces be in the correct direction. The second, bracketed, instance of $\overrightarrow{U} - \overrightarrow{U}_p$ in the equation thus ensures that the drag force is in the direction opposite to that of the particle motion. The magnitude of the first inclusion of the new value, $\overrightarrow{U} - \overrightarrow{U}_p$, ensures that the drag force is in the correct direction. However, two components have not been explained [133]: the area to be used and the drag coefficient of the spherical particle, as indicated in Figure 3.10.

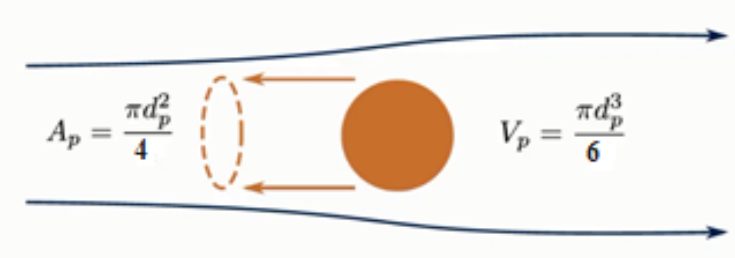

Figure 3.10: The area to be used and the drag coefficient of the spherical particle

The area used in the drag force calculation is the projected area in the direction of the flow, and spherical particles, in general, have the following drag coefficient:

$$C_D = \left\{ \begin{array}{ll} \frac{24}{R_e}(1 + 0.15\ R_e^{0.687} & R_e < 1000 \\ 0.44 & R_e > 1000 \end{array} \right\} \tag{3.13}$$

When Lagrangian particle tracks are under consideration, the common practise is to express factors in terms of particle diameter rather than radius. A spherical particle thus has a volume of $V_p = \frac{\pi d_p^3}{6}$, but its projected area, A_p is the area of a circle [133]. For a spherical particle, the front of the projected area will be $A_p = \frac{\pi d_p^2}{4}$, which confirms the A_p to be used in computing the drag force.

The next consideration is the drag coefficient, which generally, for a spherical particle, takes a form similar to that shown in the plot in Figure

3.11. It can be seen that for low Reynolds numbers, the value of the drag coefficient is initially very high.

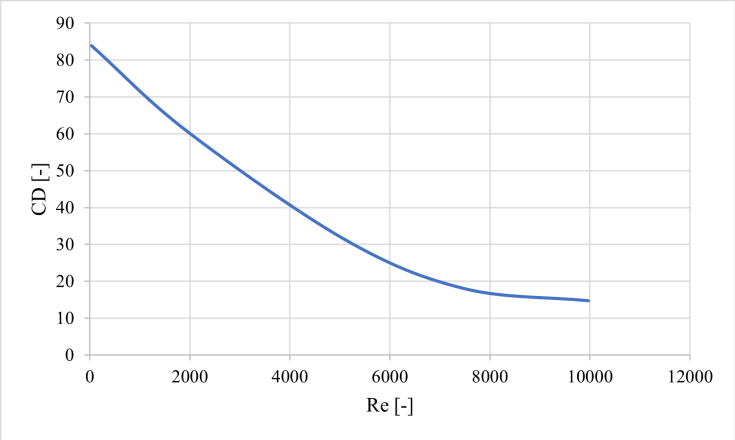

Figure 3.11: Drag coefficient for a spherical particle

It should be noted that the drag coefficient is not the drag force [16]. As the Reynolds number increases, the drag coefficient decreases until it plateaus around a Reynolds number of 10,000. With higher Reynolds numbers, an interesting transition behaviour occurs: there is a characteristic d_p in the curve that is attributable to particles being very small. An example of an empirical fit that can be used for the drag coefficient of a spherical particle is given in Equation 3.13.

This expression is called the Schiller-Naumann drag coefficient relationship and is used in the majority of CFD codes. The value of the drag coefficient is dependent on the Reynolds number, but in Equation 3.14, the Reynolds number is contingent on the velocity of the particle, $\overrightarrow{U}_p$. However, the goal here is to solve for the force balance in order to calculate the particle velocity.

$$R_e = \frac{\rho d_p \left| \overrightarrow{U}_p - \overrightarrow{U} \right|}{\mu} \tag{3.14}$$

In CFD codes, a way to circumvent this difficulty is to use the particle velocity from the previous time step or the previous section of the particle track in order to compute the Reynolds number of the particle. Once the Reynolds number has been established, the drag coefficient can be calculated, and the force balance computation can be completed. This technique constitutes a very important intuitive step for an understanding of the Lagrangian particle tracks: the Reynolds number is based on a particle velocity that is not yet known. As an aside, if a hand calculation of a particle-settling velocity is ever attempted, it will be found that the hand calculation needed for the iterations required for calculating the particle-settling velocity arises from the Reynolds number.

The drag and loop can then be updated in that manner and for that reason. However, these calculations are no problem with the CFD code, and the particle velocity from the previous step of the Lagrangian track can be employed. Thus, when an individual particle is being moved according to a time step along its track, the first procedure is to calculate the Reynolds number of that particle based on its velocity from the previous time step, as expressed in Equation 3.14. Once the Reynolds number has been determined, the drag coefficient of the particle can be calculated using the Schiller-Naumann drag model, as expressed in Equation 3.13. Once the drag coefficient has been calculated, the force balance can be determined in order to calculate the new velocity of the particle U_p. The drag coefficient can thus be used to solve Equation 3.15.

$$m_p \frac{\overrightarrow{dU}_p}{dt} = \frac{1}{2}\rho_f C_D \left|\overrightarrow{U} - \overrightarrow{U}_p\right| (\overrightarrow{U} - \overrightarrow{U}_p) A_p \ + (\rho_p - \rho_f)\overrightarrow{g} V_p \tag{3.15}$$

The entire process is then repeated from the beginning, with the position of the particle being updated based on the Eulerian explicit time-stepping approach.

$$\overrightarrow{x}_p^{i+1} = \overrightarrow{x}_p^{i} + \overrightarrow{U}_p^{i+1}\Delta t \tag{3.16}$$

This technique means that this sequence of calculations is performed for each time step for each particle as it moves along its track, a process that is then reiterated until the particle has moved all the way along its track and its full trajectory can be seen.

3.3 Summary

One aspect of this research was an examination of the modelling performance of the Lagrangian method with respect to particle focussing distribution through the lenses in the pipe. This investigation covered the exploration of particle dispersion in a circular pipe after the utilization of two lenses with a divergent nozzle. The comparison concentrated on the accuracy and reliability of the particle-focussing simulation, as well as on computational efficiency. The performance of the Lagrangian model for estimating particle dispersion was examined using identical airflow fields. The results revealed that, under steady-state conditions, the particle phase behaves more like a continuum. The Eulerian method requires less processing time than the Lagrangian method, but each step in the Lagrangian method involves hundreds of iterations since it entails tracking the evolution of each particle and needs a sufficiently large number of particles to maintain statistical stability. The conclusion is, therefore, that the Lagrangian approach is more appropriate for modelling particle motion under steady-state conditions and is hence suggested for future applications.

3.3.1 Lagrangian Fluid Motion Approach

This paragraph provides a quick summary of this introduction to Lagrangian particle tracking. The overall procedure for carrying out particle tracking for a single particle is first to calculate the Reynolds number using the particle velocity from the previous time step or the previous section along the particle track. Once the Reynolds number is known, the next stage is to calculate the drag coefficient for the particle using the Schiller-Naumann drag model. The force balance is then computed in order to calculate the new velocity of the particle. Once the new particle velocity has been established, the position of that particle can be updated based on the velocity and the time step. Particle velocity is useful for changing the trajectory of the particle as it moves through space. These four steps can then be repeated as a means of incrementally moving the particle along its trajectory until the particle track can be terminated at the end of the particle-tracking simulation. The final point is that the force balance is very general. Of the numerous forces acting on a particle, only the two main ones have been reviewed: drag and the Brownian of the particle. A further factor is that the force balance can also be written in a variety of forms. However, it is worth remembering that the general basis of this force balance is always Newton's second law, which means that the particle velocity can be calculated because, unless the mass of the particle is very small, the velocity of the particle is not necessarily the same as that of the fluid.

Chapter 4

Theory of Nanoparticle Motion in Aerodynamic Lenses and a Divergent Nozzle

4.1 Introduction

In aerodynamic focussing, lenses concentrate particles trapped in a carrier gas into collimating beams. Particles that are dispersed from the main beam are then removed through a sequence of orifices. Ones that flow into the air can be focussed in a small area of high concentration, and the resulting narrow particle flow is useful for observing the particles themselves. Currently available aerodynamic lens systems are ineffective for focussing small particles due to the natural diffusion of small particles away from the main component of the beam. Decreasing the size of the pipe will not increase the concentration of particles, although the particle flow can be reduced if a pipe of a smaller diameter is used. Aerodynamic lenses specifically designed for use with nanoparticles can produce collimating beams of small nanoparticles, enabling the focus of small particles in the beam. Aerodynamic lenses are often used in combination with Differential Mobility Analyzer (DMA) and a Faraday cup electrometer (FCE) because the concentrated beam of

small particles can be applied directly in these particle focussing systems.

Because of their rigidity, simple mechanical structure, and other well-known advantages, aerodynamic lenses are commonly used in aerodynamic flow [127], and significant research has been targeted at an examination of factors that affect their use. This chapter provides an overview of a number of aspects of aerodynamic lens systems. Computational fluid dynamics (CFD) techniques are still commonly used for the simulation and study of lens systems [116, 74], and commercial CFD is used for modelling the flow characteristics of an orifice. The importance of CFD simulations for the design of an efficient lens is illustrated through a discussion of ANSYS Fluent software (2021R1), including a preliminary explanation of specific aspects of this lens application. The focus then shifts to CFD simulations with respect to practical implementation, benefits, and future trends. A number of studies have been conducted with the goal of determining the possible particle size or particle concentration when multiple lenses are used [120, 160, 165, 80, 81, 79]. Another element of interest is the orifice. Its operation stems from the basic concept of applying the effects of velocity and pressure change caused by decreases in the area available for the flow. Extensive research has been conducted to establish the impact of the lens-to-pipe-diameter ratio. Several studies [37, 5] have involved the numerical investigation of the effect of that ratio on the rate of mass transfer behind the lens. A detailed discussion of velocity and pressure profiles from CFD simulation results is therefore included.

These considerations have led to the use of CFD in this analysis as a means of simulating fluid flow in a lens. ANSYS Fluent was employed to examine the airflow through a lens in a circular pipe containing two conventional lenses, and a CFD simulation was incorporated to provide predictions. The velocity of the fluid increases at the lens opening, but as its flow progresses and it begins to slow down, a divergent nozzle has been used as a means of decreasing the velocity to obtain the sonic speed required

for focussing the particles. Given the profound industrial importance of the substantial benefits related to the ability to concentrate particles, comprehending the flow pattern in an orifice constitutes a critical factor in enhancing its performance through accurate flow measurements.

4.2 Background

Today, the most common method of focussing nanoparticles is the use of aerodynamic lenses, which entails either a single lens or multiple lenses installed inside a pipe [87, 88, 91]. Most of the previous research efforts related to aerodynamic lenses have centred on the generation and use of particle beams under low pressure. A recent development is the theoretical analysis of aerodynamic lenses. A formula for the design of an aerodynamic lens with respect to flowrate, pressure, and particle size has been reported in several studies [68]. The research presented in this thesis was directed at facilitating the focussing of nanoparticles. Simulations have been carried out using the model that was developed and evaluated computationally. It consists of an 80 mm length of pipe that has two openings: an inlet and an outlet, both with a diameter of 10 mm. The fluid passes through the inlet from left to right. The novelty of this research is the use of a new component for focussing nanoparticles: two aerodynamic lenses with a divergent nozzle, an arrangement that enables small particles to be focussed. Figure 4.1 illustrates the components of the aerodynamic lens system developed during this research.

It should be noted that, with the divergent nozzle, this set-up included only two lenses rather than three or more. The difficulty is that detecting small nanoparticles (ranging in size from 1 nm to 100 nm) and focussing them to measure their diameters with fewer than two lenses is challenging. When attempting to quantify nanoparticle sizes with only one or two

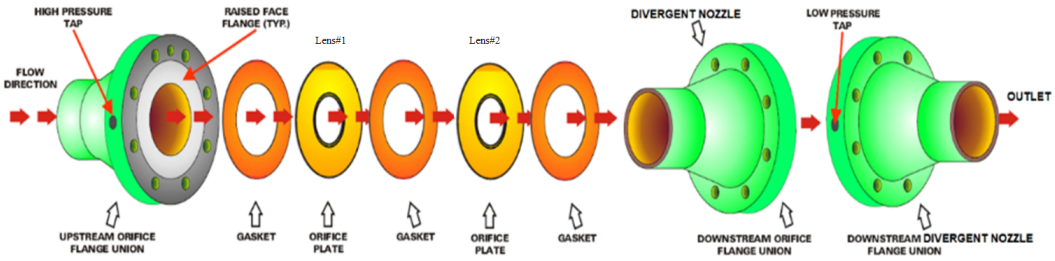

Figure 4.1: Main components of the developed aerodynamic lens system

lenses, a problem occurs. However, the research described in this thesis has addressed this issue by developing an enhanced aerodynamic lens design, that is, an improvement over the one that uses a conventional orifice. To improve the effectiveness of the particle focussing, the first step was the insertion inside the pipe of the aerodynamic lenses, whose respective diameter and thickness were 3 mm and 1.6 mm, respectively. The next upgrade was the use of a divergent nozzle, which was installed to follow the lenses, with 15 mm the length between the second lens and the divergent nozzle. Measuring particle sizes and trajectories required that the information be sent to the DMA. An FCE also needed to be fitted inside the pipe [141], which necessitated a determination of an appropriate length between the second lens and the FCE.

To minimize the effects of diffusion, the construction requirements for aerodynamic lenses were enhanced. The establishment of these variable design parameters was based on the consideration of a variety of factors, such as lens spacing, carrier gas pressure, lens thickness, etc. Small particles could then be focussed into a beam for DMA experimental evaluation and ANSYS Fluent simulation. The performance of an aerodynamic lens and a divergent nozzle at atmospheric pressure in the inlet was assessed computationally, and the results were compared with those of further detailed trajectory simulations based on CFD calculations published by Middha and

Wexler (2003). It was demonstrated that, at atmospheric pressure in the inlet, a highly focussed particle beam can be obtained when the Reynolds number Re at the orifice is Re<2100, which is considered a laminar flow [155]. The new aerodynamic lens system offers the following features and benefits for collimating nanoparticle beams:

1. **Compared** to current aerodynamic lenses that can focus only particles with a size greater than 20 nm, [141, 97], it can focus on 3 nm to 300 nm nanoparticles.
2. **The aerodynamic lens** enables the beams to be more closely collimated.
3. **The new system** allows small particles as well as other larger particles to be measured directly by a Differential Mobility Analyzer (DMA) and a Faraday Cup Electrometer (FCE), where FCE is used for calculating the concentration of the singly charged "monodisperse" particles leaving the DMA, and a DMA is normally used for characterization of the particles by size prior to counting.

In short, these aerodynamic lenses have been enhanced for the analysis of ultrasmall nanoparticles that can be focussed into a beam, evaluated experimentally with DMA, and simulated using ANSYS Fluent.

4.3 Materials and Method

4.3.1 Aerodynamic Lens

As a result of the work presented in this thesis, the design proposed for an aerodynamic lens (ADL) consisted of two sharp-edged orifices with a divergent nozzle installed after the second lens to detect and focus small

particles to measure their size. Figure 4.2 depicts the geometry of the aerodynamic lens design with the divergent nozzle.

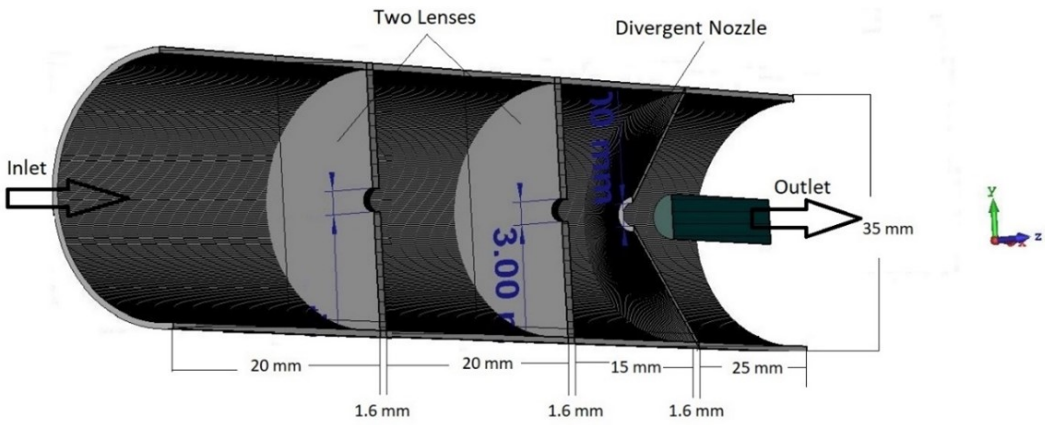

Figure 4.2: 3D schematic of the geometry of the aerodynamic lens system with the divergent nozzle

The gas streamlines of the air that flows across a sharp-edged plate on the divergent nozzle are illustrated in Figure 4.3 below.

Figure 4.4 provides a visual image of the significant flow recirculation downstream of the aperture when the track particles are larger than 300 nm. The recirculation area, as can be seen, occupies the entire space between the aperture and the divergent nozzle, resulting in reduced particle focusing. The Figure also shows the remainder of the aerodynamic lens system after the small particles (300 nm) have moved through the lenses and into the divergent nozzle. The lens and the divergent nozzle were evaluated computationally for evidence of particle focussing. No large particle focussing was evident in the divergent nozzle, thus supporting the modelling results showing that the new design reduces the recirculation inside the nozzle. As shown in Figure 4.5, the length between the second lens and the divergent nozzle was increased from 12 mm to 15 mm. Particle velocities measured at the focal point of the nozzle ranged from 370 m/s to 160 m/s for particles

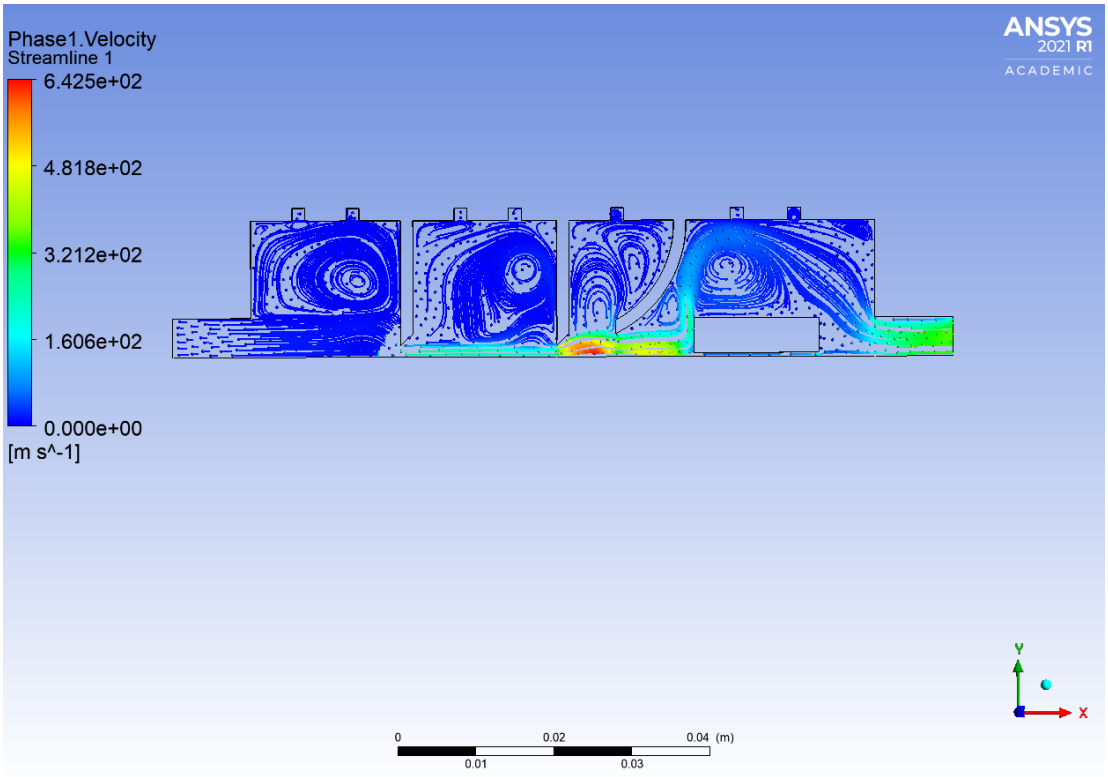

Figure 4.3: Gas streamlines of the air flowing across a sharp-edged plate with the divergent nozzle

from 8 nm to 24 nm, respectively, and followed the trend of the applicable force law with a strong correlation of 0.9884, as revealed in (Figure 4.6).

4.3.2 Divergent Nozzle

To avoid instability and shock formation, most researchers have employed multiple lenses for measuring and focussing nanoparticles by adjusting the stagnation pressure at the inlet. For this research, economic costs were reduced with the use of two lenses, and the theory, analyses, and methods for achieving the measurement of the smallest size of particles will be explained. The success of the new approach has also been demonstrated through the

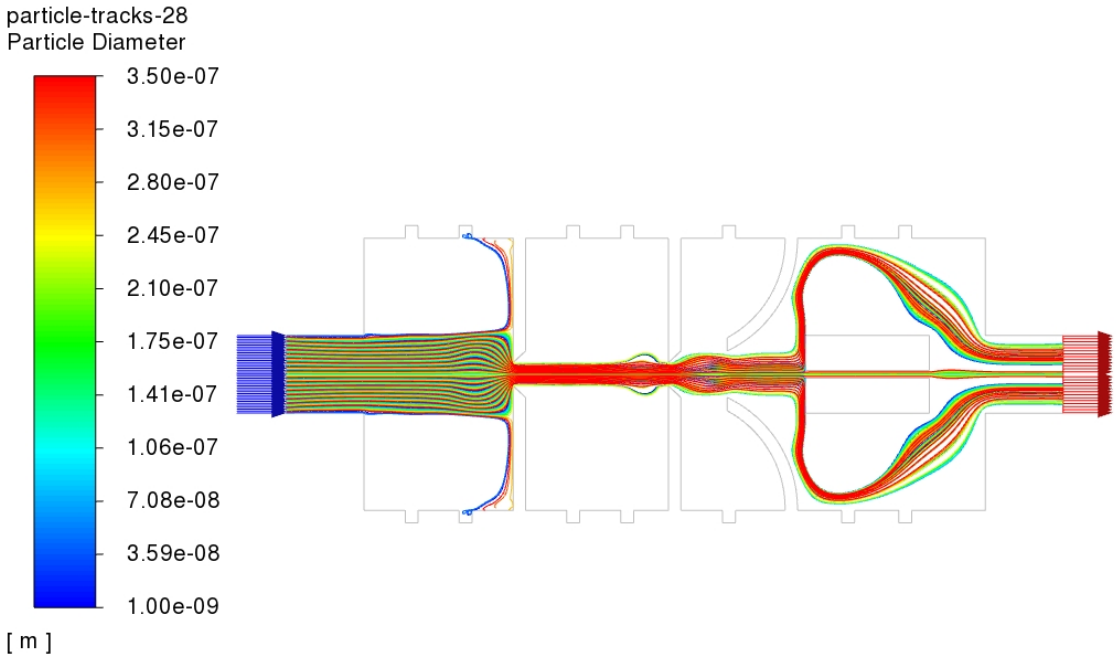

Figure 4.4: Particle tracks are larger than 300 nm

simulation and experimental laboratory testing of the developed model to validate the results.

The first step was to use two aerodynamic lenses to focus the nanoparticles on the orifice hole to detect the charged nanoparticles and to measure their size after focussing with the aerodynamic lens. However, the high speed of the gas particles, which reached levels greater than the sonic speed and caused instability in the orifice hole and shock formation in the orifice due to the high velocity of the particles, led to particle loss and lack of focussing, especially with small particle sizes. Therefore, in our research, to avoid such instability and shock formation in the orifice, a divergent nozzle was installed along with the aerodynamic lenses. A divergent nozzle is a form that offers less resistance to a flow and has a higher discharge coefficient, [3].

A nozzle (diffuser) is normally employed to regulate the flow of a fluid

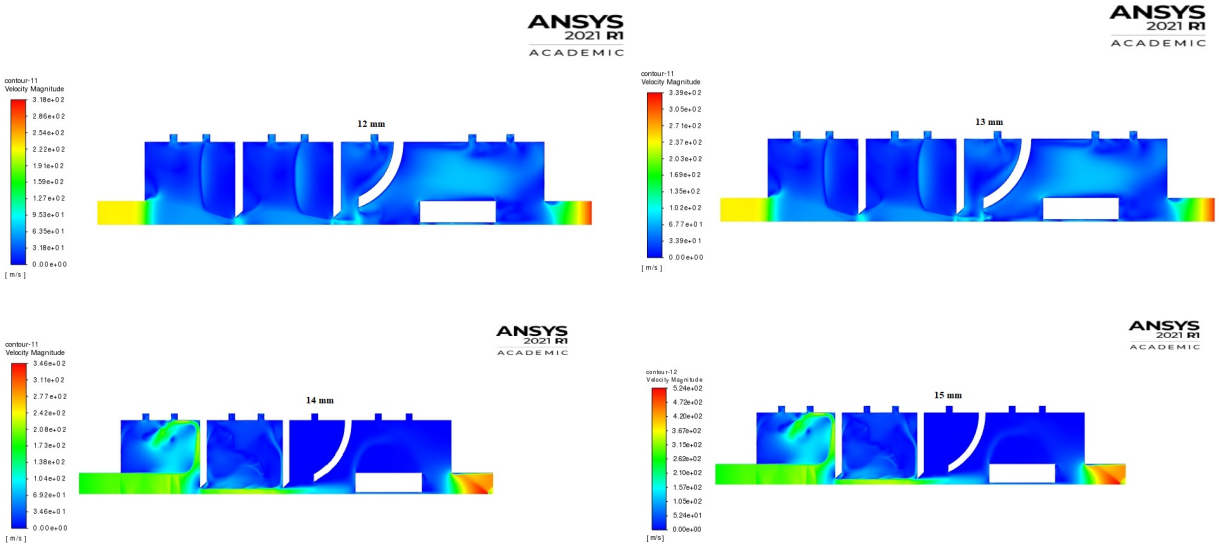

Figure 4.5: The length between the second lens and the divergent nozzle has been increased from 12 mm, 13 mm, 14 mm and 15 mm

exiting a region. Nozzles are sometimes used for producing particles and regulating the motion of an inflowing gas. Additionally, orifices can be employed for aerodynamically focussing aerosol particles so that the ones that fall within a specific size range can be dispersed into the air, or they can be used for separating and/or quantifying particles of varying sizes according to their inertial properties [26]. In this case, the goal was to have particles of various sizes flow at the same speed and trajectory in the particle stream as it passes away from the nozzle. To this end, a short (about 80 mm) reduction pipe was employed as a means of facilitating the flow of the particles in a collimated stream.

In this research, different nozzle positions were tested to determine a suitable nozzle position for measuring small nanoparticles. The lengths between the divergent nozzle and the second lens examined were 12 mm, 13 mm, 14 mm, and 15 mm, as shown in Figure 4.5, and the thicknesses were 1.2 mm, 1.4 mm, and 1.6 mm. As a consequence of multiple simu-

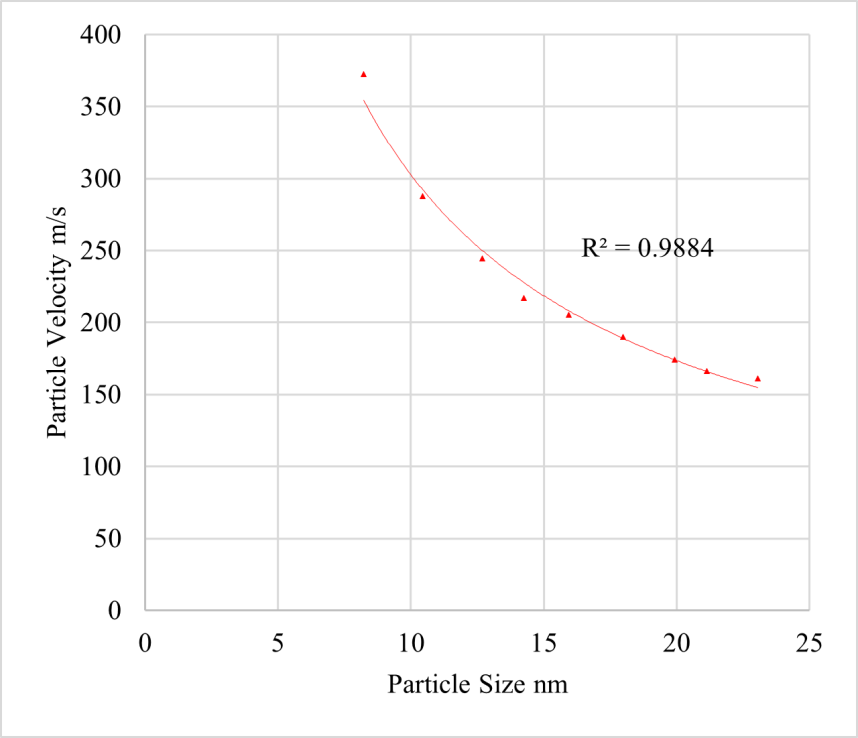

Figure 4.6: Particle sizes plotted against measured particle velocities

lations using ANSYS Fluent, the best nozzle position and measurements were discovered: The nozzle position for focussing small nanoparticles and regulating the motion of an inflowing gas is 15 mm after the second lens. As illustrated in Figure 4.7, the nozzle's thickness is equal to the orifice's thickness, which is 1.6 mm, and the divergent nozzle's hole diameter is 3 mm. When a thickness of the divergent nozzle of 1.2 mm was used, it was found that the velocity of the second lens was subsonic. Thus, the concentration of particles in the second lens will be difficult or non-existent. In the case of the divergent nozzle thickness of 1.4 mm that was used, the flow velocity was slightly less than the speed of sound. Therefore, after increasing the thickness of the divergent nozzle to 1.6 mm (which is the same thickness as the two aerodynamic lenses), it was found that the flow velocity was equal

to the speed of sound. As a result, the particles can be focussed on the second aerodynamic lens at this speed.

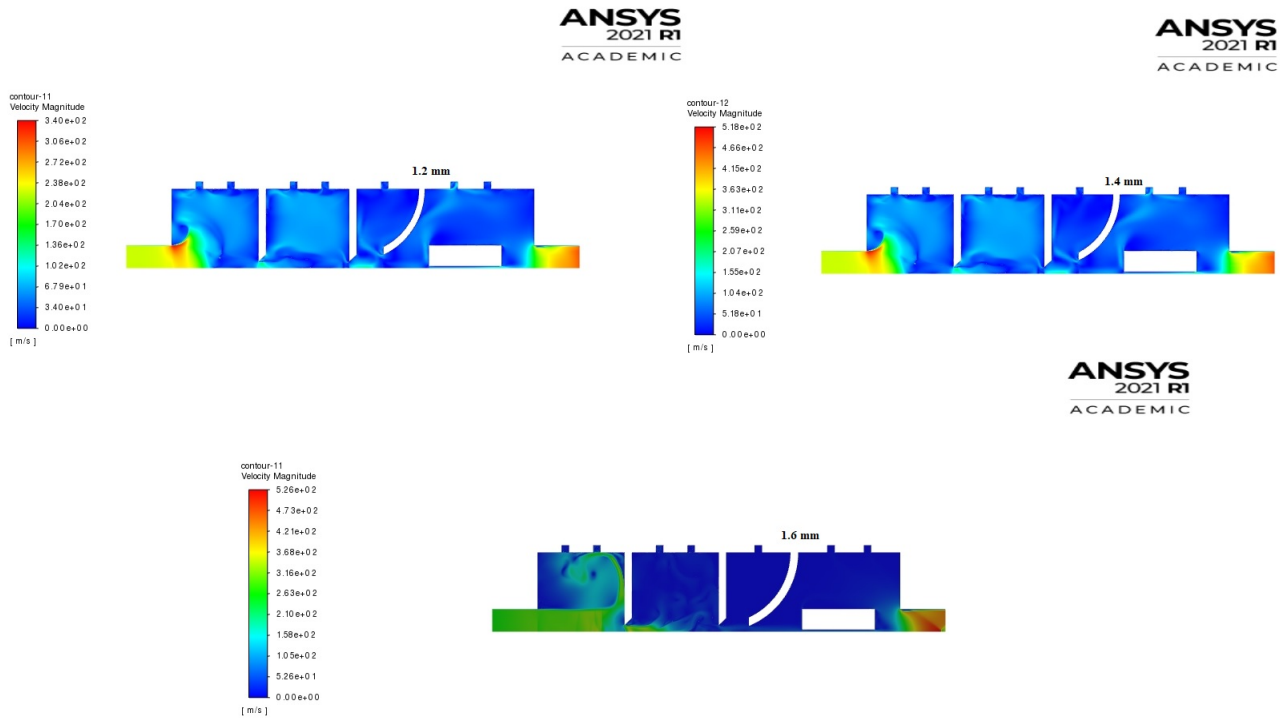

Figure 4.7: The best nozzle position and geometry was with a length of 15 mm between the divergent nozzle and the second lens, and a thickness equivalent to the thickness of the orifice, which is 1.6 mm, with a divergent nozzle hole diameter of 3 mm

Because the flow of the fluid through the orifice was at a velocity greater than the sonic speed (supersonic), the divergent nozzle was required to reduce that speed to reach sonic speed, Figures 4.8 and 4.9, because the focussing of particles can be achieved only at that speed, as shown in Figure 4.10.

After that, it was necessary to establish measurements for the position of the FCE after the aerodynamic lens. As a result of the examination of the flows in the divergent nozzle explained in this section, the following

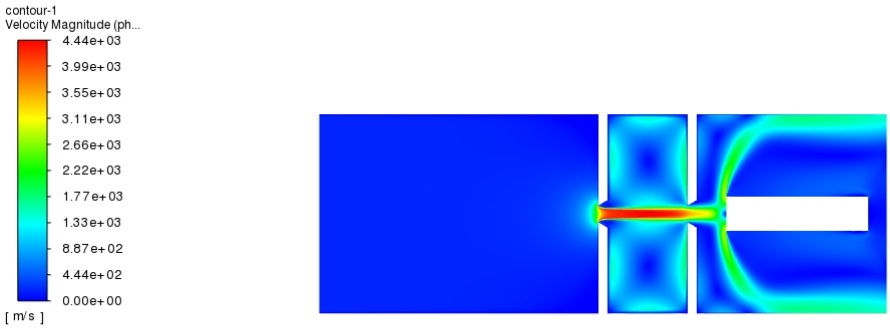

Figure 4.8: Velocity magnitude m/s by using only two orifices without a divergent nozzle

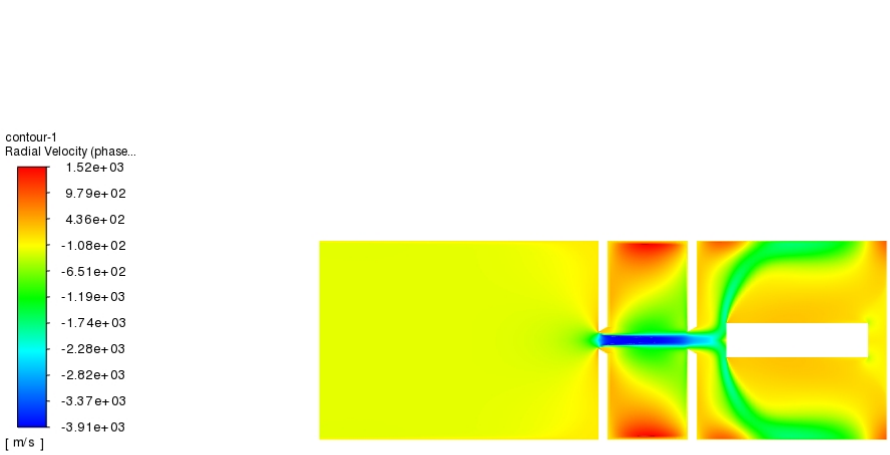

Figure 4.9: Radial velocity m/s by using only two orifices without a divergent nozzle

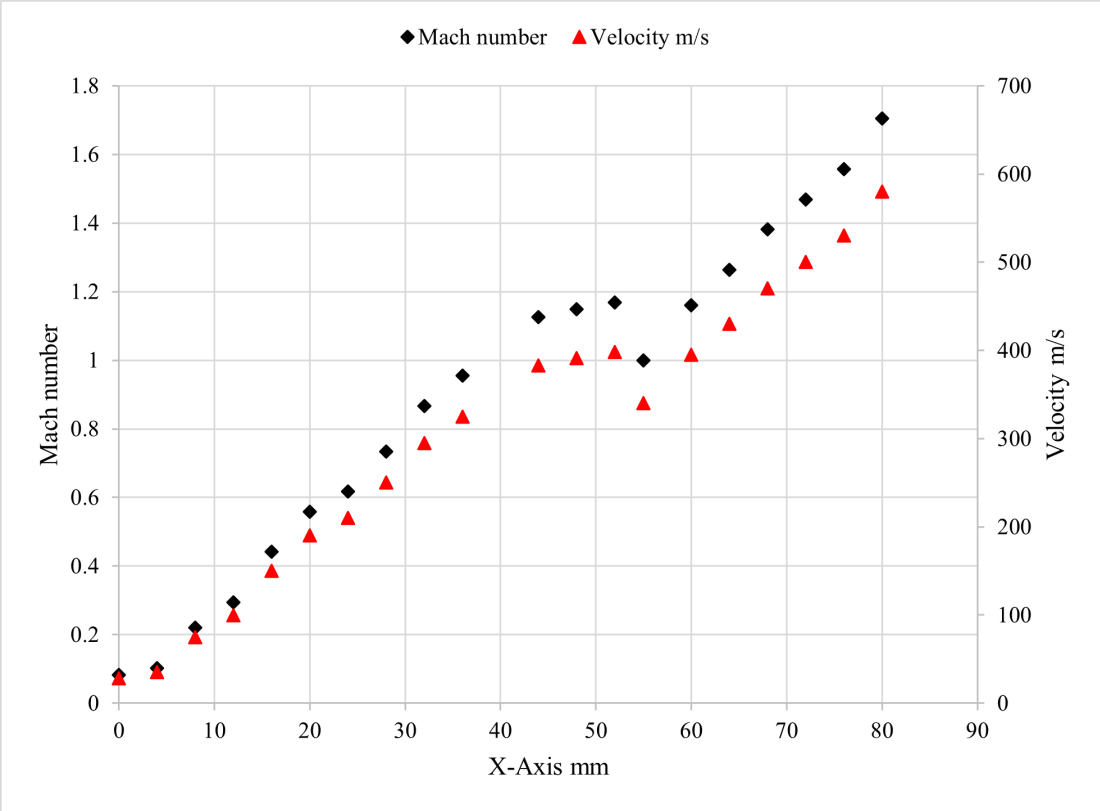

Figure 4.10: Mach number plotted against velocity

equation was developed to describe the relationship between velocity and pressure:

$$\frac{1}{\rho}\Delta P = -U\Delta U \tag{4.1}$$

The main point to note in this equation is that, if ΔU is positive, as the velocity increases, the change in pressure ΔP decreases. Furthermore, if ΔU decreases to less than zero, ΔP must be positive and therefore increase. The next consideration is the following relationship between velocity and area:

$$\frac{\Delta A}{A} = -\frac{\Delta U}{U}(1 - Ma^2) \tag{4.2}$$

Where Ma denotes the Mach number, A is the pipe size area, and U indicates the velocity. The area-velocity relation can be used to derive the necessary equations:

1. **For(Ma<1)**, decreases in the region increase the velocity and vice versa. As a consequence, velocity increases in the throat and decreases in the divergent nozzle in order to achieve sonic speed, resulting in a compressible flow.

2. **As(Ma>1)**, the area increases and the velocity decreases, i.e., the velocity increases in the throat and decreases in the divergent nozzle.

3. **For(Ma=1)**, $\left(\frac{dA}{A}\right) = 0$, indicating that the passage area is at either its minimum or maximum value at the location where the Mach number is one. It is clearly shown that the minimum area is the only realistic solution.

The purpose of using this equation is to clarify the benefit of using the divergent nozzle in this research. Because in this research, there is an attempt to reduce the loss of particles and concentrate the largest number of them through the lenses by using a short pipe, taking into account the value of the flow velocity through the lenses. Therefore, as mentioned previously, the flow velocity without using the divergent nozzle will be supersonic, while after using the divergent nozzle, the speed has reached sonic speed with a high particle concentration due to the shortness of the pipe and not losing a large number of particles.

The job of a divergent nozzle is to reduce the high velocity. Thus, to produce a sonic divergent nozzle, the goal is to reduce the area, which

results in a decrease in pressure, so that the Mach number would then be greater than 1 (1-Ma^2), after the flow passes through the nozzle. Therefore, if the velocity is reduced, as would occur in a nozzle, the change in area ΔA must decrease because the pressure would also decrease. The nozzle will thus diverge, but since the flow is supersonic, the velocity will then become that sonic speed that enables the particles to be focussed. As a result, the area of the pipe is reduced, as a pipe with a length of 80 mm was used in this study, as opposed to previous studies that used pipes longer than 100 mm. This causes the supersonic flow between the lens and the divergent nozzle to reach the desired sonic speed as the area of the pipe diminishes.

4.3.3 Faraday Cup Electrometer

Because the Faraday cup electrometer (FCE) will be installed inside the pipe containing the aerodynamic lenses, its presence inside the pipe unquestionably affects the velocity of the particles, the pressure inside the pipe, the recirculation of the flow, and the particle focussing. Consideration must therefore be given to simulating the model with a design that incorporates the FCE positioned inside the pipe and after the lens, as shown in Figure 4.11. The developed model was therefore simulated with several different lengths between the lens and the FCE. Between the second lens and the FCE, lengths of 10 mm, 12 mm, 14 mm, and 16 mm have been used, as depicted in Figure 4.12.

ANSYS Fluent was employed to design the pipe, with two orifices installed, followed by the divergent nozzle and the FCE. The requirement was to measure the size and axial velocity of the airborne nanoparticles that reach the FCE. The distance between the second lens and the FCE is shown in Figure 4.7. In reality, the FCE contains a small tube that allows the flow to continue. However, since ANSYS Fluent considers the FCE to be a solid body, as shown in Figure 4.11, the flow stops and the velocity

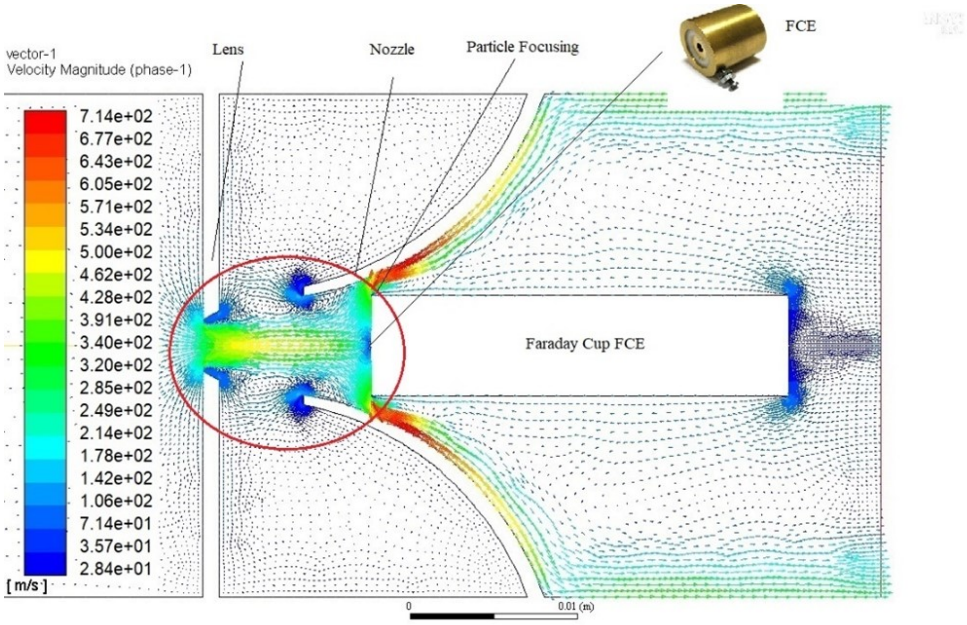

Figure 4.11: FCE installed inside the pipe

goes to 0 m/s in the FCE inlet. To solve this problem, the tube inside the Faraday cup electrometer FCE was considered in the simulation using a 1 mm diameter tube to allow a cross of fluid and particles through FCE to avoid stopping the flow in front of the Faraday cup electrometer in its simulation. Therefore, the size and axial velocity of the airborne nanoparticles were measured just through the FCE. Probing the data in this way enables a determination of the size and velocity of the airborne particles in front of the FCE.

In an FCE, nanoparticles are deposited on a filter, where they release their charge, causing a low current to flow, which is then converted to a voltage by a high-impedance resistor. This device thus provides a simple, effective, and fast process for detecting nanoparticles. However, these phenomena were not modelled in our Fluent simulations. Following the simulation of all distances investigated, the conclusion was that the optimal

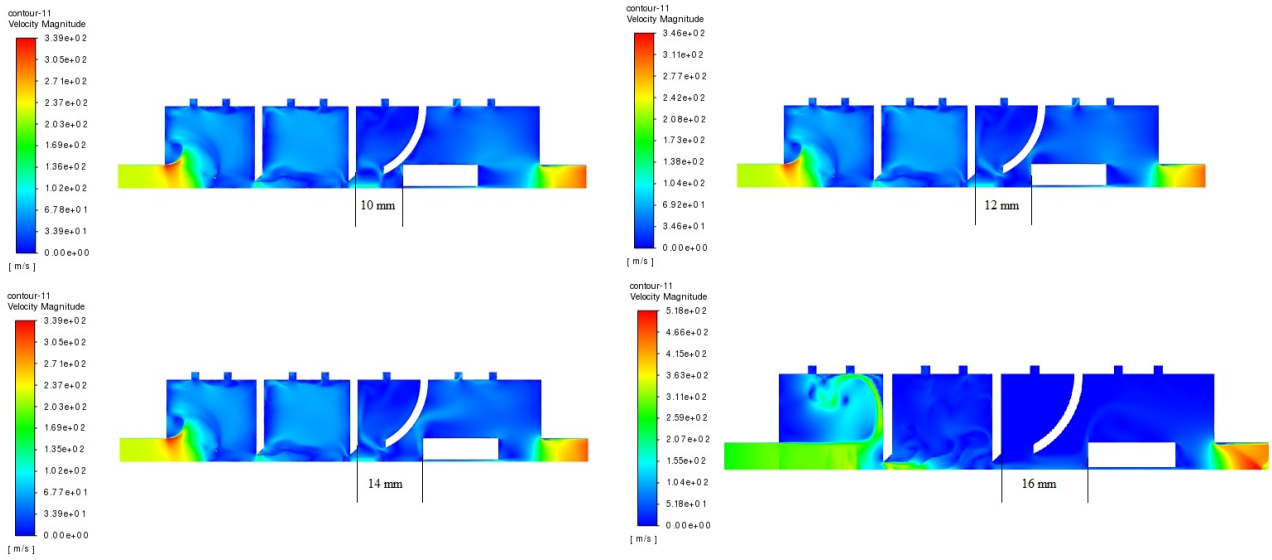

Figure 4.12: The length between the second lens and FCE has been increased from 10 mm, 12 mm, 14 mm and 16 mm

length of the section between the lens and the FCE is 16 mm, as indicated in Figure 4.13. To be precise, the volume of the flowrate through the inlet was set at 0.000024 m^3/s in this investigation.

The reason for choosing a distance of 16 mm between ADL and FCE is that at this distance, small nanoparticles that the FCE is focussed on can be detected, which in turn allows the information to be sent to the DMA so that the results can be determined.

4.3.4 Differential Mobility Analyzer

DMAs have been widely used for quantifying and distinguishing particles of various sizes, ranging from micrometers to nanometers [158, 69]. A DMA determines the size of nanoparticles based on their mobility in an electric field. A positive electrode attracts negatively charged particles, and for

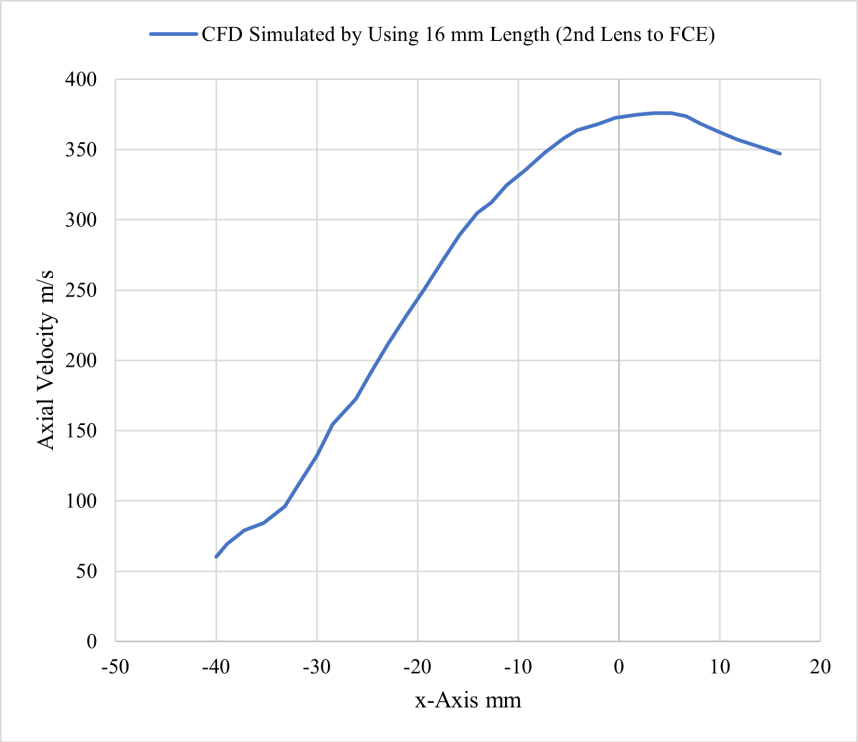

Figure 4.13: The CFD results (after using two orifices installed, followed by the divergent nozzle and the FCE) for the mean axial distance for the FCE position

a given voltage, only particles with a specific degree of mobility can pass through an exit slit in the positive electrode of the DMA. A condensation particle counter (CPC) or an FCE is then used for counting the particles. An FCE is typically employed in conjunction with a DMA, a classifier that cuts out monodisperse particle size fractions from a polydisperse aerosol sample, Figure 4.14.

The air is passed into a radioactive charger, which charges the particles according to a specific charge distribution. The particles are then separated in an electric field based on their mobility. Only particles with the appropriate charge and size move to the air sample outlet, where they reach the FCE as a monodisperse aerosol. Depending on the form of DMA used, par-

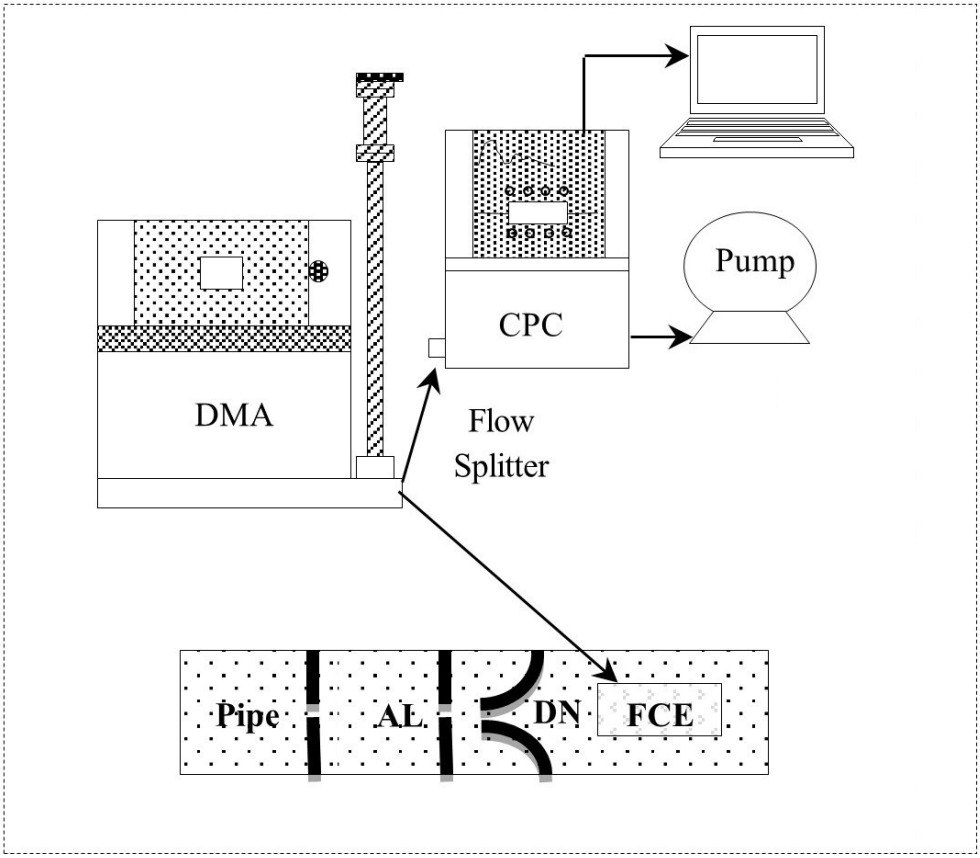

Figure 4.14: Experimental apparatus for measuring nanoparticle penetration in an aerodynamic lens

ticles are classified into the selected channels through scanning/stepping. The range of particle sizes changes with the flowrate of the sheath air in each DMA. DMAs are available on different-sized columns, as displayed in Figure 4.15. Small DMA is preferred in this research because it operates within the particle size ratio of 0.82 nm to 109.89 nm.

A DMA can thus constitute an integral component of a monodisperse aerosol generation system or a submicron particle size generator. Prior to entry into the classifier, the sample air passes the neutralizer, which is a

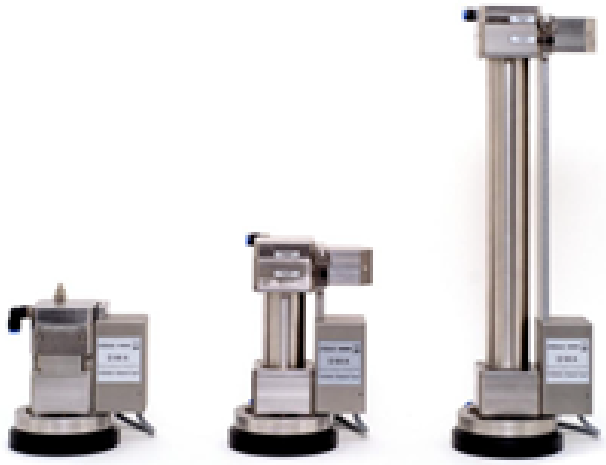

Figure 4.15: Small, medium, and large DMAs with different-sized columns [1]

radioactive source (Americium 241) in a stainless steel housing, fixed at the top of the DMA. It functions as a bipolar charger to ensure a well-defined charge distribution on the particles, which means that the polydisperse aerosol sample passes through the ionized air volume in the housing, where a constant equilibrium charge on the particles is established. The particles next enter the electrostatic column. The applied high voltage can then classify the aerosol according to the electrical mobility of the particles. The rod voltage generated by the classifier is the primary setting that controls the particle size. Settings range from 5 volts to 10,000 volts. As a particle size is selected, the appropriate voltage corresponding to this particle diameter is calculated, with the voltage being inversely related to the particle size. It should be noted that the calculation includes consideration of not only the flowrate and a charge assumption, but also the temperature and pressure of the sample. The DMA controller provides not just step-by-step control of the high voltage supply but also the supply of clean sheath air needed for the classifier. The parameters of the GRIMM Vienna-type DMA electrodes used for focussing techniques are presented in Tables 4.1 and 4.2 and in

Table 4.1: Parameters of GRIMM Vienna-type DMA electrodes used for focussing techniques [1]

DMA Type	Active Length cm	D-inner cm	D-outer cm
L-DMA	35	2.6	4
M-DMA	8.8	2.6	4
S-DMA	1.5	2.6	4

Table 4.2: Parameters of GRIMM Vienna-type DMA electrodes [1], (dp-min and dp-max are the minimum and maximum particle sizes, respectively)

DMA Type	Sheath Air l/min	3	4	5	6	8	10	12	15	20
L-DMA	dp-min	10.38	8.97	8.01	7.31	6.32	5.65	5.15	4.60	3.98
in nm	dp-max	1083.26	842.86	697.36	599.52	475.73	400.19	348.95	269.62	242.52
M-DMA	dp-min	5.16	4.47	3.99	3.64	3.15	2.82	2.57	2.30	1.99
in nm	dp-max	350.43	284.44	243.47	215.22	178.28	154.79	138.29	120.83	101.96
S-DMA	dp-min	2.12	1.84	1.64	1.50	1.30	1.16	1.06	0.95	0.82
in nm	dp-max	109.89	92.95	81.84	73.86	62.96	55.72	50.48	44.77	38.41

Figure 4.16. As a consequence, S-DMA should be utilized in this study so it works with particle sizes ranging from 0.82 nm to 109.89 nm.

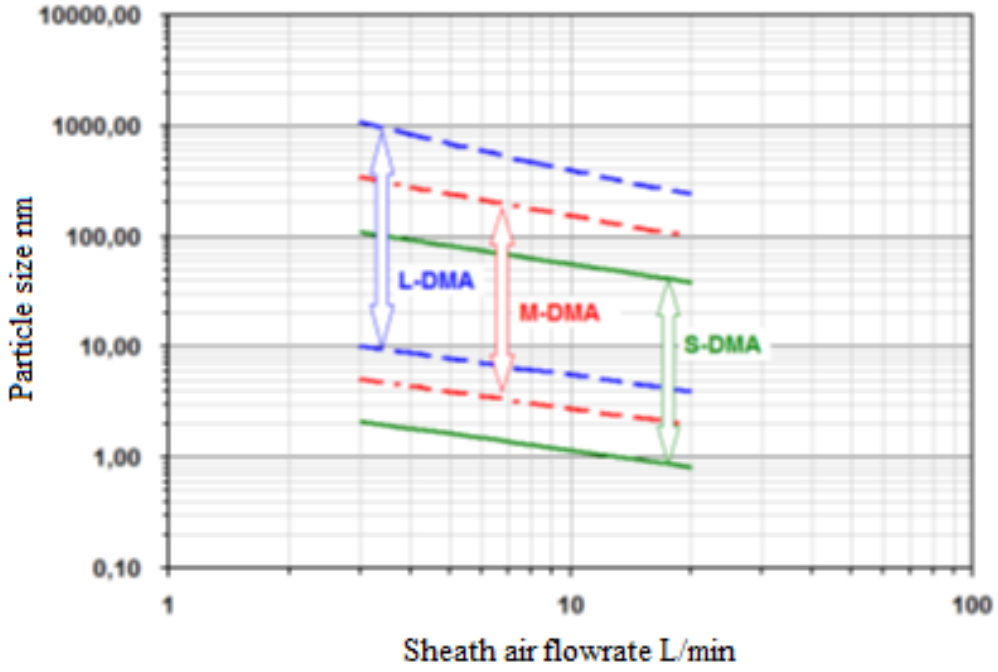

Figure 4.16: Changes in the particle size range corresponding to the sheath air flowrate for three different sizes of Vienna-type DMAs [1]

4.4 Theory of Fluid Flow

4.4.1 Theory of Fluid Flow Through Aerodynamic Lenses

For the purposes of this research, an aerodynamic lens operates with air flowing through the orifice when the Mach number equals 1, as illustrated in Figure 4.17. In this case, the boundary conditions are based on an assumed inlet pressure of $1.01325 * 10^5$ Pa, the stagnation temperature T_o at the inlet is 300 K, the static pressure p at the pipe's exit is 3,738.9 Pa, and the pressure within the chamber (This will be explained in Chapter 5)

is 1 Pa.

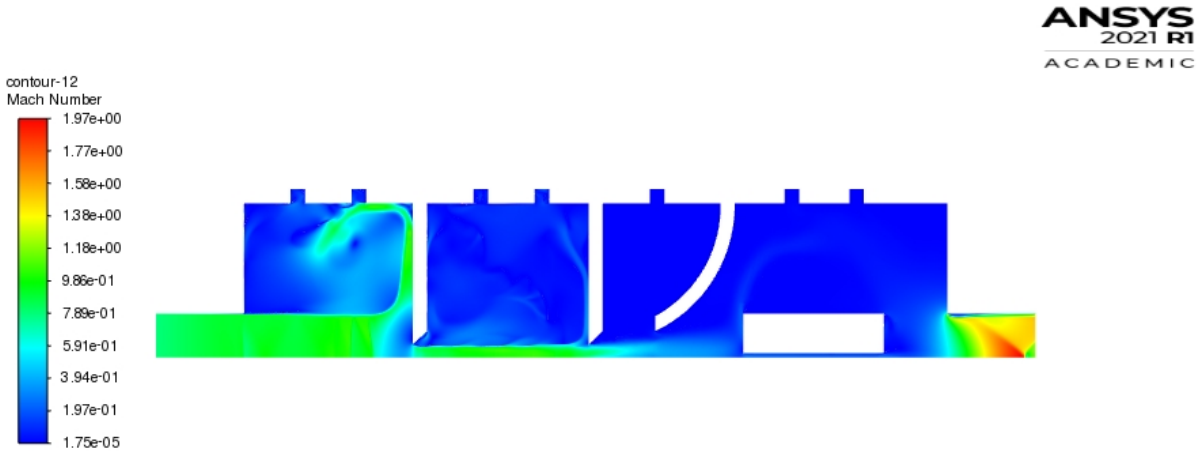

Figure 4.17: Mach number distribution calculated from the divergent nozzle simulation

For this case, the maximum flowrate of the mass in the air ($\gamma = 1.4$), ($R = 287\frac{J}{kg.K}$), is computed as follows:

$$\dot{m}_{max} = \frac{0.532\ A^*\ P_1}{\sqrt{T_1}} \tag{4.3}$$

In Equation 4.3, $\dot{m}_{max}$ is in $(\frac{kg}{sec})$; A^* is in m^2; T_1 is in (°K); P_1 is in (Pa); and P_1 and T_1 are the total pressure and the temperature at the pipe inlet, respectively. If the volume flowrate is simply the mass flow divided by the fluid density, ρ, the flowrate of the volume can be expressed as:

$$q\ \left(\frac{m^3}{sec}\right) = \dot{m}_{max}\ (\frac{kg}{sec})/\rho(\frac{kg}{m^3}) \tag{4.4}$$

$$q = \frac{\dot{m}_{max}}{\rho}\ \left(\frac{m^3}{sec}\right)$$

Since the air in the surrounding conditions is an ideal gas $\rho = \frac{P}{RT}$, the next equation thus follows:

$$q = 0.532R\left(\frac{P_1}{P}\right)\left(\frac{T}{T_1}\right) A^* \sqrt{T_1} \tag{4.5}$$

Equation 4.5 represents the flowrate of volume $\left(\frac{m^3}{sec}\right)$via any cross section of the pipe. Note that since the pressure and temperature change throughout the pipe, the volume flowrate is not the same for each cross section. While the flowrate of the volume is not constant, the mass flowrate is always constant. With respect to the use of an aerodynamic lens for sampling, it is important to know that the volume flowrate is measured not at the throat of the orifice but at the inlet.

4.4.2 Theory of Fluid Flow Through a Divergent Nozzle

A divergent nozzle consists of a cone-shaped passage that creates a partial expansion of the pipeline. Divergent nozzles are not reliant on a sharp edge, which can decompose over time, to maintain their accuracy. This means that they provide excellent long-term accuracy while reducing corrosion and decreasing the potential for distortion. These nozzles are available in three standards and are designed for either fastening between flanges, welding into a tube, or fixing between grooves. A divergent nozzle is also employed for gathering data used for process improvement in manufacturing environments. Figure 4.18 shows an example of a divergent nozzle.

A divergent nozzle is a cross-section that becomes larger in the direction of flow. It is used for minimizing gas flow at sonic speeds. However, there is a decrease in the cross-sectional area at the inlet of the divergent nozzle, as shown in Figure 4.19.

Figure 4.18: Example of a divergent nozzle

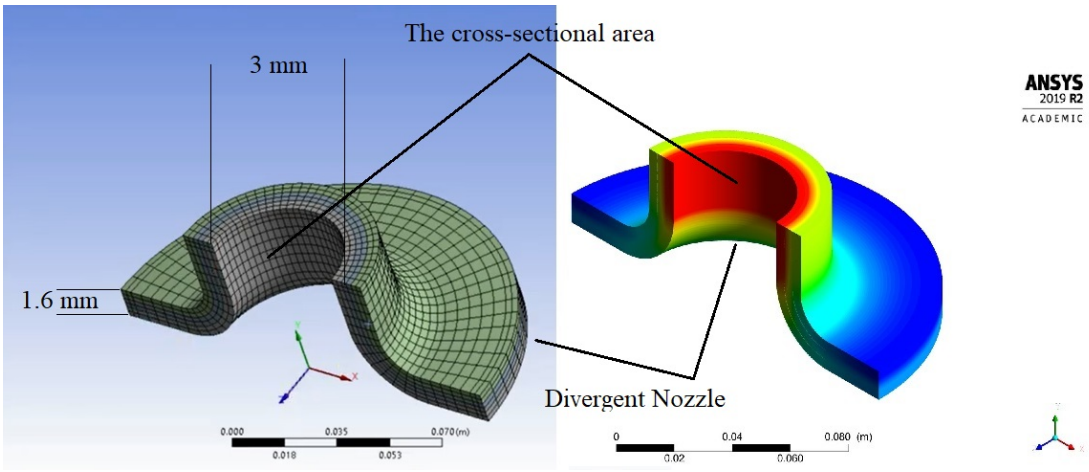

Figure 4.19: Cross-sectional area of the divergent nozzle

When the gas passes the orifice, the speed increases to that of supersonic sound (Mach number $>$ 1). However, when the gas passes through the divergent nozzle, the speed drops to a sonic speed (Mach number=1), where 0 to 40 mm is the length from the inlet to the second orifice on the x-axis, Figure 4.10, 40 mm to 55 mm is the length from the second orifice to the divergent nozzle, 40 mm to 56 mm is the length from the second lens to the FCE, and 55 mm to 80 mm is the length from the divergent nozzle to the exit. The aerodynamic lens-divergent nozzle system is designed so that the

flow reaches a speed that equates to sonic speed.

With respect to fluid flow measurements, the orifice plate and divergent nozzle simplify the use of differential pressure ΔP sensors for calculating the flow velocity. Examples of the sensors are shown in Figure 4.20.

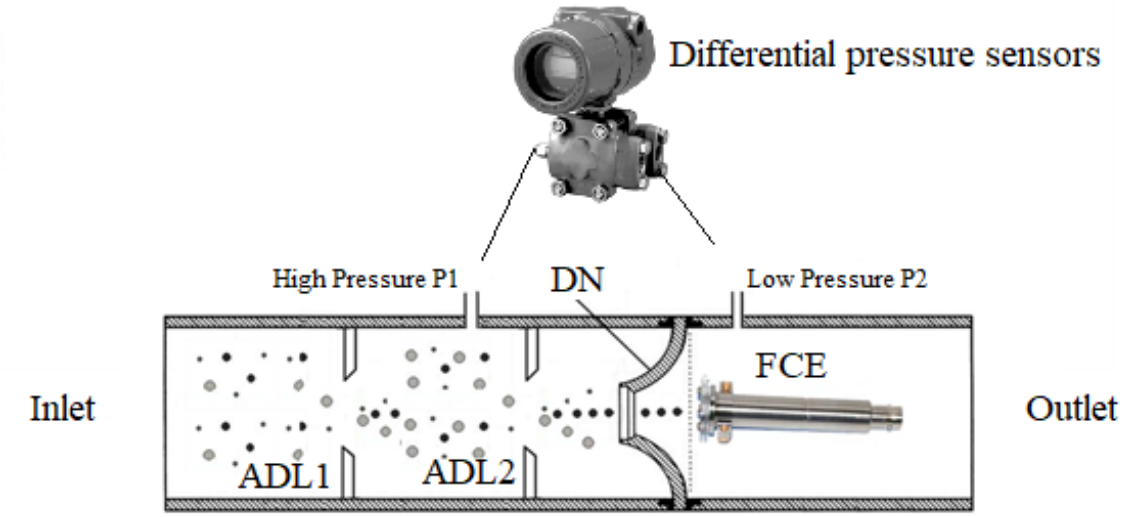

Figure 4.20: Differential pressure sensors [2]

In these cases, the following equation associates the flow with $\Delta P = (P_1 - P_2)$:

$$q = \left[C_D \frac{\pi}{4} \beta^2\right] \left[\frac{2\,(P_1 - P_2)}{\rho\,(1 - \beta^4)}\right]^{\frac{1}{2}}]$$

Where q is the volume flowrate in $\frac{m^3}{s}$;C_D is the discharge coefficient [57]; P_1 and P_2 are in Pa; ρ is the fluid density in $\frac{kg}{mm^3}$; $\beta = \frac{d_f}{D}$; d_f is the orifice diameter (in mm); D is the upstream and downstream pipe diameter (in mm). An important point is that obtaining sonic speed requires that

appropriate compression ratios be maintained across the divergent nozzle. Critical pressure determines the maximum mass flowrate through a nozzle. The pressure ratio at which the flow is accelerated to a velocity equal to the local velocity of sound in the fluid is known as the critical pressure ratio, and sonic speed is another name for the critical flow in the orifice. The sonic speed determines the constant flowrate that is unaffected by differential pressure fluctuations or variations in downstream pressure. For a nozzle, the ratio of the critical pressure to the stagnation pressure is expressed as follows:

$$\frac{P_c}{P_1} = \frac{\left(\frac{2}{\gamma+1}\right)\gamma}{\gamma - 1} \tag{4.6}$$

where P_c is the critical pressure (Pa); P_1 is the stagnation pressure (Pa); and γ is the index of isentropic expansion, or the compression constant. For air, the critical pressure ratio can be determined as follows:

$$\frac{P_c}{P_1} = \frac{\left(\frac{2}{1.4\ +1}\right)1.4}{1.4\ -1} = 0.528 \tag{4.7}$$

This equation is important since it relates to nanoparticle focussing because, at sonic speed, focussing of the particles will be achieved. Therefore, the airflow achieves the speed of sound [63] if the absolute pressure ratio is at least 0.528, which can be calculated precisely using the assumption of the ideal gas condition, as shown in Equation 4.8:

$$c = \sqrt{\frac{\gamma R T_{f1}}{M}} \tag{4.8}$$

Where γ is the specific heat ratio (1.4 for air), T_{f1} is the pre-focussing temperature, and M is the molar mass of the gas.

Therefore, to obtain the speed of sound only in the throat or nozzle, the pressure ratio $\frac{P_{Nozzle}}{P_{Inlet}} = \frac{P_c}{P_1} = 0.528$ should be maintained.

4.5 Results and Discussion

Because the FCE will be installed inside the pipe containing the aerodynamic lenses, its presence inside the pipe will very certainly affect particle velocity, pipe pressure, flow recirculation, and particle focussing. Simulating the model (inlet, pipe, two lenses, divergent nozzle, FCE, and outlet) should be considered such that the design incorporates the FCE inside the pipe and after the lens. For these reasons, as previously mentioned, the developed model was simulated with several different lengths between the lens and the FCE: 10 mm, 12 mm, and 16 mm measured between the lens and the FCE. After the separate simulations for each length were completed, the conclusion was that the best length between the lens and the FCE was 16 mm, as detailed in Figure 4.21.

The ability to detect nanoparticles between the lens and the FCE causes the second lens to concentrate on them more efficiently. Figure 4.10 shows how the space between the lens and the FCE allows the velocity to reach sonic speed, the speed at which nanoparticle focussing is feasible. This conclusion was reached after observing the effects of adjusting the length between the lens and the FCE, as described below. Figures 4.22 and 4.23 show the results for the case in which a length of 10 mm was applied, where x = -40 at the inlet of the pipe, x = 0 at the second lens, and x = 10 in front of the FCE. With the length of the section between the lens and the FCE equalling 10 mm, with the use of a divergent nozzle and two lenses, the velocity in front of the FCE was less than the sonic speed: 280.7 m/s (Figure 4.23). So, the concentration of particles at this speed is small because the velocity of the particles is less than the speed of sound.

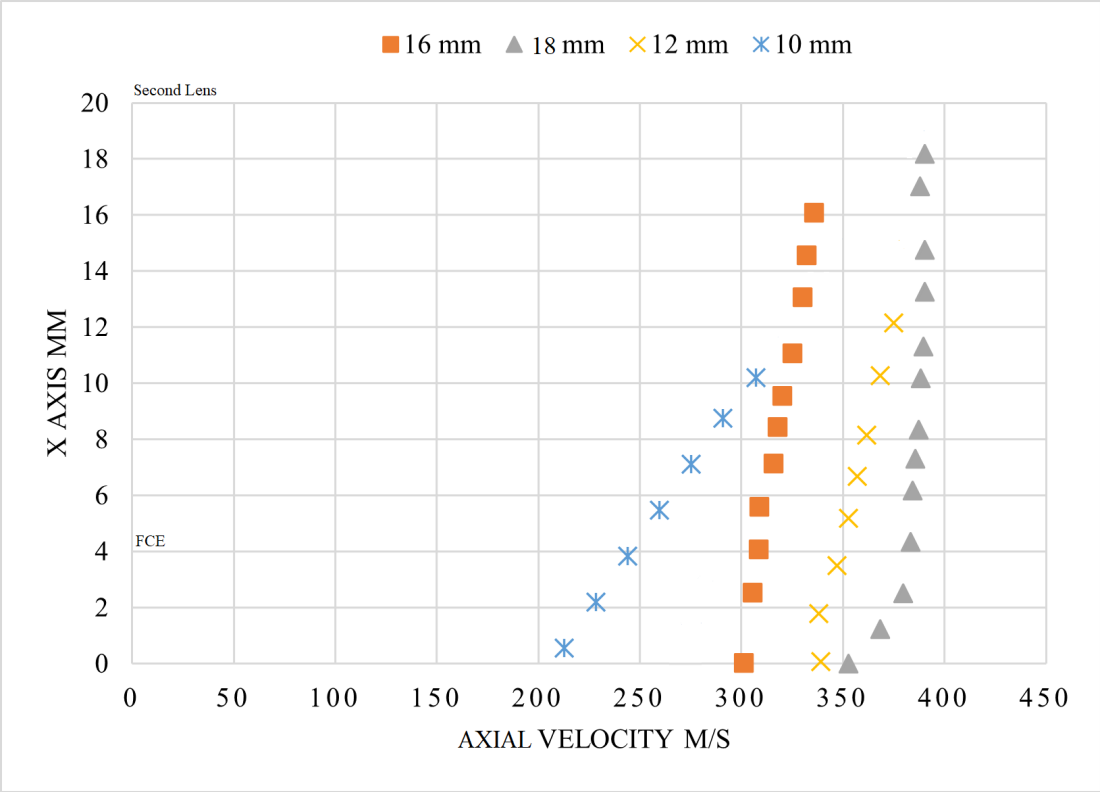

Figure 4.21: Axial velocity with an x-axis for measurements of 10 mm, 12 mm, 16 mm, and 18 mm between the lens and the FCE

Figures 4.24 and 4.25 display the results for the case in which the length was equal to 12 mm. As indicated in the Figures, when the length of the section between the lens and the FCE was increased to 12 mm, the velocity at the beginning of the FCE in the study results was 287.3 m/s.

The results when the length of the section between the lens and the FCE equalled 16 mm are displayed in Figures 4.26 and 4.27, where the velocity at the beginning of the FCE in this study was 340.29 m/s. Since the speed of sound depends on temperature, Figure 4.28 shows the temperature contour of this model.

When using the length of 18 mm between the lens and the Faraday

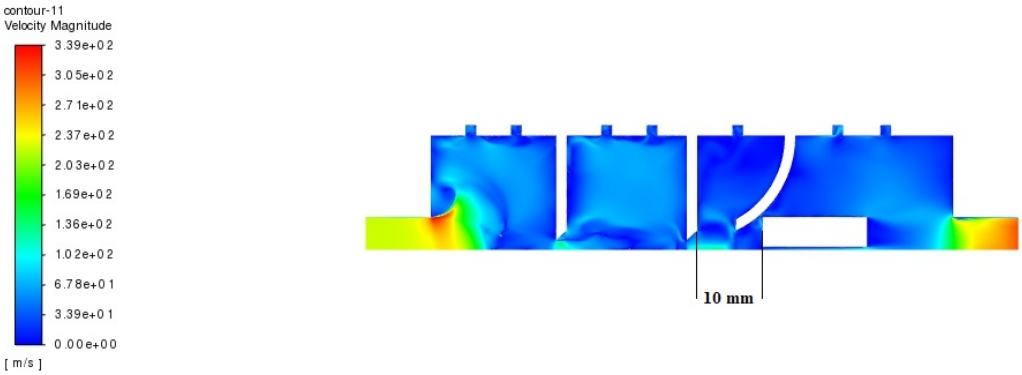

Figure 4.22: Case in which the length of the section between the lens and the FCE equalled 10 mm

cup, the velocity is erratic, which leads to unstable flow and thus leads to particles defocussing in front of the Faraday cup. However, as is evident in Figures 4.29 and 4.30, the velocity at the FCE with this length was 370.69 m/s.

These findings, based on continuous increases in the length of the section, reveal the effect of the FCE location on the results and its impact with respect to changing the flow velocity and, ultimately, focussing the nanoparticles. Finally, a sonic speed of 340.29 m/s was achieved after the flow was passed through the aerodynamic lens and the divergent nozzle, and the length of the section between the lens and the FCE was set at 16 mm, which was found to be the optimal length that enabled the flow velocity to reach the sonic speed, as previously indicated in Figure 4.13 and, for

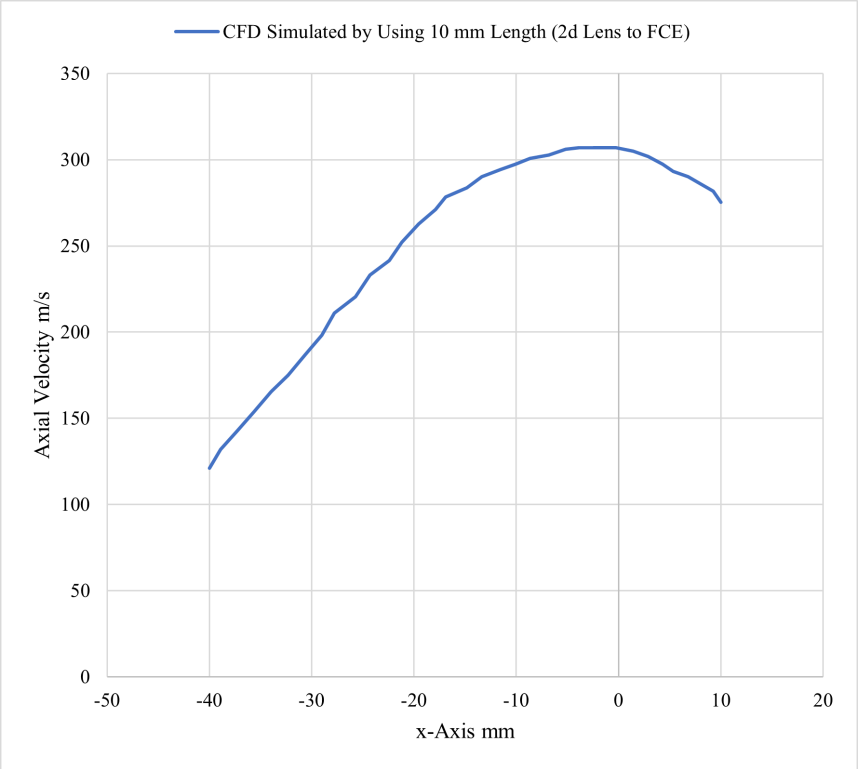

Figure 4.23: The results when the length of the section between the lens and FCE equalled 10 mm

convenience, as repeated in Figure 4.27.

By considering Rosin-Rammler flow velocity U in the ANSYS Fluent, and injecting solid particles in the inlet, the particle will start moving from the inlet. Therefore, the Stokes number is shown with particle size and velocity in the Figure 4.31 following. Because the particle size ranges from 1 nm to 300 nm, it is difficult to inject each individual particle into the system, so the Rosin-Rammler method was used, which determines the upper and lower limits of the particle size only. For example, the upper limit is considered to be 300 nm and the lower limit is 1 nm. Based on the Stokes number, which demonstrates that the closer the Stokes number is to one, the greater the particle concentration, this value may be used to measure

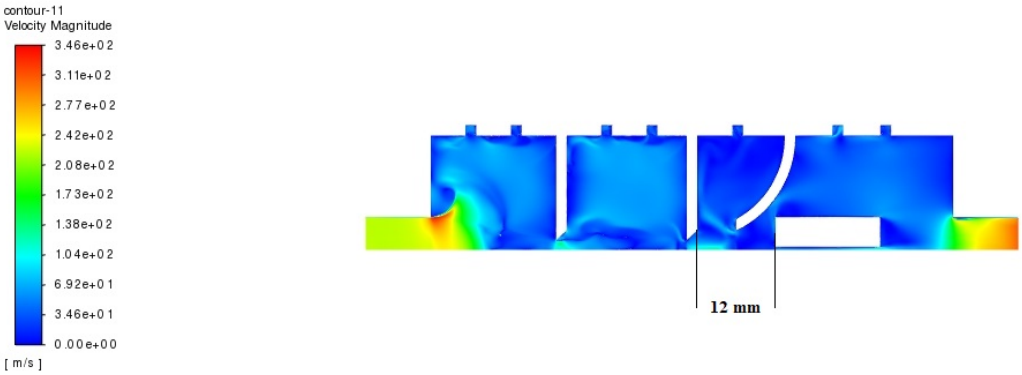

Figure 4.24: Case in which the length of the section between the lens and the FCE equalled 12 mm

the size of the concentrating particles. It can be seen from the above Figure that the particle size ranged from 2 nm to 160 nm has a Stokes number ranged between 0.012 and 0.984, while the particle size ranging from 180 nm to 200 nm has a Stokes number ranged between 1.11 and 1.23. The Stokes number ranges from 1.23 to 1.99 for particles larger than 200 nm (200 nm–320 nm). By looking at the values of the Stokes number in this result, it was found that the Stokes number particles whose sizes range from 20 nm to 80 nm can be focused on, but with difficulty, due to the small value of the Stokes number, while the Stokes number particles with sizes from 100 nm to 200 nm have a high concentration of these particles because the Stokes number is approximated to one.

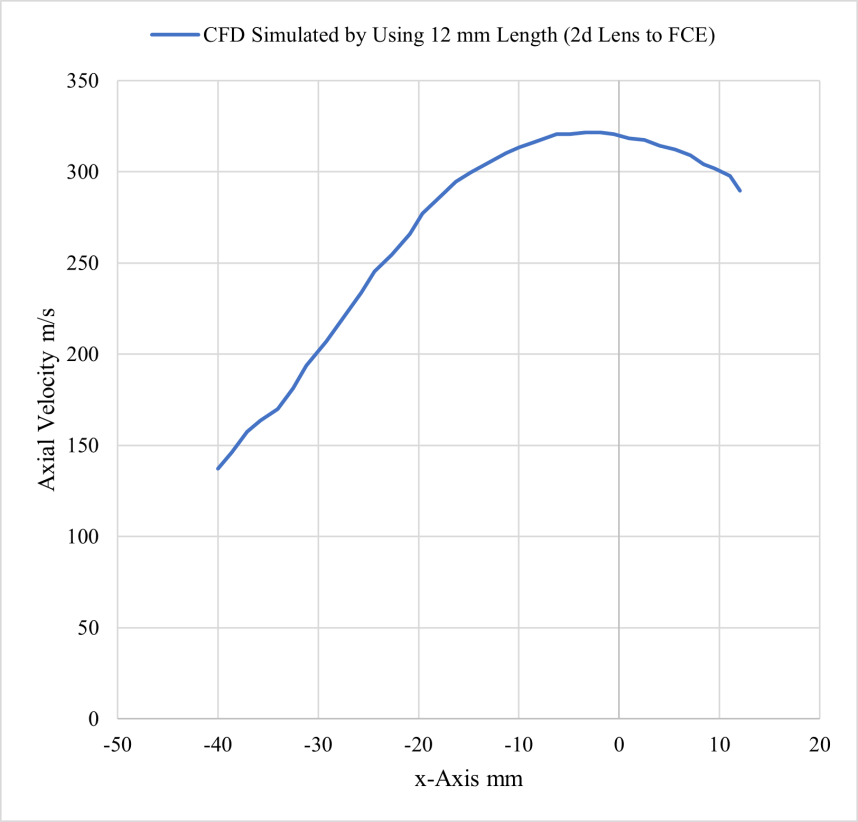

Figure 4.25: The results when the length of the section between the lens and the FCE equalled 12 mm

4.6 Summary

The study described in this chapter has focussed on evaluating the appropriate shape to enhance the aerodynamic lens' performance. This investigation represents the first systematic effort to measure the velocity of nanoparticles using an aerodynamic lens with a divergent nozzle. It has been demonstrated that this technology enables the focussing of particles on the x-axis through aerodynamic lenses, allowing them to be used directly with DMA and an FCE, as indicated in Figure 4.32. In Figure 4.32 below, 3 nm and 350 nm particles are represented by blue and red dots, respectively,

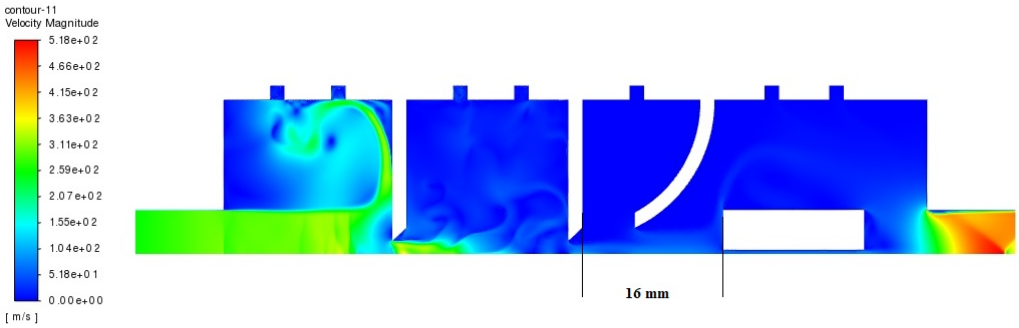

Figure 4.26: Case in which the length of the section between the lens and the FCE equalled 16 mm

and also shown are the horizontal and vertical directions that display the number distribution of the particles for each x and y value. For this size range, the modelling reveals only a small difference in particle distribution.

Computational simulations showed that the system provides the possibility of focussing nanoparticles using two lenses with a divergent nozzle installed in the short pipe (L = 80 mm) by achieving the speed of sound at which the particles can be focussed. The investigation demonstrated that this system, incorporating aerodynamic lenses with a divergent nozzle, performs well for focussing the nanoparticles. This study thus confirmed the possibility of using two lenses to focus small nanoparticles while maintaining a speed equal to the sonic speed in the second orifice when the Mach number equals 1. That corresponds to the speed at which nanoparticles can be focussed.

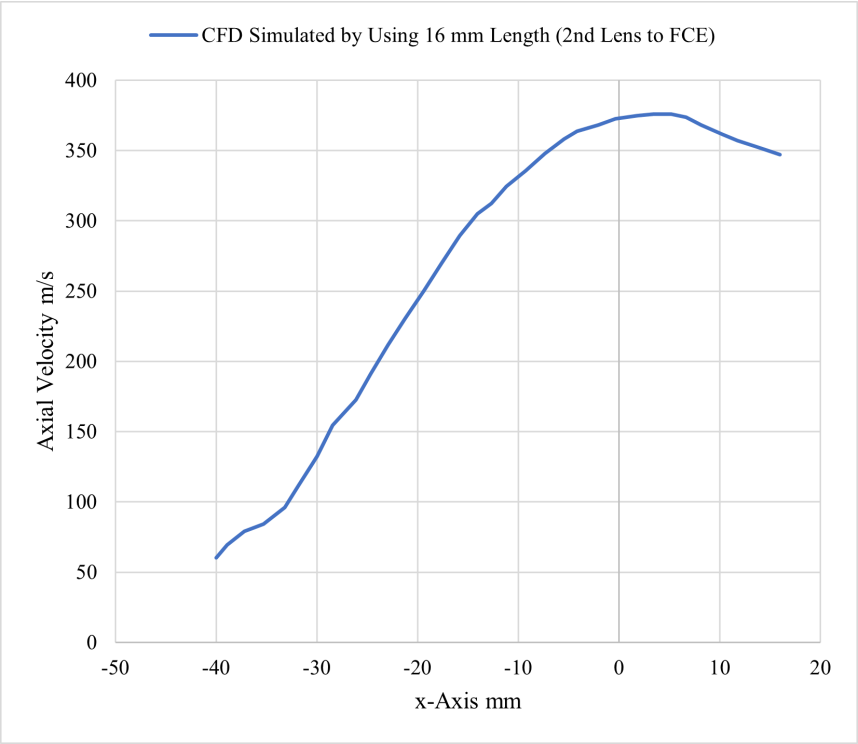

Figure 4.27: The results when the length of the section between the lens and the FCE equalled 16 mm

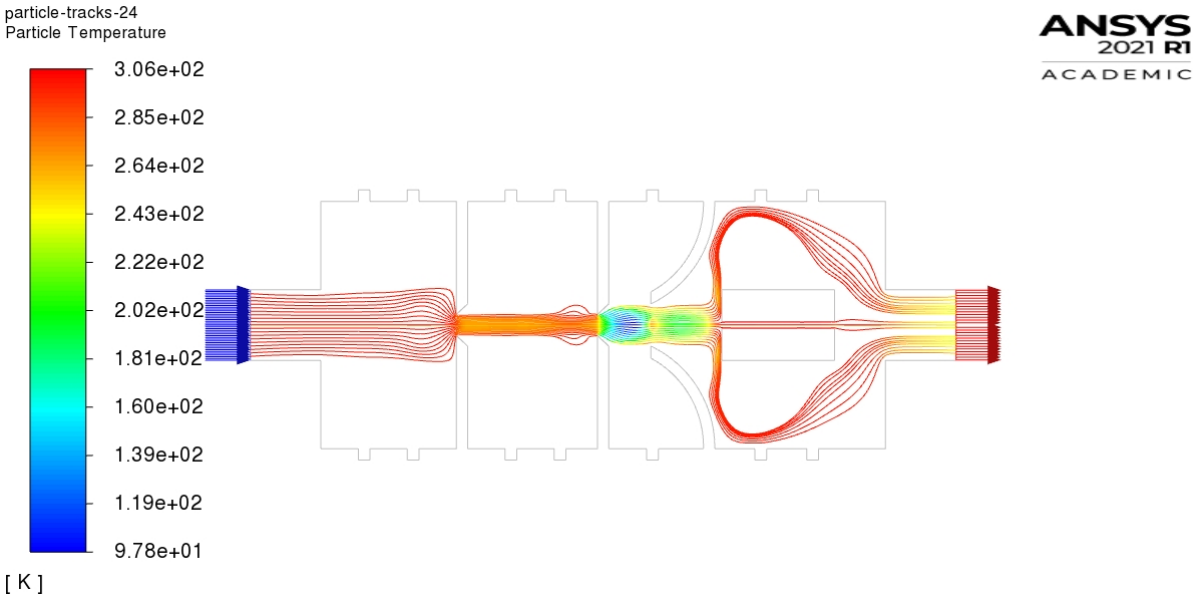

Figure 4.28: The temperature contours of this model

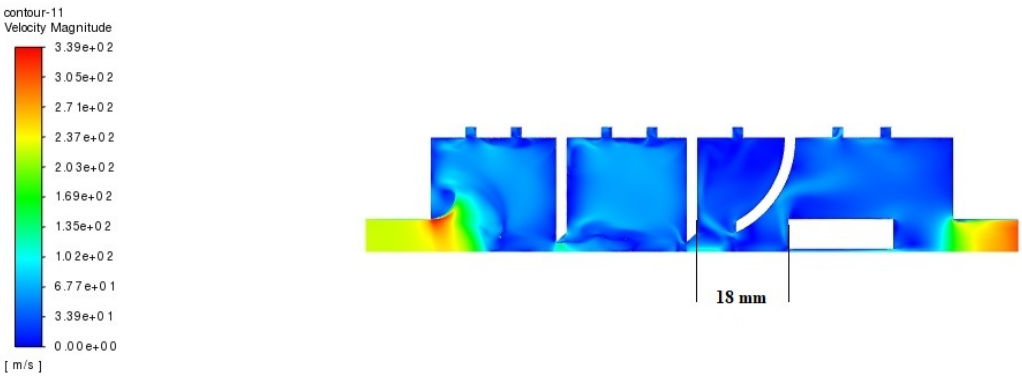

Figure 4.29: Case in which the length of the section between the lens and the FCE equalled 18mm

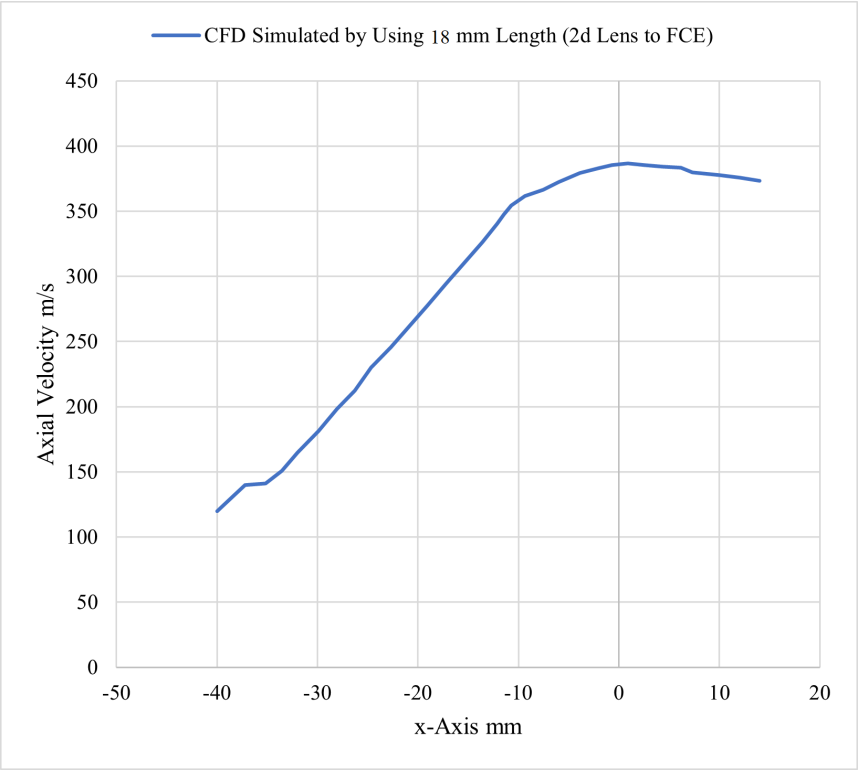

Figure 4.30: The results when the length of the section between the lens and the FCE equalled 18 mm

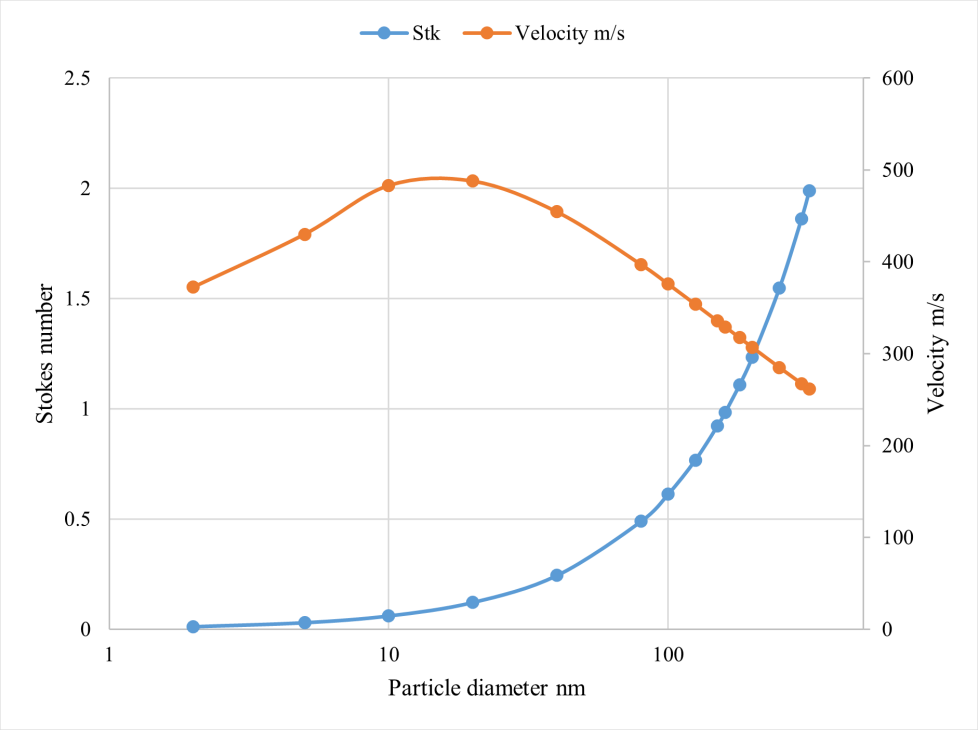

Figure 4.31: the Stokes number with particle size and velocity

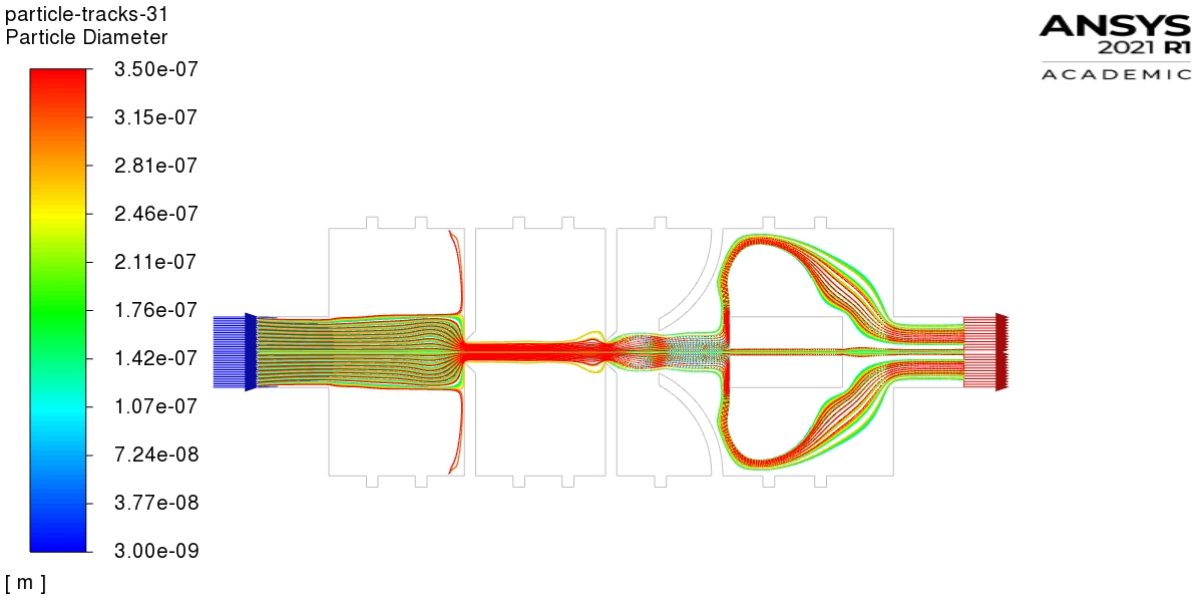

Figure 4.32: Particle distribution at the device outlet

Chapter 5

Computational Simulations of Nanoparticle Focussing Through Aerodynamic Lenses and a Divergent Nozzle

5.1 Introduction

Since its initial development by numerous researchers, an aerodynamic technique has been widely applied for focussing nanoparticles in the form of narrow beams: the use of an aerodynamic lens. Aerodynamic lens systems intended to function under conditions considerably different from those employed by former researchers have been discussed in numerous advanced studies [87]. Most of the lens systems currently utilized have typically been the same design as previously described by a number of investigators [88]. Identifying the performance and efficiency of an aerodynamic lens system requires detailed computational and experimental investigations. Several studies, however, have involved extensive computational, theoretical, and experimental examinations of aerodynamic lens systems [87]. Other investigators have replicated their simulations using a compressible flow model

[163, 49]. The aerodynamic focussing created by Liu et al. [87] is useful in many application areas, such as improving transport efficiency, enhancing measurement accuracy, and accurately depositing micropatterns on a substrate.

The use of an aerodynamic lens as a technology for focussing a wide range of nanoparticle sizes has numerous applications, such as mass spectrometry for nanoparticles [88, 62, 124, 162], micropatterning and synthesis of materials [31, 29, 160], inlets for measuring the composition of biomaterials, smooth thin metal film, and the creation of 3D microstructures. Aerodynamic lens design has been advanced through the use of computational fluid dynamics (CFD) as a means of determining the diameter of the nanoparticles. In view of the variety of aerodynamic lens applications, this study was directed at demonstrating its further development based on the use of ANSYS Fluent software (2021R1) for simulating the gas flow field and evaluating the possibility of focussing sub-300 nm nanoparticles, which can provide a foundation for reliable and quick lens evaluation and the creation of a useful design.

This chapter begins with the definition of the computational relations used for designing the dimensions of an aerodynamic lens. The challenges encountered with respect to focussing sub-300 nm nanoparticles with an aerodynamic lens are described, and the use of aerodynamic lenses for nanoparticle focussing is examined. The primary objectives of this part of the research included the following:

1. **Develop** a model of axisymmetric orifices as a useful tool that can facilitate the efficient focussing of nanoparticles smaller than 300 nm.
2. **Propose** a method of measuring the size of nanoparticles in the air using an orifice that focusses on small nanoparticles.
3. **Determine** the size and characteristics of nanoparticles in front of FCE.

4. **Validate** a new aerodynamic lens design computationally and then compare the results with other available experimental data.

Since the lens system includes a pipe and an aerodynamic lens (Figure 5.1), the first step was to calculate the pressure profile and the axisymmetric gas flow field in the lens system. In an aerodynamic lens system, the nanoparticles are carried by air that is injected in the inlet, which has a diameter of 10 mm. The flowrate was used as the inlet conditions. For this study, particles were pumped into the gas flow field upstream from the inlet. Following the solving of the 2D axisymmetric flow profile, nanoparticle trajectories were determined. Because of their low concentration, the potential effect of the particles on the gas flow was neglected, and particle-particle interactions were assumed to be ignored. This research also involved an examination of a case used for calculating the number of nanoparticles (1 nm - 300 nm in this case) entering the aerodynamic lens. The results of these comprehensive calculations were compiled and included in the orifice design specified in this research, as depicted in Figure 5.1.

An additional element presented in this chapter is the evaluation of the developed lens design based on a comparison of the predicted outcomes with the results of detailed computational studies. In contrast to previous versions of aerodynamic lens systems, which consisted of a cylindrical pipe with sharp-edged plate orifices positioned inside to allow simultaneous focussing of a range of nanoparticle sizes [88, 152], the purpose of this study was to implement a method for modelling an aerodynamic lens so that nanoparticles pass through the orifices with a group of particles smaller than 300 nm.

A variety of available methods for modelling and designing the aerodynamic lens were investigated based on the smallest particles detected and focussed in the lenses, the number of particles, and the velocity of the particles in the second lens, and the most integrated development was chosen

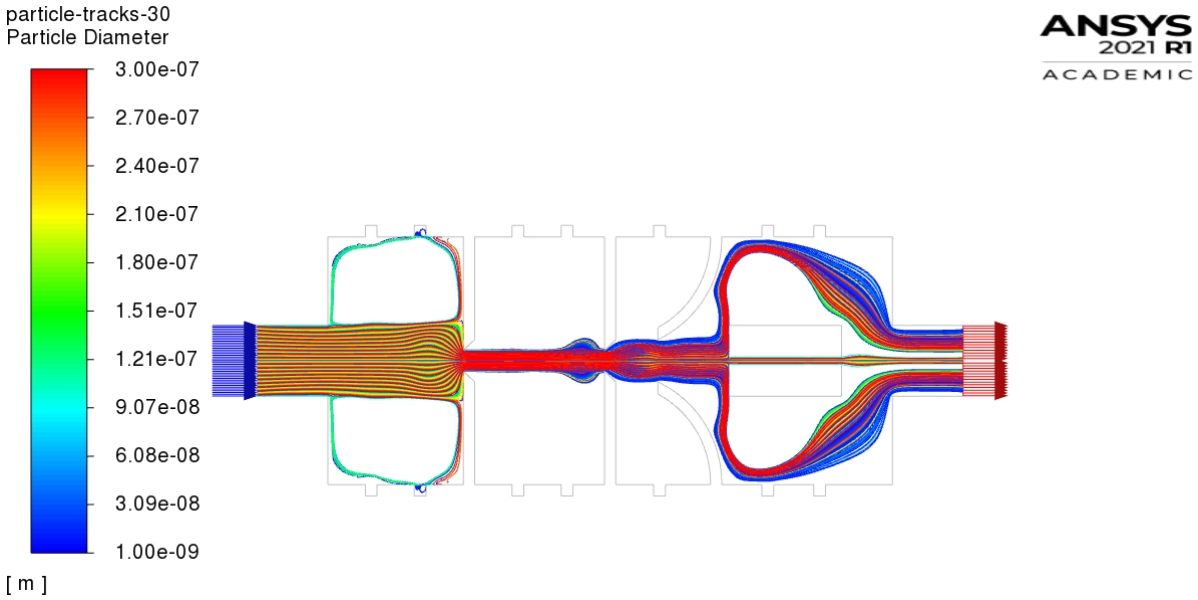

Figure 5.1: Nanoparticle trajectories that determined following the solving of the 2D axisymmetric flow profile

as the basis for implementation. The goal was to develop a technique that could satisfy the following objectives:

1. **Work** as a model within existing CFD solvers.
2. **Model** an aerodynamic lens with two orifices and a divergent nozzle is included in the simulation.
3. **Work** with multiphase flows based on the application of the Lagrangian method.

The method developed in this study is limited to two-dimensional modelling. The simulation results were compared with those from other simulations or with available experimental data reported by Tan et al. [141, 138].

5.2 Background

With respect to improving aerodynamic lenses, an important consideration is knowing what range of particle size must be focussed on. The purpose of enhancing aerodynamic lens design is to shape a lens system with the highest level of efficiency and performance, i.e., minimum particle loss, maximum particle focussing, and minimal pumping requirements based on specific input from the user, such as the density of the particle, size of the particle, and the flowrate in the inlet [151]. Achieving this goal requires adjusting the shape, position, and dimensions of the lens (lens diameter, length between the lens and the inlet or outlet of the nozzle), and the operating parameters (carrier gas, flowrate, velocity, and pressure). In this case, two lenses and one divergent nozzle were employed for measuring nanoparticle size. Figure 5.2 illustrates the particle focussing-detecting system, which is composed of six basic sections: the particle charging section, pressure reducing section, particle focusing section, particle detecting section, flow maintaining section, and data processing section [13]. They are indicated in the following schematic drawing, Figure 5.2.

In this research, an aerodynamic lens consists of several parts, the first of which is an inlet with a diameter of 10 mm, which determines the mass flow within the lens system. The lens outlet speeds up the flow of gas so that it reaches its final velocity. In this case, the Lagrangian model was used due to its popularity as a widely applied approach, where the particles are injected by using the Rosin-Rammler method in order to know the properties and effect of the particles in the fluid as well as to know whether or not the particles can be detected after focussing in the lens. Because it solves in a single continuum, this model is often preferred over the Eulerian because it is less computationally demanding when the number of particles used is not very large. Because this research was targeted at the focussing of small particles, the Lagrangian method was used for the modelling of the two

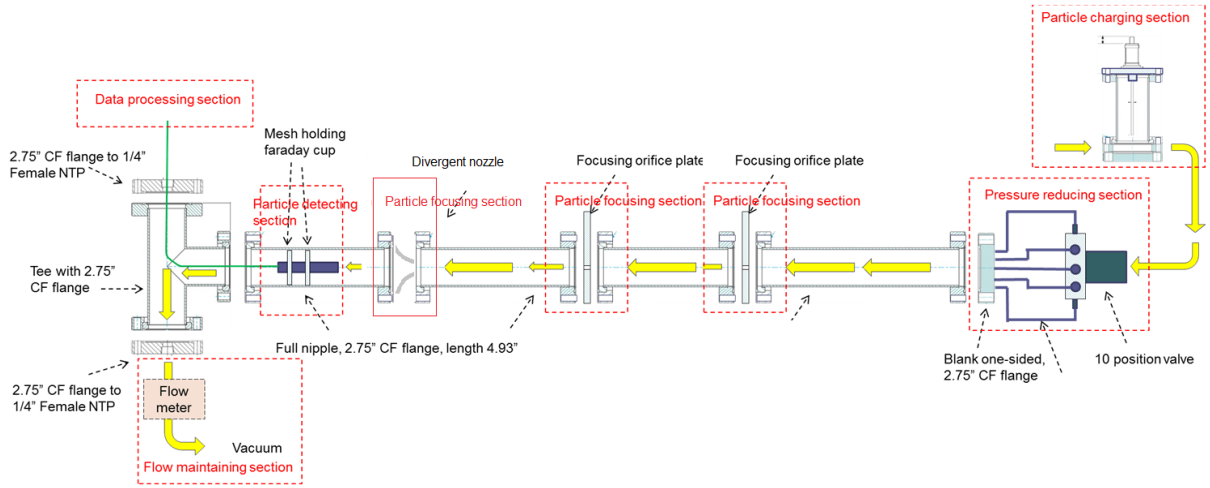

Figure 5.2: Two orifice plates and a divergent nozzle are used in a particle focussing-detecting system [13]

phases involved: air as a primary phase and carbon particles as a secondary phase. The flow within the aerodynamic lens system must be treated as a laminar, axisymmetric, and sonic speed. This is because the dimensions of the pipe stay constant and as a result, the volume of the fluid does not have a chance to change. Gas molecules accelerate and decelerate in the lens by passing through it. The degree of particle collimation is reasonably dependent on the particle size [163]. Small particles in carrier gas tend to follow flow streamlines throughout each acceleration and deceleration phase, and the results are the nanoparticles being directed toward the central axis, where the Faraday cup electrometer has been installed inside the pipe after the divergent nozzle in order to detect small particles parallel to the x-axis. A variety of aerodynamic lens designs have been used to compare nanoparticle sizes, such as those listed in the Table 5.1.

Most aerodynamic lens systems currently utilized resemble this design [87]. However, several reports have mentioned a lens system designed to work in conditions different from those published in [87]. For example,

Table 5.1: Previous aerodynamic lens designs

No.	Size of Particle	Number of Lenses	Approaches	Year	References
1	500 nm	5 lenses	Computational	2018	[120]
2	Sub 10 nm	3 lenses	Computational	2016	[160]
3	4 μm-8 μm	7 lenses	Experimental	2011	[165]
4	30 nm-10 μm	7 lenses	Computational	2013	[80]
5	5 nm-50 nm	3 lenses	Computational	2009	[81]
6	30 nm-300 nm	3 lenses	Experimental and Computational	2008	[79]
7	25 nm	1 lens	Experimental	2015	[141]
8	3 nm-30 nm	5 lenses	Computational	2005	[151]
9	10 nm-200 nm	4 lenses	Experimental and Computational	2004	[31]
10	60 nm-600 nm	5 lenses	Computational	2004	[163]
11	10 nm-100 nm	4 lenses	Computational	2000	[29]
12	340 nm-4000 nm	2 lenses	Computational	1999	[124]
13	100 nm-900 nm	7 lenses	Experimental	2005	[152]
14	1 μm-10 μm	2 lenses	Numerical and Experimental	2002	[78]

researchers have used a hydrogen-argon mixture to develop a lens system for focussing silicon carbide particles ranging from 10 nm to 100 nm [29]. Other investigators have used a lens system to focus 10 nm to 200 nm silicon particles in hydrogen [31]. Many studies have involved the creation of high-pressure aerodynamic lens systems (2.5 kPa to 20 kPa) at the inlet for examining stratospheric aerosol particles [124, 125] (Stratospheric aerosol particles are sulfur-rich particles that exist in the stratosphere region of the Earth's atmosphere. These particles consist of a mixture of sulfuric acid and water). At the atmospheric pressure range, several investigators have used two lenses to focus on micron-sized particles [78]. A number of researchers

have improved the systematic procedure for designing aerodynamic lenses for studying particles from 3 nm to 30 nm [151]. By using a frozen Maxwell-Boltzmann radial velocity distribution, Liu et al. developed an analytical expression for the diffusion-controlled particle beam width downstream of the accelerating nozzle [87, 88, 154]. Li and Ahmadi used a different integration procedure for the trajectory equation with Brownian force [30].

A need exists for detailed computational and experimental studies that can describe the performance of aerodynamic lens systems to focus nanoparticles. To this end, several investigators have conducted computational, theoretical, and empirical analyses of aerodynamic lens system performance [88]. Numerous researchers have also replicated the simulation of a compressible flow that Liu et al. created with their model [88, 163]. To study the loss of particles and expansion of the beam due to diffusion, taking into consideration the Brownian motion of particles, many studies have resulted in simulations of the flow and particle transfer in lens systems [151]. The previous designs of conventional aerodynamic lenses listed in Table 5.1 have been extensively employed for the focussing of nanoparticles with the use of multiple lenses.

A significant challenge remains, however, with respect to the use of two lenses and one divergent nozzle for focussing nanoparticles smaller than 300 nm. The difficulty is that detecting small nanoparticles (differing in size from 1 nm to 300 nm) and focussing them to measure their diameters with less than two lenses is challenging. This research, on the other hand, has been described as addressing this issue by enhancing an aerodynamic lens design (sharp-edged orifice) that surpasses a conventional flat orifice in terms of results that lead to knowledge of the lens's efficiency to detect and focus particles. To target nanoparticles, the gas flow in an aerodynamic lens is limited to continuity and sonic speed levels. As a means of addressing these limitations, [152] a number of researchers have proposed an inequality that refers to a minimum particle size $dp_{,min}$ that can be focussed, which

they expressed as follows:

$$d_p \geq \left(\frac{8St_0}{Ma^* Kn^* \rho_p}\right)\ \left(1+\frac{\pi\alpha}{8}\right)\ \mu\sqrt{\frac{M}{RT_1\gamma}} = \quad d_{p,min} \propto \frac{St_0\ \sqrt{M}}{Ma^* Kn^*}\} \quad (5.1)$$

Where Ma^* is the Mach number of the critical flow, the upper limit of the Knudsen number Kn^* for the continuum regime was calculated from Equation 5.2:

$$Kn^* = \frac{Ma^*}{Re^*}\ \sqrt{\frac{\gamma.\pi}{2}} \quad (5.2)$$

In a free molecule regime, the Stokes number can be defined using Epstein's mobility model as [89, 154]:

$$St = \frac{1}{\left(1+\frac{\pi\alpha}{8}\right)\sqrt{2\pi\gamma^3}} \frac{m^{\cdot}\ \rho_p d_p\ c^3}{p_1^2 d_f^3} \quad (5.3)$$

Where c represents the speed of sound based on the temperature of 293 K, α is the momentum accommodation coefficient, γ is the specific heat ratio of the carrier gas, $\dot{m}$ is the mass flowrate, ρ_p is the particle material density. Optimal particles ranged from a Stokes number St_0 of 0.6 to 1.0 for the nozzle [152, 79]. This study also utilized a sharp-edged plate orifice as an aerodynamic lens because of its simple geometry and relatively small St_0 value. Rearranging Equation 5.3 enables the diameter of the orifice d_f required for the focussing of d_p diameter particles to be determined:

$$d_f = \left(\frac{1}{\left(1+\frac{\pi\alpha}{8}\right)\sqrt{2\pi\gamma^3}} \frac{m^{\cdot}\ \rho_p\ d_p c^3}{p_1^2 St}\right)^{\frac{1}{3}} \quad (5.4)$$

Some researchers have used a gas carrier lighter than air in an attempt to reduce $d_{p,min}$, i.e., the carrier gas molecular weight M in Equation 5.1, which could, with a slight change in design, allow the focusing of moderately small nanoparticles [87].This model is the only one previously available for use in focussing small particles with an aerodynamic lens. However, it must be noted that their promising model operates only in helium He and not in air [151]. Since an aerodynamic lens is designed for the analysis of aerosol particles in the atmosphere, introducing helium into the system is not recommended. Thus, a critical need still exists for modern designers to discover methods of focussing nanoparticles. For these reasons, based on Equation 5.1 as a starting point, an attempt was made in this study to reduce $d_{p,min}$ by increasing Ma^* and reducing St_0. An initial suggestion was that subsonic flows be restricted to the inlet in order to avoid shock formation in the orifices, which reduces the focussing performance of sharp-edged plate orifices.

5.3 System with a Straight Pipe, Two Sharp-Edged Plate Orifices, and a Single Divergent Nozzle

The most modest form of the aerodynamic lens is composed of two central orifices installed inside a cylindrical pipe whose diameter is 35 mm and length is 80 mm. The aerodynamic lenses considered in this research have sharp-edged plate orifices with a 1.6 mm thickness and a 3 mm orifice diameter. ANSYS Fluent was utilized for finding flow field solutions with a convergence criterion lower than 10^{-5} mass residual. Figure 5.3 shows the pipe geometry with the orifices. The assumed thickness t of each orifice plate is small (1.6 mm) relative to the assumed pipe diameter D (35 mm). Further assumptions are that the orifices are sharp-edged plates, and that the length L of the pipe is 80 mm. The length of the pipe was chosen for

two reasons: the first was to reach the speed of sound in the second lens, and the second was to calculate the number of particles in the lenses and compare them with the number of particles injected into the inlet to know the particle loss.

The length of the section from the inlet to the first orifice is 20 mm, and the length of the section from the first orifice to the second orifice is 20 mm, while the length of the section from the second orifice to the divergent nozzle is 15 mm and from the nozzle to the outlet is 25 mm. The focussing of particles occurs between the second orifice and the divergent nozzle, where a 15 mm section of pipe length is also positioned between the second orifice and the divergent nozzle. The length of the section between the nozzle and outlet (25 mm) has thus been made longer than the section between the second orifice and the nozzle (15 mm) in order to avoid any backflow and to enable a sonic speed to be achieved, as illustrated in Figure 5.3.

The focussing orifices (Figure 5.3) were placed in the centre of a stainless steel tube. An orifice thickness of 1.6 mm was found to be more effective with respect to the selection of a narrow set of particles [97]. The orifice is 3 mm in diameter so that the flow can continue through the powerful pump at 12 ft^3 per min [141]. Due to their diffraction inertia, after the nanoparticles pass through the orifices, they spread in various directions according to their different sizes.

5.4 Materials and Method

The simulation systems adopted in this research are introduced, and the mesh configuration, computational geometry, and materials used in the simulations are described in this section.

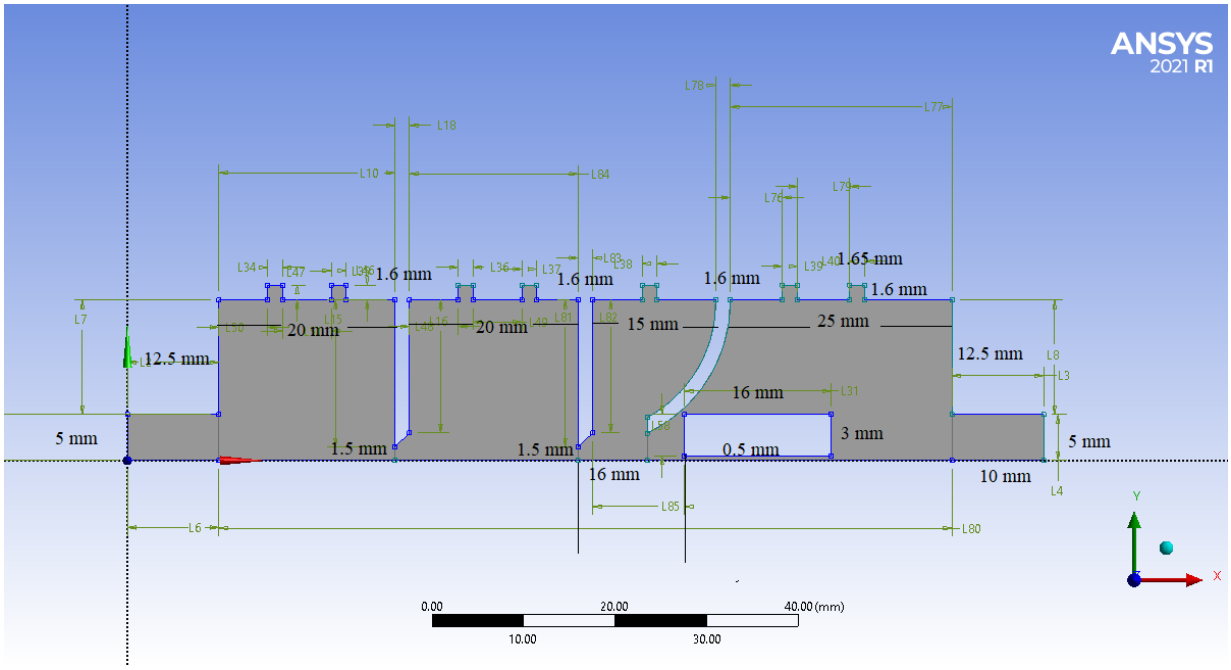

Figure 5.3: Geometry of the straight pipe with sharp-edged plate orifices, FCE, and divergent nozzle

5.4.1 CFD Simulations

CFD simulations were carried out in order to have a better understanding of the effect of the orifices on focussing and to see whether their geometry might be improved. The ideal orifice focusses on particles that fall within a restricted size range (sub-300 nm) when the mass flowrate at the inlet is considered to be $2.98{*}10^{-7}$ kg/s, and all particles falling within that size range will be focussed [102, 137]. As a result, particles outside the size range would be subject to significant deflections from the centerline immediately after exiting the orifices, as shown in Figure 5.4.

Middha and Wexler investigated this phenomenon in detail in [97]: a case in which CFD was used to model a nanoparticle-laden choked flow through an orifice [137]. This research included an attempt to reproduce

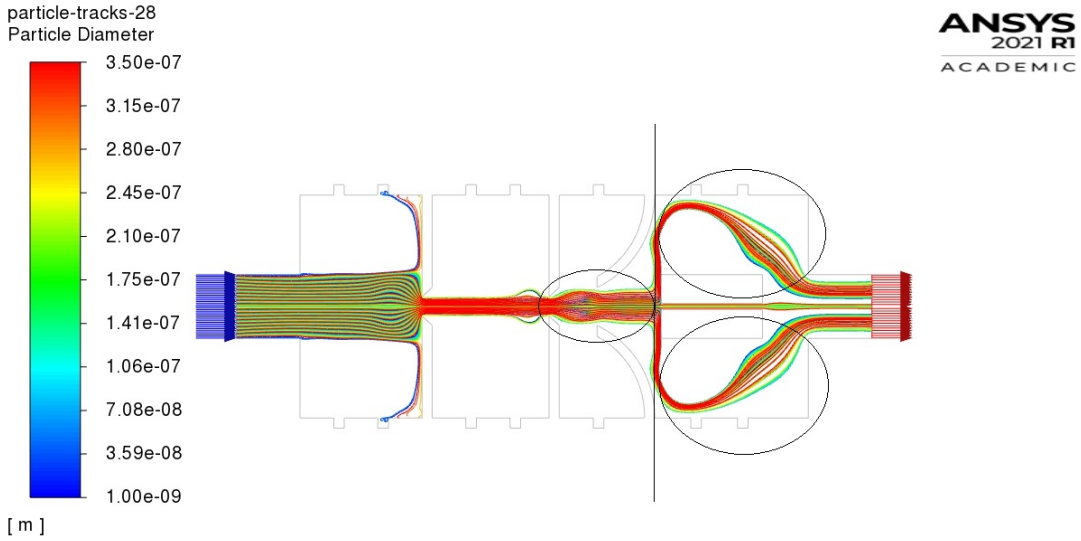

Figure 5.4: Particle-tracks, with the particles diameter 1 nm - 350 nm

the results from Middha and Wexler's report for the purpose of validating the model developed for this thesis work, as presented in subsection 5.6.1. Their model results were also applied as a baseline for other components of this research related to improving the performance of an aerodynamic lens system for focussing nanoparticles.

5.4.2 Geometry of the Computational Domain

The geometry of the system, divided into six areas with different mesh densities, is shown in Figure 5.5. As previously defined (Figure 5.5), the orifices were 3 mm in diameter and 1.6 mm thick, and the pipe was 15 mm long from the second lens to the nozzle, 25 mm from the nozzle to the outlet, and 35 mm in diameter. It is important to note that CFD analysis is valid for both two-and three-dimensional axisymmetric geometry, which means that the CFD model could use two-dimensional axisymmetric modelling to be simulated as a 2D axisymmetric problem. Besides saving meshing

effort and computing time, the 2D axisymmetric models display the entire solution, whereas the 3D solution is only visible on the surface. Individual sections of the 3D solution can only be viewed after it has been cut. The 2D models will provide sensible outcomes. The green colour in Figure 5.5 depicts how the domain was divided into six labelled areas with different mesh densities [137].

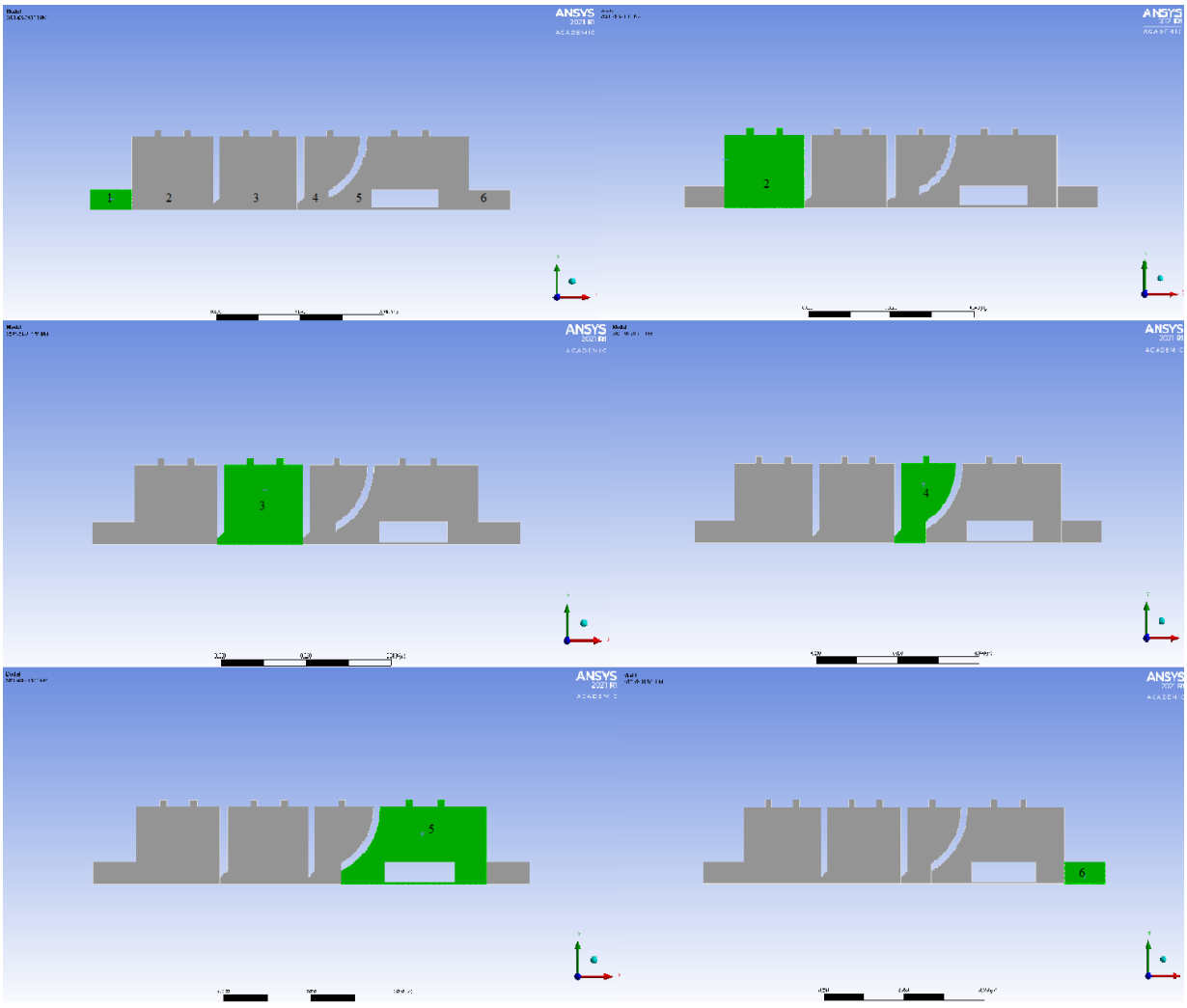

Figure 5.5: Geometry of the CFD model (mm) divided into six areas with different mesh densities

5.4.3 Mesh Configuration and Part of the Computational Cell Mesh

As indicated in the screenshot of the mesh provided in Figure 5.6, a non-uniform squared mesh is used as a compromise. As indicated in the Figure, the upper edge corresponds to the wall of the pipe, and the lower edge corresponds to the axis. It was discovered in this study that a relatively fine mesh in the vicinity of the centreline and a finer mesh in the near-wall region could be maintained, as illustrated in Figure 5.6. The magnified image depicted in Figure 5.6,((b) for the bottom right), serves to demonstrate the non-uniform mesh (the part of the pipe mesh, the wall, and the axis). The mesh becomes finer towards the wall, as indicated by the two-way arrow on the right side of the mesh in figure 5.6, ((c) for the top), and it also eventually becomes finer farther along the centreline which highlights the observations made in this research. Since a uniform mesh is used in the axis direction, there is no need for a finer mesh or a non-uniform mesh at that location because the variations in the flow characteristics along the axis are assumed to be more gradual. As a result, fewer elements are required along the axis, which constitutes another advantage of the new method.

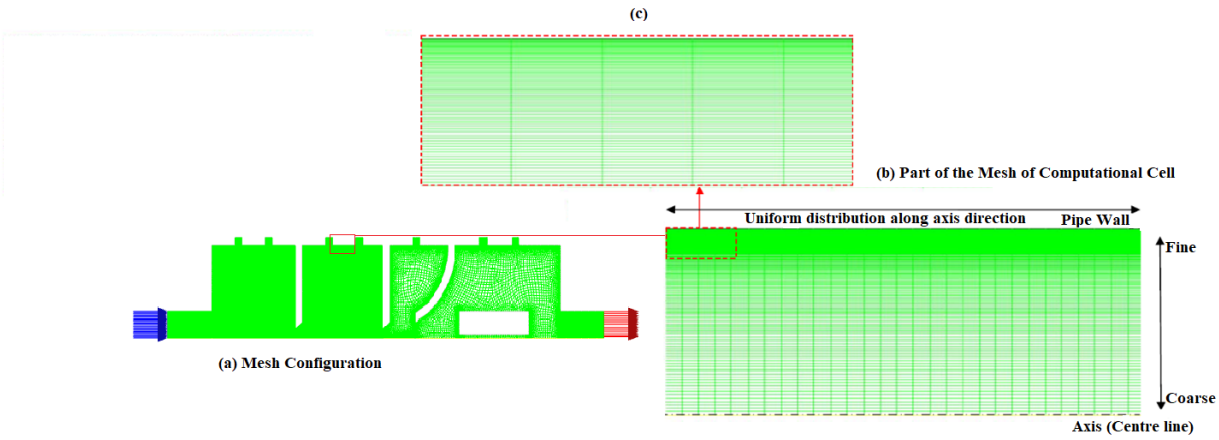

Figure 5.6: Screenshot of the mesh configuration and part of the computational cell mesh

With reference to figures 5.5 and 5.8, the elements in areas (2) and (3) were set to 0.6 mm by 0.6 mm, respectively, while in the area (4), due to flow acceleration in the x and y directions [137], the elements were arranged to be 0.4 mm by 0.5 mm. Then, in the area (5) the elements were also arranged to be 0.7 mm by 0.5 mm due to the flow acceleration in the x direction, with a bias factor of 5 in the vertical direction because of the high-velocity gradients in the y-direction.

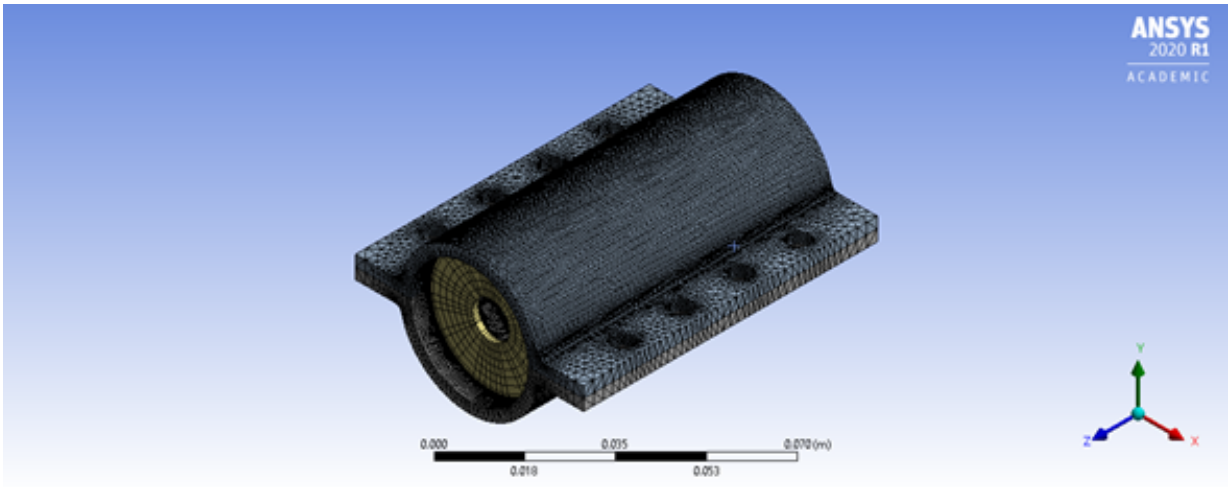

Figure 5.7: The mesh from 3D model of the base case

To obtain elements that were less skewed, face meshing was applied to the entire mesh [137]. The maximum orthogonal skew and aspect ratio were 0.4 and 4, respectively. The end result was 30,000 nodes with 31,104 elements as a result of using 50 non-uniform divisions in the direction of the radius and 50 uniform divisions in the direction of the axis (of the fine mesh), Figure 5.8. The mesh size surrounding the particle was too fine to enable accurate predictions of changes in velocity, pressure, and temperature [142]; however, the regular size near the walls served to maximize the speed of the calculations (Figure 5.6). To obtain elements with less skew, face meshing was performed on the entire mesh. Over all, there were 18,500 elements in the coarse mesh domain and 31,104 elements in the fine mesh domain

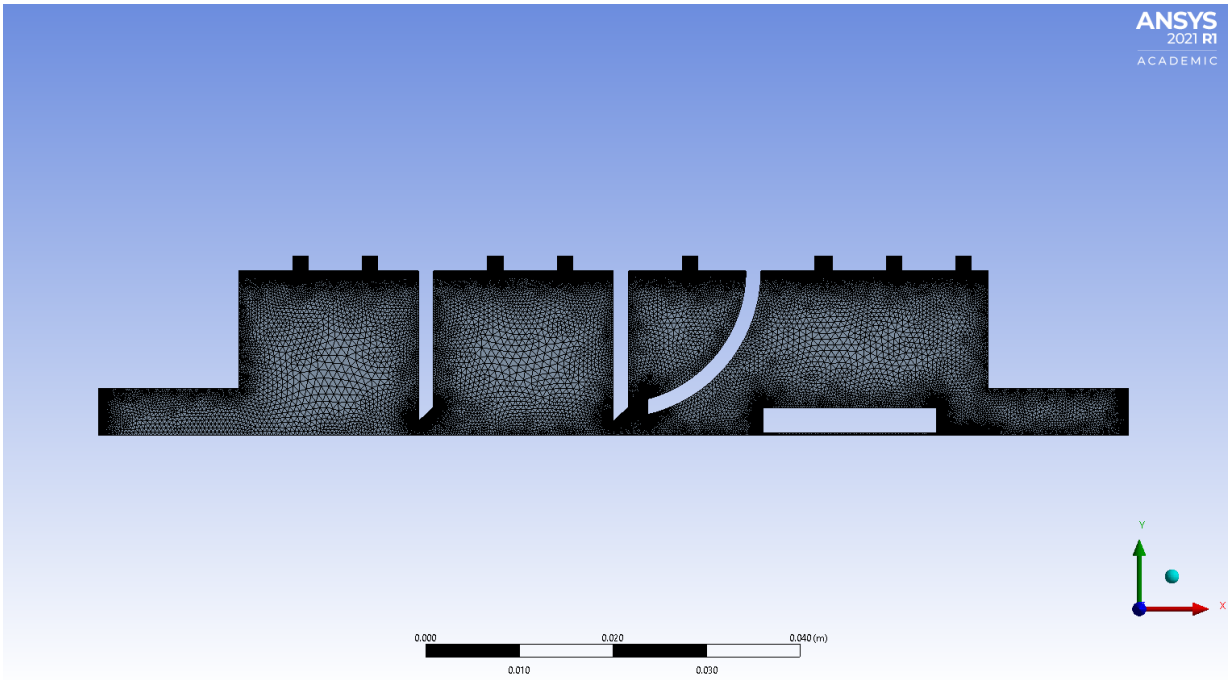

Figure 5.8: The mesh from the 2D model of the base case

(Figure 5.9). When the small particle size has been simulated (which is much less than the mesh size), it has been found that the particles near the refined mesh zone were predicted by the ANSYS Fluent. But then when the mesh size is fine, the trajectory near the refined regions (especially the leading edge) vanishes.

5.4.4 Solution Setup

Details of the ANSYS in this case, the assumptions were that the flow was axisymmetric and viscous in the carrier gas; a density-based solver type (density-based solvers are traditionally used for compressible flows); boundary conditions based on an assumed mass flowrate of $2.98{*}10^{-7}$ kg/s; an inlet pressure of $1.01325{*}10^{5}Pa$, a 35 mm pipe diameter, and no slip in

the wall. The stagnation temperature T_o at the inlet is 300 K. The static pressure p at the exit of the pipe is 3,738.9 Pa. It can be assumed that the static pressure p at the exit must be 3,738.9 Pa in order to provide a smooth supersonic flow at the outlet (without oblique shocks/expansion waves). By repeating the simulation with a finer mesh, a grid independence analysis was also carried out, Figure 5.9. When surface injection was chosen as the injection method, particles with sizes ranging from 1 nm to 300 nm were released at the inlet in a range of radial positions (Figure 5.10).

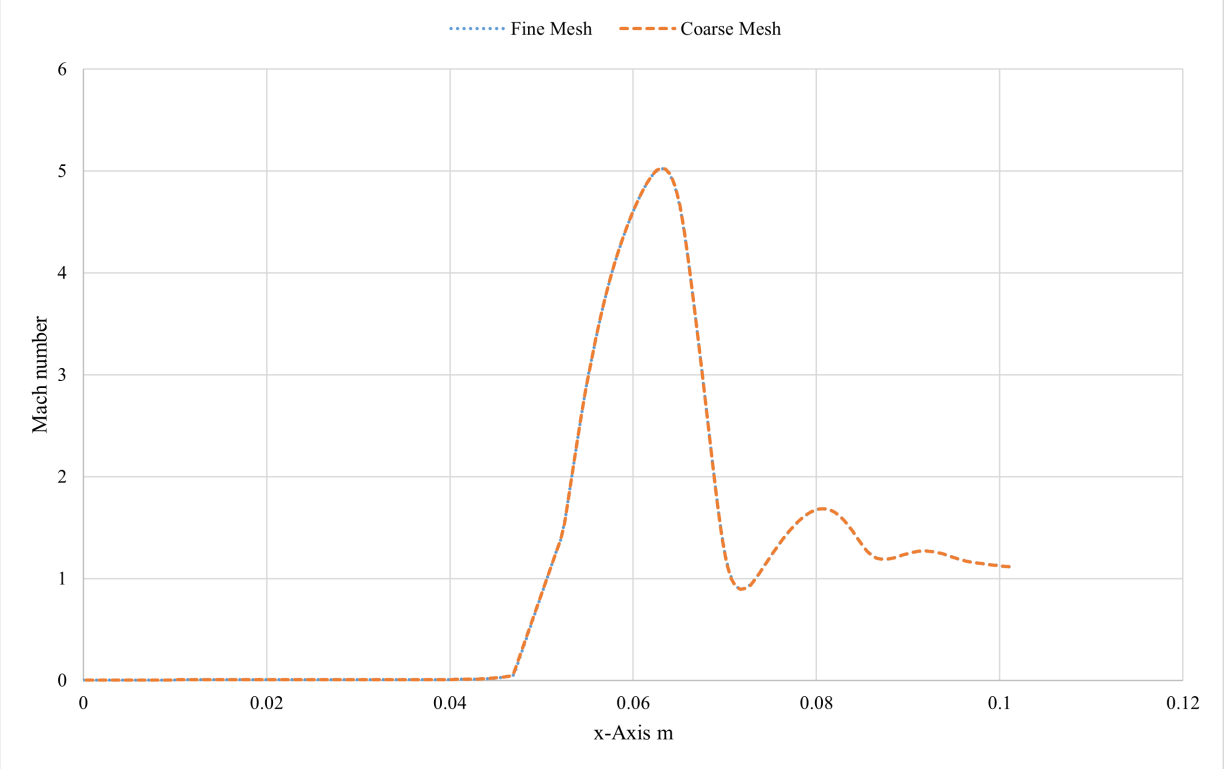

Figure 5.9: Comparing the Mach number to the x-axis when using Coarse mesh and Fine mesh

This research includes a vacuum chamber in the simulation to investigate particle motion downstream of the divergent nozzle (figure 5.11). The pressure within the chamber was assumed to be 1 Pa, and the mass flowrate

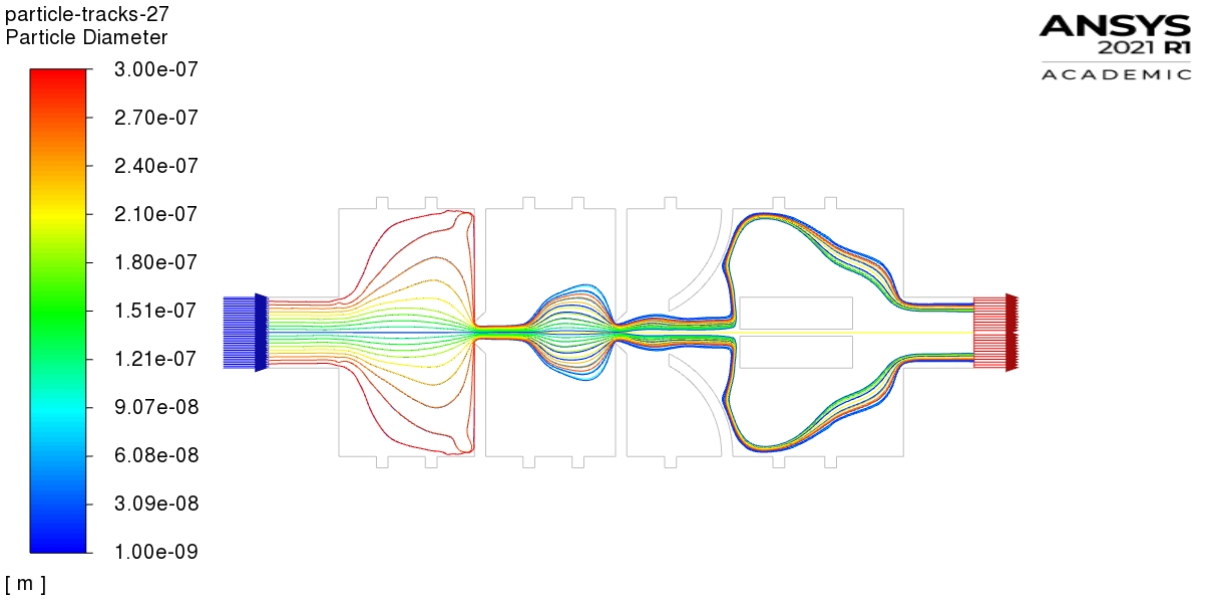

Figure 5.10: Particles with diameters from 1 nm to 300 nm released at various radial positions at the inlet

at the inlet of the lens assembly was considered to be $2.98{*}10^{-7}$ kg/s (air).

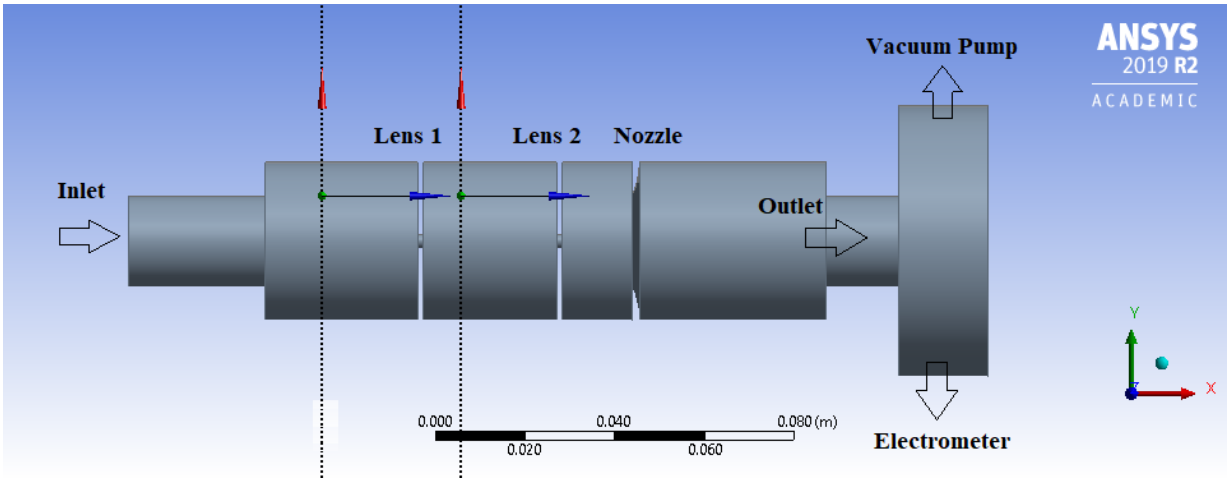

Figure 5.11: New prototype based on the divergent nozzle and aerodynamic focusing techniques

The particle material chosen was carbon, and the particle type for this simulation was gas, a selection that determined only the density of the gas used in the calculations. Fluent predetermined drag law models do not compensate for the Cunningham slip (UDF), which was used instead (Appendix A: Fluent Cunningham Drag Force UDF) [137]. The next step was to run a simulation of the mesh file in ANSYS Fluent and use the Lagrangian model to set up the model that was planned for use in conjunction with the multiphase model.

For different sizes of particle injections into the inlet, an appropriate representation of the size distribution of the droplets was the Rosin-Rammler expression. The Rosin-Rammler capability was used where it is built into ANSYS Fluent, so it was specified for this distribution without a special UDF. Figure 5.12 provides a flow chart of the Lagrangian model for modelling the solution method in ANSYS Fluent.

The particles were considered to be spherical and gravity was neglected. The flow in a horizontal pipe flow with an axisymmetrical is modelled in this study. It should not define gravity as the case is axisymmetric and the gravity vector is normal to the axis. Thus, it violates the axisymmetric condition. It could turn gravity on, but it would produce a non-physical result. However, it is estimated that the particle displacement due to gravity within one lens spacing is about a small distance for the largest particle investigated (0.011 mm). Simulations were also conducted using particles with different diameters, with an upstream temperature of 300 (°K) and an inlet flowrate of $2.98{*}10^{-7}$ kg/s. The particle injection points differed from those used for studying dependence with a focus on the primary state. After the calculations for the model were run, the following results were obtained for four different ranges of particle size diameters, as displayed in Figures 5.13, 5.14, 5.15 and 5.16:

Therefore, Figure 5.13 shows the traces of coloured particles according to the particle diameter of 1 nm–25 nm, and Figure 5.14 shows the traces

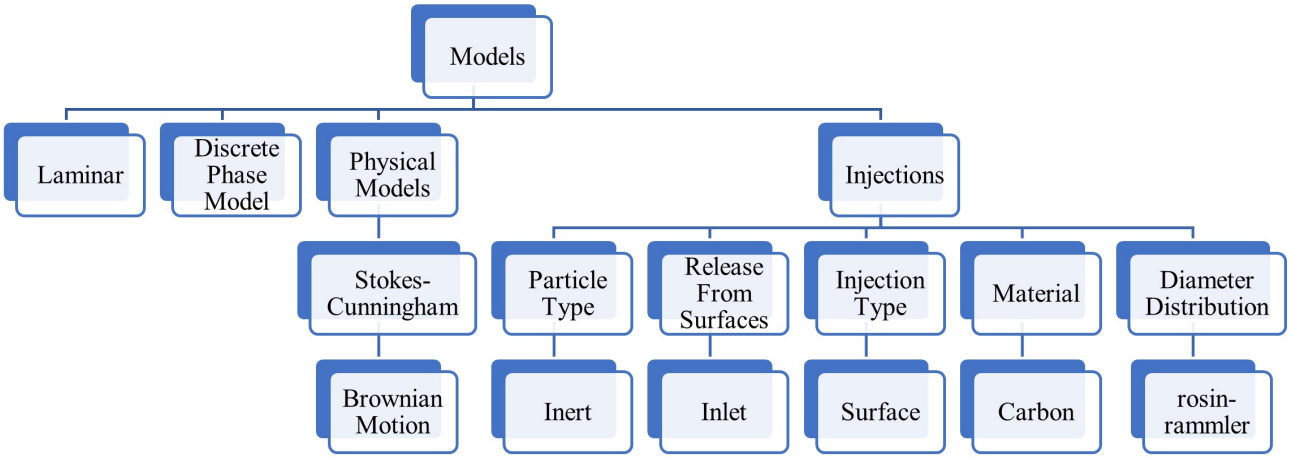

Figure 5.12: Chart of the Lagrangian multiphase model used in the ANSYS Fluent modelling of the solution method

of coloured particles according to the particle diameter of 25 nm–100 nm. Figures 5.15 and 5.16 show the particle traces coloured according to the particle diameter of 100 nm–300 nm and 1 nm–400 nm, respectively.

5.4.5 Solution Strategy

The nanoparticle inlet into the pipe is an axisymmetric orifice 10 mm in diameter, as depicted in Figure 5.17. However, at the entrance to the nanoparticle inlet, an orifice, or nozzle, is utilized for speeding up the particle to sonic speed because the sharp-edged plate orifice provides a nozzle restriction state, Figure 5.18. A sharp-edged plate orifice is more effective for focussing small particles because the maximum acceleration it produces

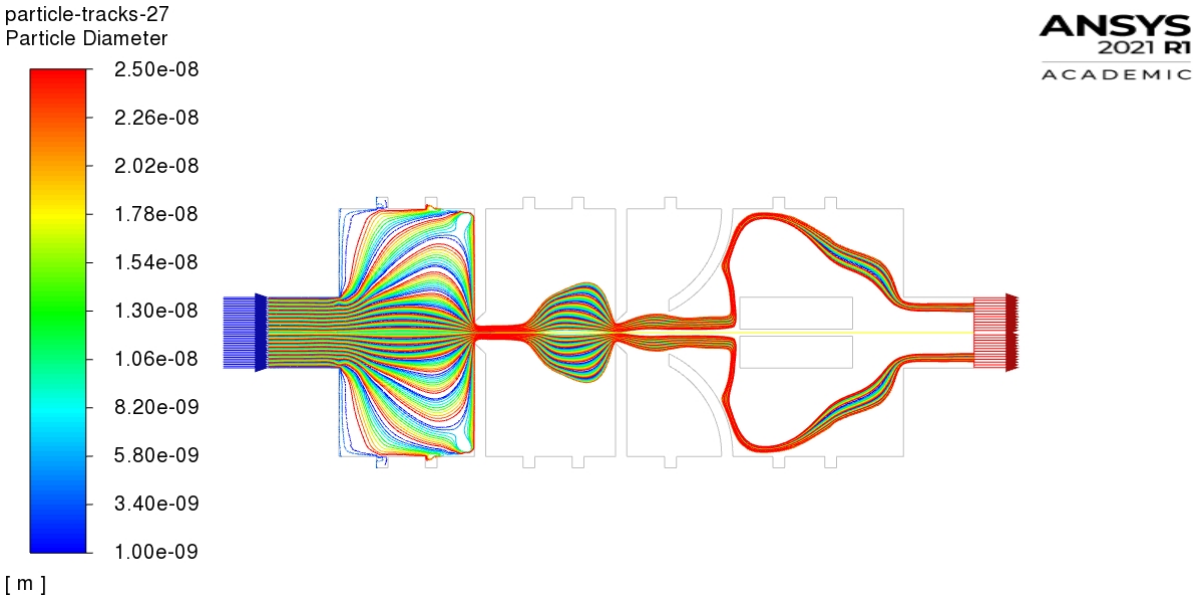

Figure 5.13: Particle traces coloured according to particle diameter 1 nm - 25 nm

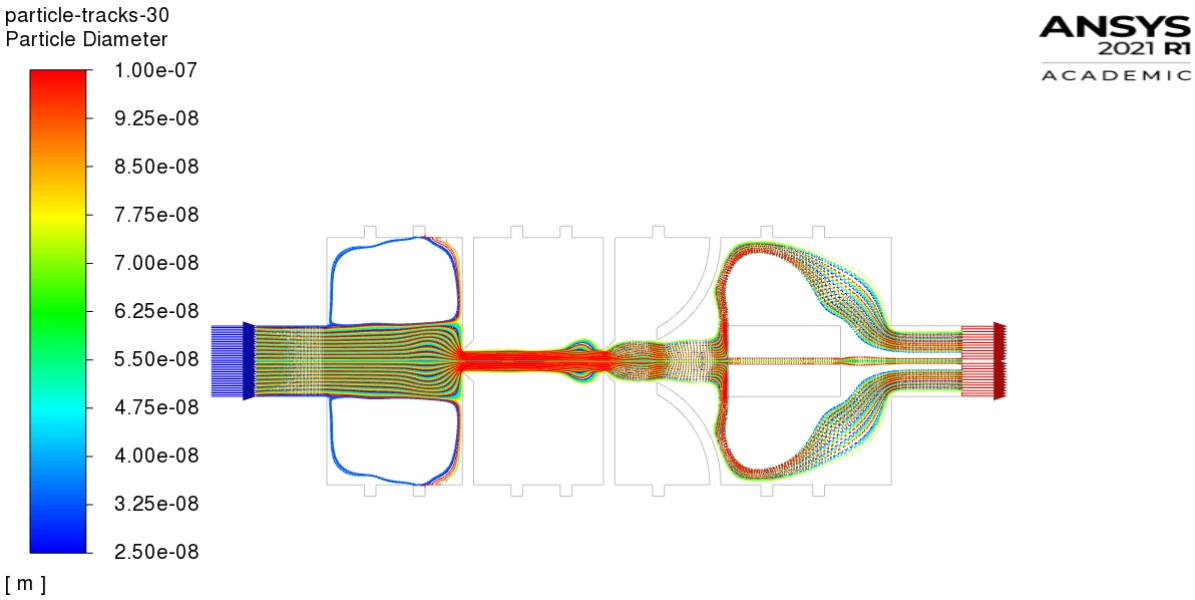

Figure 5.14: Particle traces coloured according to particle diameter 25 nm - 100 nm

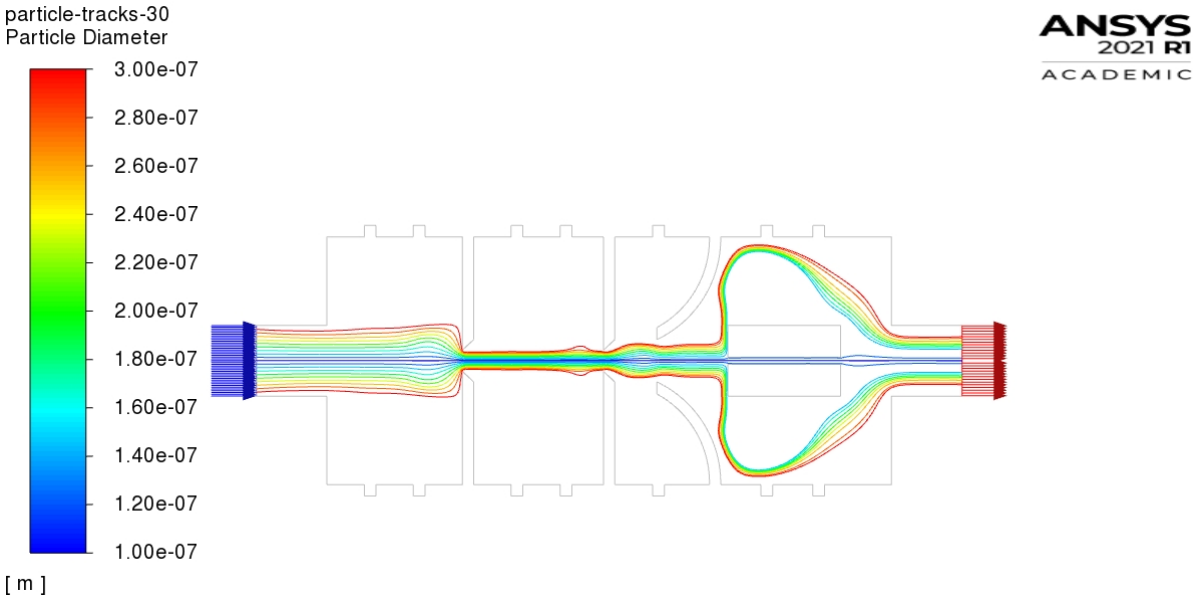

Figure 5.15: Particle traces coloured according to particle diameter 100 nm - 300 nm

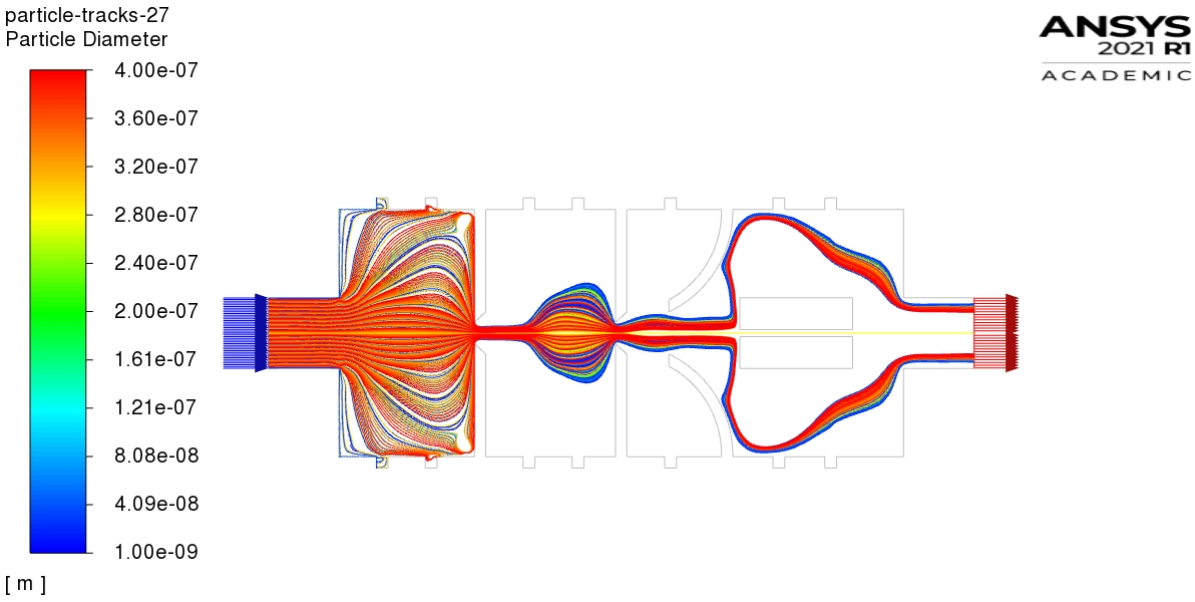

Figure 5.16: Particle traces coloured according to particle diameter 1 nm - 400 nm

facilitates the efficient focussing of smaller particles.

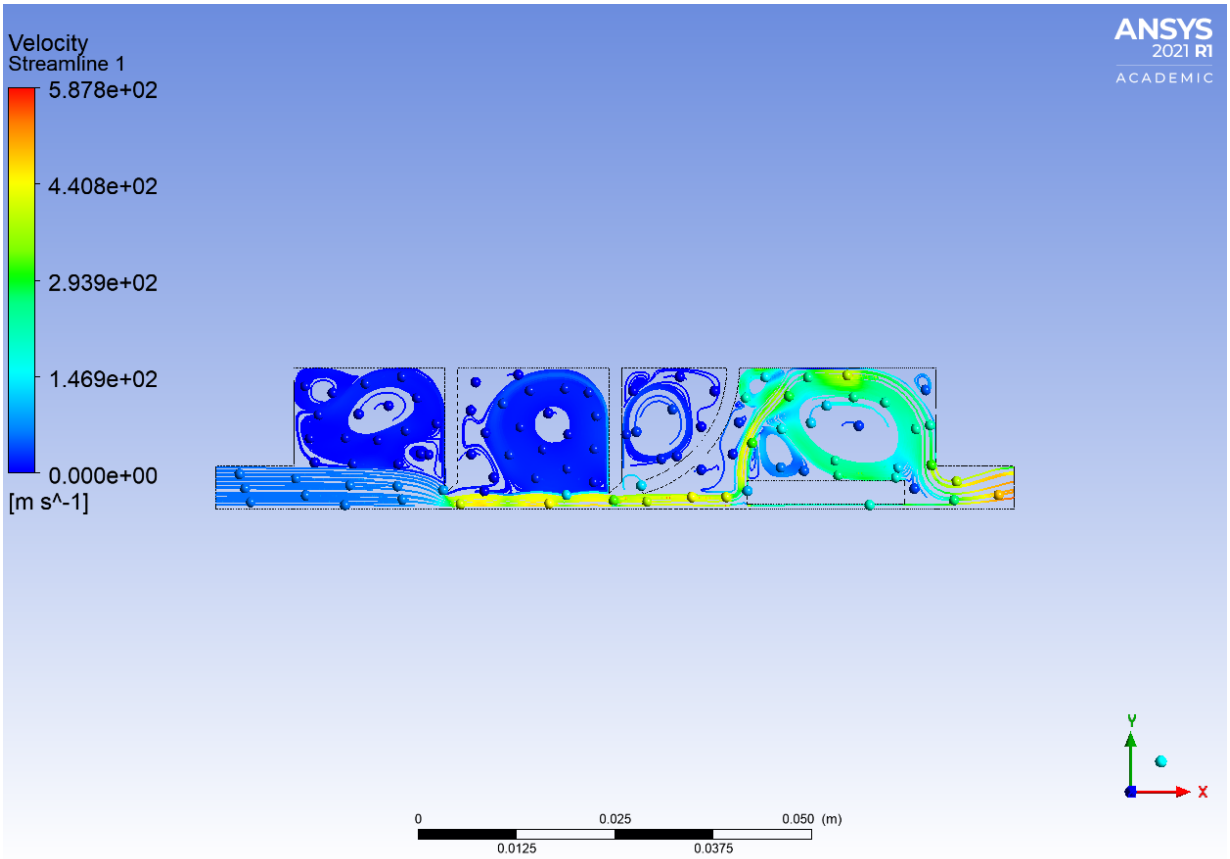

Figure 5.17: Nanoparticle inlet with an axisymmetric orifice 10 mm in diameter

5.4.6 Use of Two Aerodynamic Lenses and a Divergent Nozzle

The airborne particles pass through a series of axisymmetric aerodynamic lenses before entering the divergent nozzle. In this case, nanoparticles whose size is smaller than a critical value are transferred close to the axis by a lens, and in this case, they can be confined very near to the axis with the use of multiple lenses, as can be seen in Figures 5.19 and 5.20. The critical value is the minimum detectable particle size.

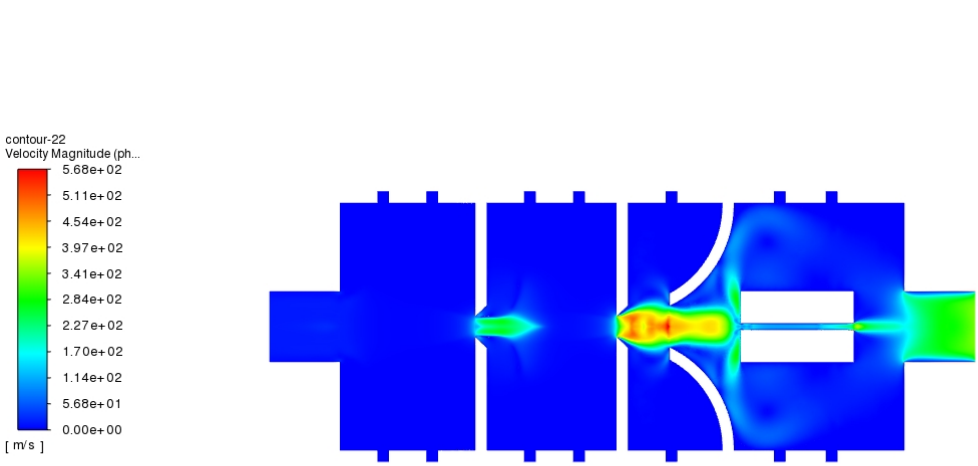

Figure 5.18: The orifice is used to accelerate the particles to the sonic speed

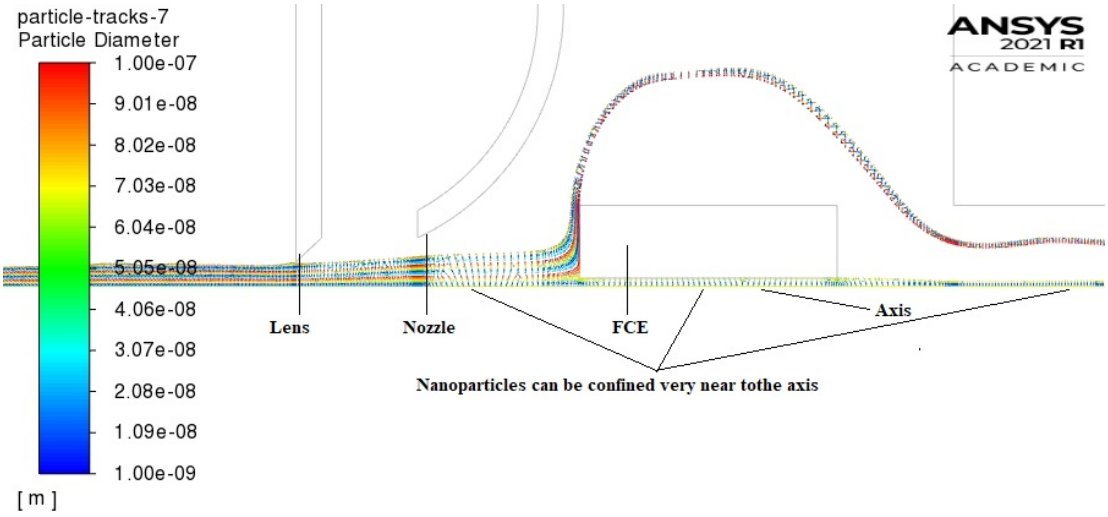

Figure 5.19: Nanoparticles confined very near to the axis with the use of multiple lenses

A particle beam is generated by the expansion of an aerosol into a vacuum through a nozzle. Many researchers have used particle beams to study

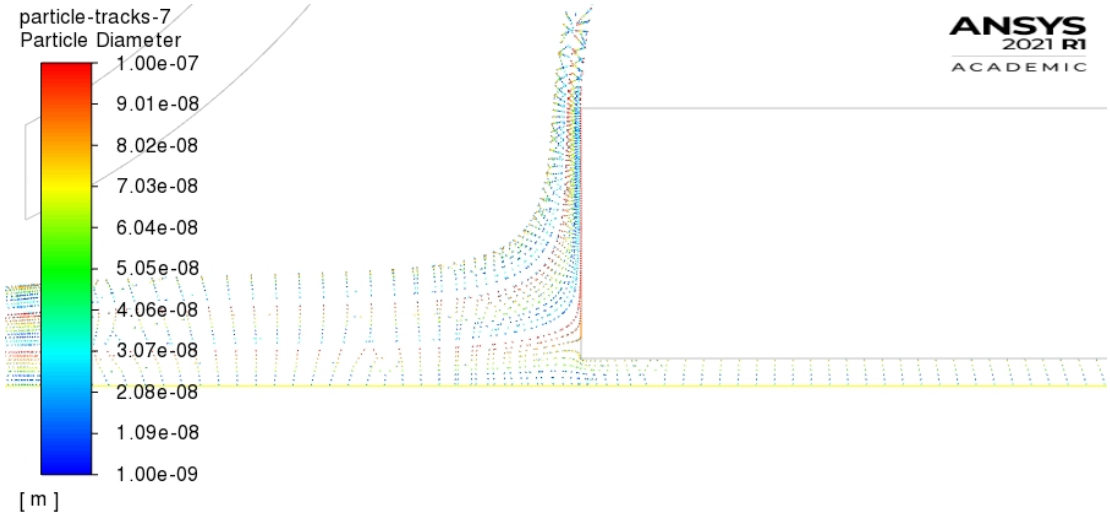

Figure 5.20: Nanoparticles moved closer to the centreline after passing through an aerodynamic lens

aerosol particles since Murphy and Sears [103] invented them [7, 49, 130]. In their study, [103], continuum nozzle sources have been utilized as sources for high-speed particle beams since the advent of particle measurements. Particles are typically accelerated and focussed into a narrow beam prior to any measurements in order to facilitate further analysis. Narrow particle beams achieved using aerodynamic lenses are ideal for numerous applications that require a high degree of efficiency for transporting nanoparticles from a sampling regime to a detector as well as high levels of resolution for measuring nanoparticle sizes [24, 39, 66]. With the multiple lenses used in this research, the nanoparticles move closer to the axis after passing through each lens.

5.5 Results and Discussion

This section presents the results of the focussing and separation of particles in the air with the use of the aerodynamic lens developed for this purpose.

The behaviour of a range of particle sizes, from 3 nm to 300 nm, in the aerodynamic lens was numerically simulated, and the simulation results were then compared with available experimental data reported by Tan et al. [141, 138] in order to facilitate consideration of both the basic theory and the possibility of enhancing the design of the lens. The separation of mixtures of different types of nanoparticles through a flow according to their spherical structures was also explored. The grid has nearly 30,000 nodes. However, when the number of nodes is doubled four times [106], the convergent solution does not change dramatically, as shown in Figure 5.9. Solution convergence is achieved within 1000 iterations using the grid and numerical techniques illustrated above. The next three sections present three cases of laminar fluid flows for varying sizes of nanoparticles:

5.5.1 Case 1: Laminar Fluid Flow with 1 nm to 10 nm Nanoparticles

In this case, the study measured the nanoparticles in the inlet of the pipe with air. The particles, with sizes ranging from 1 nm to 10 nm, moved through the fluid in the x-direction. The applicable boundary and initial conditions were a temperature of 300 (°K), a mass flowrate of $2.98{*}10^{-7}$ kg/s, a pressure of $1.01325{*}10^{5}Pa$, and the inlet nanoparticle velocity of 0.001 m/s. Figure 5.21 provides details of the typical simulation of particle traces, coloured according to particle residence, for 3 nm to 10 nm particles in the flow pipe, which moved close to the axis after the first stage of the modelling. Also, it is seen that some small particles close to 1 nm - 2 nm in size have just been deposited in the wall.

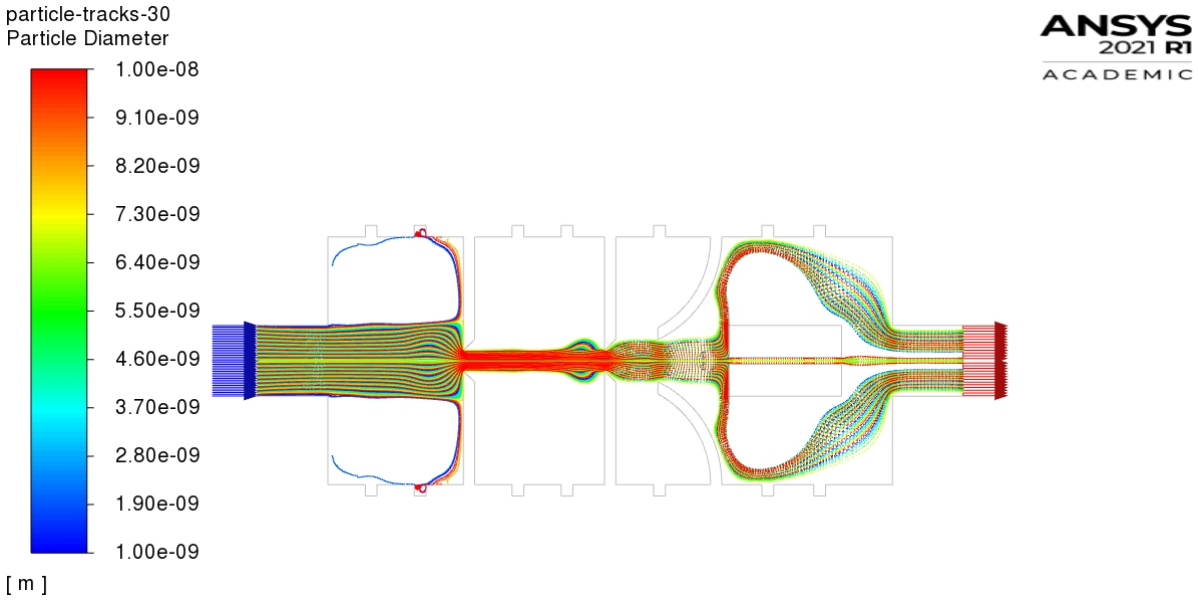

Figure 5.21: Particle traces for the 1 nm to 10 nm particle gradient expected in the flow tube, coloured according to particle diameter

5.5.2 Case 2: Laminar Fluid Flow with 1 nm to 25 nm Nanoparticles

In the second case, to illustrate the effect of the nanoparticle interactions with the centreline in the fluid flow, the model was first run with nanoparticles ranging in size from 1 nm to 25 nm; the effect of nanoparticle interactions was then examined. According to the particle trace counter, the gradient of the parameter is high in the entrance orifice and not completely formed, as shown in Figure 5.22.

5.5.3 Case 3: Laminar Fluid Flow with Many Adjacent 25 nm to 100 nm Nanoparticles

This case involved an examination of the effect of the nanoparticles with sizes of 25 nm to 100 nm, rather than 1 nm to 25 nm. The initial conditions

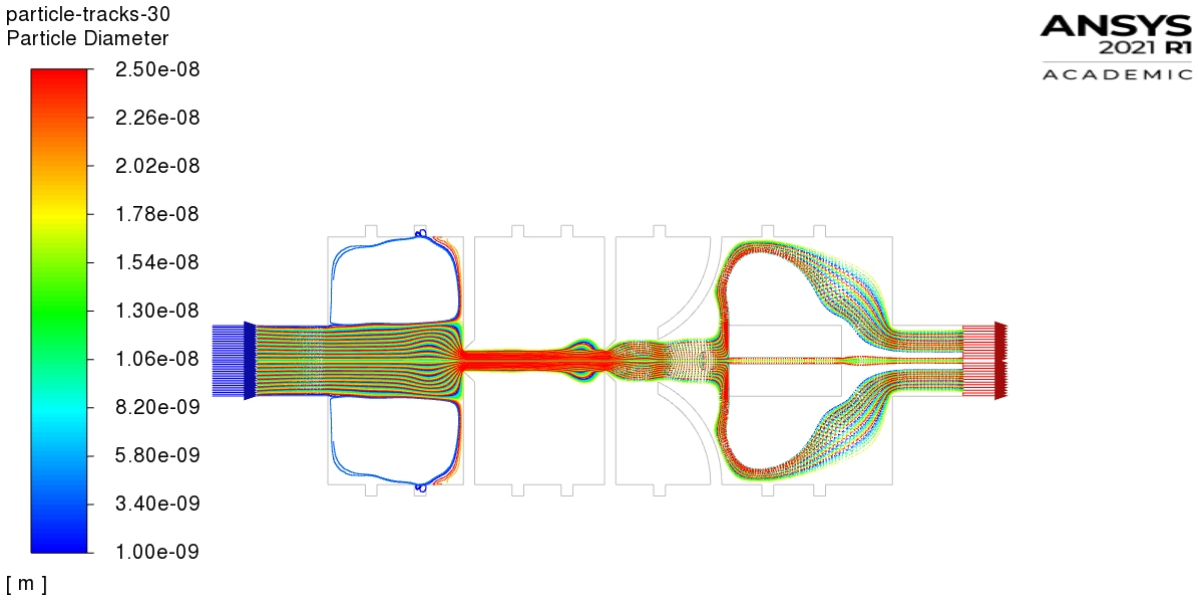

Figure 5.22: Particle traces for the 1 nm to 25 nm particle gradient expected in the flow tube, coloured by particle diameter

and the boundary values are the same as in Case 1. Figure 5.23 illustrates the particle traces for the gradient of 25 nm to 100 nm particles expected in the flow pipe, coloured according to particle residence.

Compared to the expected results and based on the model results depicted in Figures 5.21 and 5.22, it is apparent that, as they pass through two lenses, increased distribution from the axis to the fluid is stimulated by nanoparticles, as revealed by the particle tracking shown in these two Figures. The model involving nanoparticle sizes (Case 3) illustrates how nanoparticle interaction with the centreline affects fluid flow. As well, the modelling of Cases 1 and 2 highlights the influence of nanoparticle size on the interaction of the nanoparticles with the centreline in the fluid flow.

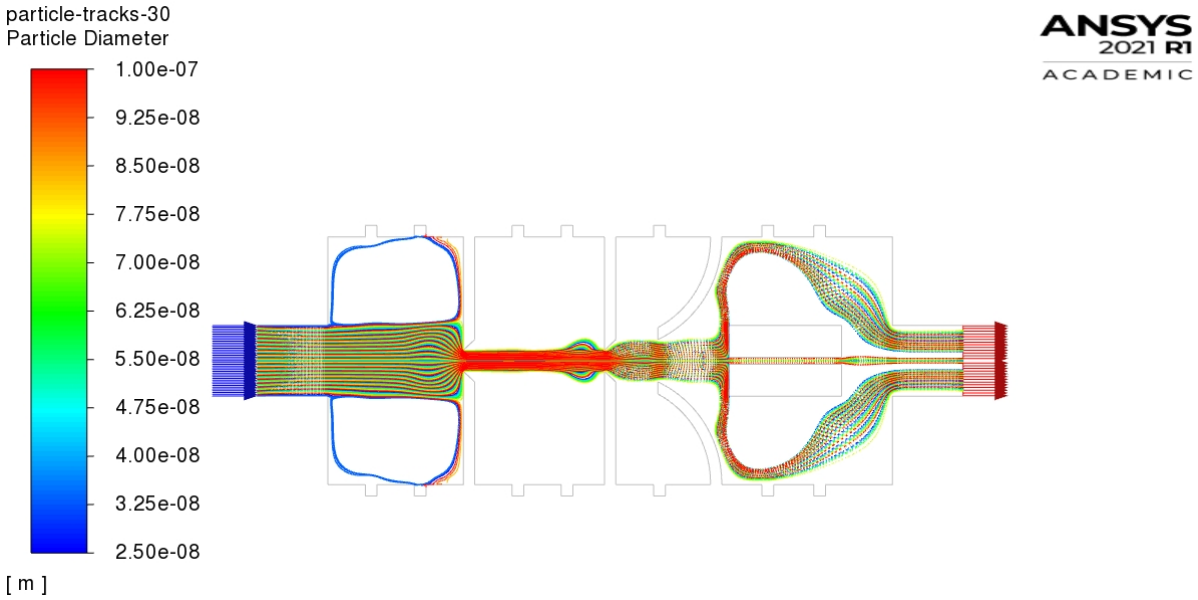

Figure 5.23: Particle traces for the 25 m to 100 nm particle gradient expected in the flow tube, coloured according to particle diameter

5.6 Validation of the Model

5.6.1 Validating the Model Against the Simulations by Middha and Wexler (2003) [97]

The initial step in the validation was a comparison of the simulation environment used in this study with the simulations developed by Middha and Wexler. The geometry and conditions published in Middha and Wexler's report were replicated in Figure 5.24. The results were a very close match to those from the previously recorded simulations, as can be seen from an examination of Figures 5.24 and 5.25, which enables a comparison with the results obtained by Middha and Wexler. Only a marginal deviation in the outlet region of the actual aerodynamic lens is evident, a deviation that was defined based on the various outlet boundary conditions, so that the boundary conditions were in the work of Middha and Wexler: In the inlet:

2700 Pa, 35 mm hydraulic diameter, while in the outlet: 50 Pa, 35 mm backflow hydraulic diameter, in the walls: no-slip.

The particles begin in the upstream direction and follow the production lines until they are near the orifice, at which point they are very close to the axis. Particles pass radially away from the axis and then move downstream through the orifice (Figure 5.26).

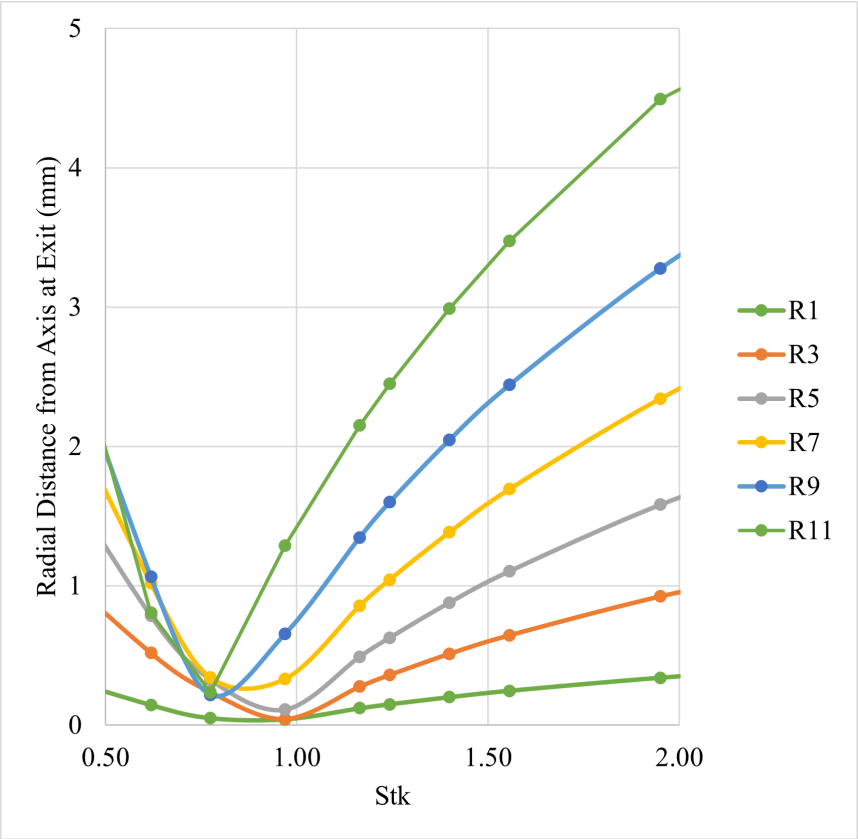

Figure 5.24: Replicated the Middha and Wexler's report [97]

Figure 5.27 depicts the Mach number in the flow. As predicted, subsonic flow occurs before the orifice, and supersonic flow occurs thereafter, as predicted. A focussing effect can be seen as more particles are brought closer to the axis after the orifice. The simulation results matched well with the work

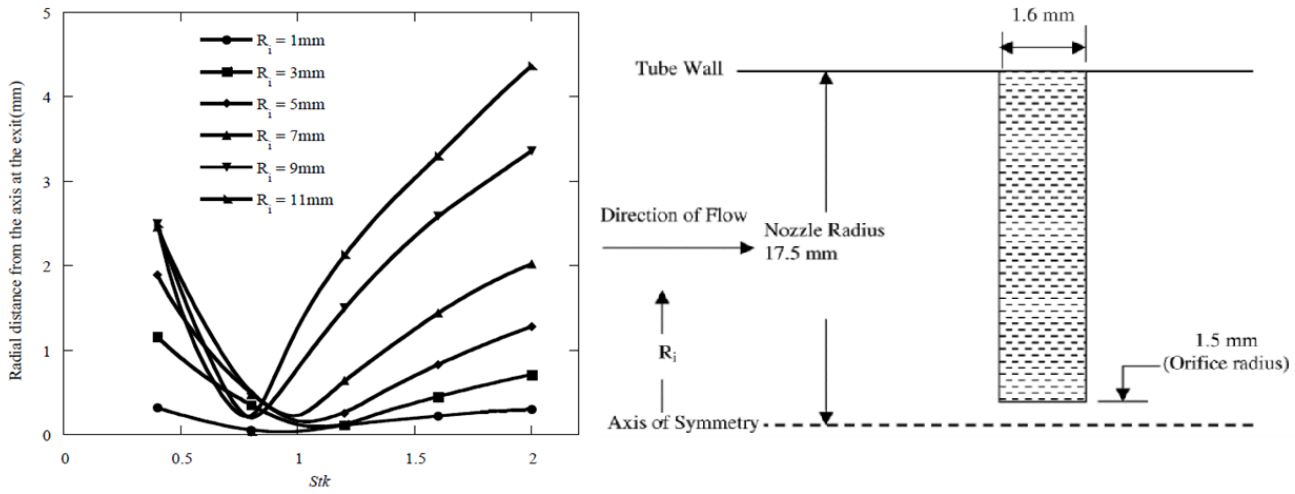

Figure 5.25: Results of the work by Middha and Wexler and their axisymmetric orifice [97]

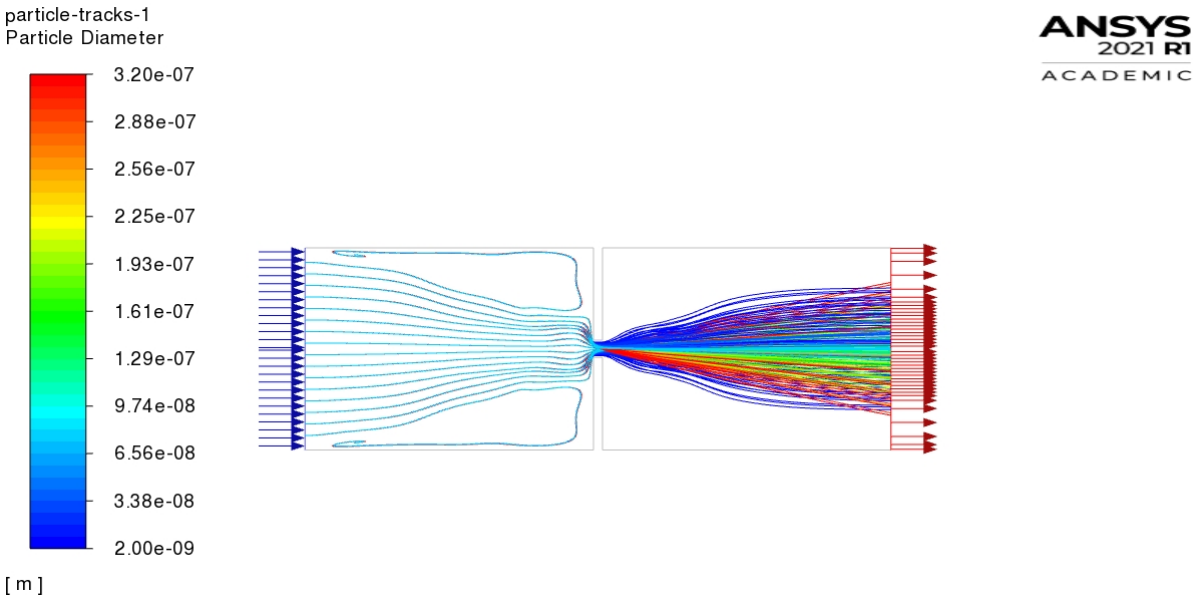

Figure 5.26: Particles pass radially away from the axis then move downstream through the orifice

of Middha and Wexler (2003). A focussing effect can be observed for parti-

cles with a Stokes number of 1.0. Some differences can be seen with particle sizes that are not focussed. The particle trajectories were also tracked up to the orifice outlet in the downstream direction. There is a unique focal point for some particle sizes. However, off-axis particles do not inevitably move through this point. As expected, to ensure choking flow conditions, provided that the downstream pressure is low enough, the focussing of the particles was discovered to be independent of the downstream pressure, [97]. It has been noted that the orifice focusses a narrow set of particles based on the size of their diameters. The range of the particles focussed reduces the radial distance of the axis and is a function of the radial distance, as indicated in Figure 5.25.

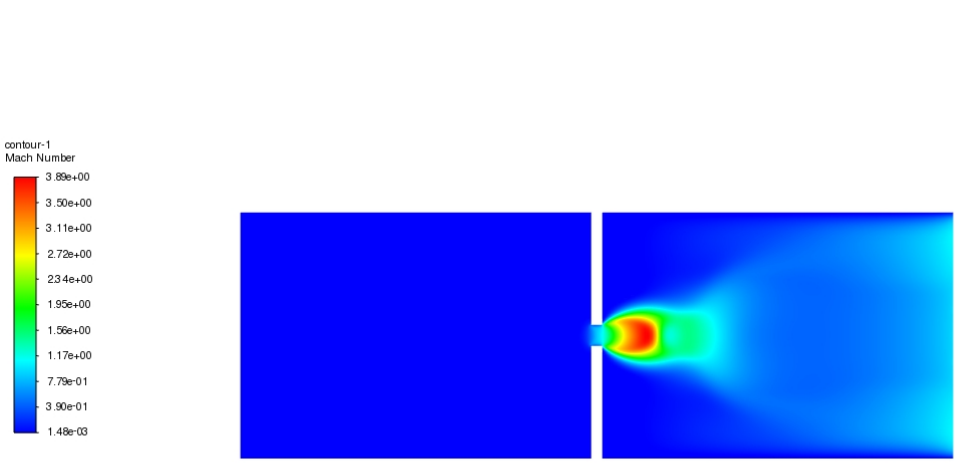

Figure 5.27: Contours of Mach number in the flow (Replicated the Middha and Wexler's paper [97])

The model analysis demonstrates that focussing is also dependent on the initial position of the upstream particles. As well, in a small orifice with a diameter of 3 mm, a wide range of nanoparticles will be focussed. All of

Table 5.2: Summary of the results for a 3 mm orifice with upstream pressure

Pressure (Pa)	St
101,325 Pa	0.01–1.99

these aspects had to be addressed in order to improve the performance of the aerodynamic particle focussing (Figures 5.24 and 5.25). Although a solution for achieving a choked flow was to reduce the diameter of the orifice hole [137], this remedy would result in fewer particles entering the orifice.

By following all the steps that were applied in Middha and Wexler's paper except for the boundary condition, these steps will be applied to the model in this research consisting of two sharp-edged plate orifices and a divergent nozzle. As a result, the boundary conditions used to simulate this model will be $2.98{*}10^{-7}$ kg/s in the inlet and 1 Pa pressure in the outlet. All of the operating conditions will be applied in this case, and two lenses and a divergent nozzle will be used to ensure that this model is appropriate for usage under these conditions after following all the steps that were applied in Middha and Wexler's paper. As a result, the boundary conditions were applied in this work, and the model was simulated by using ANSYS Fluent in conducted to evaluate it under conditions other than the atmospheric conditions. The boundary conditions obtained in this work are as follows: The flowrate at the inlet is $2.98{*}10^{-7}$ kg/s, and the pressure at the outlet is 1 Pa. Table 5.2 provides sample results for upstream pressure. The results show that this model is appropriate for usage under atmospheric conditions, as can be seen from an examination of Figure 5.28, which enables a comparison with the results obtained by Middha and Wexler in Figure 5.25.

ANSYS Fluent can track the motion of particles through a fluid using the Discrete Phase Model (DPM). In the most basic approach to implementing particles in a CFD analysis, the user specifies injection location,

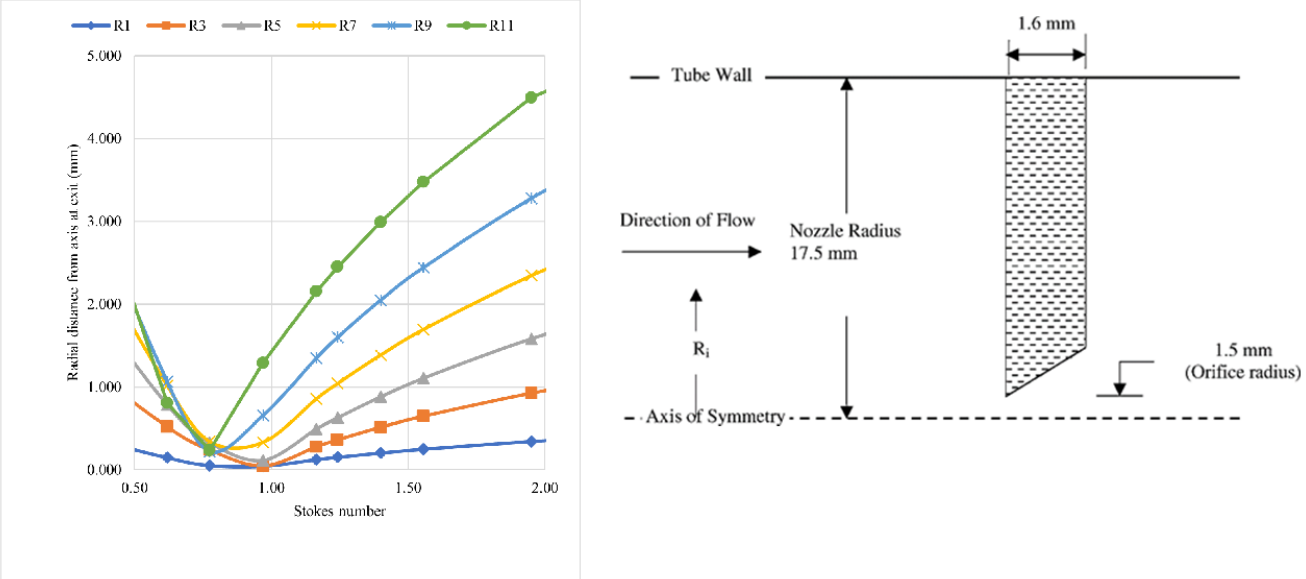

Figure 5.28: Focussing characteristics of a sharp-edged plate orifice and the axisymmetric geometry of the orifice

speed, mass flowrate, particle size, and material. Particle Tracks are the primary tool for post-processing particle behaviour. In addition to creating a graphical display of particle paths, this tool offers a powerful option to quantify particle behaviour. From the Particle Tracks menu, it needs to activate Report Type-Summary and Report To-Console or File, as shown in Figures 5.29 and 5.30. Therefore, using this step, the results of particle residence time, particle X-position, particle Y-position, particle X-velocity, Y-particle velocity, particle diameter, and particle radial position can be obtained. Therefore, based on these results, the penetration and beam width of the particles can be calculated, since they depend on the values of these results. The text interface will report statistics for individual boundaries where particles exit the system, including particle count, elapsed time, and mass flow. The number of particles in the parcel N_p is determined as follows:

$$N_p = \frac{\dot{m}\Delta t}{m_p} \tag{5.5}$$

Where N_p denotes the number of particles in a parcel, $\dot{m}$ denotes a particle's mass flowrate, Δt denotes a time step, and m_p denotes particle mass.

$$m_p = \frac{\pi d^3}{6} \tag{5.6}$$

In Figure 5.28, it is shown that the particles were injected into the inlet at six positions. It also shows that the radial distances at the inlet are higher than the radial distances at the outlet. So it is possible to measure the particle beam in this case based on the difference in the particle radial distances at the inlet and outlet. In this case, particles are injected by using surface injection type from the inlet; however, the number of particles is restricted by the number of meshed cells at the inlet (no specified number of streams like point or group injection types). Figure 5.31 depicts particle penetration through the aerodynamic lenses using two lenses and a divergent nozzle with and without F_{Br}. Penetration is carried out by determining the ratio of the number of particles leaving the outlet to the number entering the inlet.

When the F_{Br} is ignored, most nanoparticles with diameters of less than 300 nm pass through the aerodynamic lenses. In addition, since most of these nanoparticles are only deposited on the pipe or lens wall, there is a slight decrease in the penetration of nanoparticles above 250 nm. The second lens results in the fewest lost nanoparticles. It outperforms the other two models (the first lens and the divergent nozzle) that aim to focus on nanoparticles of the same size when it comes to particle concentrations of sub-300 nm. Diffusion causes most of the 1 nm–10 nm particles to be deposited on the walls, while the penetrations range from 53.333% to 98.125%.

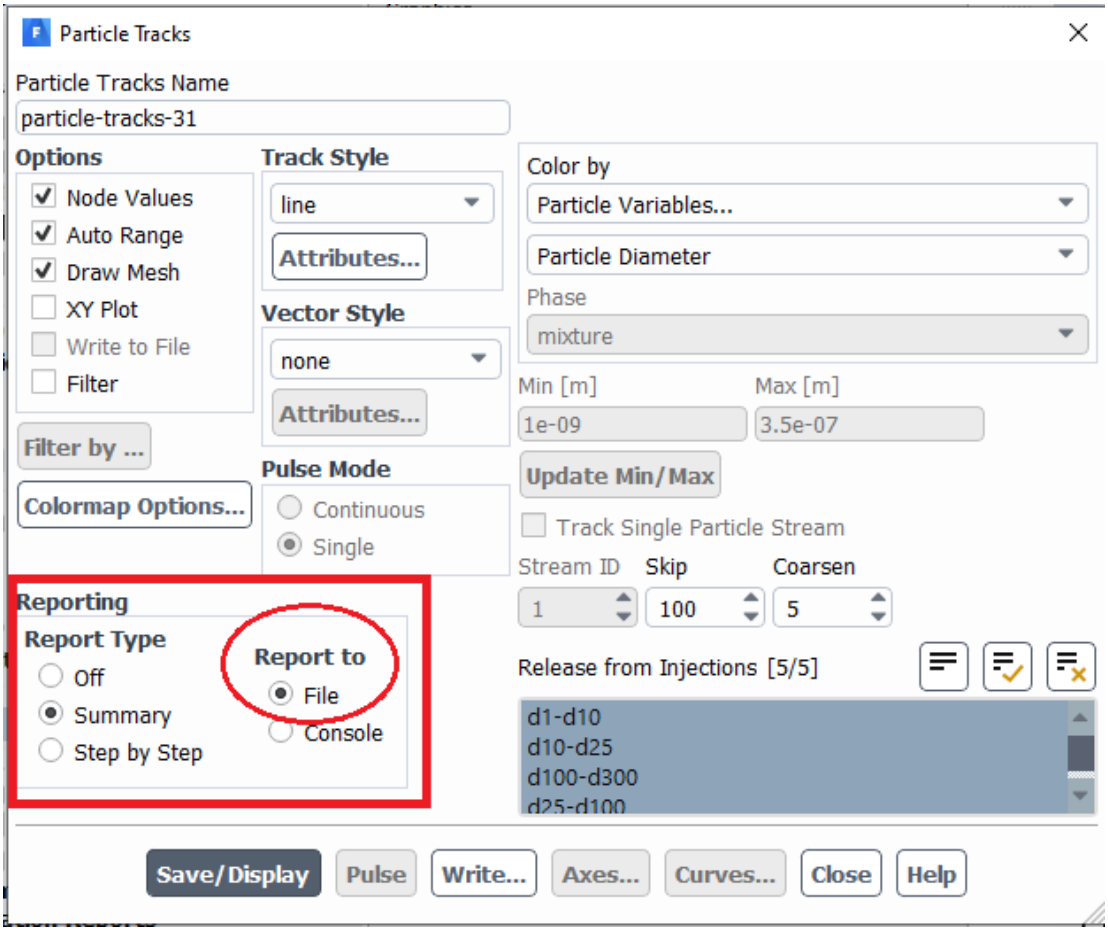

Figure 5.29: Graphical display has been created of particle paths to offer a powerful option to quantify particle behavior

The particle beam width at the exit of the second lens with and without F_{Br} of the particles in the range of 1 nm-300 nm is shown in Figure 5.32.

As shown in Figure 5.32, the particle beam width increases near 250 nm, the size of the nanoparticles. Inertial transport has a significant effect on nanoparticles larger than 250 nm. Figure 5.33 shows the particle beam penetration through two lenses and a divergent nozzle, while Figure 5.34 shows the beam width produced by two lenses and one divergent nozzle.

TITLE: TRACK HISTORY

COLUMN	TYPE	VARIABLE	(UNITS)
1	2	ParticleResidenceTime	(s)
2	10	ParticleXPosition	(m)
3	10	ParticleYPosition	(m)
4	10	ParticleZPosition	(m)
5	10	ParticleXVelocity	(m/s)
6	10	ParticleYVelocity	(m/s)
7	10	ParticleZVelocity	(m/s)
8	10	ParticleDiameter	(m)
9	10	ParticleTemperature	(K)
10	10	ParticleDensity	(kg/m3)
11	10	ParticleMass	(kg)
12	10	ParticleRadialPosition	(m)

0.00000e+00	2.62879e-10	2.47567e-05	0.00000e+00	2.80000e+01	0.00000e+00	0.00000e+00	3.00000e-09	3.00000e+02	1.55000e+03	2.19126e-23	2.47567e-05
3.15096e-10	7.59021e-09	2.47567e-05	0.00000e+00	2.25245e+01	-8.53254e-04	0.00000e+00	3.00000e-09	2.99689e+02	1.55000e+03	2.19126e-23	2.47567e-05
6.30192e-10	1.46875e-08	2.47567e-05	0.00000e+00	2.25241e+01	-8.54474e-04	0.00000e+00	3.00000e-09	2.99683e+02	1.55000e+03	2.19126e-23	2.47567e-05
9.45288e-10	2.17848e-08	2.47567e-05	0.00000e+00	2.25241e+01	-8.55644e-04	0.00000e+00	3.00000e-09	2.99682e+02	1.55000e+03	2.19126e-23	2.47567e-05
1.26038e-09	2.88820e-08	2.47567e-05	0.00000e+00	2.25240e+01	-8.56813e-04	0.00000e+00	3.00000e-09	2.99682e+02	1.55000e+03	2.19126e-23	2.47567e-05
1.57548e-09	3.59792e-08	2.47567e-05	0.00000e+00	2.25240e+01	-8.57982e-04	0.00000e+00	3.00000e-09	2.99682e+02	1.55000e+03	2.19126e-23	2.47567e-05
1.89058e-09	4.30764e-08	2.47567e-05	0.00000e+00	2.25239e+01	-8.59152e-04	0.00000e+00	3.00000e-09	2.99682e+02	1.55000e+03	2.19126e-23	2.47567e-05
2.20567e-09	5.01736e-08	2.47567e-05	0.00000e+00	2.25238e+01	-8.60321e-04	0.00000e+00	3.00000e-09	2.99682e+02	1.55000e+03	2.19126e-23	2.47567e-05
2.52077e-09	5.72707e-08	2.47567e-05	0.00000e+00	2.25238e+01	-8.61491e-04	0.00000e+00	3.00000e-09	2.99682e+02	1.55000e+03	2.19126e-23	2.47567e-05
2.83586e-09	6.43679e-08	2.47567e-05	0.00000e+00	2.25237e+01	-8.62660e-04	0.00000e+00	3.00000e-09	2.99682e+02	1.55000e+03	2.19126e-23	2.47567e-05
3.15096e-09	7.14650e-08	2.47567e-05	0.00000e+00	2.25236e+01	-8.63829e-04	0.00000e+00	3.00000e-09	2.99682e+02	1.55000e+03	2.19126e-23	2.47567e-05
3.46606e-09	7.85621e-08	2.47567e-05	0.00000e+00	2.25236e+01	-8.64999e-04	0.00000e+00	3.00000e-09	2.99682e+02	1.55000e+03	2.19126e-23	2.47567e-05
3.78115e-09	8.56592e-08	2.47567e-05	0.00000e+00	2.25235e+01	-8.66168e-04	0.00000e+00	3.00000e-09	2.99682e+02	1.55000e+03	2.19126e-23	2.47567e-05
4.09625e-09	9.27562e-08	2.47567e-05	0.00000e+00	2.25235e+01	-8.67337e-04	0.00000e+00	3.00000e-09	2.99682e+02	1.55000e+03	2.19126e-23	2.47567e-05
4.41134e-09	9.98533e-08	2.47567e-05	0.00000e+00	2.25234e+01	-8.68507e-04	0.00000e+00	3.00000e-09	2.99682e+02	1.55000e+03	2.19126e-23	2.47567e-05
4.72644e-09	1.06950e-07	2.47567e-05	0.00000e+00	2.25233e+01	-8.69676e-04	0.00000e+00	3.00000e-09	2.99682e+02	1.55000e+03	2.19126e-23	2.47567e-05
5.04154e-09	1.14047e-07	2.47567e-05	0.00000e+00	2.25233e+01	-8.70846e-04	0.00000e+00	3.00000e-09	2.99682e+02	1.55000e+03	2.19126e-23	2.47567e-05
5.35663e-09	1.21144e-07	2.47567e-05	0.00000e+00	2.25232e+01	-8.72015e-04	0.00000e+00	3.00000e-09	2.99682e+02	1.55000e+03	2.19126e-23	2.47567e-05
5.67173e-09	1.28241e-07	2.47567e-05	0.00000e+00	2.25231e+01	-8.73184e-04	0.00000e+00	3.00000e-09	2.99682e+02	1.55000e+03	2.19126e-23	2.47567e-05
5.98682e-09	1.35338e-07	2.47567e-05	0.00000e+00	2.25231e+01	-8.74354e-04	0.00000e+00	3.00000e-09	2.99682e+02	1.55000e+03	2.19126e-23	2.47567e-05
6.30192e-09	1.42435e-07	2.47567e-05	0.00000e+00	2.25230e+01	-8.75523e-04	0.00000e+00	3.00000e-09	2.99682e+02	1.55000e+03	2.19126e-23	2.47567e-05
6.61702e-09	1.49532e-07	2.47567e-05	0.00000e+00	2.25230e+01	-8.76692e-04	0.00000e+00	3.00000e-09	2.99682e+02	1.55000e+03	2.19126e-23	2.47567e-05
6.93211e-09	1.56629e-07	2.47567e-05	0.00000e+00	2.25229e+01	-8.77862e-04	0.00000e+00	3.00000e-09	2.99682e+02	1.55000e+03	2.19126e-23	2.47567e-05
7.24721e-09	1.63726e-07	2.47567e-05	0.00000e+00	2.25228e+01	-8.79031e-04	0.00000e+00	3.00000e-09	2.99682e+02	1.55000e+03	2.19126e-23	2.47567e-05
7.56230e-09	1.70823e-07	2.47567e-05	0.00000e+00	2.25228e+01	-8.80200e-04	0.00000e+00	3.00000e-09	2.99682e+02	1.55000e+03	2.19126e-23	2.47567e-05
7.87740e-09	1.77919e-07	2.47567e-05	0.00000e+00	2.25227e+01	-8.81370e-04	0.00000e+00	3.00000e-09	2.99682e+02	1.55000e+03	2.19126e-23	2.47567e-05
8.19250e-09	1.85016e-07	2.47567e-05	0.00000e+00	2.25227e+01	-8.82539e-04	0.00000e+00	3.00000e-09	2.99682e+02	1.55000e+03	2.19126e-23	2.47567e-05
8.50759e-09	1.92113e-07	2.47567e-05	0.00000e+00	2.25226e+01	-8.83708e-04	0.00000e+00	3.00000e-09	2.99682e+02	1.55000e+03	2.19126e-23	2.47567e-05
8.82269e-09	1.99210e-07	2.47567e-05	0.00000e+00	2.25225e+01	-8.84878e-04	0.00000e+00	3.00000e-09	2.99682e+02	1.55000e+03	2.19126e-23	2.47567e-05
9.13778e-09	2.06307e-07	2.47567e-05	0.00000e+00	2.25225e+01	-8.86047e-04	0.00000e+00	3.00000e-09	2.99682e+02	1.55000e+03	2.19126e-23	2.47567e-05
9.45288e-09	2.13403e-07	2.47567e-05	0.00000e+00	2.25224e+01	-8.87216e-04	0.00000e+00	3.00000e-09	2.99682e+02	1.55000e+03	2.19126e-23	2.47567e-05
9.76798e-09	2.20500e-07	2.47567e-05	0.00000e+00	2.25223e+01	-8.88386e-04	0.00000e+00	3.00000e-09	2.99682e+02	1.55000e+03	2.19126e-23	2.47567e-05

Figure 5.30: Example of the results that obtained by using the Discrete Phase Model (DPM)

The beam width and penetration of the effective lens to focus the nanoparticles must be narrow. Therefore, the beam width of the focussing system is determined by the diffuse displacement and aerodynamic focus. It is known that the turbulence and instability of the flow are the causes of the destruction of particle concentration and diffusion. According to the simulations carried out in this research and previous research, the possibility of nanoparticle deposition on the wall of the tube or lenses arises because Brownian diffusion causes perturbation of the nanoparticle trajectories dictated by the carrier gas.

To summarize, in this research, two lenses and one divergent nozzle were used for focussing nanoparticles, consisting of spherical particles of carbon

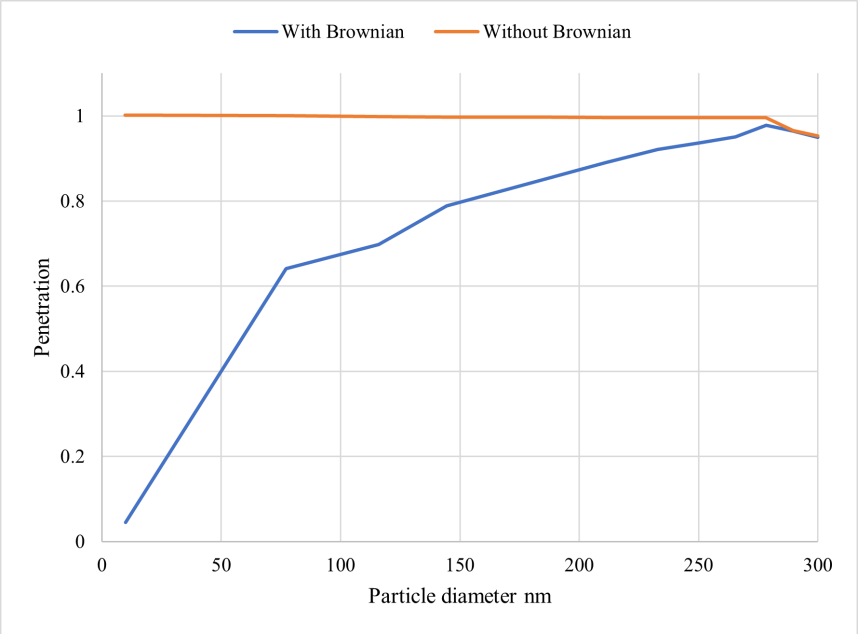

Figure 5.31: Particle penetration through the aerodynamic lens with and without F_{Br}

as small as 300 nm, through the inlet of the pipe. The particles were then passed through a set of two lenses, 20 mm apart, with an inner diameter of 3 mm for each lens. To explain why the Faraday cup electrometer is installed inside the pipe so that the particles move through the Faraday cup electrometer (FCE) after passing through the aerodynamic lenses, the observed particles are then captured and transferred to the Differential Mobility Analyzer (DMA) for an examination of the effects since, at any point in time, each particle has an individual velocity that varies according to time or location.

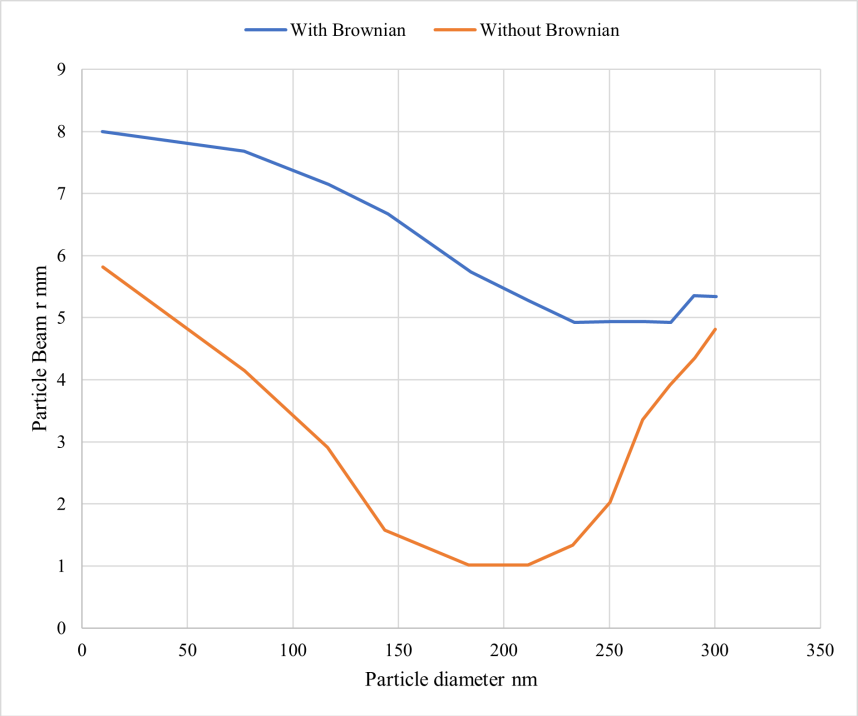

Figure 5.32: Particle beam width in the lens exit with and without F_{Br}

5.6.2 Validating the Model Against the Simulations by Wang et al. (2005) [152]

Axisymmetric elements such as orifices are commonly used for separating particles from flow streamlines and moving them closer to the axis. To focus the particles, these elements require that the particles have sufficient inertia. However, in this research, as the particle size decreases to sub-300 nm, focussing performance is drastically degraded because the low levels of inertia and a high degree of diffusivity of sub-300 nm particles make focussing them difficult. Due to their small inertia, nanoparticles tend to follow gas streamlines very closely, and only slight focussing can be accomplished [154]. Smaller particles, with a Stokes number less than one, thus tend to follow the streamlines in order to avoid crossing the centreline, while

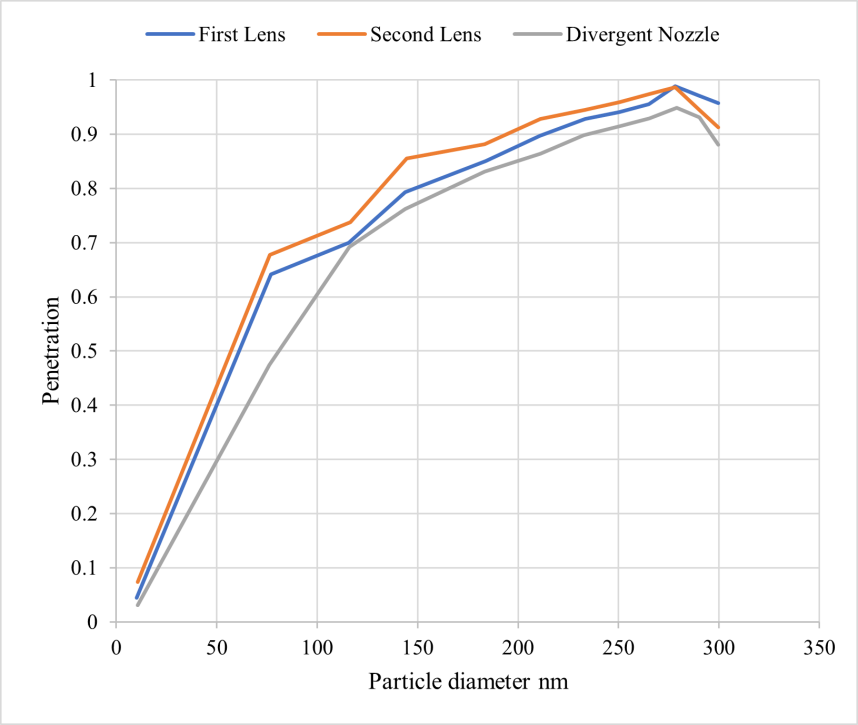

Figure 5.33: The penetration of particles through two lenses and a divergent nozzle with diffusion

larger particles, with a Stokes number greater than one, are less disturbed by the flow and therefore cross the centreline. Particles with intermediate inertia are separated from the streamlines and focussed on the axis so that particles with specific Stokes numbers are carried to the axis [98].

To verify the section of the model under consideration, this study attempted to replicate the results from the analysis published by Wang et al. [152]. Theoretical modelling of particle motion and fluid flow through orifices was utilized to validate the work under investigation. According to Wang et al. (2005), the orifice diameter and operating pressure are the two most essential parameters to consider when designing an aerodynamic lens. As a result, for a given mass flowrate and particle properties, they established the lens operating pressure range as a function of orifice diameter.

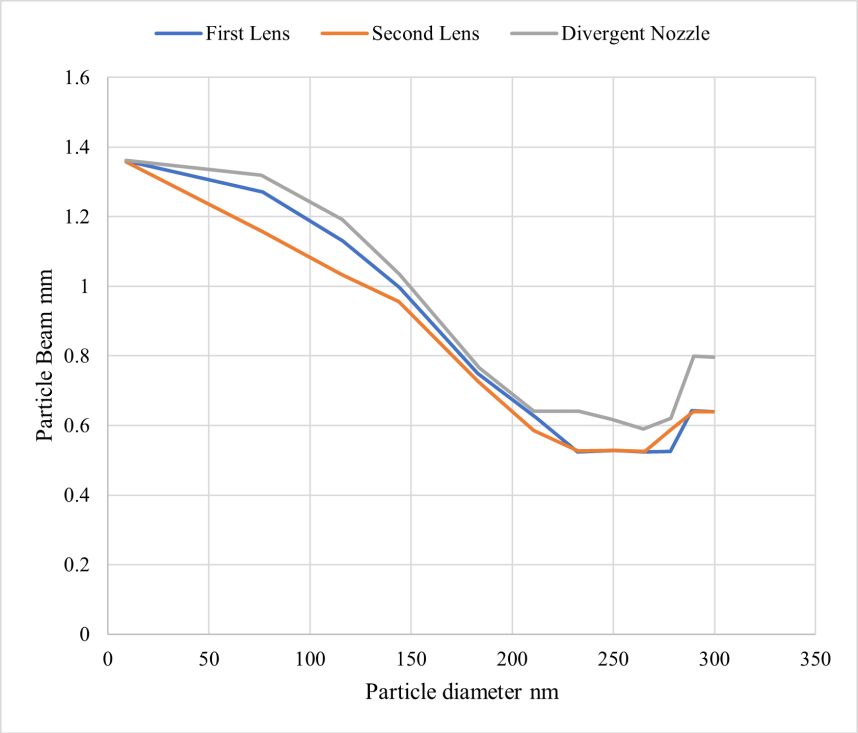

Figure 5.34: Particles beam width through two lenses and a divergent nozzle with diffusion

They computed the minimum pressure for subsonic flow P_{ma}, the minimum pressure for continuous flow P_{kn}, and the maximum operating pressure of an aerodynamic lens $P_{focusing}$ using equations 5.7, 5.8, and 5.9 [152]:

$$P_{ma} = \frac{\frac{\dot{m}_c}{C_d Y_c A_f}}{\sqrt{\frac{2M}{RT_1} x_c}} \tag{5.7}$$

$$P_{kn} = \frac{2}{d_f K_n} \lambda_r \frac{T_1}{T_r} p_r \frac{1 + \frac{S}{T_r}}{1 + \frac{S}{T_1}} \tag{5.8}$$

$$P_{focusing} = \left[\frac{1}{(1 + \frac{\pi\alpha}{8})\sqrt{2\pi\gamma^3}} \frac{\dot{m}\rho_p d_p c^3}{d_f^3 St_0}\right]^{\frac{1}{2}} \tag{5.9}$$

Where λ_r is the gas molecule mean free path at the reference conditions, T_r and p_r are 296.15 K and 101,325 Pa, respectively [154]. S is the Sutherland constant (110.4 K). Therefore, Wang et al. demonstrated that the operating pressure ($P_{focussing}$) of an aerodynamic lens must be higher than P_{ma} so that the flow is subsonic. For focusing particles, the operating pressure range is where $P_{focusing}$ is greater than both P_{ma} and P_{kn}. The point where the P_{ma}, P_{kn}, and $P_{focussing}$ curves intersect in Figure 5.35 below indicates the smallest size that may be focused dp. In addition, the smallest size of the particles that can be focused is determined by the intersection of the P_{ma}, P_{kn}, and $P_{focusing}$ curves. It's also important to obtain a low enough pressure to achieve particle concentration.

The main point is that for the overall research reported in this thesis, the results of the model that was developed were validated based on a comparison with the replicated research results produced by Wang et al. in order to evaluate the new focussing system. The first step was to validate the results produced by the simulations replicated in the new model against the results from the simulations created by Wang et al. (2005). Particle trajectories were simulated by replicating the geometry and parameters from the Wang et al. paper. The results of the equations 5.7, 5.8, and 5.9 closely matched those from the previously published formulas , as revealed by a comparison of Figures 5.35 (the results replicated for this study) and 5.36 (results from Wang et al.'s paper [152]). The conclusion was that the base formulas presented by Wang et al. were well replicated and the results of the replicated formulas agreed well with those of the original formulas, as Figures 5.35, and 5.36 confirm.

Multiple lenses operating at Stokes numbers smaller than the optimum Stokes number must be employed to focus on small particles, according to Wang et al. [152, 154]. Therefore, in this study, the diameter of the orifices was set at 3 mm, and the volume of the flowrate through the focussing orifice was adjusted to be 0.000024 m^3/s. Therefore, by calculating the minimum

pressure of subsonic flow P_{ma}, a minimum pressure of continuous flow P_{kn}, and maximum operating pressure of an aerodynamic lens $P_{focussing}$ using the same equations that are used in the work of Wang et al. (Equations 5.7, 5.8, and 5.9), so the result was shown in Figure 5.37:

In the Figure 5.37, three lens diameters are used, 0.1, 3, and 100 mm. For the $P_{focussing}$ measurement, a range of particles (1 nm, 10 nm, 20 nm, 25 nm, 100 nm, and 300 nm) was chosen and compared to P_{ma} and P_{kn}. Because the diameter of the orifice in this study was 3 mm, this diameter was focussed on in order to ensure the efficiency of the lens with a diameter of 3 mm with regard to focussing and detecting particles. Based on the results shown in Figure 5.37, it is demonstrated that the $P_{focussing}$ line with respect to particle sizes from 10 nm - 100 nm is higher than the P_{ma} and P_{kn} lines. Therefore, the model for this research proved its effectiveness in the concentration of particles smaller than 100 nm up to 10 nm. For the point of intersection with $P_{focussing}$ line for 10 nm with the P_{ma} line, it shows the smallest particle size that can be focussed on. The area of intersection of $P_{focussing}$ curves for 10 nm and 25 nm with P_{kn} line also shows the possibility of focussing of these sizes of particles ranging from 10 nm - 25 nm. The $P_{focussing}$ lines for 100 nm - 300 nm intersect with P_{ma} line and continue to be higher than P_{kn} line, so the focussing of these particles is very high in this case. This Figure proved the effectiveness of the orifice diameter used in this research, which is 3 mm, as well as the possibility of focussing and detecting nanoparticles whose sizes range from 10 nm - 300 nm in this case.

In Figure 5.38, particles that enter from the inlet in radial positions close to the centerline pass through the orifice with little direction change. The selected particle in the inlet follows the gas toward the lens at a radial position of $rp\_i = 2.5$ mm, considerably upstream of the lens, as illustrated in Figure 5.38. Particles starting from intermediate radial positions may approach or cross the centerline depending on the Reynolds number and particle inertia. The ultimate particle beam size at the exit is determined by

the critical particle trajectory, which is the trajectory of a particle starting from the outermost radial position at the inlet among the particles that do not deposit on the orifice [78]. Equation 5.9 shows that when a Stokes number less than St_0 is employed, focussing is larger. The critical streamline is defined as the streamline that starts at the same position at the inlet as the critical particle trajectory. As particle inertia increases, the critical particle trajectory deviates more and more from the corresponding critical streamline. The contraction factor, defined in Equation 5.10, which is the ratio of the radial distances from the axis of the critical particle trajectory and the critical streamline, may be used to determine the extent of this deviation owing to particle inertia [78]:

$$\eta = \frac{rp_{-o}}{rp_{-i}} \tag{5.10}$$

The gas is radially accelerated inward as it approaches the lens, and the particles overshoot the gas streamlines toward the axis [162]. The particle moves radially outward downstream of the lens, but only slightly, before settling onto a streamline with a smaller radial position, rp_{-o}, as shown in Figure 5.39. The trajectory of sub-300 nm particles with and without Brownian force is depicted in Figure 5.40. It is worth noting that in the absence of diffusion, particles that are initially positioned near the axis can be focussed very close to the axis [166]. Because of velocities, particles further from the axis are not as effectively focussed, and their Stokes numbers are smaller as a result of viscous effects. The focussing effect is still evident when Brownian motion is present.

Nanoparticles follow gas streamlines due to inertia, and only a small fraction of nanoparticles can be focussed. Nanoparticles' defocusing is exacerbated by their high diffusivities, which results in particle loss. According to computational methods of size-resolved particle trajectories, the majority of small nanoparticles are lost to the wall by diffusion. The particle

beam escaping the aerodynamic lenses was directed into the downstream exit boundary, which was maintained at 1 Pa pressure. The pipe length and the length between the aerodynamic lenses assembly have been shortened to reduce particle loss caused by Brownian diffusion, and a high inlet flow feature has been included to reduce the residence time. So, the distance between the lenses is set at 20 mm. According to the simulations performed in this research and previous research, the possibility of nanoparticle deposition on the wall of the pipe or lenses arises because Brownian diffusion causes perturbation of the nanoparticle trajectories dictated by the carrier gas. When the F_{Br} is ignored, a large number of nanoparticles with diameters of less than 300 nm pass through the orifices. The second lens system results in the lowest number of nanoparticles lost. It outperforms the two other focussing systems (a first lens and a divergent nozzle) meant to concentrate particles of the same size whenever it comes to concentrating sub-300 nm particles.

Comparison of the CFD Simulation Results Against the Simulations by Wang et al. (2005) [152]

To focus particles on the centreline of the exit nozzle, this system employs a single sharp turn in the aerosol flow path through the holes of the orifices. Table 5.3 provides a comparison of the specifications for three lens systems: a variation of an Italian focuser instrument with a typical five-aerodynamic-lens assembly; the one employed by Liu et al., [87], which Wang et al. [152] used in their research; and the new system presented here with two lenses and one divergent nozzle.

The work conducted for this thesis was concentrated on designing an aerodynamic lens system for focussing nanoparticles. The first stage of this work was to validate the new calculation model against the results produced by Wang et al., [152]. The results were a very close match to those from

Table 5.3: Specification of 1) A typical aerodynamic lens assembly and Italian focuser (Tafreshi et al.) [135]; 2) The system used by Liu et al. [87]; and 3) The set-up employed in this study with two lenses with one divergent nozzle (Details in the Table 5.4)

No.	Number of Lenses	Carrier Gas	Pressure, KPa	Flow Time, Sec	St_o	Focussing Range, nm	References
1	Focuser	Helium	1.067-4	0.003	0.1	1–6	[135, 136]
2	5 Lenses	Air	0.267	0.1	0.7–1.5	40-250	[87, 88]
3	2 Lenses & 1 Nozzle	Air	101.325	0.001	0.01–1.99	1-320	This Research

the previously recorded calculations, as can be seen from Figures 5.35 and 5.36, which enable a comparison with the results obtained by Wang et al. (2005). Wang et al. [152] have developed this model for calculating the smallest particle size that can be precisely focussed on the axis, with a focus region at the aperture exit in the absence of diffusion. Further investigation was targeted at designing a procedure for reducing the size of a particle that can be focussed compared to the number of particles in the focus region while also minimizing the effects of diffusion (Figure 5.41).

Figures 5.42 and 5.41 show a comparison between the simulation results for this study and the results from the Italian focuser device reported by Wang et al (2005). Some differences in particle sizes can be seen in these Figures. According to Figure 5.41, the simulation produced for this study seems to have accurately determined the size of the nanoparticles identified for focussing by the Italian focuser device. As a result, the smallest, most focussed particles have a diameter of about 3.9 nm, while the largest have a diameter of close to 5 nm in the lens. In this study, a simulation method was used for measuring the size of the nanoparticles. With respect to the absence of diffusion, the focus area was the region in the aperture exit of the second orifice just before FCE. The small, focussed particles examined

Table 5.4: The result of this study using two lenses and a divergent nozzle

No.	dp (nm)	St
1	2	0.01
2	5	0.03
3	10	0.06
4	20	0.12
5	40	0.24
6	80	0.49
7	100	0.61
8	125	0.77
9	150	0.92
10	160	0.98
11	180	1.11
12	200	1.23
13	250	1.55
14	300	1.86
15	320	1.99

have a diameter of about 3 nm, while the largest have a diameter of 3.6 nm,Figure 5.42. The target aperture can focus on particles larger than 3.6 nm but not particles smaller than 3 nm. Figure 5.42 illustrates how targeting the focus area at the aperture outlet enabled the calculation of the smallest particle size that can be focussed precisely on the axis.

The size of the particles passing through a divergent nozzle (from the lens to the FCE) is compared to the number of particles in the focus area passing through the divergent nozzle between the second lens and the FCE, and the

measurements of the size of the nanoparticles in this region are identified in the Figure 5.42. The small, concentrated particles were thus found to have a diameter of about 3.1 nm, while the largest have a diameter of 3.6 nm. This procedure thus reduced the particle size that can be focussed compared to the number of particles in the region selected for focussing. The differences can be attributed to the use of a divergent nozzle, which has a hole with a 3 mm diameter. The model results were then validated computationally by comparing the simulation outcome in Figure 5.42 with data from Wang et al. in Figure 5.41 as a means of evaluating the accuracy and efficiency of the lens and nozzle used for measuring the size of nanoparticles smaller than 300 nm.

5.7 Summary

In this chapter, aerodynamic lenses and a divergent nozzle for nanoparticle size measurements have been developed, evaluated, and validated. The approach taken in this research was based on computational simulations. The computational method included the development and investigation of an aerodynamic lens with a sharp-edged plate orifice rather than a conventional flat orifice for focussing nanoparticles. The diameter of the larger particles focussed was greater than 300 nm, while that of the smallest was 3 nm. Figures 5.43 and 5.44 provide the simulation results.

Because computational simulations of lens systems offer enhanced accuracy, this approach was adopted for validating the theoretical and analytical simulation results with respect to measuring the size of nanoparticles on an aerodynamic lens, with the following results:

Through the development of techniques for predicting nanoparticle diameter, the present study has advanced the design of aerodynamic lens systems. This study also demonstrated that the use of air as the carrier gas

is preferable for focussing on small-sized particles. The work presented here also involved the development of a model of the flow through the sharp-edged plate of the orifice, along with a computational method employing CFD-ANSYS Fluent for simulating the flow and motion of particles through an aerodynamic lens. Compressible, laminar, viscous, and Navier-Stokes equations were initially applied for computing the gas flow field, followed by the integration of the Lagrangian model in order to obtain the particle trajectories. This approach was used to evaluate the possibility of focussing nanoparticles smaller than 300 nm. This research represents the first systematic effort to identify the size of nanoparticles using an aerodynamic lens and computational simulation. The results to this point in the research can be summarized as follows:

1. **This study** led to the development of an aerodynamic lens system for focussing spherical particles with sizes of 3 nm to 300 nm. Air was utilized as a carrier gas and constituted the first phase, with carbon particles as the secondary phase. Two lenses with divergent nozzles were employed for focussing the nanoparticles and measuring their sizes. It is also demonstrated that the possibility of focussing and measuring particles larger than 300 nm but not those smaller than 3 nm is demonstrated.

2. **The results** of this study revealed that when an aerodynamic lens system is combined with a divergent nozzle, it provides better performance of nanoparticles. As a result, this study indicated that using air as a gas carrier can enhance focussing.

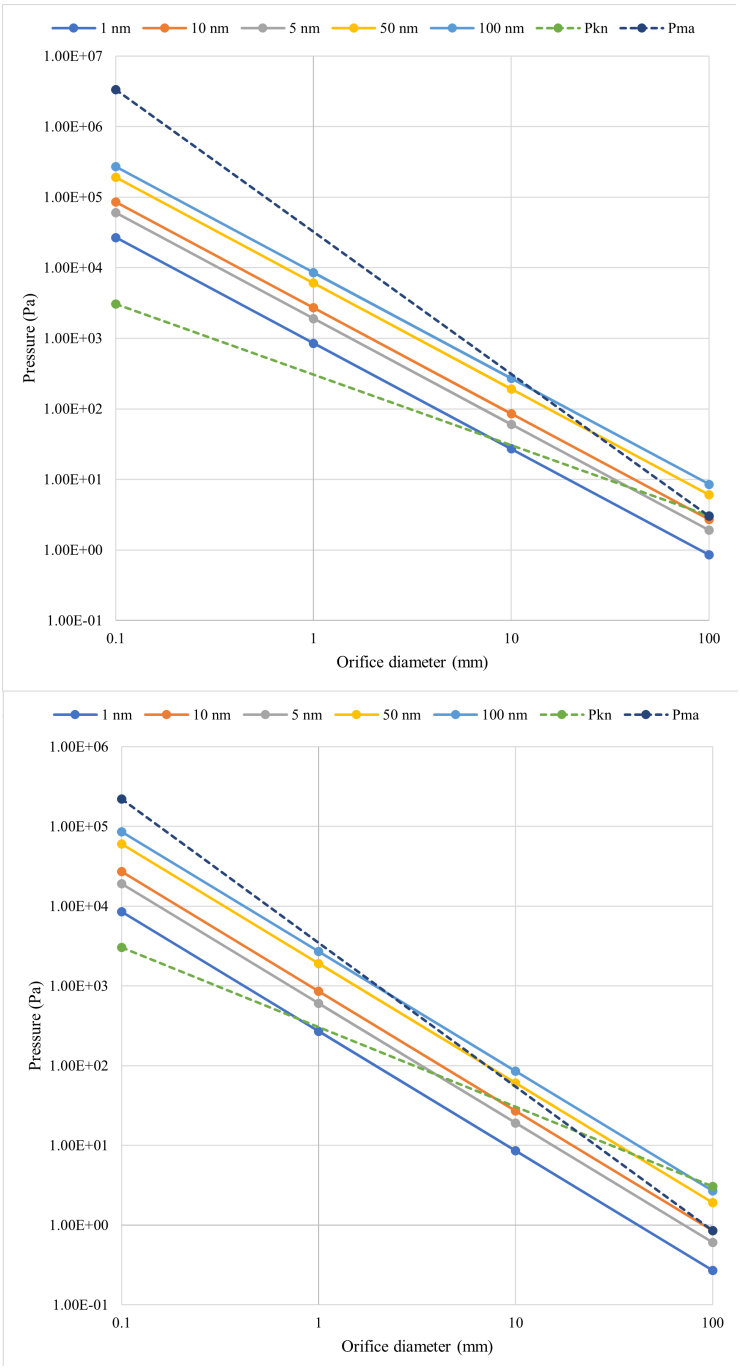

Figure 5.35: Particle trajectories calculated for this study as replications of the geometry and parameters from the Wang et al. report [152]

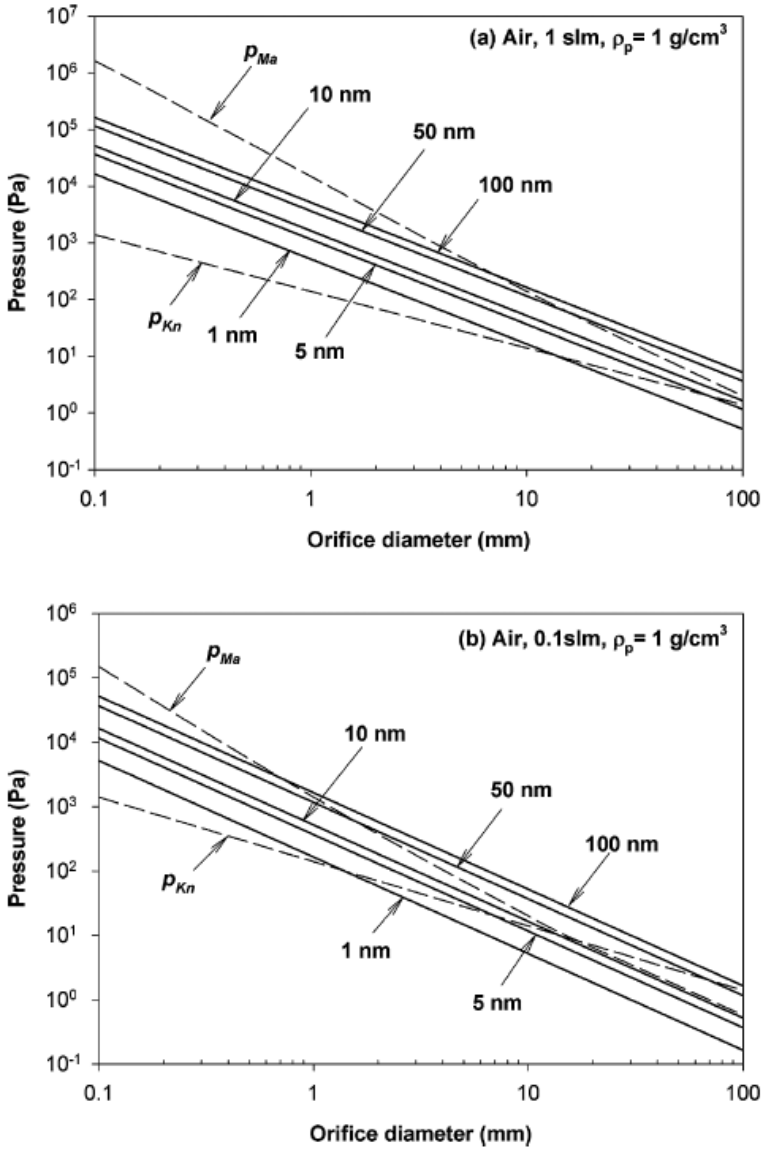

Figure 5.36: Pressure limits of the Mach and Knudsen numbers as well as focussing results from Wang et al. [152]

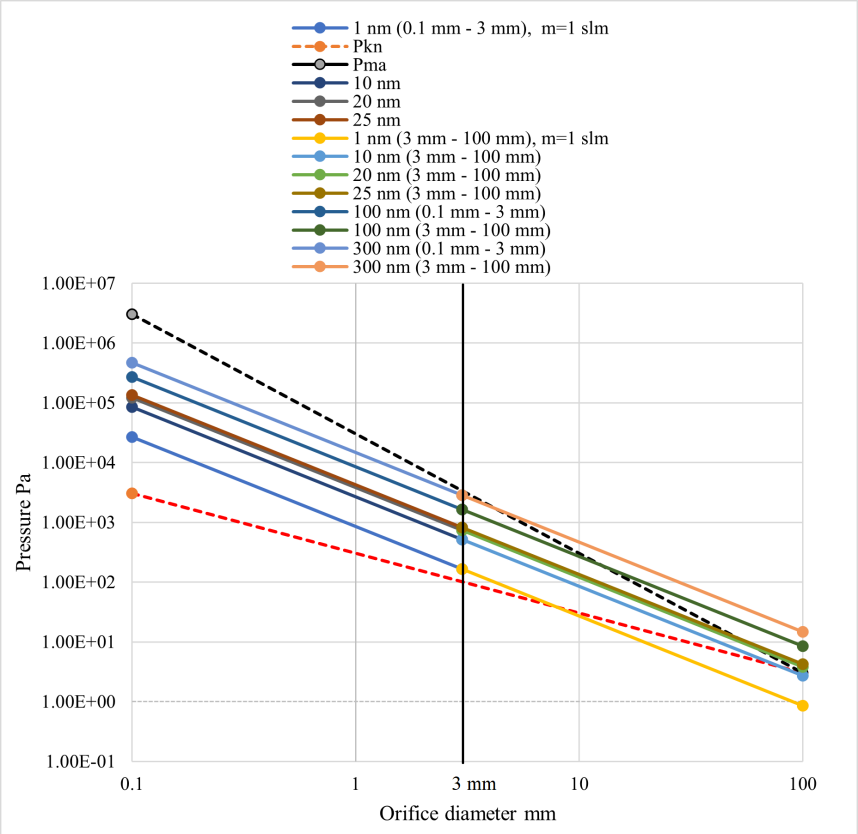

Figure 5.37: The $P_{focussing}$ curve with respect to particle sizes from 10 nm - 300 nm compared to the P_{ma} and P_{kn} curves for the diameter of the orifices 3 mm

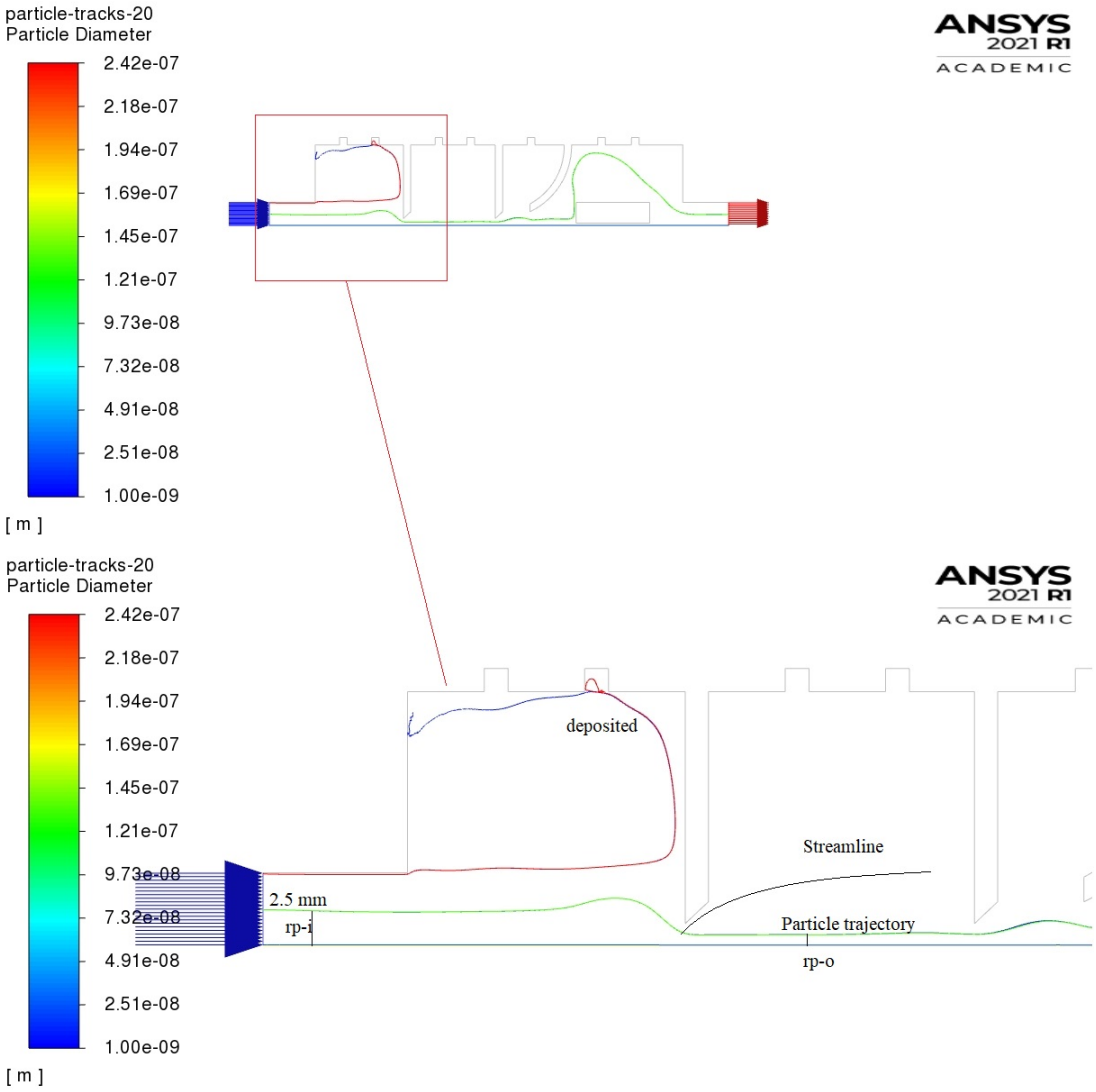

Figure 5.38: The critical particle trajectory and the critical streamline

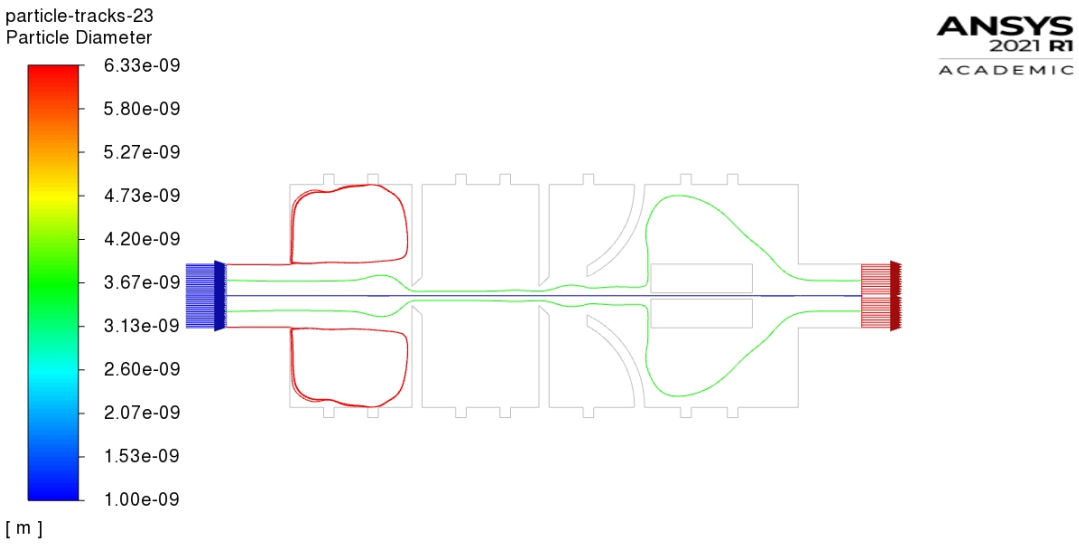

Figure 5.39: The particle moves radially outward downstream of the lens

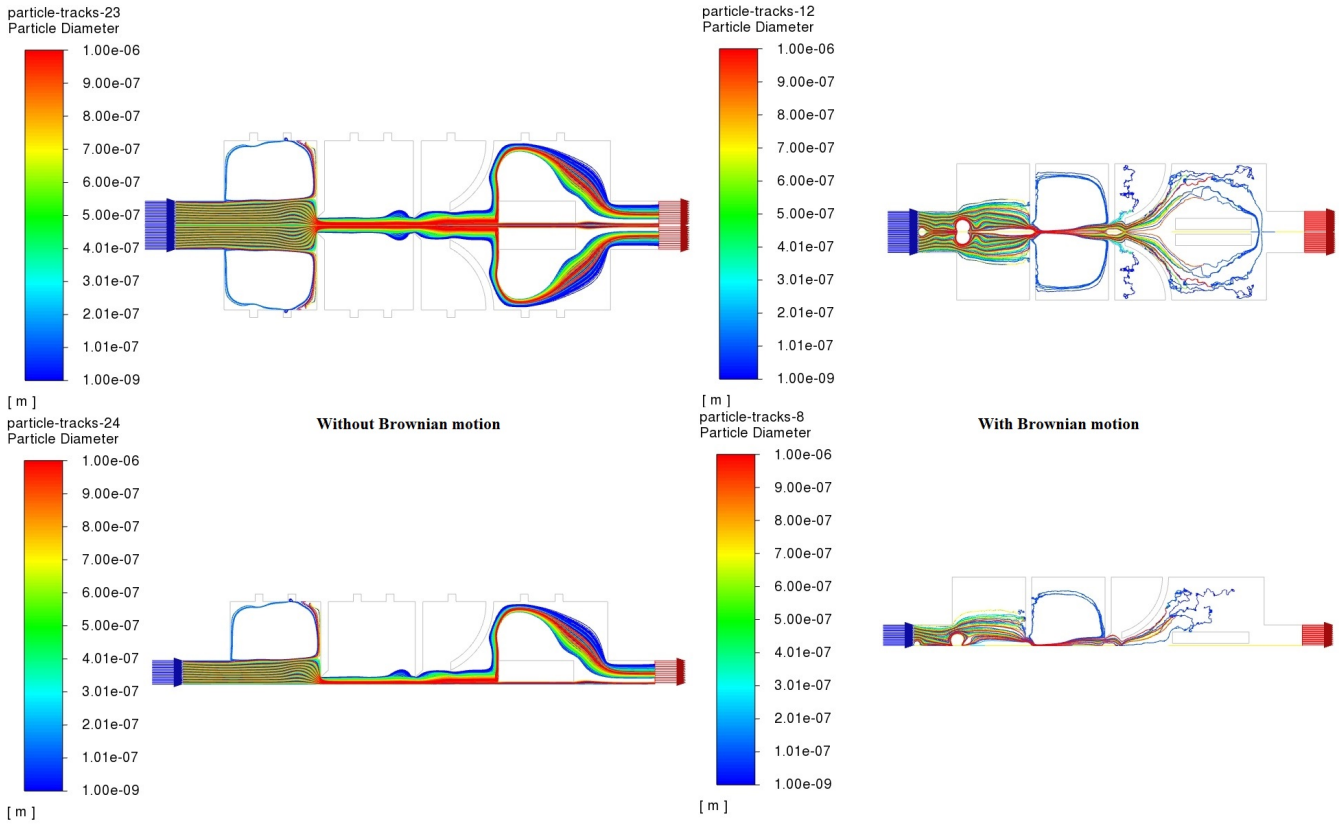

Figure 5.40: Trajectories of the spherical particles in the aerodynamic lens with or without Brownian force

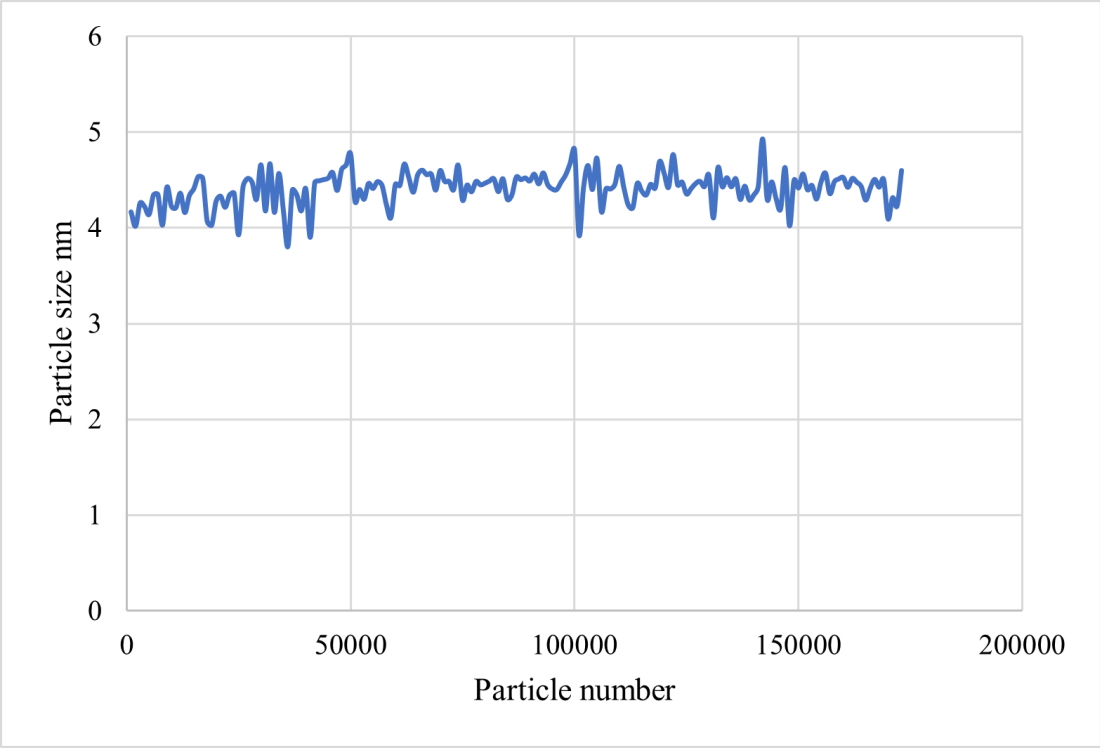

Figure 5.41: Results for reducing the particle size that can be focussed when the number of particles in the focus region is compared to the particle size that can be focussed [152]

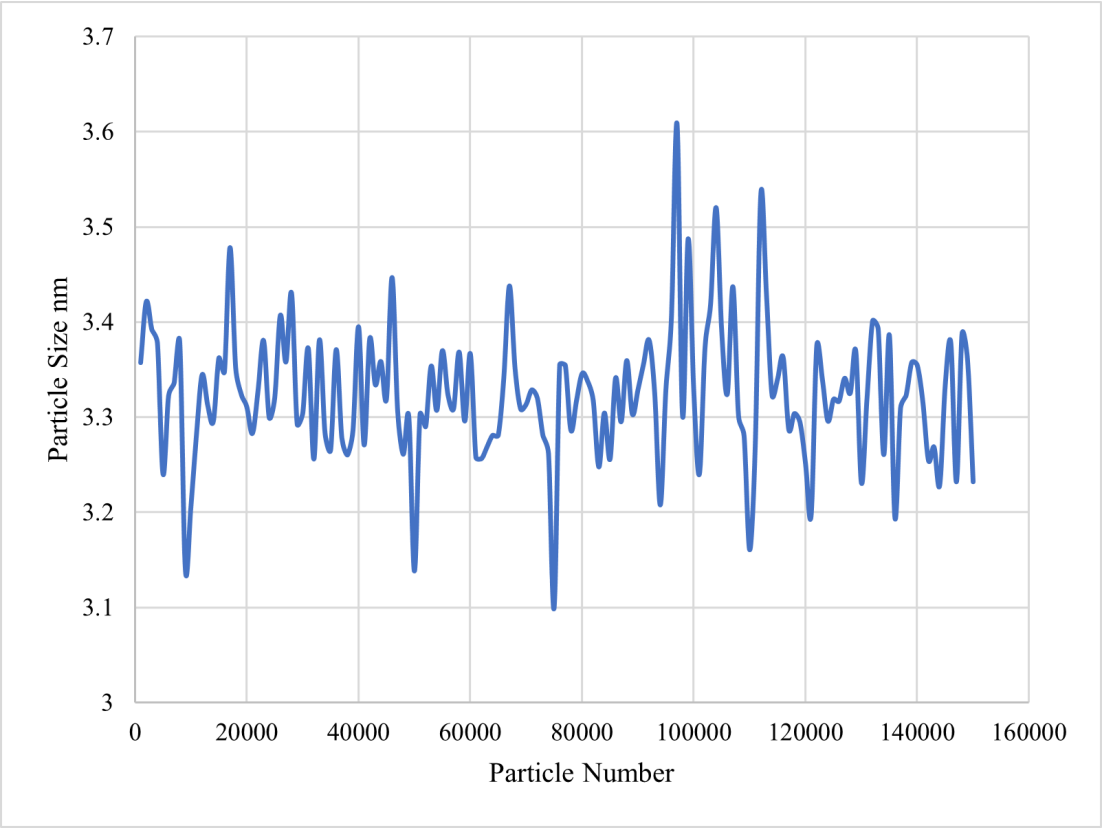

Figure 5.42: Examining the focus area at the aperture outlet to determine the smallest particle size that can be focussed precisely on the axis for this research

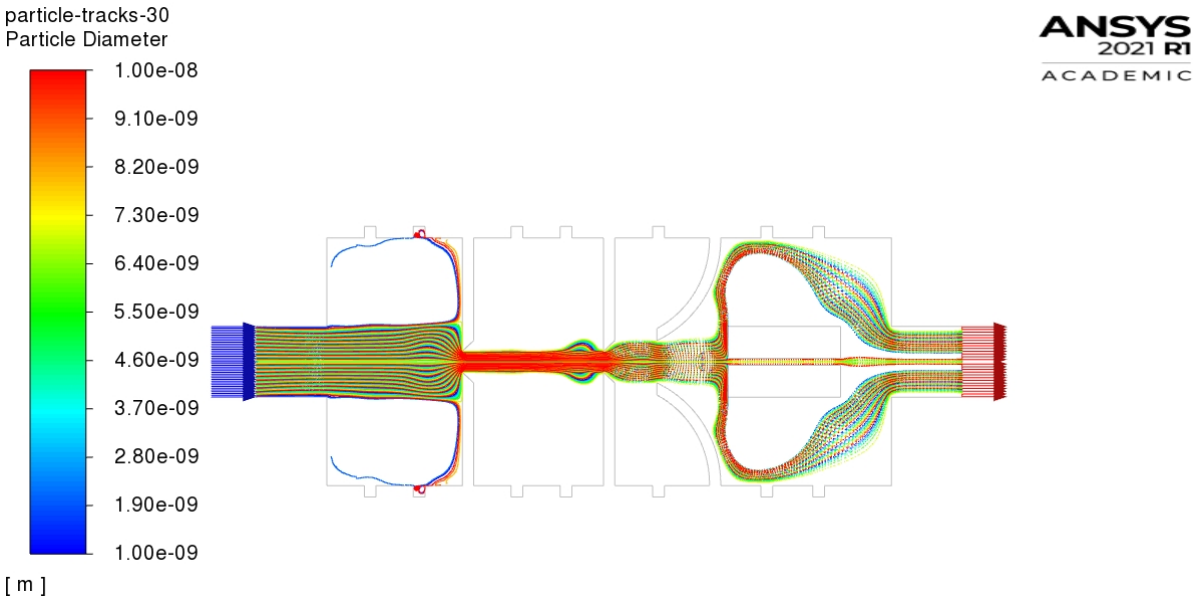

Figure 5.43: Focussing of 1 nm to 350 nm nanoparticles

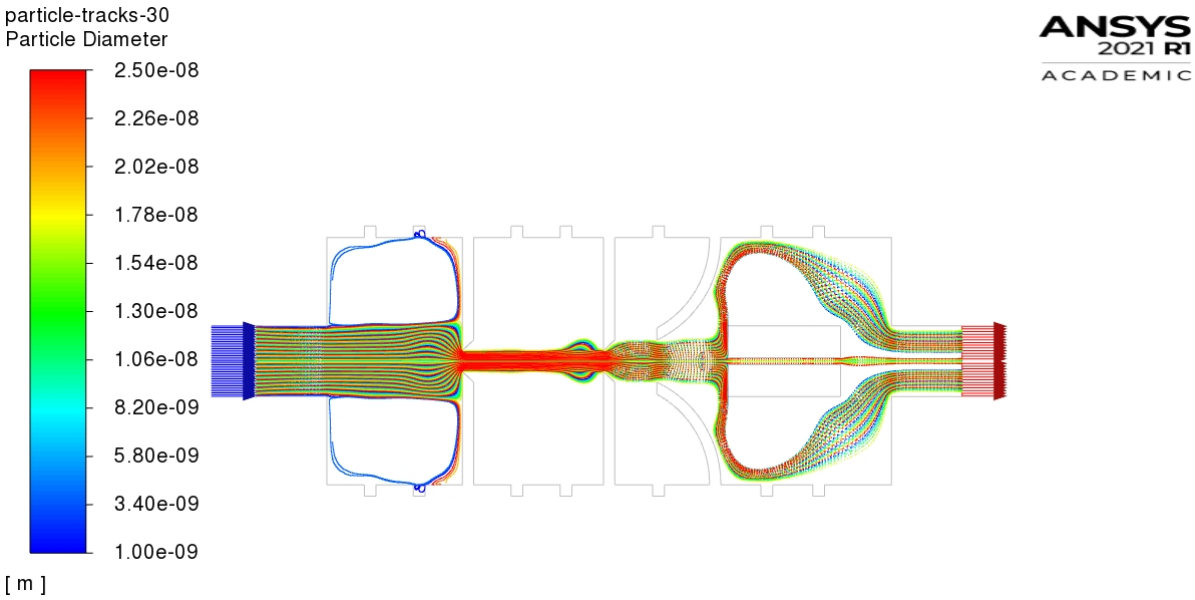

Figure 5.44: Focussing of 1 nm to 25 nm of nanoparticles

Chapter 6

Focussing of Airborne Particles in Aerodynamic Lenses Held by Grooves in the Pipe

6.1 Introduction

Nanoparticles suspended in the air are known as airborne nanoparticles [54]. In several aerosol measurement instruments, collimation of airborne particle beams to a narrow region with a low level of beam divergence is a desirable first step [52, 30, 92]. Collimated particle beams not only enable the efficient transport of aerosols to a narrow low-divergence area [166] but also ensure that the particles move through and into the centre of the focal point of the narrow area and toward the Faraday Cup electrometer (FCE) particle detectors. The use of aerodynamic focussing lenses [87, 88] or sheath air [25, 20] for the design and efficient achievement of collimated beams of aerosol particles in particle detectors has previously been documented. Sheath gas focussing of aerosol particles is a well-established method for focussing aerosol beams on large-scale aerosol devices with high flowrates ($>$ 1 L/min) [14, 19, 92]. The flow of the gas (sheath) and their method of injection (axial) have a very substantial influence on the speed of the par-

ticles and, consequently, on the size of the particles. The sheath gas adds additional stretching and focussing forces to the ejecting particles. Extending aerosol focussing to include the vertical direction represents success in addressing one obstacle standing in the way of the application of aerosol focussing with aerodynamic lenses.

An aspect of the research conducted for this thesis led to the development of a method for producing varied shapes of aerodynamic lens systems based on the incorporation of grooves within the pipe to create miniaturized, inexpensive, and compact lab-on-a-chip devices for monitoring aerosols and gases [30, 112, 92]. This chapter describes the design, evaluation, and computational simulation of an aerodynamic lens system that incorporates these grooves within the pipe to hold the orifices, inlet, and outlet lenses mounted for focussing airborne particles in the air. This device permits the location of the lenses to be adjusted within the pipe if they need to be moved to the left or right, and also allows additional lenses to be added or one lens to be used for the entire pipe employed in an experiment. As well, if required for a particular study, a longer or shorter pipe can be obtained by moving the inlet and outlet lenses from one groove to another, without the need to fabricate another pipe of the right length [92] as illustrated in Figure 6.1. This is a good method because it saves time and money and has also been proven to decrease particle loss by minimizing the openings or sections between the model components.

The new model is composed of two parts: the upper half of the pipe with grooves and eight holes for fitting threaded rods (Figure 6.2) and the lower half of the pipe, which also contains grooves and threaded rod holes. These two parts are screwed together, with a gasket around the inside of the pipe to ensure that fluid does not escape from the pipe.

Gaskets are also installed before and after each orifice plate in order to maintain a constant pressure between the plates, thus ensuring the enhanced reliability of the results. ANSYS Fluent 2021R1 software was used

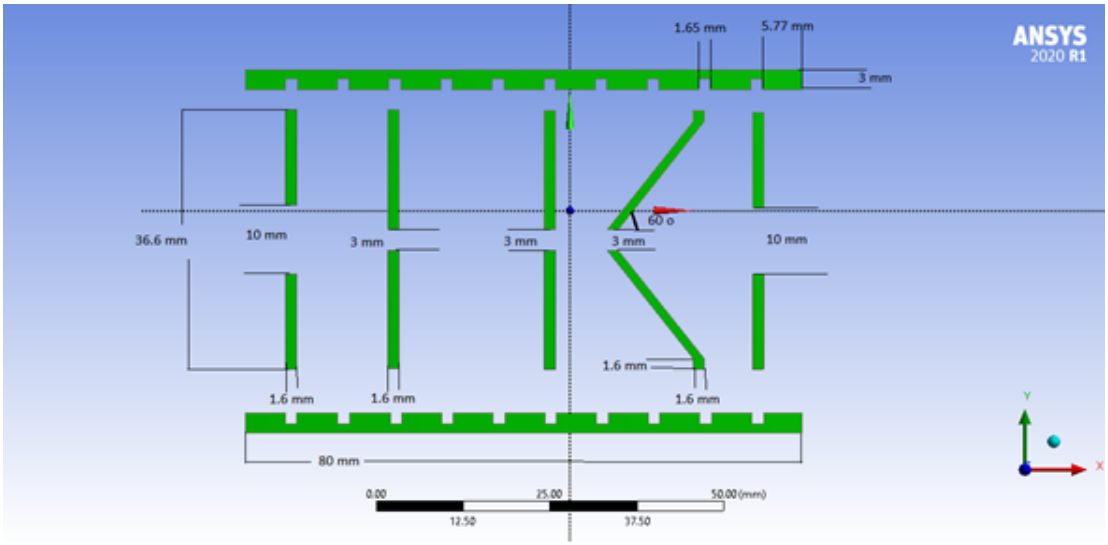

Figure 6.1: Use of grooves within the pipe to hold the orifices, inlet, and outlet lenses

to simulate this model for focussing the aerosols in the main flow through a narrow beam that passes through the focal point in the middle of the lens and is confined to the centre of the FCE particle detector. No previous studies have examined or implemented grooves within the pipe to hold the orifices [92], which makes this new model design an important contribution to this research. The use of these grooves within the pipe for focussing aerosol particles in an aerodynamic lens system has been demonstrated in this study. This chapter details the design process and presents the computational results of the simulation of the designed prototype with aerosolized monodispersed spherical carbon particles, which confirmed the validity of the flow-focussing system, as described in the previous chapter.

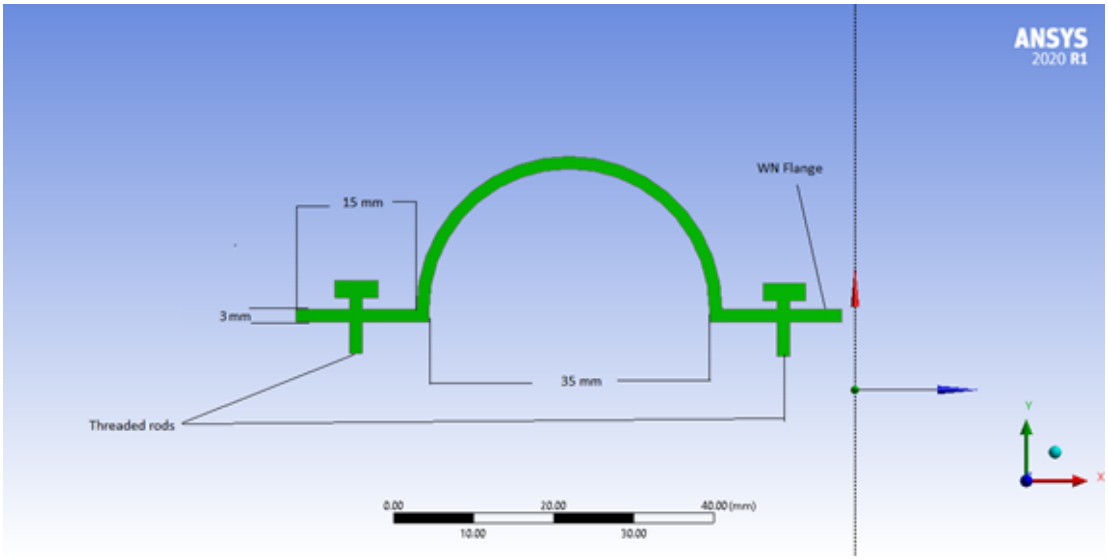

Figure 6.2: Upper half of the pipe with grooves

6.2 Materials and Methods

6.2.1 Aerodynamic Lens Stack

An aerodynamic lens stack is a particle injector that compresses aerosol particles into a collimated beam [87]. As shown in Figures 6.3 and 6.4, such a lens stack consists of several axisymmetric contractions in a pipe. The aerosol travels through these lenses together with a lighter carrier gas (e.g., air). While the carrier gas quickly expands after each contraction, the heavier aerosol particles tend to stay closer to the centre of the flow field. The flow field of a light carrier gas (lines) and the trajectories of particles with different masses (points) are shown in Figure 6.4.

The mass of the particles determines the focussing effect of this type of lens. The particles in the top rectangle of the Figure are lighter than the optimal mass, so they follow the flow field, resulting in only a minimal focussing effect. The trajectories of the particles with the optimal mass can

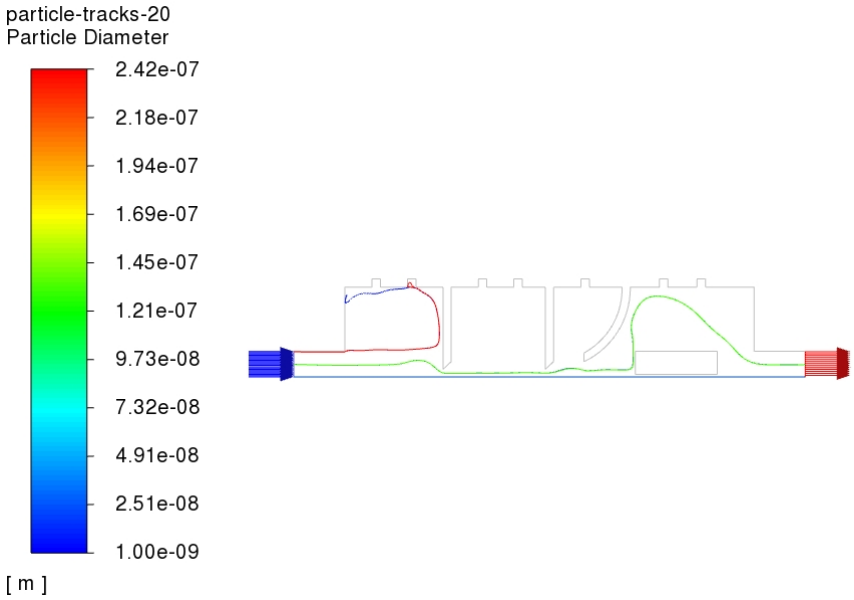

Figure 6.3: Aerosol travelling through the lenses together with a lighter carrier gas, such as air

be seen in the middle portion of the Figure. The bottom section of the Figure represents the trajectories of heavy particles that interact with the walls of the lens, resulting in low levels of particle distribution efficiency and no focus. To appreciate the effect of this contraction on the focussing, it should be understood that the only force acting on the aerosol particles is the drag force:

$$\frac{\overrightarrow{dU}_p}{dt} = \frac{\overrightarrow{U} - \overrightarrow{U}_p}{\tau} \tag{6.1}$$

Where $\overrightarrow{U}_p$ is the particle velocity, $\overrightarrow{U}$ is the velocity of the flow field, and τ is the relaxation time (the time constant in the exponential decay of the particle velocity due to drag). This approximation neglects the effects of lift forces and Brownian motion and can be used when the local Reynolds number does not exceed a few hundred. The Reynolds number is the ratio

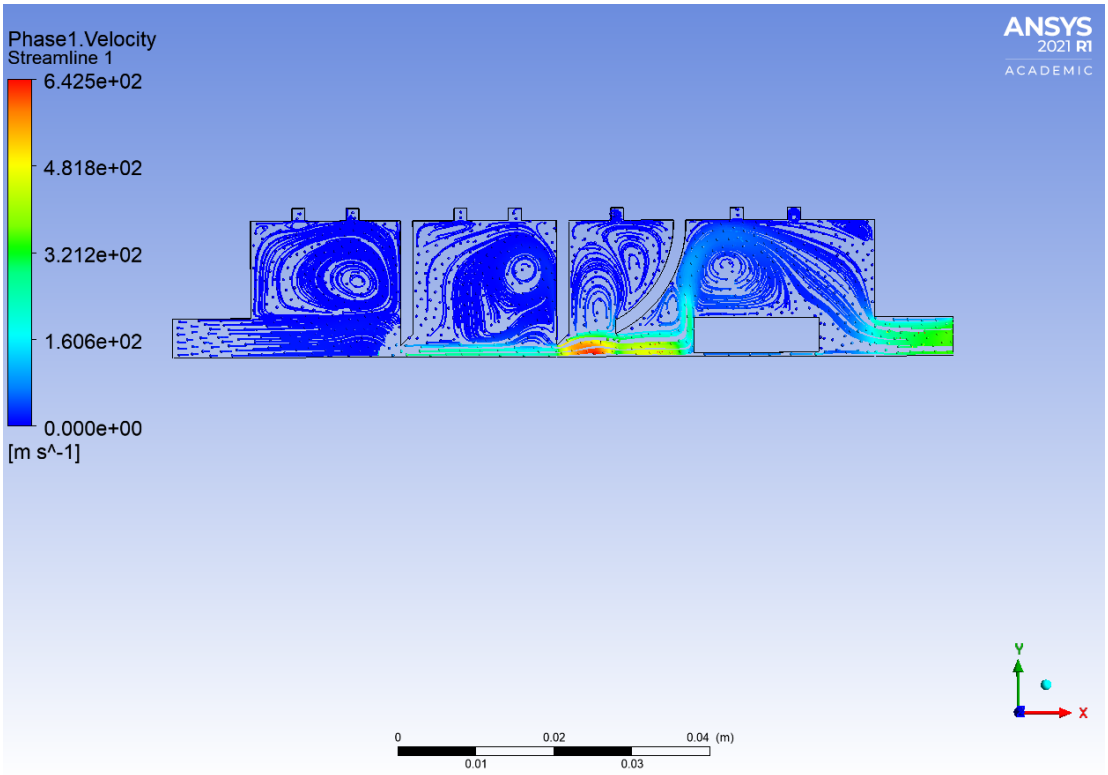

Figure 6.4: Flow field of a light carrier gas (lines) and the trajectories of particles with different masses (points)

of the inertia of a fluid to its viscosity. Low Reynolds numbers correspond to a high degree of viscosity compared to the inertia, which leads to a laminar flow.

6.2.2 Aerodynamic Focussing Using Grooves inside the Pipe

A velocity field is created by the inclusion of geometric features in the pipe, such as grooves and threaded rods, which add a pressure gradient in the direction perpendicular to the direction of the flow [92] (Figure 6.5). As a result of this effect, the airflow inside the lenses can be rearranged as a result.

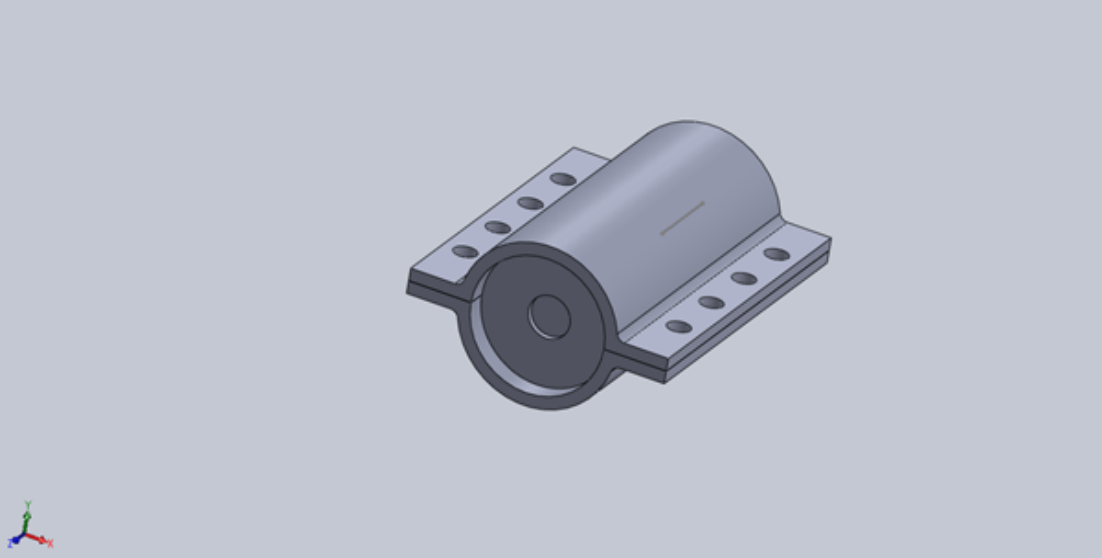

Figure 6.5: Pipe with grooves and eight holes to fit threaded rods

For lenses to work effectively, inertial effects in the flow must be minimal; it must be a laminar flow. Due to the viscosity of air and particles, the fluid tends to adhere to the wall. So, the flow is laminar because the layers do not mix in this type of fluid flow. At sufficiently low Reynolds numbers, Re, only the equilibrium between the viscous and pressure forces determines the velocity field, as defined in Equation 6.2 [92]. The dimensionless Reynolds number, Re, measures the ratio of inertial to viscous forces and is defined in [54, 92] as:

$$Re = \frac{\rho \ u \ l}{\mu} \tag{6.2}$$

where ρ represents the density, μ indicates the dynamic viscosity, u signifies the flow speed, and l denotes the length scale. A theoretical study of the geometrical function and pressure force, and thus the velocity field introduced by them, is impractical due to the complex collection of boundary conditions needed for solving Navier-Stokes equations [92]. Figure 6.6

depicts a three-dimensional CAD model of the grooves inside the pipe for holding the lenses and nozzles.

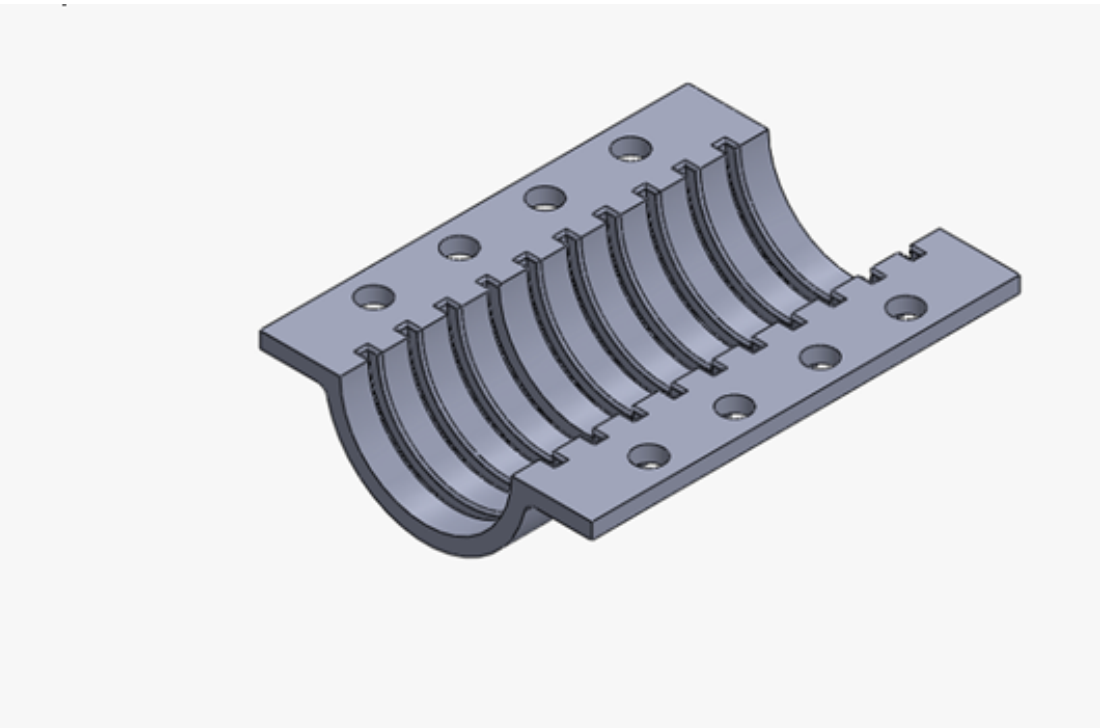

Figure 6.6: Three-dimensional CAD model of the grooves inside the pipe for holding the lenses and nozzles

The developed system incorporates multiple grooves for adjusting the positions of the lenses in order to obtain the optimal particle size measurements, i.e., establishing the smallest particle size. These grooves also facilitate the acceleration and initial concentration of the main flow into the base of the lenses. The sheath coming from the inlet port then squeezes the main flow. Grooves are etched deep into the top and bottom of the pipe. The outlet port is the point at which the central beam of particles exits the lenses. In this study, the first step was to employ ANSYS Fluent to perform a CFD simulation of the pressure-driven flow inside the system. For the particle trajectory tracing, the CFD model considered viscous, iner-

tial, drag, and Brownian forces. The resulting velocity field was applied to determine the trajectories of particles subjected to drag and inertial forces using a Newtonian particle-tracing algorithm.

The drag force F_{drag} and Brownian force F_{Br} were the main forces examined [42]. Despite not including all of the possibilities, this list highlights the majority of the forces that can affect particle trajectories.

6.2.3 Designing Aerodynamic Lens Systems for Focussing Nanoparticles

The research for this thesis included consideration of the challenges associated with the focussing of nanoparticles of sub-300 nm into tightly collimated beams. Because of their low inertia and high degree of diffusivity, sub-300 nm particles are difficult to focus. Their low inertia means that nanoparticles tend to follow gas streamlines very closely, with only slight focussing possible, and as particle size decreases sub-300 nm, focussing performance is degraded even further. This research therefore included an examination of a case study involving the design of an aerodynamic lens for focussing particles smaller than 300 nm, with diffusion being neglected. The aerodynamic lens system under investigation consisted of three components: a flow control orifice, focussing lenses, and an acceleration (divergent) nozzle, as illustrated in Figure 6.7.

The inlet orifice fixes the mass flowrate of the device and reduces pressure from ambient to the level required for aerodynamic focus. The focussing lenses are a pair of orifices that produce converging-diverging flow accelerations and decelerations, allowing particles to be separated from the carrier gas and guided into a tight particle beam [154]. The second lens controls the operating pressure inside the lens assembly and accelerates the particles downstream. This system focusses the aerosol flow with the use of two aerodynamic lenses (sharp-edged plates) for focussing the particles at the

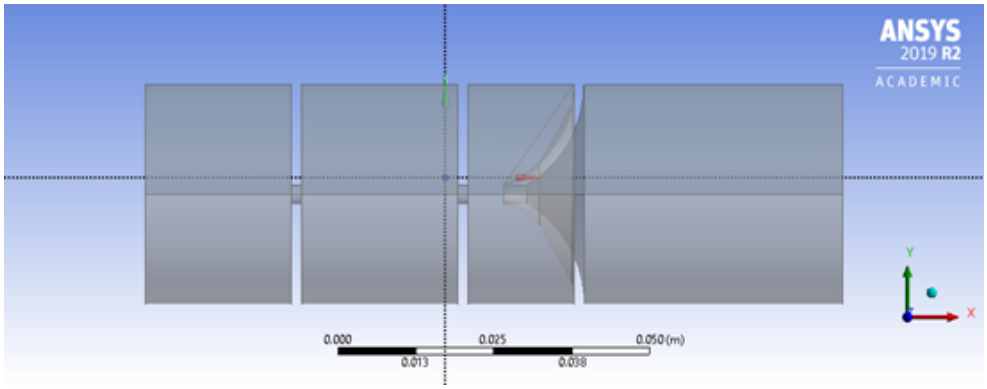

Figure 6.7: The three components of the aerodynamic lens system

centreline of the exit nozzle. The focus of this particular study, however, was on airborne nanoparticles with diameters smaller than 300 nm. Figure 5.11 provides a schematic representation of the aerodynamic lens-nozzle configuration used in this study, which demonstrates how two lenses and one divergent nozzle can be used to effectively transfer the particles into the vacuum. ANSYS Fluent can predict particle trajectories through the lens for spherical particles with diameters of less than 300 nm where the inlet boundary conditions are: flowrate of $2.98{*}10^{-7} kg/s, 1 Pa pressure$.

ANSYS Fluent CFD was employed for calculating the gas-particle flow field in an aerodynamic lens-nozzle expansion and generating a grid. ANSYS Fluent can simulate the full spectrum of subsonic, transonic, and supersonic flows in an aerodynamic lens-nozzle inlet without reliance on significant assumptions such as constant entropy or incompressibility [162]. A typical calculation of the low-speed flow in a lens requires approximately 2–4 h, and it takes about 10 h to complete the high-speed flow in the nozzle. An objective of this study was to acquire a basic understanding of the factors that impact a fluid (air) containing nanoparticles (carbon) with diameters varying from 3 nm to 300 nm as the particles pass through two lenses and one divergent nozzle. The particles are impelled into the centreline by the first two orifices, and particle acceleration into the vacuum field is regulated

by the final exit nozzle, which produces a supersonic gas expansion. During the final expansion, particles are characterized by a distribution of terminal velocities that is dependent on particle diameter, with smaller-diameter particles accelerating to higher velocities and larger-diameter particles accelerating to slower velocities [162]. Instruments employed in conjunction with aerodynamic lens systems can calculate nanoparticle diameter based on measurements of the terminal velocity of the particles.

6.3 Computational Analysis of Aerodynamic Lenses

Computational simulations were performed for specific basic but practical flows in order to evaluate the effects of nanoparticles and their trajectories away from the axis. This research was concentrated on the lens system and nozzle geometry illustrated in Figure 6.7, in which fluid flows into a pipe with an inner diameter of 35 mm and a length of 80 mm and through the lenses and a nozzle with an inner diameter of 3 mm. This section first introduces the CFD measurement and calculation methods and then explores the characteristics of particle motion in the lens-nozzle system. A dilute suspension of particles in an ideal gas was assumed, which translates into negligible particle-particle interactions and no effect on the gas flow. The flow field was established based on the computational solving of the continuity, momentum, and energy equations related to ideal gases. CFD analysis was applied for the simulations performed in this study, with priority given to compressible flows. The initial analysis revealed that the results obtained under the computational conditions employed for this study did not vary substantially from those reported by Liu et al. [87]. The flow field for a given lens-nozzle geometry was specified according to the Reynolds number of the lens, Re, and the Mach number of the lens, M, which can be classified as follows:

$$Re = \frac{\rho\, U d_f}{\mu} \tag{6.3}$$

$$M = \frac{U}{c} \tag{6.4}$$

Where μ signifies the fluid viscosity, ρ indicates density, c represents the speed of sound , d_f denotes the orifice diameter, and U designates the velocity of the flow at the orifice. After the flow field was obtained, the forces acting on the materials were added to the calculations, and the trajectories were computed numerically based on the combining of the calculations to give Equation 6.5:

$$\frac{\overrightarrow{dU}_p}{dt} = \frac{\overrightarrow{U} - \overrightarrow{U}_p}{\tau} \tag{6.5}$$

The dynamic properties of the particles were calculated for a given flow field according to the Stokes number St and the Knudsen number of the particle Kn_p or based on the Reynolds number of the particle Re_p, which can be characterized as follows:

$$St = \frac{U\tau}{d_n} \tag{6.6}$$

$$Kn_p = \frac{\lambda}{d_p} \tag{6.7}$$

$$Re_p = \frac{\rho d_p U}{\mu} \tag{6.8}$$

Where τ is the particle relaxation time, λ is the molecular mean free path of the fluid, and d_n is the nozzle diameter. A diameter of $d_n = 3$ mm was

chosen for the divergent nozzle. The following concept measurements were determined: an estimated mass flowrate of the air at $2.98{*}10^{-7}$ kg/s and the density of the carbon particles at 1.48 g/cm^3, with the particle diameters varying from 3 nm to 300 nm, all of which corresponded to the values used in the simulations performed for this study. Based on the results from previous research, it is evident that the geometry of the divergent nozzle is a critical factor in the control of particle focussing.

The nozzle in the system under study was a divergent nozzle with a radius of 15 mm from the front of the nozzle and a thickness of 1.6 mm, which was installed immediately downstream from a sharp-edge plate orifice with a hole diameter of 3 mm. The nozzle diameter, d_n, was kept constant at 3 mm for all of these calculations, and the diameter of the inlet of the pipe was set at 10 mm. The divergent nozzle balances particle acceleration inward with particle acceleration outward into the nozzle stream, resulting in a short, low-divergence beam. In this study, the diameter of the divergent nozzle was measured immediately upstream from the nozzle and was found to vary from 2 mm to 9 mm. For these calculations, to avoid particle loss, the FCE was mounted quite close to the nozzle opening. Figures ref 6.8 and 6.9 show the results.

The computed near-axis particle trajectories in the divergent nozzle are indicated in Figure 6.9 for a variety of nozzle diameter d_n values. Negative values in both this Figure and Figure 6.8 indicate that the particle has passed close to the axis. According to Figure 6.9, the best overall performance is provided by a nozzle with a $d_n = 3$ mm, meaning that a divergent nozzle with $d_n = 3$ mm should be the optimal configuration. Figure 6.10 depicts the axial velocities calculated for particles in a variety of nozzle geometries. These findings were integrated into the concept measurements that followed.

This research has involved an exploration of the theoretical and computational aspects of a modern approach for focussing nanoparticles. The de-

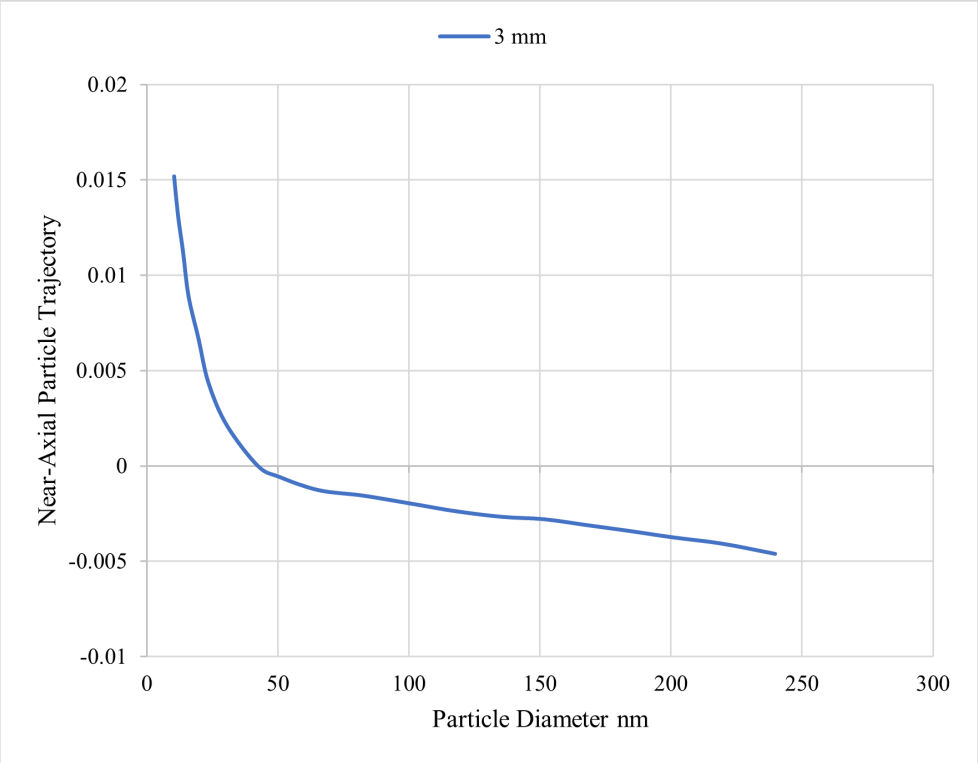

Figure 6.8: For the given 3 mm nozzle geometry, the near-axis particle trajectory plotted against particle diameter

veloped system incorporates two aerodynamic lenses for confining nanoparticles to the midline of an aerosol flow once a divergent nozzle generates a particle beam. These lenses were constructed based on an axisymmetric design that produces convergent-divergent flow accelerations. The use of these multiple lenses enables nanoparticles to be moved very close to the axis after passing through a lens.

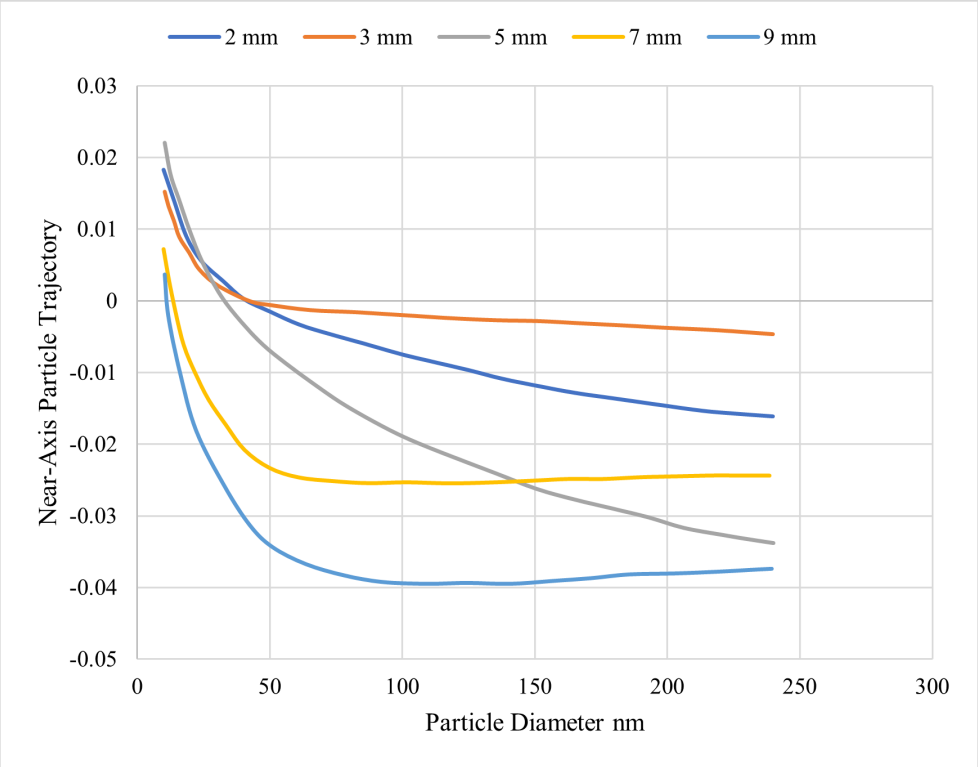

Figure 6.9: For the given nozzle geometry, near-axis particle trajectories plotted against particle diameter, for divergent nozzle diameters varying from 2 mm to 9 mm measured immediately upstream from the nozzle

6.4 Experimental Setup and Procedure

The usual method for fabricating aerodynamic lenses requires considerable time and effort in order to produce them with the appropriate shape for focussing nanoparticles. For each experiment, researchers must fabricate a new model in case the lens needs to be repositioned inside the pipe. This fabrication process creates delays and also increases financial expenses due to the frequent need to fabricate several versions of the lenses and pipe. For this reason, a component of this research was the design of a new, versatile, time-and cost-saving method for experimental focussing and size

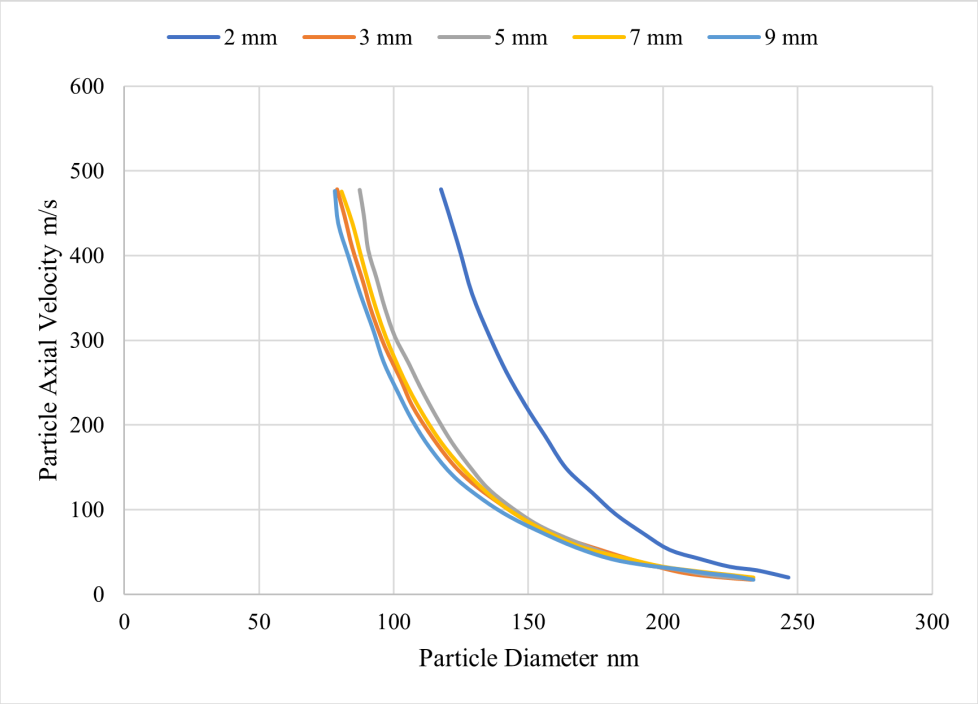

Figure 6.10: Axial velocity (m/s) of particles by particle diameter in divergent nozzles with varying nozzle diameters

measurement of nanoparticles. As mentioned previously, this novel model is a pipe that contains inside grooves that match the diameter and thickness of the lenses used for focussing the nanoparticles. As explained, the benefit of these grooves is that they enable the position of the lenses inside the pipe to be modified in case the lens must be moved to the left or right, or other lenses need to be added, or only one lens for the same pipe is required in the experiment. This design also permits the lenses to be used at the inlet or outlet. As well, depending on the length of the pipe and the number of grooves inside it, the new pipe can also be used as either a long or a short pipe.

6.5 Calculation Results

Figures 6.11, 6.12 and 6.13 show the velocity contour, Mach number contour, and velocity vectors, respectively. As can be seen in these Figures, when air passes through a small hole in the lens, it usually creates a free flow, which moves along the downstream fluid. The velocity is at its maximum, and the boundary layer separation can be seen near the lens edge in the downstream direction. The approaches employed for modelling lens flow capture the flow pattern extremely effectively [127]. The findings of this investigation are similar to those reported in [87, 97].

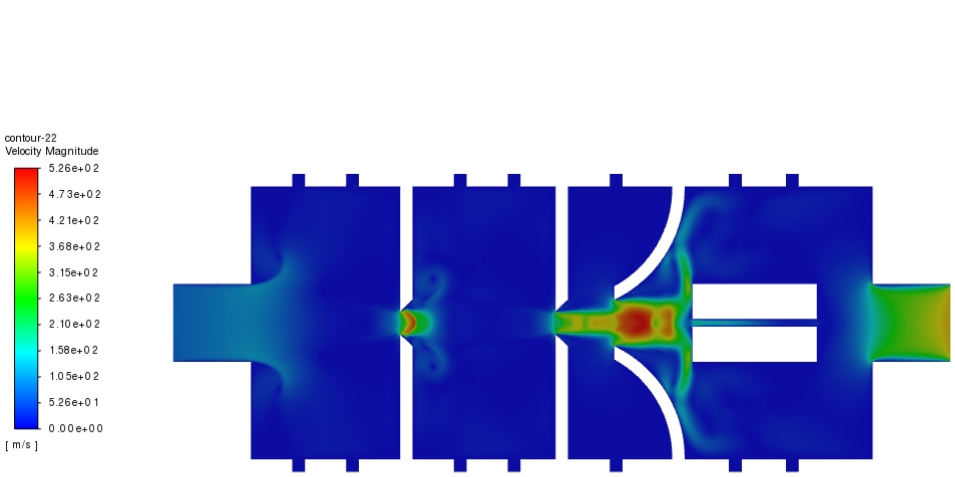

Figure 6.11: Magnitude of the fluid velocity - Velocity contours

Contours of the velocity upstream from the lens are shown in Figures 6.14. The non-slip condition caused a considerable reduction in the velocity near the wall of the pipe. When this region is very small, it is referred to as the boundary layer. The boundary layers thicken of the pipe as more fluid is impacted by the viscous friction generated by the gradients produced as

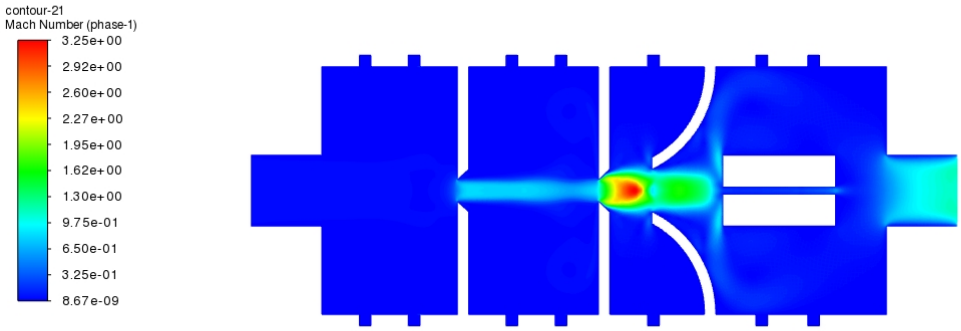

Figure 6.12: Mach number contours

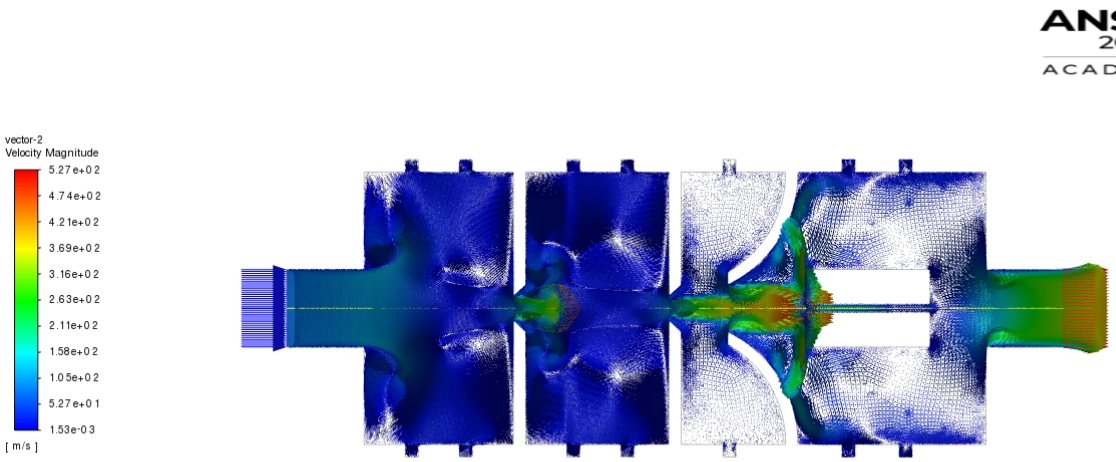

Figure 6.13: Magnitude of the fluid velocity - Velocity vectors

a result of the non-slip condition [147]. The entire laminar flow is produced upstream from the lens, as indicated in Figure 6.11, which is an indication that the length selected was appropriate for the upstream pipe [127].

Figure 6.14: Contours of the radial velocity upstream from the lens

When the flow enters the throat of the lens, the centreline axial velocity increases. The maximum velocity was demonstrated at the vena contracta, with the velocity decreasing after that point. Because the pressure enables the energy to be conserved at all locations in the domain, as can be seen from Figure 6.15, the pressure dropped as the flow entered the lens and reached a minimum at the vena contracta, following which it continued to rebound as the flow proceeded downstream. These observations were confirmed based on a comparison with the results given in the review published by [97].

Figure 6.15: Static pressure of the fluid

6.6 Summary

This chapter has presented the use of designed grooves inside the pipe for holding the lenses in order to focus airborne particles. The pressure on the main flow caused by the gas flow from the inlet of the orifices led to a horizontal focus [92]. The focussing was extended to the vertical direction by placing the lenses in grooves engraved in the top and bottom sections of the pipe. The grooves were formed by a unique delayed-etch design process that is also compatible with the construction of divergent nozzles and lenses, thus facilitating their incorporation into the pipe, as illustrated in Figure 6.16. Pressure, particle loss, and particle size were applied as metrics for assessing the performance of the new system. ANSYS Fluent was used for modelling and investigating particle distribution, and CFD was employed for simulating a lens in a pipeline and for approximating the position of the vena contracta [127]. In flowmetry research, consideration of

the effects of ratio on flow mechanics, such as the vena contracta position, the characteristic length, and measurements of the velocity of the lens flow, is regarded as essential. CFD technology was also considered to be a cost-effective alternative to experimental methods for measuring the discharge coefficient.

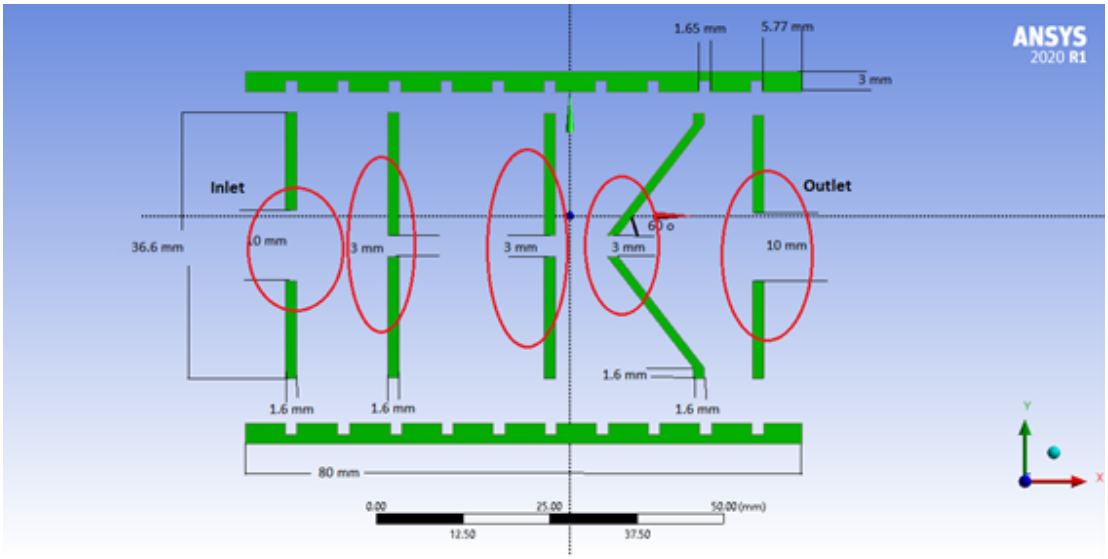

Figure 6.16: Grooves fabricated using a novel delayed-etch technique also consistent with the fabrication of divergent nozzles and lenses

The test data validated the efficacy of using lenses and a divergent nozzle to focus particles in a horizontal direction. Because the number distribution of particles less than 3 nm cannot be resolved based on ANSYS Fluent code sampling, the effect of diffusion with respect to degrading the performance of the lenses and nozzle for focussing nanoparticles cannot be measured. Future studies should focus on the influence of the particles' resident time in the tube, as well as their diffusion, on lens performance in a longer tube.

Chapter 7

An Experimental Study of Nanoparticle Focussing with an Aerodynamic Lens and a Divergent Nozzle

7.1 Introduction

Recent advances in the field of nanotechnology have highlighted the importance of the ability to measure nanoparticles, which is a critical element in this area [83]. Electrically charging the nanoparticles is one method for controlling their transport and deposition, [128] and is typically required for managing submicron and nanometer-size particles in aerosol technologies. A number of approaches for measuring nanoparticle size in a laboratory setting have been developed:

1. **Scanning** mobility particle sizer (SMPS+E) (0.8 nm to 1100 nm) [44].
2. **Fast** mobility particle sizer (FMPS) (5.6 nm to 560 nm) [85].
3. **Engine** exhaust particle sizer (EEPS) (5.6 nm to 560 nm) [99].

4. **Nanometer** aerosol size analyzer (NASA) (3 nm to 100 nm) [50].

A scanning mobility particle sizer (SMPS+E) can provide precise particle size measurements down to a couple of nanometers within 3 to 5 minutes for a single measurement. SMPS+E also employs a differential mobility analyzer (DMA) for classifying nanoparticles based on their electrical mobility after they pass through a bipolar charger [140]; DMA performance is mostly limited to 0.8 nm to 1100 nm nanoparticles characterized by low levels of charging efficiency. SMPS+E uses a combination of a Faraday cup electrometer (FCE) and an electrometer to measure the distribution of the particles according to their charges. An FCE can be utilized for evaluating nanoparticle focussing under different operating conditions, including establishing the effects of aerosol flowrate, particle type, particle shape, and particle concentrations. The focussed particles are then passed through an orifice into an aerodynamic lens system, and the effects of particle focussing with an aerodynamic lens can be investigated. However, extending the same approach to the focussing of sub-300 nm nanoparticles with an aerodynamic lens and developing a procedure for designing aerodynamic lens systems for such small nanoparticles has proven challenging.

By finding available experimental results for a model with a range of particle sizes similar to the range of particle sizes that this research focuses on (sub-300 nm), then comparing these experimental results with the computational results of this research, Tan & Wexler (2007) [138] worked on a range of particle sizes of 25 nm to 300 nm using a single aerodynamic lens but with a tube length of more than 600 mm. And since the experimental setup used in Tan & Wexler's research is the same as in our research except for the number of aerodynamic lenses and tube length (Figure 7.1), the good thing here is that they conducted experiments for particle sizes ranging from 25 nm to 300 nm (which are the same sizes of particles that will be studied in this research). So, in this research, it will be conducted

to validate the results of Tan & Wexler (2007) [138], then the experimental results will be compared with the computational results obtained from the ANSYS Fluent simulation of two aerodynamic lenses and one divergent nozzle.

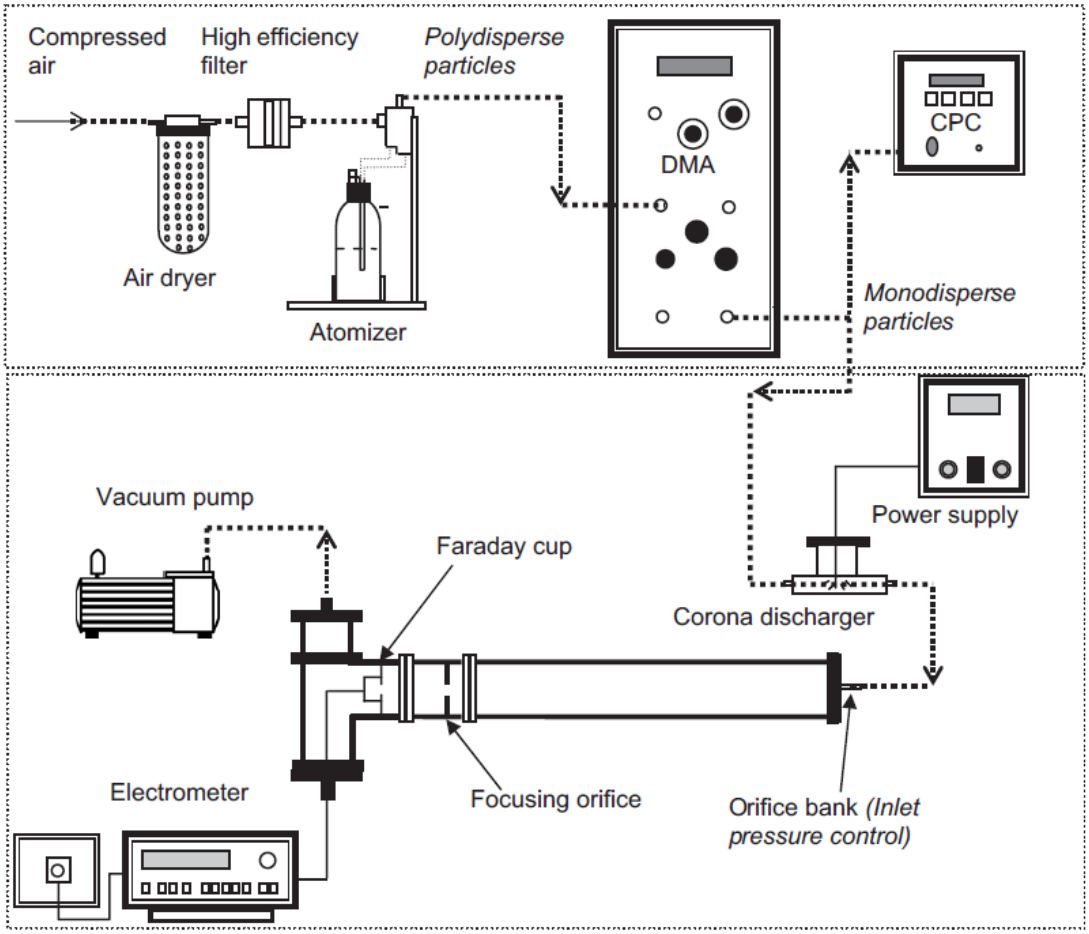

Figure 7.1: Experimental setup in Tan & Wexler's research [138]

With the goal of resolving the issues associated with the focussing of sub-300 nm nanoparticles with an aerodynamic lens, this research included the development of a two-part system: a particle-focussing system, and a method for measuring particle size. A new lens, consisting of two sharp-

edged plate orifices and one divergent nozzle, was designed computationally. An important phase of the research was to implement an experimental setup in order to facilitate laboratory experiments targeted at examining and confirming the success of the new aerodynamic lens design.

7.2 Experimental Method

7.2.1 Focussing Section

The experimental setup employed for evaluating the performance of an aerodynamic lens for the purposes of this research is illustrated in Figure 7.2.

Particles were generated by an aerosol generator, which was either a tube furnace or an electrospray, and then charged using a unipolar charger. A nanoparticle DMA (TSI 3085 Nano-DMA) was employed for selecting charged particles within a narrow range of electric mobility [153]. The concentration of these singly charged "monodisperse" particles exiting the DMA was measured with an FCE. After replicating the Tan & Wexler models experimentally, a choking orifice was utilized during one of the measurements, which served as the concentration point that enabled the selection of particles to be directed into the FCE. The conceptual design of the focussing sections and the reduction in pressure is depicted in Figure 7.3. To enable the aerodynamic focussing of particles of a given size, the velocity of the gas in the focussing orifice c should reach the speed of sound [138]. The new system is the only flow system developed thus far that enables specific degrees of focussing to be observed [28, 93]. If the absolute pressure ratio is at least 0.528 (Equations 7.2 and 7.3), the airflow reaches the speed of sound [63], which can be calculated accurately, based on an assumption of the ideal gas condition, as in Equation 7.1:

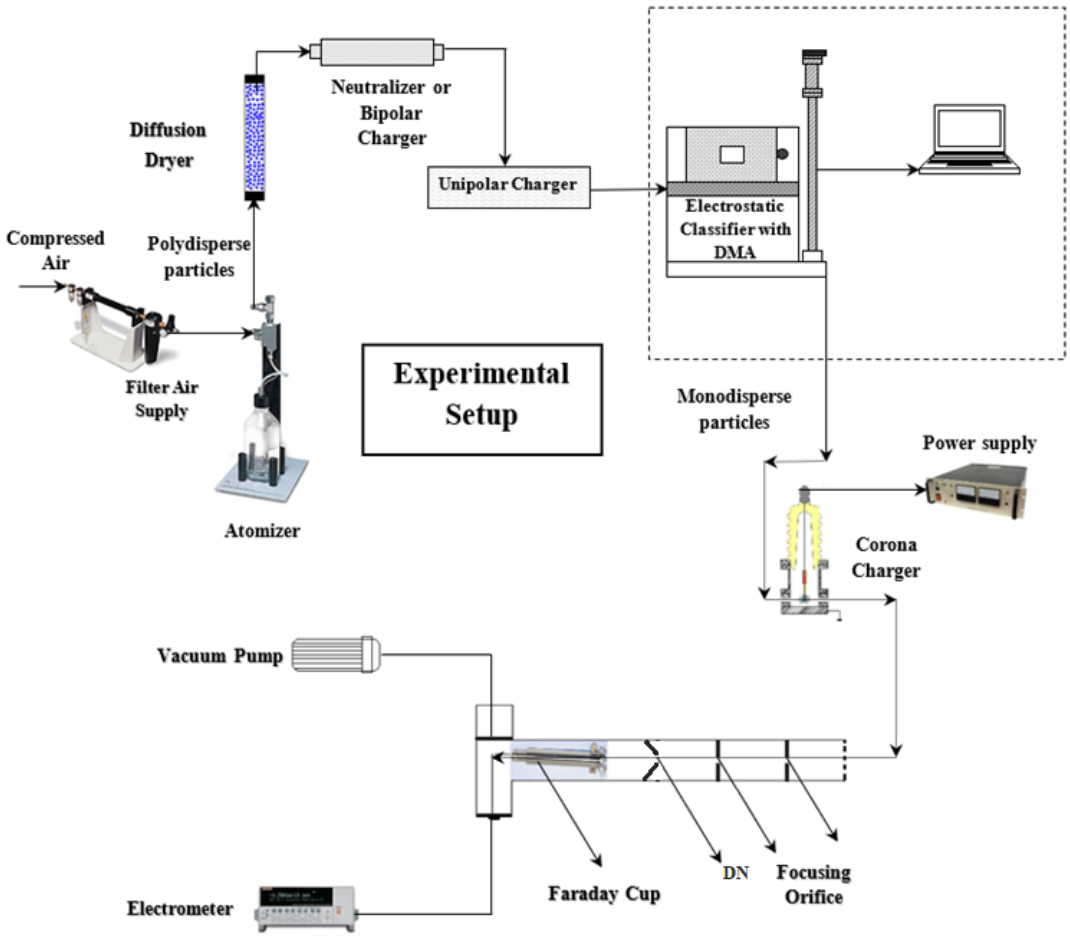

Figure 7.2: Experimental setup to be used in this research

$$c = \sqrt{\frac{\gamma R T_{f1}}{M}} \tag{7.1}$$

Where γ represents the specific heat ratio (1.4 for air), T_{f1} signifies the pre-focussing temperature, and M denotes the molar mass of the gas.

It's worth noting that achieving sonic speed necessitates maintaining appropriate compression ratios across the divergent nozzle. The maximum gas flow via a nozzle is determined by the critical pressure. The critical

pressure ratio is the pressure ratio at which the flow is accelerated to a velocity equal to the local velocity of sound in the fluid [104]:

$$\frac{P_c}{P_1} = \frac{\left(\frac{2}{\gamma+1}\right)\gamma}{\gamma - 1} \tag{7.2}$$

where P_c is the critical pressure (Pa); P_1 is the stagnation pressure (Pa); and γ is the index of isentropic expansion, or the compression constant. For an air nozzle, the critical pressure ratio can be determined as follows:

$$\frac{P_c}{P_1} = \frac{\left(\frac{2}{1.4\ +1}\right)1.4}{1.4\ -1} = 0.528 \tag{7.3}$$

As indicated in Figure 7.3, the focussing orifice was installed in a stainless-steel pipe (the 0.5-mm thick focusing orifice was used in the experiments that followed [138]). Several examples of particle trajectories are also shown in the Figure in order to demonstrate the aerodynamic focussing mechanism. The region that should collect optimally sized particles is the point of entry into the FCE. The particles exhibit optimally sized tracks with a focal point at the position of the FCE. In this way, particles of sizes that differ from the selected sizes are propelled through the powerful pump so that, theoretically, particles of the specific, desired size can be captured only from the suspended gas and are then focussed through the FCE.

The variables whose values are to be established for the calculation of the diameters of the focussed particles are temperature T_{f1}, the dynamic viscosity of the gas μ, the density of the particles ρ_p, the velocity of the gas at the focussing orifice c, and pressure P_{f1}. As determined through simulations, the temperature T_{f1} was always 25°C before focussing by the orifice. As a result, the dynamic viscosity of the air μ, which is solely a function of the temperature, was a corresponding constant with a value of $1.81{*}10^{-5} kg/m.s$. Carbon nanoparticles were utilized in the simulation for

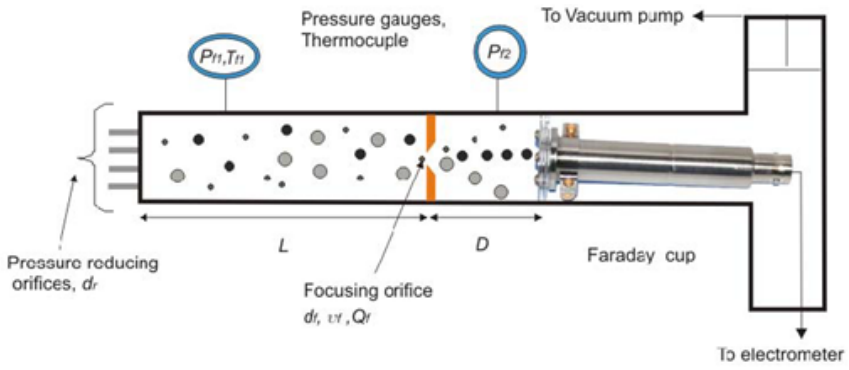

Figure 7.3: Aerodynamic focussing of particles [141]

this study. However, the density of the carbon particles is 2250 kg/m^3 and the shape of the carbon particles is estimated to be spherical. The velocity in the focus orifice is always equal to sonic speed, which is dependent only on the temperature. For air, at 25°C, the speed of sound is 340.29 m/s (Figure 7.4).

Several computational simulations were performed in order to demonstrate that the gas reaches sonic speed in the focussing orifice. The choke flow condition occurs only if the ratio between the absolute pressure P_{f2} and P_{f1} is equal or less than 0.528 (Figure 7.6). The values of P_{f1} and P_{f2}, as well as their ratio, were plotted against the diameter of the pressure-reducing aperture, as displayed in Figure 7.5. Figure 7.6 presents the compression ratio required for achieving sonic speed. As can be seen, the air in the simulated focussing orifice travelled at the speed of sound and was constant. The volume of the flowrate through the focussing orifice was also adjusted so that it was 0.000024 m$^3/s$.

As shown in Figure 7.7, the diameter of the focussed particles in the region before the focussing orifice was plotted as a function of the absolute pressure. The diameter of the larger focussed particles was about 280.94 nm. Larger particles are present because the flow is no longer choked at that point [123].

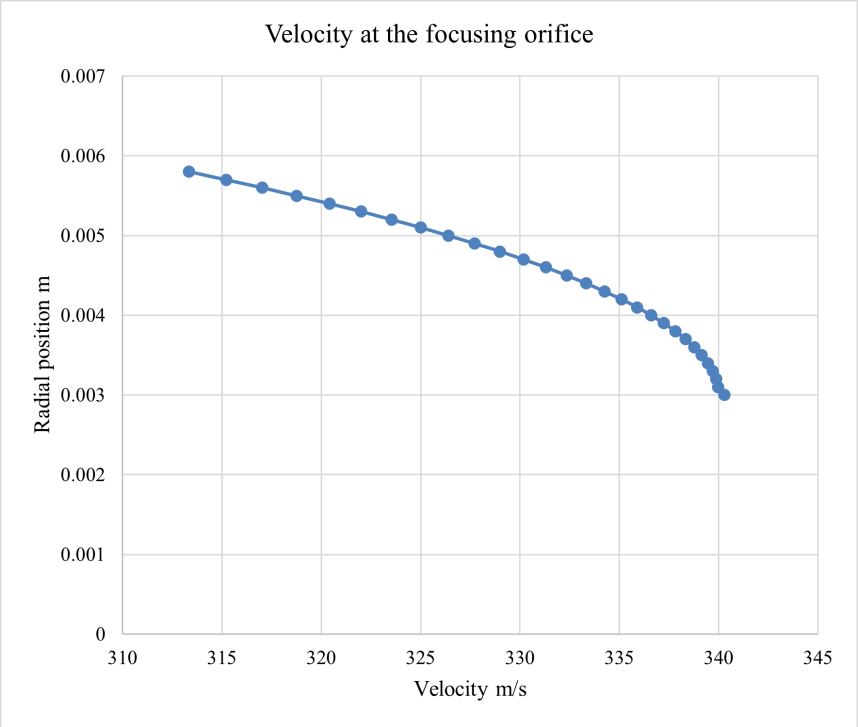

Figure 7.4: Velocity at the focussing orifice

7.2.2 Particle Size Distribution

A thermal mass flowmeter should be used to measure the volume flowrate, q before the inlet. To measure the temperature Tf_1 and pressure Pf_1 before the inlet, a digital pressure gauge and thermocouple connected to the stainless-steel pipe must be used. Because the results will be analyzed using ANSYS Fluent, the pressures before and after the focussing orifice, Pf_1 and Pf_2, are assumed to be 600 KPa and 4,600 KPa, respectively. The volume flowrate at the focussing orifice was calculated using Equation 7.4.

$$q = \frac{\pi d_f^2 v_f}{4} \tag{7.4}$$

The following equation 7.5 can be used to describe the gas mean free

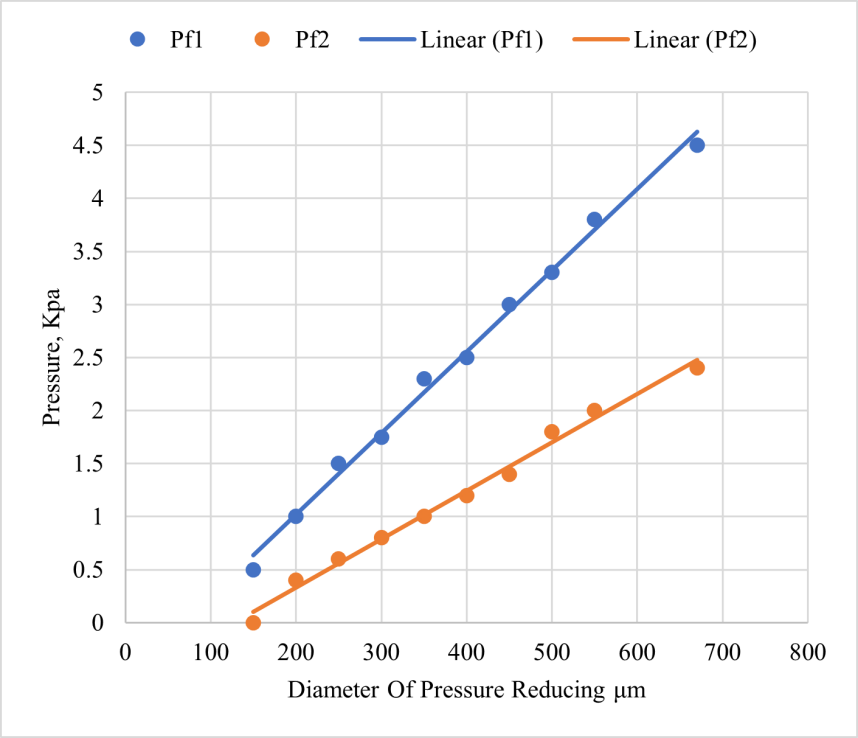

Figure 7.5: Pressure ratio before and after the focussing orifice (the experimental results)

path λ_f before the focussing orifice in terms of the observed variables Tf_1 and $Pf1$, as well as constants.

$$\lambda = \frac{RT}{\sqrt{2\pi D^2 N_A P}} = \frac{\mu}{P\sqrt{2M/\pi RT}} \tag{7.5}$$

$$d_p^* = \sqrt{(1.657\lambda)^2 + \left(d_p^m\right)^2} - 1.657\lambda \tag{7.6}$$

$$d_p^m = \left(\frac{18\mu d_f St^*}{\rho_p v_f}\right)^{\frac{1}{2}} \tag{7.7}$$

As a result, using Equations 7.5, 7.6, and 7.7 , the diameter dp^* of the particle optimally focussed into the Faraday cup electrometer will be calculated:

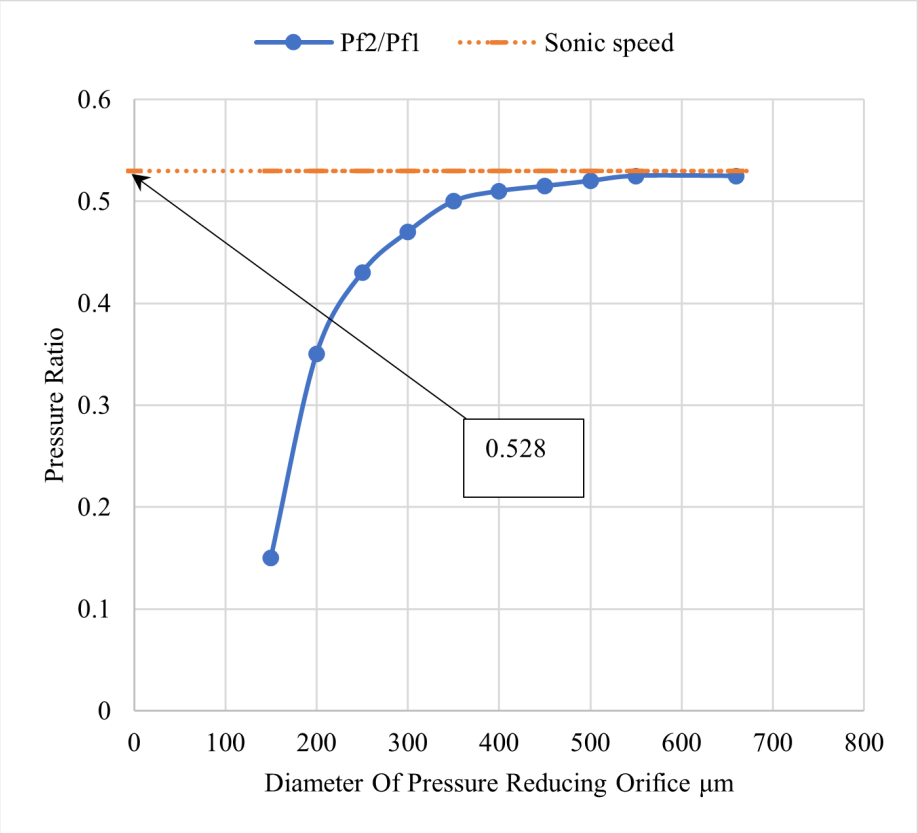

Figure 7.6: Absolute pressure before and after the focussing orifice

$$d_p^* = \sqrt{\frac{12229 * 10^{-4}}{P_{f1}^2} + 1.2976 * 10^{-12}} - \frac{11059 * 10^{-2}}{P_{f1}} \tag{7.8}$$

The aerodynamic focussing of a narrow particle size range requires varying either the mean free path or the maximum diameter dp_m that an orifice can focus on, as shown in equation 7.4. It is impossible to change dp_m since virtually all of the parameters that make it up are resolved: viscosity and velocity through the orifice. Variating the focusing orifice diameter is also unsuitable since the orifice with a variable diameter is not vacuum-tight. Furthermore, the orifice's size is restricted by the pump's capacity. As a

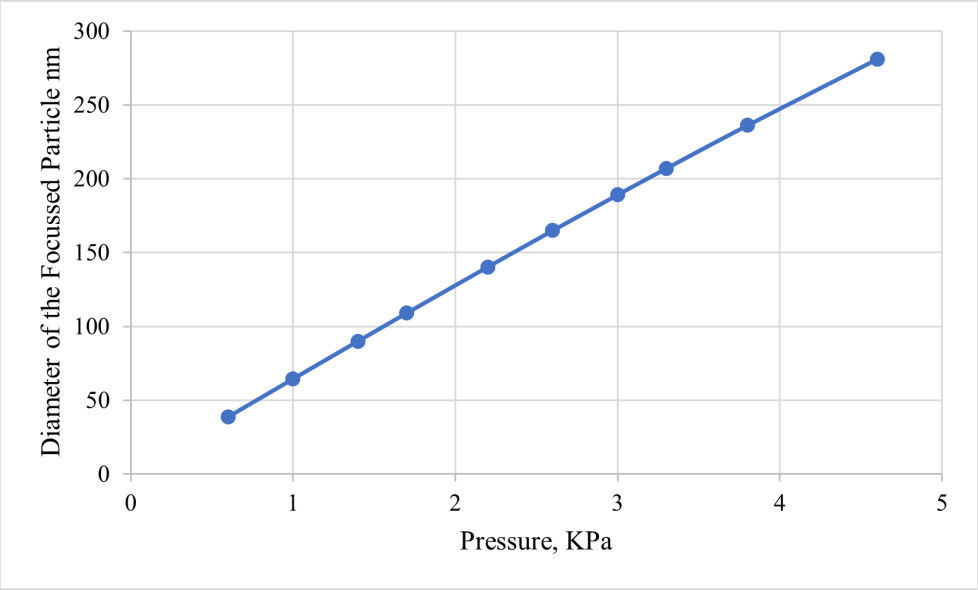

Figure 7.7: As a function of absolute pressure, the diameter of the focussed particles expands [123]

result, varying the carrier gas's mean free path by adjusting the orifice operating pressure is the simplest approach to changing the size of the optimally focussed particles.

The value of the critical Stokes number St^*, which specifies the size of the focussed particles, is the unknown parameter in Equation 7.7. According to the data obtained in this study, St^* was ranged between (0.001 -1.99). The Faraday cup electrometer current is proportional to the number of particles that reach the cup as well as the charge on each focussed particle [55], Equation 7.9.

$$I = \frac{q}{t} \tag{7.9}$$

If all focussed particles hit the Faraday cup, the volume flowrate via the focussing aperture is correct. The optimally concentrated particle number concentration is obtained by combining 7.7 and 7.8.

$$N = \frac{I}{33972 * 10^{-15} d_p^* \ln(1 + 21314 * 10^{-5} d_p^* N t_i} \tag{7.10}$$

N is the number concentration ($particles/m^3$) achieved by the focussing orifice. It is now feasible to find a comparison between the size of the particles and the total concentrated particles using the equations 7.8 and 7.10 . Figure 4.17 displays the size of the particles versus the total concentrated particles.

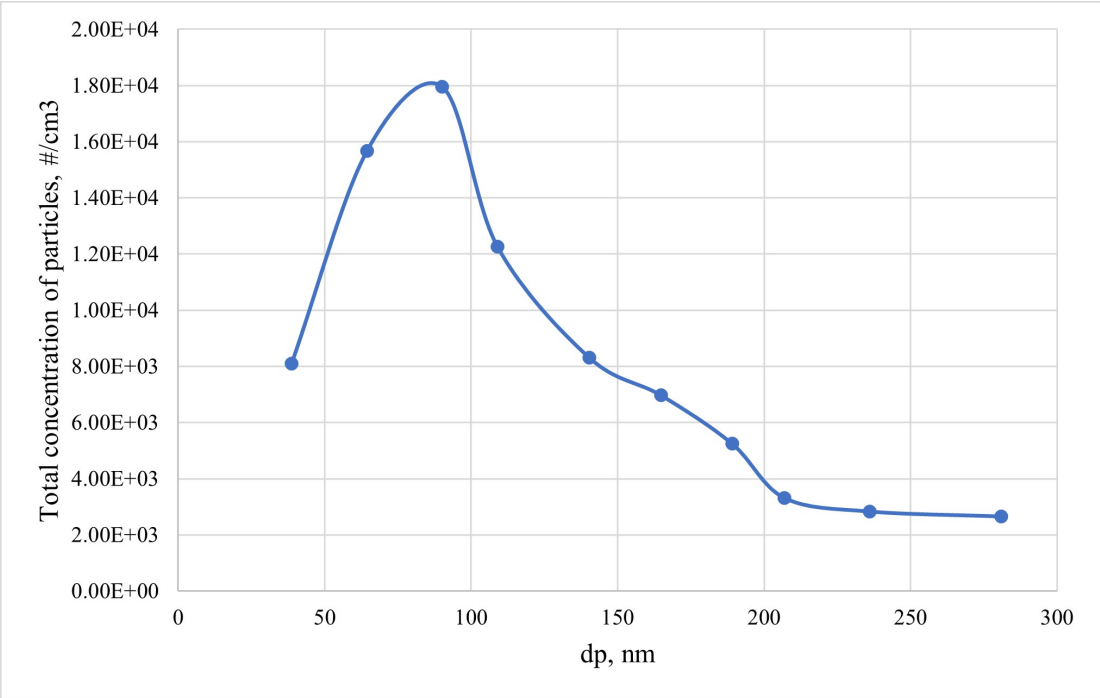

Figure 7.8: The size of the particles versus the total concentrated particles

The particle size distribution was measured in this investigation, as shown in Figure 7.8. On the other hand, the concentration observed for particles smaller than 50 nm is very small. There are numerous theories that may be used to explain this. It's important to note that smaller particles are less effective at charging than larger ones. Due to the develop-

ment of a boundary layer within the orifice, a large number of particles are not focussed and may be pumped out. Furthermore, because particles are charged, some particles may be lost due to deposition on the pressure wall surface.

7.3 Results and Discussion

7.3.1 Comparison of the CFD Simulation Results and the Experimental Data

The results from the CFD simulations of the gas-solid (air-particle) flows were compared with the experimental data (that obtained after experimentally replicating Tan and Wexler's work) generated from the electrodynamics focussing with the aerodynamic lens. Some data was also taken from the work of Tan et al. [141], for which they employed a stainless steel pipe as the low-pressure region. The distance between the pressure-reducing orifices and the focussing lens was 600 mm. They also used only one lens with a long pipe for detecting particle sizes up to 40 nm, as illustrated in Figure 7.8.

Because the diameter of the divergent nozzle measured immediately upstream from the nozzle ranged from 2 mm to 9 mm, for this study, the mean axial CFD results were computed and compared to the experimental data (for one lens) for each of these diameters. The CFD simulations, on the other hand, produced axial velocity profiles that indicate an upward flow pattern at the centre of the pipe and a downward flow pattern toward the wall [4]. Figures 7.10 to 7.14 offer a comparison of the mean axial velocity profiles as determined by the CFD simulation (for the two lenses and one divergent nozzle) and DMA measurements (obtained after experimentally replicating Tan and Wexler's work) versus the results produced using electrodynamics focussing and the aerodynamic lens.

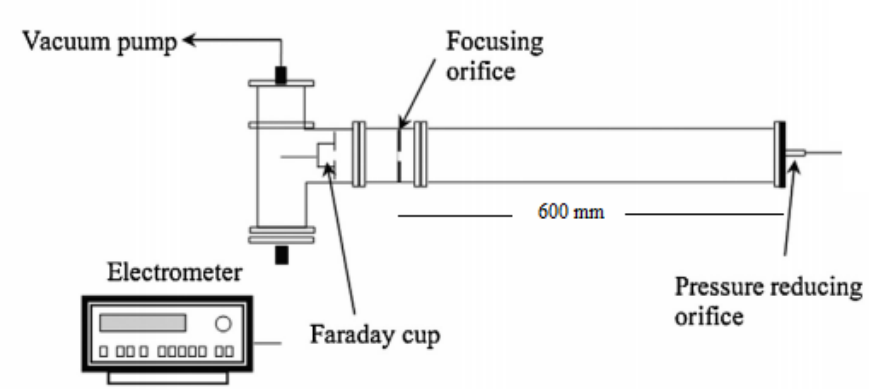

Figure 7.9: Stainless steel pipe used by Tan et al. as the low-pressure region with a 600 mm distance between the pressure-reducing orifices and the focussing lens [141, 123]

As shown in these Figures, the CFD simulation's curves were always lower than the experimental curves for the axial velocity profiles. Figures 7.12 and 7.13 show the measured and predicted axial velocity profiles for a divergent nozzle with a diameter of 5 mm and 2 mm, respectively, indicating that there is a difference in the shape of the curves in these Figures due to the difference in the values of the velocities. Where, when using a nozzle diameter of 5 mm, the fluid velocity at the divergent nozzle opening is 323.37 m/s, while in the case of using a divergent nozzle diameter of 2 mm, the fluid velocity at the orifice is 342.30 m/s. The reason for the increase in fluid velocity at the divergent nozzle with a diameter of 2 mm is the narrowing of this nozzle opening.

When compared to experimental data (for one lens), the axial velocity profiles shown in Figures 7.10 and 7.11 reveal that the simulation findings are lower than predicted. In these two Figures of the CFD simulation results, when using a nozzle diameter of 9 mm, the fluid velocity at the divergent nozzle opening is 309.04 m/s, while in the case of using a divergent nozzle diameter of 7 mm, the fluid velocity at the orifice is 320.52 m/s. Figure 7.12 indicates, for example, that the greatest upward axial velocity

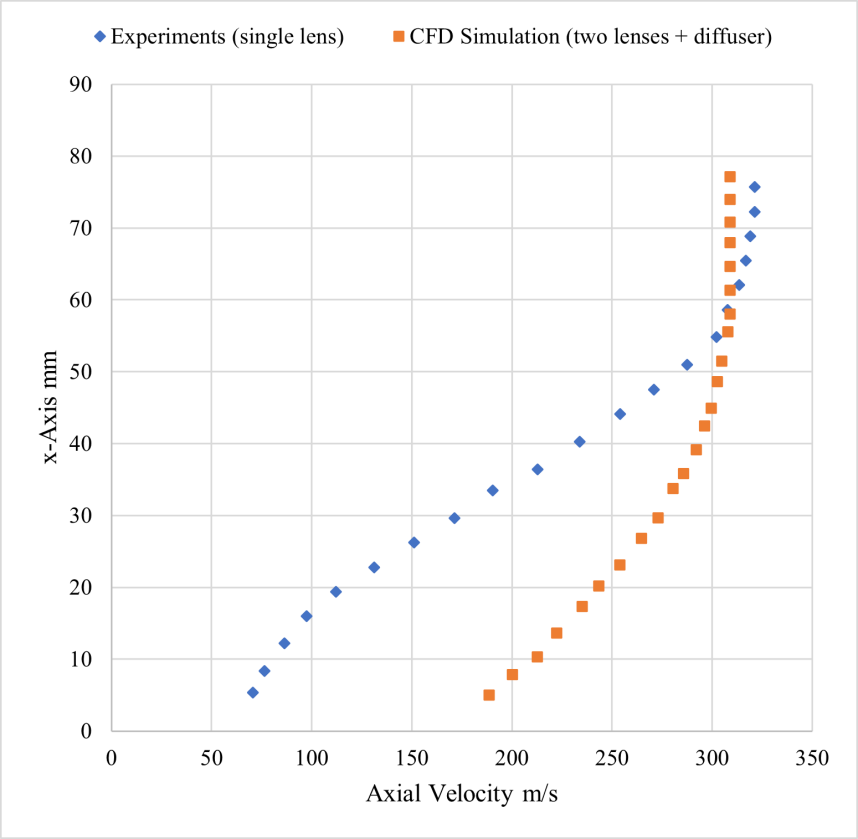

Figure 7.10: Mean axial CFD results for a divergent nozzle having a diameter of 9 mm compared to experimental data for one lens

estimated by the simulation is 323.37 m/s, whereas the experimental data finding was 323.75 m/s. In the Figures above, there is a big difference between the computational and experimental results near the inlet (x = 0). In the experimental results, these results were not taken at the inlet, but rather after the middle of the pipe (which is more than 600 mm in length) at the point where the distance from it to the exit is equal to the length of the pipe used in this research (80 mm), so this is why there is a difference between the results at (x = 0).

In Figures 7.13 and 7.14 of the CFD simulation results, the divergent

nozzles with a diameter of 2 mm and 3 mm produced the best results that were predicted by the CFD simulation based on the value of the velocity at the divergent nozzle that is closer to the speed of sound, which is the velocity at which particles can be focussed. According to Figures 7.13 and 7.14, the greatest axial velocity estimated by the simulation is 346.32 m/s for a divergent nozzle with a diameter of 2 mm, and 340.29 m/s for a divergent nozzle with a diameter of 3 mm.

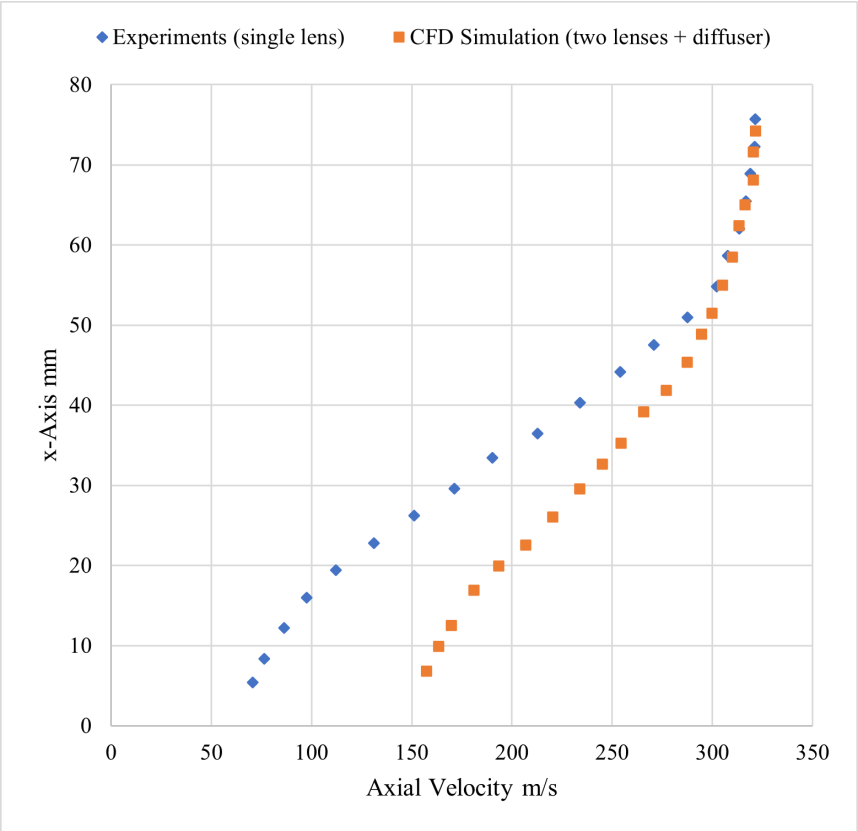

Figure 7.11: Mean axial CFD results for a divergent nozzle having a diameter of 7 mm compared to experimental data for one lens

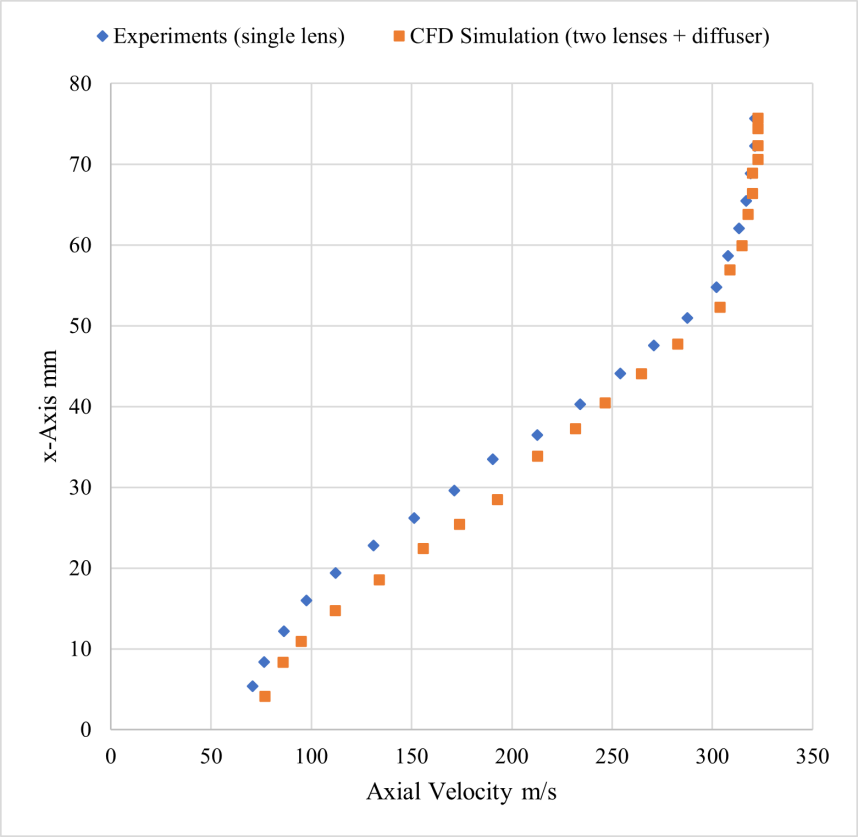

Figure 7.12: Mean axial CFD results for a divergent nozzle having a diameter of 5 mm compared to experimental data for one lens

7.3.2 Validating the Model Against the Simulations by Tan & Wexler (2007) [138]

Monodisperse particles from the DMA were fed into the developing prototype and the CPC for counting in Tan & Wexler's study, [138], Figure 7.15.

In Tan & Wexler's results, the new systems laboratory prototype successfully detected fine particles in all particle sizes that focussed in their research. According to their findings, the two instruments exhibited a high

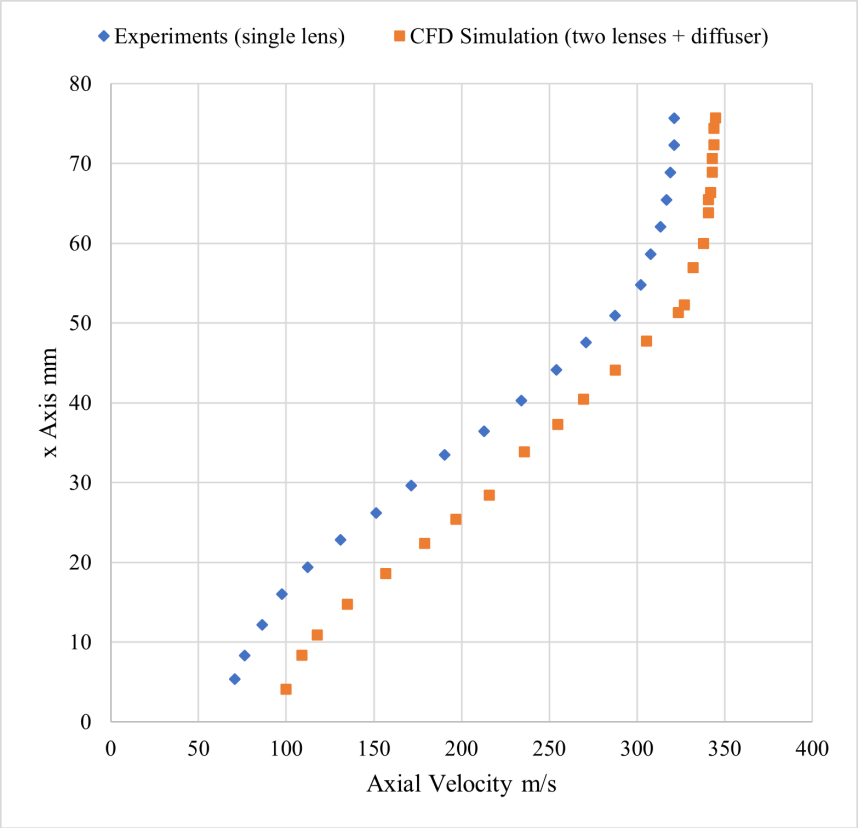

Figure 7.13: Mean axial CFD results for a divergent nozzle having a diameter of 2 mm compared to experimental data for one lens

agreement in counting particles larger than 60 nm in diameter when comparing the two curves. Meanwhile, for particles smaller than 60 nm, there was a considerable disagreement [138]. The new system detected a large number of particles smaller than 60 nm. Figure 7.16 summarizes the equivalent total counts at various particle sizes in comparison to this study's findings.

First and foremost, the new system's ANSYS output successfully detected nanoparticles of all sizes. The developing prototype [138] and ANSYS's results of this research demonstrate that the two instruments had a good agreement in counting particles with diameters ranging from 42 nm

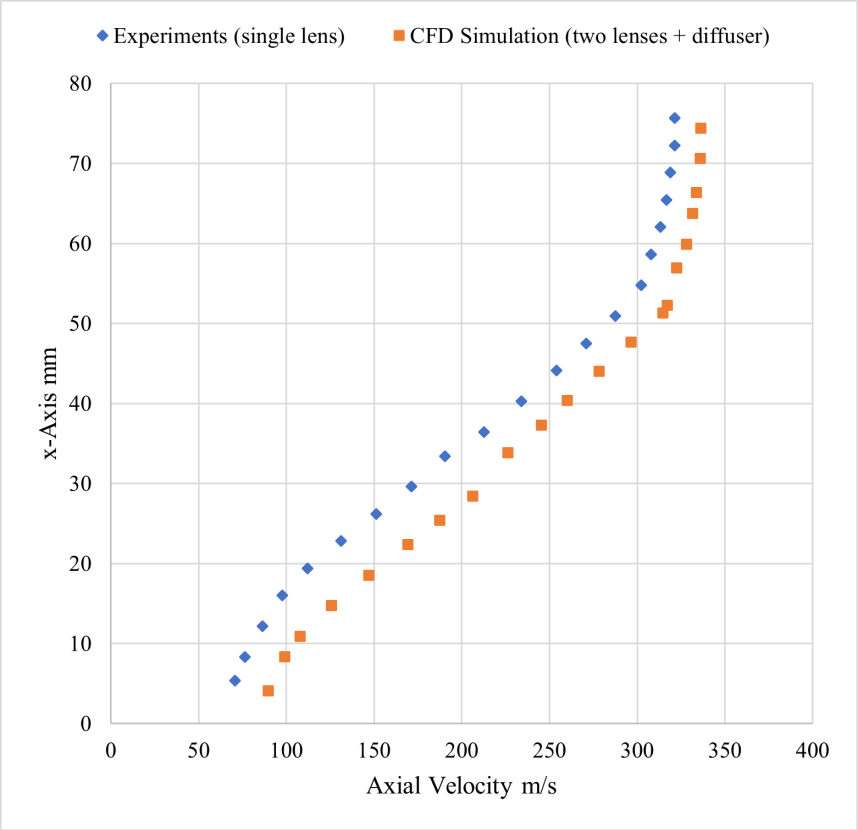

Figure 7.14: Mean axial CFD results for a divergent nozzle having a diameter of 3 mm compared to experimental data for one lens

to 53 nm. Meanwhile, there was a lot of disagreement for particles with diameters ranging from 54 nm to 146 nm. The model used in this study (two lenses + divergent nozzle), which was simulated using ANSYS Fluent, detected a significant number of particles smaller than 42 nm, while in the other two models in Tan & Wexler's study [138], particles up to 25 nm were detected.

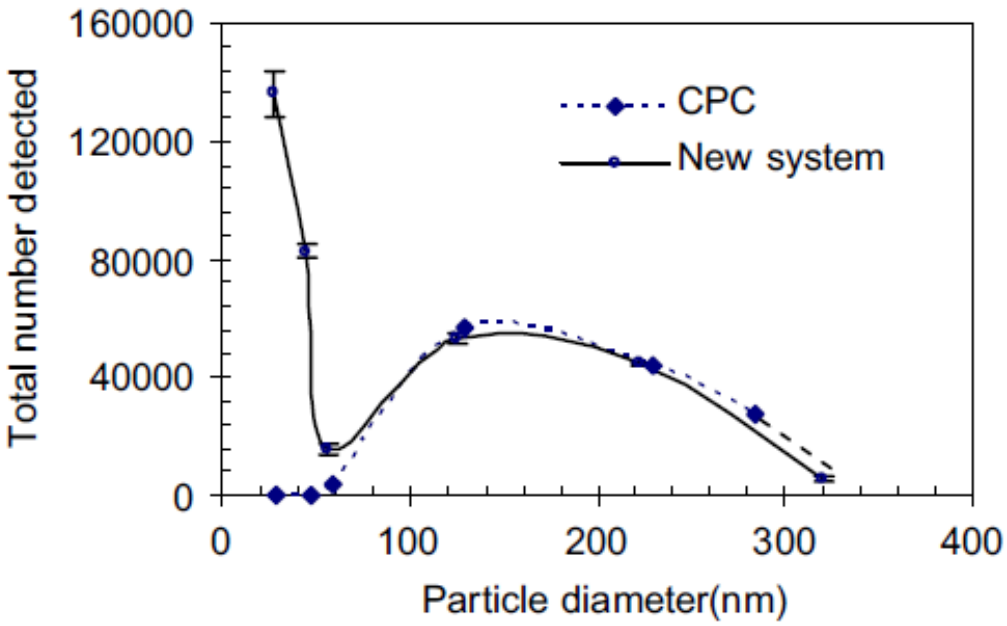

Figure 7.15: The total number of particles measured by the CPC and the prototype are compared [138, 123]

7.4 Summary

Due to the difficulty of experimentally verifying the results of this research due to the closure of the laboratories due to the COVID-19 pandemic, the alternative solution was to find available experimental results that have a range of particle size close to or similar to the range of particle size required to be focussed and detected in this research. Therefore, replicating the experimental setup used by Tan and Wexler was performed experimentally. Then, the results obtained experimentally were compared with the computational results of this research (since the experimental setup to be used in this research is completely similar to the experimental setup used in Tan and Wexler's research, except for the number of aerodynamic lenses, orifice

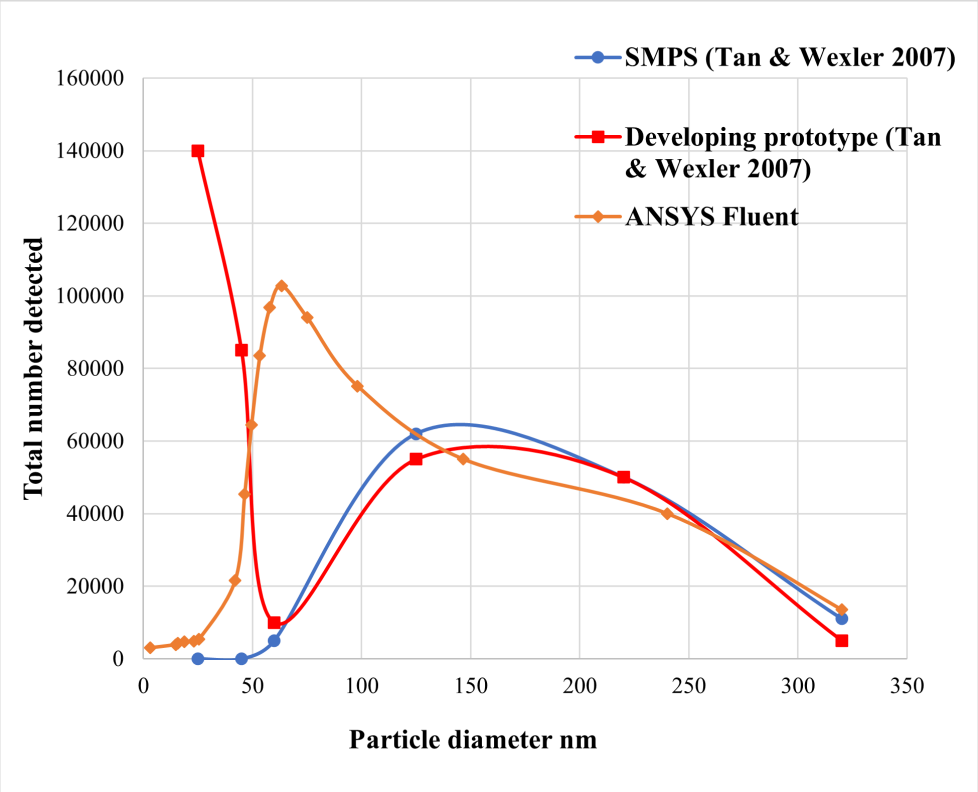

Figure 7.16: The total number of particles measured by the CPC, prototype [138], and the ANSYS Fluent result are compared

diameter and thickness, and pipe length).

A measurement system consisting of a small DMA (S-DMA) and an FCE was applied to investigate the performance of a system for measuring the size distribution of submicron and nanometer airborne particles. The S-DMA provided an extended classification zone that could be used for classifying particles up to 0.83 nm and converting the electrical mobility distribution data obtained with the FCE into a distribution based on particle size [129].

For the computational result, the ANSYS Fluent software was used to simulate two lenses and a divergent nozzle computationally to establish that the size distribution of the particles determined by the developed sys-

tem agreed with that measured by a combination of the S-DMA for one lens [129] that has been used in Tan & Wexler research. The focussing of nanoparticles with an aerodynamic lens was also investigated. A major area of concentration in this research was the enhancement of the design of the orifice and nozzle that focusses on nanoparticles passing through them in order to measure the size of nanoparticles smaller than 300 nm. Initial efforts were directed at optimizing the modelling of the flow through a sharp-edged plate orifice. To allow the aerodynamic focussing of particles of a given size, the velocity of the gas in the focus orifice c must reach the speed of sound.

In previous chapters, a model has been introduced as a means of examining the characteristics of two sharp-edged plate orifices and one divergent nozzle through the use of ANSYS Fluent CFD simulation, and the simulated results were compared against experimental data after replicating Tan & Wexler's work. The operating conditions related to designing a system for focussing nanoparticles have already been explained. The comparison results show that the developed system in this research performs well and provides a useful tool for measuring a wide range of particle sizes [129]. Therefore, the process of using aerodynamic lenses + divergent nozzle for focussing particles smaller than 300 nm has been demonstrated in this study.

Chapter 8

Thesis Conclusions, Work Accomplished, and Avenues for Future Investigation

The approach taken in this research was computational coupled with validation against available experimental data [141, 138]). The computational method included the development of an aerodynamic lens and its subsequent investigation with respect to the sharp-edged plate orifice that was incorporated for focussing the nanoparticles, rather than the conventional flat orifice. Because computational simulation and evaluation for testing the performance of lens systems provide more accurate results, simulations were conducted in combination with an experimental approach based on the use of available empirical data [141, 138] for validating the theoretical and analytical simulations devised for measuring the size of nanoparticles with an aerodynamic lens.

8.1 Conclusions

In conclusion, through the work conducted for this thesis, the challenges associated with the focussing of sub-300 nm nanoparticles with an aerodynamic lens were identified, and a technique was developed for enhancing aerodynamic lens systems for measuring the size of nanoparticles. An aerodynamic lens was designed with a divergent nozzle for focussing the flow so that particles as small as 300 nm could be transmitted through a sharp-edged plate orifice. In this study, the Lagrangian model was applied to determine the size of nanoparticles based on two-dimensional computational fluid dynamics (CFD) analysis for gas-solid flows. This study also demonstrated how ANSYS Fluent 2021R1 software could be used for the CFD simulation of an operational lens and nozzle configuration.

An innovative aerodynamic lens design with two sharp-edged plate orifices instead of a traditional flat orifice was implemented as a means of overcoming the problem under investigation. Theoretical and computational analyses of the concentrating of nanoparticles smaller than 300 nm were conducted in this study. ANSYS Fluent, which automates lens configuration, was utilized for simulating the gas flow field and evaluating the possibility of focussing sub-300 nm nanoparticles. The efficiency of conventional aerodynamic lens focussing degrades significantly as particle diameters drop below 300 nm due to the low inertia and high diffusivity of particles in that size range.

The first step was the invention of a system for optimizing the dimensions and operating conditions of nanoparticle-focussing lenses. It was discovered that large nanoparticles are easier to focus with lighter carrier gases and that multiple lenses with suboptimal Stokes numbers can focus on a wide range of nanoparticle sizes.

Operating pressure and lens measurement expressions that reduce particle diffusion while preserving subsonic flow were devised, and a compu-

tational simulation methodology for analyzing the performance of aerodynamic lens systems was developed.

A novel technique for use in nanoparticle focussing was created: a new pipe model with inside grooves that match the diameter and thickness of the lenses. The advantage of these grooves is that they enable adjustments to the location of the lenses within the pipe if the lens must be moved to the left or right, if other lenses need to be added, or if one lens is to be employed for an entire experiment.

The lens and nozzle configuration were improved through the application of CFD for determining particle trajectories. A case study was designed to facilitate the measurement of the diameter of sub-300 nm nanoparticles moving through a divergent nozzle and an aerodynamic lens. The aerodynamic lens, which throws the nozzle at 1 atm pressure, is injected with nanoparticles.

A computational method for determining the precise focussing characteristics of aerodynamic lens systems was also established. Particle trajectories were tracked using the Lagrangian process. From both modelling and computational viewpoints, the research has effectively summarized the advances and remaining difficulties associated with using an aerodynamic lens for measuring the minimum size of nanoparticles.

The initial belief was that the flow was constant and subsonic, and the investigation led to the calculation of the smallest particle size that could be reliably centred on an axis with two lenses if diffusion was ignored. A method was then defined for establishing the smallest size of particles that could be focussed. In the final analysis, it was found that success could be achieved with the application of the Lagrangian method and a superior aerodynamic lens design for focussing sub-300 nm spherical particles, with air as the primary phase and carbon particles as the secondary phase.

A nanoparticle lens system was designed, developed, and evaluated both

computationally and theoretically. Nanoparticles ranging in size from 3 nm to 300 nm were able to be focussed. The simulation results were then compared to more detailed trajectory simulations based on CFD calculations.

The lens output of the new system proved to be close to the design guideline predictions, suggesting that, according to the simulation, the aerodynamic lens and divergent nozzle could concentrate particles as small as 300 nm. To ensure the validity and reliability of the new aerodynamic lens, the model results were then compared with available experimental data [141, 138]. The conclusion was that the new model has been proven to be successful in detecting and focussing small particles larger than 3 nm.

The research presented in this thesis represents the first systematic attempt to use aerodynamic lenses to calculate the size of nanoparticles based on computational models and theoretical methods. The results of the work can be summarized as follows:

1. Aerodynamic lens systems for focussing nanoparticles have been improved so that the diameters of nanoparticles can be measured (Chapter 4). Air has been demonstrated to be the preferred fluid for focussing small-sized particles, and two lenses with a divergent nozzle can be designed to work effectively based on the Stokes number, St_0 for the focussing of a wide range of nanoparticles. The flow through the sharp-edged plate orifices has been modelled.

2. A computational method based on ANSYS Fluent CFD has been developed for simulating the flow and motion of particles passing through an aerodynamic lens (Chapter 5). Compressible, viscous, laminar, and Navier-Stokes equations are initially solved in order to obtain the gas flow field, followed by the integration of the Lagrangian model for establishing particle trajectories. This approach was used to evaluate the possibility of focussing nanoparticles smaller than 300 nm.

3. Following the instructions in Chapter 5 led to the development of an aerodynamic lens system that focusses on spherical particles smaller than 300 nm (Chapter 4). Air is utilized as a carrier gas and as the primary phase, with carbon particles as the secondary phase, along with two lenses for focussing the nanoparticles and measuring their sizes. Computational simulations revealed penetrations ranging from 53.33% to 98.125% of 3 nm to 300 nm nanoparticles. Computational simulations also confirmed the possibility of focussing and measuring particles larger than 300 nm but an inability to focus or measure particles smaller than 3 nm.

4. The developed aerodynamic lens system described in Chapter 6 was determined to perform better than lens systems that rely on a multiphase flow for focussing nanoparticles. It was therefore confirmed that high-density nanoparticles, such as (ρ_{Carbon}= 2250 kg/m^3), offer greater potential and that using air as a gas carrier is preferable.

8.2 Recommendations for Future Work

Based on this research, opportunities for further investigation can be divided into two groups: additional simulations designed to expand the range of data obtained from the use of aerodynamic lenses and to increase the knowledge base related to nanoparticle behaviour, and additional experiments for validating the model developed through the research conducted for this thesis.

8.2.1 Additional Simulations

For the results produced by the simulations presented here to be applied in experiments requires one or two changes to the present simulation pa-

rameters: first, a significant reduction in the size/density of the particles being tested; second, a significant increase in the inflow velocity; or possibly a combination of these changes. Changing either of these variables will create a number of difficulties from a simulation perspective. Despite the refinement of the mesh, the computational capacity required to run the present simulation configuration in the finest mesh ($\tilde{1}$00,000 nodes) within the capabilities of ANSYS Fluent (Figure 5.8) puts an enormous strain on the available system.

For a comprehensive assessment, further studies will consequently require additional computing assets. On the other hand, an expanded range of particle sizes has been tested: the work presented here involved an examination of a variety of particle sizes *dp* (1 nm to 10 nm), (1 nm to 25 nm), and (25 nm to 100 nm). Despite limitations that prevented the simulation from operating efficiently, this model was established as viable with respect to attempts to simulate the entire geometry under investigation (Figure 5.3). Suggestions for additional simulations are explained below.

1. **Explore other lens geometries**: A sharp-edged plate orifice with a 30° angle at the edge of the orifice was used as the focussing element in this additional research, as illustrated in Figures 8.1 and 8.2.

   In the work reported in this thesis, the focussing of particles with a lower Stokes number was optimized with the use of an orifice characterized by an increased edge angle. This finding indicates that the orifice is at the 30° angle preferred for nanoparticle focussing, but that does not mean that an orifice cannot be designed to have another angle, such as 45°, or 60°. The results obtained with these angles could then be compared with the results of the work presented here in order to ascertain the angle that produces the optimal results [102]. Examining the focussing performance of these elements would consequently be valuable. Aerodynamic lenses in other shapes could also be applied and

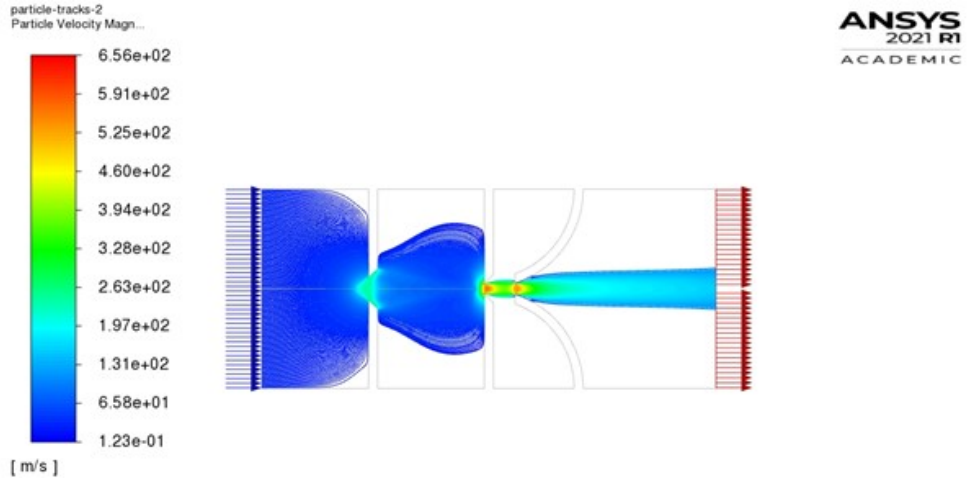

Figure 8.1: Velocity magnitude

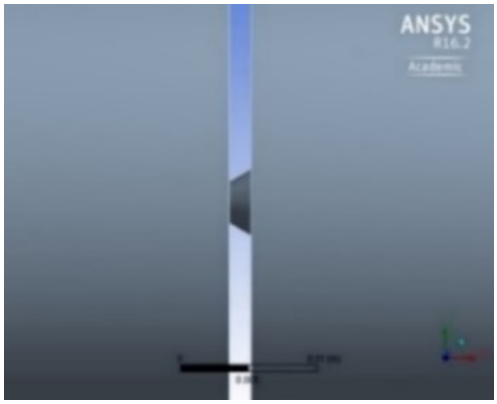

Figure 8.2: Lens geometry

the results compared in order to determine which of these lens shapes is most suitable for measuring the smallest sizes of nanoparticles, as shown in figures 8.3, 8.4, and 8.5.

2. **Study the effects of non-spherical particles**: The first phase utilized in the simulation presented here was air, with the nanoparticles used as the secondary phase being spherical carbon particles with diameters of 3 nm to 300 nm. A useful investigation would be to study

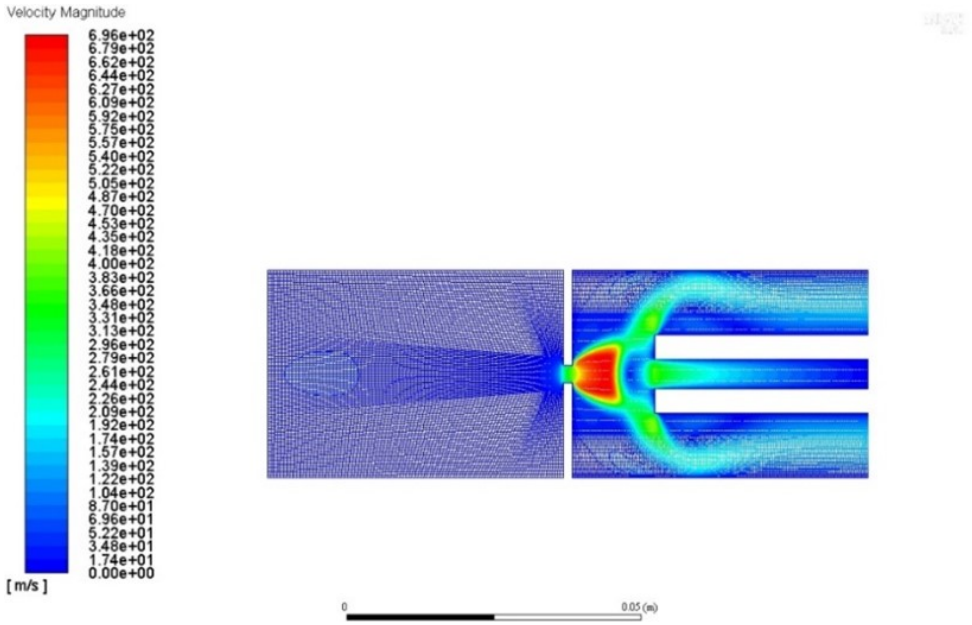

Figure 8.3: Other shapes of aerodynamic lenses – example 1

the effects of incorporating a non-spherical particle into the new model. Theoretical expressions have been derived based on drag and Brownian forces acting on a wide variety of particle shapes [88, 61, 54, 72, 67, 82]. It would be exciting to predict the width of the particle beam based on these forces as calculated for other shapes and then to compare the findings with experimental results. This extension of the research would offer insights into the effect of shape on particle transfer in accelerated flows and would also provide validation of the expressions of these forces for those shapes [109]. Further, plans include an analysis of the simulation components of the new model, with the following objectives:

1. **Compare** density-based solvers and pressure-based solvers.
2. **Compare** the effects of grid adaptation on the solution.

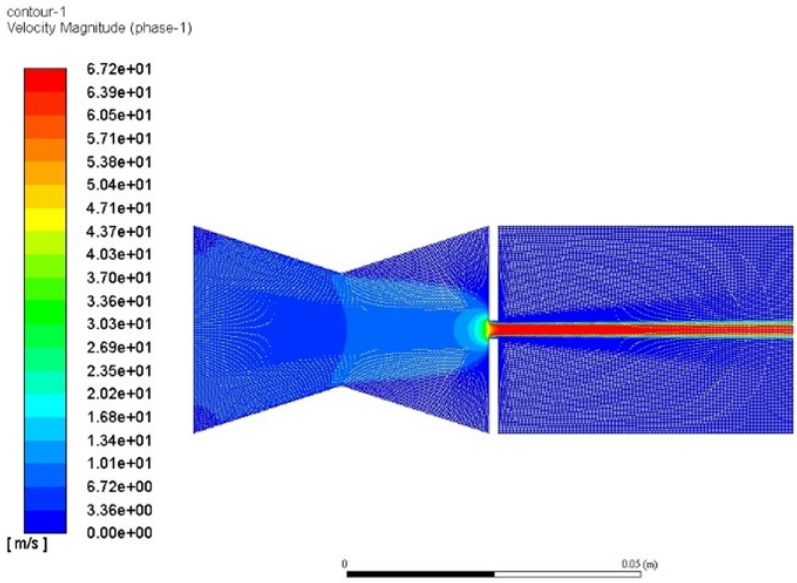

Figure 8.4: Other shapes of aerodynamic lenses – example 2

3. **Compare** ANSYS CFD predictions with the DMA experimental measurement results.

8.2.2 Additional Experimentation

Additional preliminary experimental work is directed at exploring the validation of the developed aerodynamic lens system model for focussing small nanoparticles based on their size measurements. Simulation results associated with particle dispersion can have a significant impact on the accuracy of future models, although the outcome of at least some simulations can be expected, such as the effect of the velocity in the orifice. The following specific areas of interest have been identified:

1. **Validate the Aerodynamic Lens and the Divergent Nozzle Design Experimentally**:

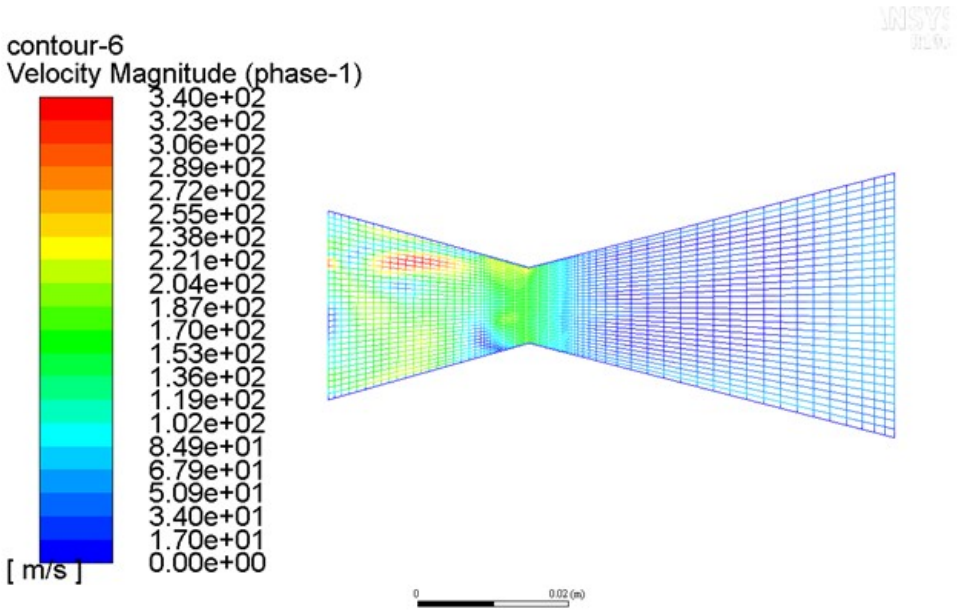

Figure 8.5: Other shapes of aerodynamic lenses – example 3

In this research, the results were calculated based on a simulation method for measuring the size of the nanoparticles: the smaller focussed particles were about 3 nm in diameter, and the largest were 300 nm. The orifice in this study was able to focus particles larger than 300 nm but not particles smaller than 3 nm. The plan is to enhance this lens for use in experiments based on a design that incorporates electrodynamics focussing with the aerodynamic lens. The experimental findings will then be compared with simulation results as a further means of assessing the accuracy of the calculations presented here.

2. **Examine Potential Medical Applications**:

   Nanoparticles provide a new form of drug delivery to the respiratory system [83]. They can be inhaled as a means of improving drug therapies, lung imaging, gene delivery and therapy, and tuberculosis diagnosis and treatment. Very limited reports of real cases of occupational

exposure are available. Systematic research should be conducted on a global scale in order to address increasing concerns about potentially harmful public and occupational exposure to particles [139]. In this context, a major requirement is the development of a stationary or portable instrument for measuring particles for industrial applications. A promising approach could be offered by using nanoaerosols, which are chemical particles that can be applied for measuring particle size distribution. However, light scattering and laser-based ionization render nanoaerosols inefficient, which hinders advances in their online chemical analysis. These considerations have also been targeted for further inquiry. In addition, despite the challenges mentioned above, this technique might be used to monitor viruses, airborne fine and ultrafine particles, and other pollutants in indoor environments. Ultrafine particles (such as COVID-19) have been shown to go to the lungs, then to the circulatory system and the brain, producing increased blood coagulability, respiratory failure, gastroenteritis, nephritis, hepatitis, encephalitis, and progressive demyelinating disease (symptoms of COVID-19).

8.3 Future Research

Other avenues for future investigation include the following:

1. **Analyze and compare** different techniques for improving lens specifications and operating conditions as a means of addressing the low inertia and high diffusivity of nanoparticles in order to build a more efficient aerodynamic lens-nozzle system for focussing nanoparticles.

2. **Construct** an aerodynamic lens and divergent nozzle system for focussing particles smaller than 300 nm.

3. **Extend** the CFD simulation method introduced in **Chapters 4 & 5**. **Chapter 5** details the computational simulation technique used for accurately characterizing the focussing performance of aerodynamic lens-nozzle systems. The flow field is obtained by solving Navier-Stokes equations, and the particle trajectories are established by solving Lagrangian equations. Opportunities for enhancing this method could include an examination of the modelling and effects of laminar flows; the general principles of multiphase flow simulation based on the Lagrangian method; and techniques related to a theoretical method, computational research, and data analysis.

4. **Evaluated** the effectiveness of the aerodynamic lens system described in **Chapter 5**, which is designed to concentrate on nanoparticles with diameters of less than 300 nm. On focussing efficiency, the effects of carrier gas, particle density, and lens design were investigated [152].

5. **Extend** the novel technique proposed in **Chapter 6** whereby grooves are installed inside the pipe to hold the orifices as well as the inlet and outlet lenses. Additional research could explore the effects and potential additional benefits of adjusting the parameters and application of the grooves, or of developing similar new models.

6. **Further develop** the CFD ANSYS Fluent 2021R1computational method presented in **Chapters 4 & 5** to simulate the flow and motion of particles through an aerodynamic lens. The compressible, viscous, laminar, and Navier-Stokes's equations were initially resolved to obtain the gas flow field, followed by the integration of the Lagrangian model in order to obtain particle trajectories.

7. **Perform** additional empirical laboratory testing beyond that presented in **Chapter 7** to increase the experimental data available for validating future devices.

8.4 Work Accomplished

The work accomplished for this thesis can be summarized as follows:

1. The published literature related to nanoparticles and their focussing, CFD concepts, and principles of particle dispersion was reviewed (**Chapter 2**).

2. Based on the concept of using aerodynamic lenses with the Lagrangian method, a nanoparticle-detection technique was introduced and its computational and experimental verification was described (**Chapter 3**).

3. An understanding of the Lagrangian method for fluid motions was provided, and the performance of a Lagrangian method for modelling the distribution of particles focussed through the lenses in the pipe was described, together with its numerical and experimental validation (**Chapter 3**).

4. The development and optimization of a simulation technique for assessing the performance of an aerodynamic lens system was presented (**Chapter 4**).

5. A novel methodology for using aerodynamic lenses and a divergent nozzle for focussing nanoparticles and detecting their size was analyzed in detail using ANSYS Fluent software (**Chapter 5**).

6. A method for enhancing the area of detection in nanoparticle focussing systems was proposed. The new technique entails the use of a divergent nozzle for regulating the flow of the fluid exiting a specific region (**Chapter 5**).

7. To investigate the performance of the developed system with respect to detecting the size distribution of the nanoparticles, a focussing

and measurement system consisting of aerodynamic lenses and interior grooves at the top and bottom of the pipe was constructed (**Chapter 6**).

8. The application of a measurement system consisting of a small Differential Mobility Analyzer (S-DMA) and a Faraday cup electrometer (FCE) for investigating the performance of the system developed for measuring the size distribution of submicron and nanometer airborne particles was explained (**Chapter 7**).

8.5 Summary

The research reported in this thesis involved the development of an aerodynamic lens and an investigation of the proposed use of a sharp-edged plate orifice rather than the conventional flat orifice for focussing nanoparticles. A system comprising aerodynamic lenses and a divergent nozzle for focussing a flow that transmits particles as small as 300 nm through a sharp-edged plate orifice was designed and evaluated. ANSYS Fluent was applied for the CFD simulation of a feasible lens and nozzle configuration. The use of the Lagrangian method combined with the enhanced aerodynamic lens design for focussing sub-300 nm spherical particles was found to be successful. The simulations demonstrated the effective focussing of particles ranging in size from 3 nm to 300 nm. The results were compared with more detailed trajectory simulations based on CFD calculations, and the new aerodynamic lens system model was used for examining nanoparticle behaviour. Further studies can be divided into two groups: additional simulations and further experiments. These findings could have significant implications for the accuracy of future particle dispersion models, such as those directed at exploring velocity in the orifice. Enhancements to aerodynamic lens and divergent nozzle systems for the focussing of particles smaller than 300 nm

could be investigated. The CFD simulation method introduced in **Chapters 4 & 5** could be extended to include the modelling and examination of the effects of laminar flow, the general principles of multiphase flow simulation, and other computational research.

References

[1] www.grimm-aerosol.com.

[2] www.transmittershop.com.

[3] Nozzle geometry variations on the discharge coefficient. *Alam, MMA and Setoguchi, T and Matsuo, S and Kim, HD*, 2009.

[4] EA Afolabi and JGM Lee. An eulerian-eulerian cfd simulation of air-water flow in a pipe separator. *The Journal of Computational Multiphase Flows*, 6(2):133–149, 2014.

[5] Wael H Ahmed, Mufatiu M Bello, Meamer El Nakla, and Abdelsalam Al Sarkhi. Flow and mass transfer downstream of an orifice under flow accelerated corrosion conditions. *Nuclear Engineering and Design*, 252:52–67, 2012.

[6] H Ali, H Soleimani, N Yahya, MK Baig, and A Rostami. Finite element method for modelling of two phase fluid flow in porous media. In *Journal of Physics: Conference Series*, volume 1123, page 012002. IOP Publishing, 2018.

[7] Jonathan Allen and Robert K Gould. Mass spectrometric analyzer for individual aerosol particles. *Review of Scientific Instruments*, 52(6):804–809, 1981.

[8] Habib Aminfar, Mousa Mohammadpourfard, and Ramin Mortezazadeh. Numerical simulations of the influence of brownian and gravitational forces on the stability of cuo nanoparticles by the eulerian–lagrangian approach. *Heat Transfer—Asian Research*, 47(1):72–87, 2018.

[9] Habib Aminfar, Mousa Mohammadpourfard, and Ramin Mortezazadeh. Numerical simulations of the influence of brownian and gravitational forces on the stability of cuo nanoparticles by the eulerian–lagrangian approach. *Heat Transfer—Asian Research*, 47(1):72–87, 2018.

[10] Katrine Alling Andreassen and Ida Lykke Fabricius. Biot critical frequency applied to description of failure and yield of highly porous chalk with different pore fluids. *Geophysics*, 75(6):E205–E213, 2010.

[11] David J Benson. Computational methods in lagrangian and eulerian hydrocodes. *Computer methods in Applied mechanics and Engineering*, 99(2-3):235–394, 1992.

[12] Laurence Bergougnoux, Gilles Bouchet, Diego Lopez, and Élisabeth Guazzelli. The motion of solid spherical particles falling in a cellular flow field at low stokes number. *Physics of Fluids*, 26(9):093302, 2014.

[13] Wala Bkari. Modeling nanoparticle generation in a corona charger. Master's thesis, University of Waterloo, 2018.

[14] JE Brockmann, RC Dykhuizen, R Cote, and T Roemer. Aerodynamic focusing of large particles. *Journal of Aerosol Science*, 29:S1067–S1068, 1998.

[15] Alexander N Brooks and Thomas JR Hughes. Streamline upwind/petrov-galerkin formulations for convection dominated flows

with particular emphasis on the incompressible navier-stokes equations. *Computer methods in applied mechanics and engineering*, 32(1-3):199–259, 1982.

[16] R MUNSON Bruce, FY Donald, and HO Theodore. Fundamentals of fluid mechanics, 2006.

[17] Peter R Buseck and Kouji Adachi. Nanoparticles in the atmosphere. *Elements*, 4(6):389–394, 2008.

[18] Paola Castellano, Riccardo Ferrante, Roberta Curini, and Silvia Canepari. An overview of the characterization of occupational exposure to nanoaerosols in workplaces. In *Journal of Physics: Conference Series*, volume 170, page 012009. IOP Publishing, 2009.

[19] Da-Ren Chen, David YH Pui, George W Mulholland, and Marco Fernandez. Design and testing of an aerosol/sheath inlet for high resolution measurements with a dma. *Journal of aerosol science*, 30(8):983–999, 1999.

[20] YS Cheng and BE Dahneke. Properties of continuum source particle beams: Ii. beams generated in capillary expansions. *Journal of Aerosol Science*, 10(4):363–368, 1979.

[21] Matteo Chiesa, Vidar Mathiesen, Jens A Melheim, and Britt Halvorsen. Numerical simulation of particulate flow by the eulerian–lagrangian and the eulerian–eulerian approach with application to a fluidized bed. *Computers & chemical engineering*, 29(2):291–304, 2005.

[22] Kwang-Leong Choy. *Innovative processing of films and nanocrystalline powders*. World Scientific, 2002.

[23] CT Crowe, JD Schwarzkopf, M Sommerfeld, and Y Tsuji. *Multiphase flows with droplets and particles. 2011*, volume 10. 2011.

[24] Barton Dahneke and Hermann Flachsbart. An aerosol beam spectrometer. *Journal of Aerosol Science*, 3(5):345–349, 1972.

[25] BE Dahneke and YS Cheng. Properties of continuum source particle beams. i. calculation methods and results. *Journal of Aerosol Science*, 10(3):257–274, 1979.

[26] BE Dahneke and SK Friedlander. Velocity characteristics of beams of spherical polystyrene particles. *Journal of Aerosol Science*, 1(4):325–339, 1970.

[27] J Fernandez de la Mora. Drastic improvement of the resolution of aerosol size spectrometers via aerodynamic focusing: the case of variable-pressure impactors. *Chemical engineering communications*, 151(1):101–124, 1996.

[28] J. Fernandez De La Mora and P. Riesco-Chueca. Aerodynamic focusing of particles in a carrier gas. *Journal of Fluid Mechanics*, 195(8):1–21, 1988.

[29] F Di Fonzo, A Gidwani, MH Fan, D Neumann, DI Iordanoglou, JVR Heberlein, PH McMurry, SL Girshick, N Tymiak, WW Gerberich, et al. Focused nanoparticle-beam deposition of patterned microstructures. *Applied Physics Letters*, 77(6):910–912, 2000.

[30] Mingzhi Dong, Elina Iervolino, Fabio Santagata, Guoyi Zhang, and Guoqi Zhang. Integrated virtual impactor enabled pm 2.5 sensor. *IEEE Sensors Journal*, 17(9):2814–2821, 2017.

[31] Y Dong, A Bapat, S Hilchie, U Kortshagen, and SA Campbell. Generation of nano-sized free standing single crystal silicon particles. *Journal of Vacuum Science & Technology B: Microelectronics and Nanometer Structures Processing, Measurement, and Phenomena*, 22(4):1923–1930, 2004.

[32] Y Dong, A Bapat, S Hilchie, U Kortshagen, and SA Campbell. Generation of nano-sized free standing single crystal silicon particles. *Journal of Vacuum Science & Technology B: Microelectronics and Nanometer Structures Processing, Measurement, and Phenomena*, 22(4):1923–1930, 2004.

[33] Zhongwang Dou, Andrew D Bragg, Adam L Hammond, Zach Liang, Lance R Collins, and Hui Meng. Effects of reynolds number and stokes number on particle-pair relative velocity in isotropic turbulence: a systematic experimental study. *Journal of Fluid Mechanics*, 839:271–292, 2018.

[34] Frank Drewnick, Silke S Hings, Peter DeCarlo, John T Jayne, Marc Gonin, Katrin Fuhrer, Silke Weimer, Jose L Jimenez, Kenneth L Demerjian, Stephan Borrmann, et al. A new time-of-flight aerosol mass spectrometer (tof-ams)—instrument description and first field deployment. *Aerosol Science and Technology*, 39(7):637–658, 2005.

[35] Michael D Durham and Dale A Lundgren. Evaluation of aerosol aspiration efficiency as a function of stokes number, velocity ratio and nozzle angle. *Journal of Aerosol Science*, 11(2):179–188, 1980.

[36] Albert Einstein. *Investigations on the Theory of the Brownian Movement*. Courier Corporation, 1956.

[37] M El-Gammal, WH Ahmed, and CY Ching. Investigation of wall mass transfer characteristics downstream of an orifice. *Nuclear Engineering and Design*, 242:353–360, 2012.

[38] Andreas Elsaesser and C Vyvyan Howard. Toxicology of nanoparticles. *Advanced drug delivery reviews*, 64(2):129–137, 2012.

[39] Thomas J Estes, Vincent L Vilker, and Sheldon K Friedlander. Characteristics of a capillary-generated particle beam. *Journal of Colloid and Interface Science*, 93(1):84–94, 1983.

[40] MM Francois, MJ Shashkov, TO Masser, and ED Dendy. A comparative study of multimaterial lagrangian and eulerian methods with pressure relaxation. *Computers & Fluids*, 83:126–136, 2013.

[41] Katrin Fuhrer, Silke Weimer, Jose L Jimenez, Kenneth L Demerjian, Stephan Borrmann, and Douglas R Worsnop. A new time-of-flight aerosol mass spectrometer (tof-ams)—instrument description and first field deployment. 2004.

[42] Mohamed Gad-el Hak. The fluid mechanics of microdevices—the freeman scholar lecture. 1999.

[43] Ashok Gidwani. *Studies of flow and particle transport in hypersonic plasma particle deposition and aerodynamic focusing.* University of Minnesota, 2003.

[44] B Giechaskiel, R Chirico, PF DeCarlo, M Clairotte, T Adam, G Martini, MF Heringa, R Richter, ASH Prevot, U Baltensperger, et al. Evaluation of the particle measurement programme (pmp) protocol to remove the vehicles' exhaust aerosol volatile phase. *Science of the Total Environment*, 408(21):5106–5116, 2010.

[45] Raheleh Givehchi. Filtration of nacl and wox nanoparticles using wire screens and nanofibrous filters. 2016.

[46] Paul S Grassia, E John Hinch, and Ludwig C Nitsche. Computer simulations of brownian motion of complex systems. *Journal of Fluid Mechanics*, 282:373–403, 1995.

[47] J Grund, Ch E Düllmann, K Eberhardt, Sz Nagy, JJW van de Laar, D Renisch, and F Schneider. Implementation of an aerodynamic lens

for triga-spec. *Nuclear Instruments and Methods in Physics Research Section B: Beam Interactions with Materials and Atoms*, 376:225–228, 2016.

[48] Thomas Hagemeier, Dominique Thévenin, and Thomas Richter. Settling of spherical particles in the transitional regime. *International Journal of Multiphase Flow*, 138:103589, 2021.

[49] TD Hall and WW Beeman. Secondary electron emission from beams of polystyrene latex spheres. *Journal of Applied Physics*, 47(12):5222–5225, 1976.

[50] Hee Siew Han. *Nanometer aerosol size analyzer (nASA) and data inversion*. University of Minnesota, 2003.

[51] Peter Hansbo and Anders Szepessy. A velocity-pressure streamline diffusion finite element method for the incompressible navier-stokes equations. *Computer Methods in Applied Mechanics and Engineering*, 84(2):175–192, 1990.

[52] Roy M Harrison and Jianxin Yin. Particulate matter in the atmosphere: which particle properties are important for its effects on health? *Science of the total environment*, 249(1-3):85–101, 2000.

[53] Celia Henry. Dust in the wind. *Analytical chemistry*, 70(13):462A–465A, 1998.

[54] William C Hinds. *Aerosol technology: properties, behavior, and measurement of airborne particles*. John Wiley & Sons, 1999.

[55] https://www.epa.gov/environmental-topics/air topics. How nitrogen oxides affect the way we live and breathe. *https://www.epa.gov/environmental-topics/air-topics*, 5(1):22–33, 2016.

[56] Yue Huang, Sung Hwan Yoon, Scott R Heron, Christophe D Masselon, J Scott Edgar, František Tureček, and David R Goodlett. Surface acoustic wave nebulization produces ions with lower internal energy than electrospray ionization. *Journal of the American Society for Mass Spectrometry*, 23(6):1062–1070, 2012.

[57] Fluent Incorporated. *FLUENT 5 users guide volume 4 july 1998*. Fluent Incorporated, 1998.

[58] Gerhard W Israel and SK Friedlander. High-speed beams of small particles. *Journal of Colloid and Interface Science*, 24(3):330–337, 1967.

[59] R Israel and Daniel E Rosner. Use of a generalized stokes number to determine the aerodynamic capture efficiency of non-stokesian particles from a compressible gas flow. *Aerosol Science and Technology*, 2(1):45–51, 1982.

[60] Kazunori Ito, Hidehiro Katsui, Masashi Mochizuki, and Masahiko Isobe. Non-reflected multi directional wave maker theory and experiments of verification. pages 443–456, 1997.

[61] N Jawahar and Gowtham Reddy. Nanoparticles: A novel pulmonary drug delivery system for tuberculosis. *Journal of Pharmaceutical Sciences and Research*, 4(8):1901, 2012.

[62] John T Jayne, Danna C Leard, Xuefeng Zhang, Paul Davidovits, Kenneth A Smith, Charles E Kolb, and Douglas R Worsnop. Development of an aerosol mass spectrometer for size and composition analysis of submicron particles. *Aerosol Science & Technology*, 33(1-2):49–70, 2000.

[63] James John and Theo Keith. *Gas Dynamics, 3rd Edition, Prentice Hall, Toledo, USA*. 2006.

[64] Murray V. Johnston and Anthony S Wexler. Ms of individual aerosol particles. *Analytical Chemistry*, 67(23):721A–726A, 1995.

[65] O Kievit, M Weiss, PJT Verheijen, JCM Marijnissen, and B Scarlett. The on-line chemical analysis of single particles using aerosol beams and time of flight mass spectrometry. *Chemical Engineering Communications*, 151(1):79–100, 1996.

[66] OJCM Kievit, JCM Marijnissen, PJT Verheijen, and B Scarlett. Some improvements on the particle beam generator. *Journal of Aerosol Science*, 21:S685–S688, 1990.

[67] Myung-man Kim and Andrew L Zydney. Effect of electrostatic, hydrodynamic, and brownian forces on particle trajectories and sieving in normal flow filtration. *Journal of Colloid and Interface Science*, 269(2):425–431, 2004.

[68] Patrick D Kinney, Gwi-Nam Bae, David YH Pui, and Benjamin YH Liu. Particle behavior in vacuum systems. *Journal of the IEST*, 39(6):40, 1996.

[69] EO Knutson and KT Whitby. Aerosol classification by electric mobility: apparatus, theory, and applications. *Journal of Aerosol Science*, 6(6):443–451, 1975.

[70] Richard Korpus, Paul Jones, Owen Oakley, and Leonard Imas. Prediction of viscous forces on oscillating cylinders by reynolds-averaged navier-stokes solver. 2000.

[71] Takahiko Koyama, Daniel Platt, and Laxmi Parida. Variant analysis of sars-cov-2 genomes. *Bulletin of the World Health Organization*, 98(7):495, 2020.

[72] Wolfgang G. Kreyling, Manuela Semmler-Behnke, and Winfried Möller. Health implications of nanoparticles. *Journal of Nanoparticle Research*, 8(5):543–562, 2006.

[73] Rep Kubo. The fluctuation-dissipation theorem. *Reports on progress in physics*, 29(1):255, 1966.

[74] Perumal Kumar and Michael Wong Ming Bing. A cfd study of low pressure wet gas metering using slotted orifice meters. *Flow Measurement and Instrumentation*, 22(1):33–42, 2011.

[75] Alvin CK. Lai and FZ. Chen. Comparison of a new eulerian model with a modified lagrangian approach for particle distribution and deposition indoors. *Atmospheric Environment*, 41(25):5249–5256, 2007.

[76] Li Lan, Pawel Wargocki, David Peter Wyon, and Zhiwei Lian. Effects of thermal discomfort in an office on perceived air quality, sbs symptoms, physiological responses, and human performance. *Indoor air*, 21(5):376–390, 2011.

[77] Iman Lashgari, Francesco Picano, Wim Paul Breugem, and Luca Brandt. Channel flow of rigid sphere suspensions: particle dynamics in the inertial regime. *International Journal of Multiphase Flow*, 78:12–24, 2016.

[78] Jin-Won Lee, Min-Young Yi, and Sang-Min Lee. Inertial focusing of particles with an aerodynamic lens in the atmospheric pressure range. *Journal of Aerosol Science*, 34(2):211–224, 2003.

[79] Kwang-Sung Lee, Sung-Woo Cho, and Donggeun Lee. Development and experimental evaluation of aerodynamic lens as an aerosol inlet of single particle mass spectrometry. *Journal of Aerosol Science*, 39(4):287–304, 2008.

[80] Kwang-Sung Lee, Tae-Hyun Hwang, Seok-Hwan Kim, Soo Hyung Kim, and Donggeun Lee. Numerical simulations on aerodynamic focusing of particles in a wide size range of 30 nm–10 μm. *Aerosol Science and Technology*, 47(9):1001–1008, 2013.

[81] Kwang-Sung Lee, Songkil Kim, and Donggeun Lee. Aerodynamic focusing of 5–50 nm nanoparticles in air. *Journal of Aerosol Science*, 40(12):1010–1018, 2009.

[82] Amy Li and Goodarz Ahmadi. Dispersion and deposition of spherical particles from point sources in a turbulent channel flow. *Aerosol science and technology*, 16(4):209–226, 1992.

[83] Dongqing Li. *Encyclopedia of microfluidics and nanofluidics*. Springer Science & Business Media, 2008.

[84] L-Y Lin, C-Y Lin, Y-C Lin, and K-J Chuang. The effects of indoor particles on blood pressure and heart rate among young adults in taipei, taiwan. *Indoor air*, 19(6):482–488, 2009.

[85] Yue Lin, Liem Pham, Xiaoliang Wang, Roya Bahreini, Heejung S Jung, et al. Evaluation of fast mobility particle sizer (fmps) for ambient aerosol measurement. *Aerosol and Air Quality Research*, 21, 2021.

[86] Jing J. Liu, Cai Y. Ma, Yang D. Hu, and Xue Z. Wang. Effect of seed loading and cooling rate on crystal size and shape distributions in protein crystallization—a study using morphological population balance simulation. *Computers & Chemical Engineering*, 34(12):1945–1952, 2010.

[87] Peng Liu, Paul J. Ziemann, David B Kittelson, and Peter H McMurry. Generating particle beams of controlled dimensions and divergence: I.

theory of particle motion in aerodynamic lenses and nozzle expansions. *Aerosol Science and Technology*, 22(3):293–313, 1995.

[88] Peng Liu, Paul J. Ziemann, David B Kittelson, and Peter H McMurry. Generating particle beams of controlled dimensions and divergence: Ii. experimental evaluation of particle motion in aerodynamic lenses and nozzle expansions. *Aerosol Science and Technology*, 22(3):314–324, 1995.

[89] PNPDBPH Liu, NP Rao, David B Kittelson, and Peter H McMurry. Optimizing the detection efficiency of a low pressure, in-situ particle monitor using aerodynamic focusing lenses. pages 217–224, 1996.

[90] Yuan Liu, Zhi Ning, Yu Chen, Ming Guo, Yingle Liu, Nirmal Kumar Gali, Li Sun, Yusen Duan, Jing Cai, Dane Westerdahl, et al. Aerodynamic analysis of sars-cov-2 in two wuhan hospitals. *Nature*, 582(7813):557–560, 2020.

[91] L. López Castañón, JR. Castillón Fantova, G. Lumbreras Garcia, MÁ. Somoza Calvo, Á. López Llerena, and B. Cordero de las Heras. Taller de educación para la salud sobre prevención de osteoporosis en mujeres. efectividad de una intervenciónenfermera en atención primaria. *Nutr. clín. diet. hosp*, pages 75–85, 2012.

[92] Omid Mahdavipour, Dorsa Fahimi, and Igor Paprotny. Focusing of airborne particles using groove-induced envelope (grip) flow air-microfluidic concentrator. *Journal of Microelectromechanical Systems*, 28(3):453–459, 2019.

[93] Ramakrishna V Mallina, Anthony S Wexler, and Murray V. Johnston. High-speed particle beam generation: simple focusing mechanisms. *Journal of aerosol science*, 30(6):719–738, 1999.

[94] Johan Marra, Matthias Voetz, and Heinz-Jürgen Kiesling. Monitor for detecting and assessing exposure to airborne nanoparticles. *Journal of Nanoparticle Research*, 12(1):21–37, 2010.

[95] John D McKenna, James H Turner, and James P McKenna Jr. *Fine particle (2.5 microns) emissions: regulations, measurement, and control*. John Wiley & Sons, 2008.

[96] Kerrie Mengersen, Lidia Morawska, Hao Wang, N Murphy, F Tayphasavanh, K Darasavong, and NS Holmes. Association between indoor air pollution measurements and respiratory health in women and children in lao pdr. *Indoor air*, 21(1):25–35, 2011.

[97] Prachi Middha and Anthony S Wexler. Particle focusing characteristics of sonic jets. *Aerosol Science & Technology*, 37(11):907–915, 2003.

[98] Prachi Middha and Anthony S Wexler. Particle–focusing characteristics of matched aerodynamic lenses. *Aerosol science and technology*, 39(3):222–230, 2005.

[99] Richard H Moore, Michael A Shook, Luke D Ziemba, Joshua P DiGangi, Edward L Winstead, Bastian Rauch, Tina Jurkat, Kenneth L Thornhill, Ewan C Crosbie, Claire Robinson, et al. Take-off engine particle emission indices for in-service aircraft at los angeles international airport. *Scientific data*, 4(1):1–15, 2017.

[100] Lidia Morawska, Congrong He, Graham Johnson, Hai Guo, Erik Uhde, and Godwin Ayoko. Ultrafine particles in indoor air of a school: possible role of secondary organic aerosols. *Environmental science & technology*, 43(24):9103–9109, 2009.

[101] C Motzkus, C Chivas-Joly, E Guillaume, S Ducourtieux, L Saragoza, D Lesenechal, T Macé, J-M Lopez-Cuesta, and C Longuet. Aerosols

emitted by the combustion of polymers containing nanoparticles. *Journal of nanoparticle research*, 14(3):1–17, 2012.

[102] Hasan Jumaah Mrayeh and Fue-Sang Lien. Using divergent nozzle with aerodynamic lens to focus nanoparticles. *World Academy of Science, Engineering and Technology–International Journal of Energy and Environmental Engineering*, 13(4):231–237, 2019.

[103] WK Murphy and GW Sears. Production of particulate beams. *Journal of Applied Physics*, 35(6):1986–1987, 1964.

[104] Ibrahim Nejatian, Mojtaba Kanani, Milad Arabloo, Alireza Bahadori, and Sohrab Zendehboudi. Prediction of natural gas flow through chokes using support vector machine algorithm. *Journal of Natural Gas Science and Engineering*, 18:155–163, 2014.

[105] Adair B. D. Yoshioka C. Quispe J. D. Orca G. Kuhn P. ... Buchmeier M. J. Neuman, B. W. Supramolecular architecture of severe acute respiratory syndrome coronavirus revealed by electron cryomicroscopy. *Journal of virology*, 80(16):7918–7928, 2006.

[106] JJ Nijdam, TAG Langrish, and DF Fletcher. Assessment of an eulerian cfd model for prediction of dilute droplet dispersion in a turbulent jet. *Applied Mathematical Modelling*, 32(12):2686–2705, 2008.

[107] Günter Oberdörster, Robert M Celein, Juraj Ferin, and Bernard Weiss. Association of particulate air pollution and acute mortality: involvement of ultrafine particles? *Inhalation toxicology*, 7(1):111–124, 1995.

[108] Günter Oberdörster, Eva Oberdörster, and Jan Oberdörster. Nanotoxicology: an emerging discipline evolving from studies of ultrafine particles. *Environmental health perspectives*, 113(7):823–839, 2005.

[109] Günter Oberdörster, Vicki Stone, and Ken Donaldson. Toxicology of nanoparticles: a historical perspective. *Nanotoxicology*, 1(1):2–25, 2007.

[110] Berk Öktem, Michael P Tolocka, and Murray V. Johnston. On-line analysis of organic components in fine and ultrafine particles by photoionization aerosol mass spectrometry. *Analytical Chemistry*, 76(2):253–261, 2004.

[111] Ming Jun Pang and Jin Jia Wei. Analysis of drag and lift coefficient expressions of bubbly flow system for low to medium reynolds number. *Nuclear engineering and design*, 241(6):2204–2213, 2011.

[112] Igor Paprotny, Frederick Doering, Paul A Solomon, Richard M White, and Lara A Gundel. Microfabricated air-microfluidic sensor for personal monitoring of airborne particulate matter: Design, fabrication, and experimental results. *Sensors and Actuators A: Physical*, 201:506–516, 2013.

[113] P Piseri, H Vahedi Tafreshi, and P Milani. Manipulation of nanoparticles in supersonic beams for the production of nanostructured materials. *Current Opinion in Solid State and Materials Science*, 8(3-4):195–202, 2004.

[114] Kerri A Pratt, Joseph E Mayer, John C Holecek, Ryan C Moffet, Rene O Sanchez, Thomas P Rebotier, Hiroshi Furutani, Marc Gonin, Katrin Fuhrer, Yongxuan Su, et al. Development and characterization of an aircraft aerosol time-of-flight mass spectrometer. *Analytical chemistry*, 81(5):1792–1800, 2009.

[115] Rajini Rao, Daniela Drummond-Barbosa, and Carolyn W Slayman. Transcriptional regulation by glucose of the yeast pma1 gene encoding the plasma membrane h+-atpase. *Yeast*, 9(10):1075–1084, 1993.

[116] LCBS Reis, JA Carvalho Jr, MAR Nascimento, LO Rodrigues, FLG Dias, and PM Sobrinho. Numerical modeling of flow through an industrial burner orifice. *Applied Thermal Engineering*, 67(1-2):201–213, 2014.

[117] P Riesco-Chueca et al. Aerodynamic focusing of particles in carrier gas. *J. Fl. Mech.*, 195:1, 1988.

[118] Abraham Robinson. On the motion of small particles in a potential field of flow. *Communications on pure and applied mathematics*, 9(1):69–84, 1956.

[119] Emil Roduner. Size matters: why nanomaterials are different. *Chemical Society Reviews*, 35(7):583–592, 2006.

[120] Nils Roth, Salah Awel, Daniel A Horke, and Jochen Küpper. Optimizing aerodynamic lenses for single-particle imaging. *Journal of Aerosol Science*, 124:17–29, 2018.

[121] Sol I Rubinow and Joseph B Keller. The transverse force on a spinning sphere moving in a viscous fluid. *Journal of Fluid Mechanics*, 11(3):447–459, 1961.

[122] PGT Saffman. The lift on a small sphere in a slow shear flow. *Journal of fluid mechanics*, 22(2):385–400, 1965.

[123] Alena Saprykina. Airborne nanoparticle sizing by aerodynamic particle focusing and corona charging. Master's thesis, University of Calgary, 2009.

[124] J Schreiner, U Schild, C Voigt, and K Mauersberger. Focusing of aerosols into a particle beam at pressures from 10 to 150 torr. *Aerosol Science & Technology*, 31(5):373–382, 1999.

[125] J Schreiner, C Voigt, K Mauersberger, P McMurry, and P Ziemann. Aerodynamic lens system for producing particle beams at stratospheric pressures. *Aerosol science and technology*, 29(1):50–56, 1998.

[126] J Schreiner, C Voigt, P Zink, A Kohlmann, D Knopf, C Weisser, P Budz, and K Mauersberger. A mass spectrometer system for analysis of polar stratospheric aerosols. *Review of scientific instruments*, 73(2):446–452, 2002.

[127] Manish S Shah, Jyeshtharaj B Joshi, Avtar S Kalsi, CSR Prasad, and Daya S Shukla. Analysis of flow through an orifice meter: Cfd simulation. *Chemical engineering science*, 71:300–309, 2012.

[128] Manabu Shimada, Bangwoo Han, Kikuo Okuyama, and Yoshio Otani. Bipolar charging of aerosol nanoparticles by a soft x-ray photoionizer. *Journal of Chemical Engineering of Japan*, 35(8):786–793, 2002.

[129] Manabu Shimada, Ferry Iskandar, and Kikuo Okuyama. Development of dma-faraday cup electrometer system for measurement of submicron aerosol particles. In *AIP Conference Proceedings*, volume 534, pages 773–776. American Institute of Physics, 2000.

[130] MP Sinha and SK Friedlander. Mass distribution of chemical species in a polydisperse aerosol: measurement of sodium chloride in particles by mass spectrometry. *Journal of colloid and interface science*, 112(2):573–582, 1986.

[131] Sebastiano Sonego and Marc Massar. Covariant definition of inertial forces: Newtonian limit and time-dependent gravitational fields. *Classical and Quantum Gravity*, 13(1):139, 1996.

[132] Yongxuan Su, Michele F Sipin, Hiroshi Furutani, and Kimberly A Prather. Development and characterization of an aerosol time-of-

flight mass spectrometer with increased detection efficiency. *Analytical Chemistry*, 76(3):712–719, 2004.

[133] Shankar Subramaniam. Lagrangian–eulerian methods for multiphase flows. *Progress in Energy and Combustion Science*, 39(2-3):215–245, 2013.

[134] Maria Svane, Magnus Hagström, and Jan Pettersson. Chemical analysis of individual alkali-containing aerosol particles: Design and performance of a surface ionization particle beam mass spectrometer. *Aerosol science and technology*, 38(7):655–663, 2004.

[135] H Vahedi Tafreshi, G Benedek, P Piseri, S Vinati, E Barborini, and P Milani. A simple nozzle configuration for the production of low divergence supersonic cluster beam by aerodynamic focusing. *Aerosol Science & Technology*, 36(5):593–606, 2002.

[136] H Vahedi Tafreshi, P Piseri, E Barborini, G Benedek, and P Milani. Simulation on the effect of brownian motion on nanoparticle trajectories in a pulsed microplasma cluster source. *Journal of Nanoparticle Research*, 4(6):511–524, 2002.

[137] Ben Tan. Laboratory evaluation of low to medium cost particle sensors. Master's thesis, University of Waterloo, 2017.

[138] ZC Tan and AS Wexler. Fine particle counting with aerodynamic particle focusing and corona charging. *Atmospheric Environment*, 41(25):5271–5279, 2007.

[139] Zhongchao Tan. *Air pollution and greenhouse gases: from basic concepts to engineering applications for air emission control*. Springer, 2014.

[140] Zhongchao Tan. Nanoaerosol. In *Air Pollution and Greenhouse Gases*, pages 395–425. Springer, 2014.

[141] Zhongchao Tan, Raheleh Givehchi, and Alena Saprykina. Submicron particle sizing by aerodynamic dynamic focusing and electrical charge measurement. *Particuology*, 18:105–111, 2015.

[142] Mohammad Reza Tarybakhsh, Ali Akbar Lotfi Neyestanak, and Hamed Tarybakhsh. Cfd study on wall/nanoparticle interaction in nanofluids convective heat transfer. *Advances in Materials Science and Engineering*, 2013, 2013.

[143] Herbert J Tobias, Peter M Kooiman, Kenneth S Docherty, and Paul J Ziemann. Real-time chemical analysis of organic aerosols using a thermal desorption particle beam mass spectrometer. *Aerosol Science & Technology*, 33(1-2):170–190, 2000.

[144] M Amouei Torkmahalleh, I Goldasteh, Y Zhao, N Mgbo Udochu, A Rossner, PK Hopke, and AR Ferro. Pm2. 5 and ultrafine particles emitted during heating of commercial cooking oils. *Indoor Air*, 22(6):483–491, 2012.

[145] Candace S-J Tsai, David White, Henoc Rodriguez, Christian E Munoz, Cheng-Yu Huang, Chuen-Jinn Tsai, Carol Barry, and Michael J Ellenbecker. Exposure assessment and engineering control strategies for airborne nanoparticles: an application to emissions from nanocomposite compounding processes. *Journal of Nanoparticle Research*, 14(7):1–14, 2012.

[146] Akira Tsuda, Frank S Henry, and James P Butler. Particle transport and deposition: basic physics of particle kinetics. *Comprehensive Physiology*, 3(4):1437–1471, 2011.

[147] MM Tukiman, MNM Ghazali, A Sadikin, NF Nasir, N Nordin, A Sapit, and MA Razali. Cfd simulation of flow through an orifice plate. 243(1):012036, 2017.

[148] T Vazquez-Gonzalez, A Llor, and Christophe Fochesato. Ransom test results from various two-fluid schemes: Is enforcing hyperbolicity a thermodynamically consistent option? *International Journal of Multiphase Flow*, 81:104–112, 2016.

[149] Jing Wang and David YH Pui. Characterization, exposure measurement and control for nanoscale particles in workplaces and on the road. 304(1):012008, 2011.

[150] Lian-Ping Wang and Davd E Stock. Dispersion of heavy particles by turbulent motion. *Journal of Atmospheric Sciences*, 50(13):1897–1913, 1993.

[151] Xiaoliang Wang, Ashok Gidwani, Steven L Girshick, and Peter H McMurry. Aerodynamic focusing of nanoparticles: II. numerical simulation of particle motion through aerodynamic lenses. *Aerosol science and technology*, 39(7):624–636, 2005.

[152] Xiaoliang Wang, Frank Einar Kruis, and Peter H McMurry. Aerodynamic focusing of nanoparticles: I. guidelines for designing aerodynamic lenses for nanoparticles. *Aerosol Science and Technology*, 39(7):611–623, 2005.

[153] Xiaoliang Wang and Peter H McMurry. An experimental study of nanoparticle focusing with aerodynamic lenses. *International Journal of Mass Spectrometry*, 258(1-3):30–36, 2006.

[154] Xiaoliang Wang, Peter H Mcmurry, and Einar Kruis. Aerodynamic focusing of nanoparticle or cluster beams, January 13 2009. US Patent 7,476,851.

[155] Yifan Wang, Peng Liu, Feng Shan, Zhichun Liu, and Wei Liu. Effect of longitudinal vortex generator on the heat transfer enhancement of a circular tube. *Applied Thermal Engineering*, 148:1018–1028, 2019.

[156] C Yu Wen. *Mechanics of fluidization*, volume 62. 1966.

[157] Alla Zelenyuk and Dan Imre. Single particle laser ablation time-of-flight mass spectrometer: an introduction to splat. *Aerosol Science and Technology*, 39(6):554–568, 2005.

[158] Jingjie Zhang and Daren Chen. Differential mobility particle sizers for nanoparticle characterization. *Journal of Nanotechnology in Engineering and Medicine*, 5(2), 2014.

[159] Jinlin Zhang. Computational fluid dynamics (cfd) modeling of proppant transport in a plug-and-perf completion with different perforation phasing. 2014.

[160] Lianhua Zhang, Jianxiong Shao, Ximeng Chen, Jingxiang Zhang, and Qingzong Si. Design and evaluation of aerodynamic lens system for focusing sub-10 nm nanoparticles. *Applied Physics A*, 122(11):1–6, 2016.

[161] Ning Zhang, Zhongquan Zheng, Steven Eckels, Venkata B Nadella, and Xiaoyang Sun. Transient response of particle distribution in a chamber to transient particle injection. *Particle & Particle Systems Characterization*, 26(4):199–209, 2009.

[162] Xuefeng Zhang, Kenneth A Smith, Douglas R Worsnop, Jose Jimenez, John T Jayne, and Charles E Kolb. A numerical characterization of particle beam collimation by an aerodynamic lens-nozzle system: Part i. an individual lens or nozzle. *Aerosol Science & Technology*, 36(5):617–631, 2002.

[163] Xuefeng Zhang, Kenneth A Smith, Douglas R Worsnop, Jose L Jimenez, John T Jayne, Charles E Kolb, James Morris, and Paul Davidovits. Numerical characterization of particle beam collimation:

Part ii integrated aerodynamic-lens–nozzle system. *Aerosol Science and Technology*, 38(6):619–638, 2004.

[164] Yong Zhang, Baosheng Jin, Wenqi Zhong, Bing Ren, and Rui Xiao. Dem simulation of particle mixing in flat-bottom spout-fluid bed. *Chemical Engineering Research and Design*, 88(5-6):757–771, 2010.

[165] Kun Zhou and Tat Leung Chan. Simulation of homogeneous particle nucleation in a free turbulent jet. *Aerosol Science and Technology*, 45(8):973–987, 2011.

[166] Paul J. Ziemann, Peng Liu, Nagaraja P. Rao, David B. Kittelson, and Peter H. McMurry. Particle beam mass spectrometry of submicron particles charged to saturation in an electron beam. *Journal of aerosol science*, 26(5):745–756, 1995.

APPENDICES

Appendix A

Drag and Brownian Forces User Defined Functions (UDF)

A.1 Fluent Cunningham Drag Force UDF

// Hasan.h

/**

The UDF for computing the nanoparticle drag coefficient is established using the Stokes drag with the Cunningham correction factor as a function of temperature and pressure [137]:

lambda = 0.26/(sqrt(2)*3.141592654*6.02214*pow(10,23)*pow(3.7*pow(10,-10),2)*C_R(c,t));

**/

#include "udf.h"

#include "math.h"

DEFINE_DPM_DRAG (cunningham_drag_force, Re, P)

{

cell_t c =P_CELL_THREAD(P);

```
    real lambda, Kn, Cc;
    lambda = 0.175*133.322*pow (10, -6) *C_T (c, t)/C_P (c, t);
    Kn=2*lambda/P_DIAM(P);
    Cc = 1+2.657*Kn;
    real Cd, drag force;
    if (RE < 1)
    {
        Cd = 24 / Re;
        drag_force = 18*Cd*Re/(24*Cc);
        return (drag_force);
    }
    else if (Re < 1000)
    {
        Cd = 24*(1+0.15*pow (Re,0.687))/Re;
        drag_force = 18*Cd*Re/(24*Cc);
        return (drag_force);
    }
    else
    {
        Cd = 0.44;
        drag_force = 18 *Cd*Re/(24*Cc);
        return (drag_force);
    }
}
```

A.2 Fluent Brownian force UDF

```
/*****************************************************************/
/ Brownian force from Fluent Manual [152] /
/ Hasan.h /
/*****************************************************************/
DEFINE_DPM_BODY_FORCE(myBrownian, p, i)
{
double bforce;
cell_t c = RP_CELL(&p->cCell);
Thread *t = RP_THREAD(&p->cCell);
double pressure=C_P(c,t);
double temp=C_T(c,t);
double mu=C_MU_L(c,t);
double rho=C_R(c,t);
double nu=mu/rho;
double Dp=P_DIAM(p);
double rhop=P_RHO(p);
double pdt=P_DT(p);
double conc,mfp,Cc;
double x1,x2,w,y1,y2;
double ss;
/* conc=pressure/gasconst/temp;*/
/*calculate mean free path and slip correction*/
```

```
mfp=mfp_r*temp/T_r*p_r/pressure*(1.0+S/T_r)/(1.0+S/temp);
Cc=1.0+2.0*mfp/Dp*(1.257+0.4*exp(-1.1*Dp/2.0/mfp));
y1=cheap_gauss_random();
y2=cheap_gauss_random();
/* if(pdt<1.0e-12) pdt=1.336637e-05;*/
if(P_TIME(p)==0.0) bforce=0.0;
else
{
ss=216.0*nu*gasconst*temp/pow(pi,2.0)/rho/pow(Dp,5.0)/pow((rhop/rho),2.0)/Cc;
if(i==0) bforce=y1*sqrt(pi*ss/pdt);
else if(i==1) bforce=y2*sqrt(pi*ss/pdt);
/*printf("%e,%e,%e,%e\n",nu,rho,rhop,mu);*/
/*printf("%e,%e,%e,%e,%e,%e\n",y1,y2,ss,pdt,Cc,bforce);*/
}
/* an acceleration should be returned */
return (bforce);
}
```

Appendix B

Experimental Setup for Studying Nanoparticle Focussing

The Model 5.705 particle counter is a Faraday cup electrometer (FCE), used for measuring charged airborne particles. A Differential Mobility Analyzer (DMA) is normally used for characterizing the particles by size prior to counting. Figure B.1 provides photos of the equipment.

Figure B.1: PC with S-DMA 55-100 connected to a DMA Controller 5706

The DMA instrument is specially adapted for measuring very small particles up to very high concentrations. A sample of the airflow is drawn through a particle filter, which is placed in a metal cage isolated from the

housing of the instrument. The attached particles also transport their electrical charges to the filter. The amount of the electrical charge over a specified time unit is measured as an electric current. If the sample airflow and the charging probability are known, the particle concentration can be calculated. Producing a defined charge distribution in the aerosol requires the use of a neutralizer. The electronics component consists primarily of a reactance amplifier for changing the current into a voltage, and three consecutively mounted amplifier stages. The process can be itemized as follows:

1. An aerosol generator, either a tube furnace or an electrospray, generates the particles.
2. The aerosol is then charged using a unipolar charger.
3. A DMA is used as a means of selecting charged particles within a narrow range of electric mobility.
4. An FCE is used for calculating the concentration of the singly charged "monodisperse" particles leaving the DMA. At the same time, operating in parallel, a fraction of the aerosol flow is passed through a critical orifice, lowering the pressure from atmospheric to the lens operating pressure (2700 Pa).
5. As they pass through the aerodynamic lens system, particles are directed into a narrow beam and delivered to a vacuum chamber.
6. A unipolar charger is used for increasing the percentage of negatively charged nanoparticles, and the DMA therefore identifies the particle concentration as "monodisperse."
7. To avoid wasting air, the DMA sheath flow is kept constant at 15 l/min and recirculated. A 2.5 l/min polydisperse aerosol flowrate reaches the

DMA, with a 0.731 l/min flowrate exiting via the bypass port. The FCE (1.681 l/min) and the aerodynamic lens system (88 cm3/min) have thus split the monodisperse aerosol flowrate leaving the DMA.

B.0.1 Scanning Mobility Particle Sizer

A scanning mobility particle sizer (SMPS) spectrometer is a high-resolution nanoparticle sizer that has long been hailed as the researcher's choice for characterizing nanoparticle size for nano applications including nano research and development. SMPS spectrometer sizing is a discreet technique in which the numbers in the concentrations are measured directly without assumptions about the shape or size distribution of the particles. This instrument is pictured in Figure B.2.

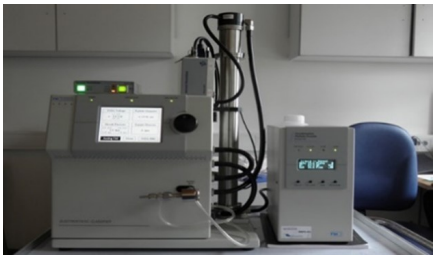

Figure B.2: Scanning mobility particle sizer (SMPS)

The method on which this instrument is based is independent of the refractive index of the particle or fluid and offers a high degree of absolute sizing accuracy and measurement repeatability. Trusted by researchers, the TSI Scanning Mobility Particle Sizer Spectrometer (SMPS) used in this research has provided high-quality data for more than 30 years. It has three components: an electrostatic classifier, a diffusion dryer, and a condensation aerosol generator.

B.0.2 Electrostatic Classifier

An electrostatic classifier can be used as the main component for generating or sizing aerosols with either the long or nano version of a DMA (Figures B.3 and B.4). Given a polydisperse input aerosol, the instrument can output a stream of a monodisperse aerosol containing a known particle size (particle electrical mobility). An electrostatic classifier separates particles by size for high-resolution measurements of particle size distribution. A photo of this instrument is provided in Figure B.5. When used in SMPS spectrometers, for example, monodisperse aerosol exiting the electrostatic classifier passes to a condensation particle counter (CPC), which measures the concentrations of particle numbers. By scanning a portion of the size range from 2 nm to 1000 nm (size range varies according to the SMPS configuration), the SMPS provides precise measurements of the size distribution of the aerosol particles.

Figure B.3: Differential Mobility Analyzer (DMA)

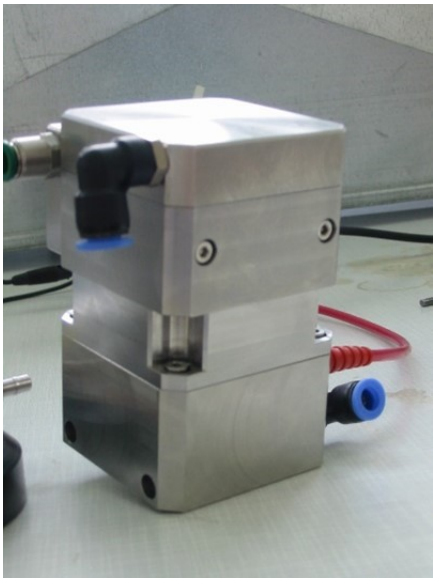

Figure B.4: Nano Differential Mobility Analyzer (S-DMA)

Figure B.5: Electrostatic classifier

B.0.3 Diffusion Dryer

A diffusion dryer is designed as a general-purpose aerosol dryer whose use is accompanied by minimal aerosol loss. The aerosol inlet incorporates a water

trap that collects coarse water droplets. Two concentric cylinders formed by an inner wire screen cylinder and an acrylic outer cylinder contain an annular volume of silica gel. As the wet aerosol flows through the inner cylinder, water vapour diffuses through the wire screen and into the silica gel. Particle loss is minimized because the particles do not come into contact with the silica gel. Figure B.6 displays an image of a diffusion dryer.

Figure B.6: Diffusion dryer

B.0.4 Condensation Aerosol Generator

The aerosol generator used in this research evaporates a tungsten wire through indirect heating. The subsequent controlled condensation of gaseous tungsten oxides generates monomer and polymer tungsten oxide clusters and thus very small tungsten oxide (WOx) particles. The generator needs an external supply of pressurized air for three airflows. The air flows and the heating rate can be adjusted manually by the user in order to influence particle size and concentration. A photo of the condensation aerosol generator used in this research can be seen in Figure B.7.

Figure B.7: Condensation aerosol generator

B.0.5 Faraday Cup Electrometer (FCE 5705) and Scanning Mobility Particle Sizer (SMPS+E)

The circuit was designed for a very fast FCE response time. The FCE contains no slow low-pass filter, which means that the DMA Controller (the analyzing device) must filter the signal so that the difference between the signal and the noise can be optimized. This step can be accomplished digitally with the use of a finite-impulse-response (FIR) filter much more efficiently than with an analog technique. For optimizing the fast response time of the FCE circuit, it is beneficial to run the FCE with a rinse airflow. A clean airflow from the DMA Controller (Figure B.9)is fed into a closed circuit without affecting the particle flow. This rinse airflow prevents particles from entering the area between the housing and the filter head. Improved response times with the use of the rinse airflow have been demonstrated based on a comparison of the results. For this test, a high concentration was measured over one minute and then quickly changed to a low concentration. Figure B.8depicts the operating scheme for this instrumentation setup.

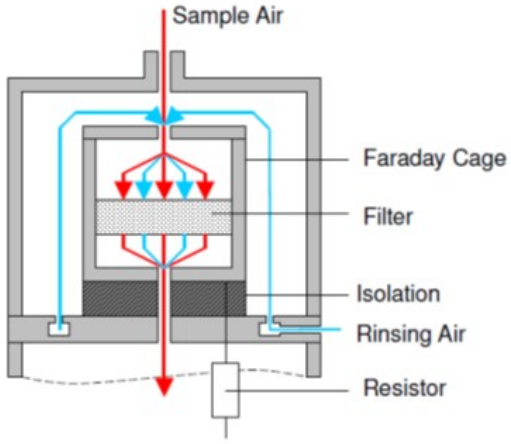

Figure B.8: Faraday cup electrometer (FCE 5705) and scanning mobility particle sizer (SMPS+E)

Figure B.9: DMA Controller

Grimm's unique FCE 5705 design avoids internal contamination through the use of clean rinse air around the isolation area of the cup. This technique results in superior long-term stability, a fast response time, and a very low noise level. This FCE is usually combined with a DMA Controller 5706, which can generate all of the air flows needed, read the FCE signal, and control the voltage of an optional DMA. The DMA Controller 5706 offers a variety of settings for sheath and sample air and thus provides a high degree

of flexibility for varied experimental setups. These instruments are pictured together in Figure B.10.

Figure B.10: FCE 5705 with S-DMA 55-100 and DMA Controller 5706